



**STUDYING EXCITED STATES:  
FROM SMALL MOLECULES TO LARGE  
BIOLOGICAL SYSTEMS**

Inaugural-Dissertation

zur Erlangung des Doktorgrades der  
Mathematisch-Naturwissenschaftlichen Fakultät  
der Heinrich-Heine-Universität Düsseldorf

vorgelegt von

**You Lu**  
aus Changchun

Mülheim an der Ruhr/Düsseldorf 2011



---

Aus dem Institut für Theoretische Chemie und Computerchemie der  
Heinrich-Heine-Universität Düsseldorf

Gedruckt mit Genehmigung der Mathematisch-Naturwissenschaftlichen  
Fakultät der Heinrich-Heine-Universität Düsseldorf

Referent: Prof. Dr. Walter Thiel

Korreferent: Prof. Dr. Christel Marian

Tag der mündlichen Prüfung:





---

Hiermit versichere ich, die hier vorgelegte Arbeit eigenständig und ohne unerlaubte Hilfe angefertigt zu haben. Die Dissertation wurde in der vorgelegten oder in ähnlicher Form noch bei keiner Institution eingereicht. Ich habe keine erfolglosen Promotionsversuche unternommen.

Düsseldorf, den

(You Lu)



**Magna opera Domini,  
exquisita in omnes voluntates ejus.**

上帝作為，精深博大，  
凡樂之處，皆可掘發。



**I dedicate this thesis to my  
loving parents.**



## **Acknowledgements**

First and foremost, I would like to express my sincere and fervent gratitude to my supervisor Prof. Dr. Walter Thiel. It would not have been possible to accomplish this doctoral thesis without his impeccable kindness, immense knowledge, heuristic advice, or indefatigable chasing of perfection.

It is a pleasure to thank the many others who made this thesis possible. I am grateful to Prof. Dr. Christel Marian for reviewing this thesis and giving wonderful lectures of quantum chemistry. I am so thankful to the co-authors in the papers, Prof. Dr. Zhenggang Lan, Dr. Axel Koslowski, Dr. Eduardo Fabiano, Dr. Ganglong Cui, Dr. Oliver Weingart, and the experimental chemists from Heinrich-Heine-Universität, with all of whom I had pleasant and fruitful collaborations.

I would like to acknowledge the kind and generous help over the years by Frau Ursula Scheifhacken, Dr. Jürgen Breidung, and Herr Horst Lenk. I have greatly benefitted from the discussions with Dr. Thomas Keal, Dr. Dongqi Wang, Dr. Tell Tuttle, Dr. Yan Zhang, and Dr. Mario Barbatti. I am also indebted to Yue Chi for translating the abstract of this thesis into German.

Finally, I appreciate the continuous financial support from the Max-Planck-Society.





## List of papers

### Included as part of this thesis:

- (1) *Fluorophores as Optical Sensors for Local Forces*  
S. Marawske, D. Dörr, D. Schmitz, A. Koslowski, Y. Lu, H. Ritter, W. Thiel, C. A. M. Seidel, R. Kühnemuth, *ChemPhysChem* **2009**, *10*, 2041-2048.  
*Own contribution: theoretical calculations*
- (2) *QM/MM Nonadiabatic Decay Dynamics of 9H-Adenine in Aqueous Solution*  
Z. Lan, Y. Lu, E. Fabiano, W. Thiel, *ChemPhysChem* **2011**, *12*, 1989-1998.  
*Own contribution: analyses of decay channels, gradients, and hydrogen-bonding interactions*
- (3) *Hydrogen Bonding Regulates the Monomeric Nonradiative Decay of Adenine in DNA Strands*  
Y. Lu, Z. Lan, W. Thiel, *Angew. Chem.* **2011**, *123*, 6996-6999; *Angew. Chem. Int. Ed.* **2011**, *50*, 6864-6867.  
*Own contribution: all calculations and quantitative analyses*
- (4) *Monomeric Adenine Decay Dynamics Influenced by DNA Environment*  
Y. Lu, Z. Lan, W. Thiel, *J. Comput. Chem.*, **2011**, *33*, 1225-1235.  
*Own contribution: all calculations and quantitative analyses*
- (5) *Nonadiabatic Decay Dynamics of a Benzylidene Malononitrile*  
Z. Lan,<sup>a</sup> Y. Lu,<sup>a</sup> O. Weingart, W. Thiel, *J. Phys. Chem. A*, **2012**, *116*, 1510-1518.  
*Own contribution: surface-hopping dynamics simulations, optimizations, PES scan, and LIIC paths*
- (6) *Electronic Excitation Energies, Three-State Intersections, and Photodissociation Mechanisms of Benzaldehyde and Acetophenone*  
G. Cui, Y. Lu, W. Thiel, *Chem. Phys. Lett.*, **2012**, *537*, 21-26.  
*Own contribution: single-point calculations*

---

<sup>a</sup> contributed equally

**Not included as part of this thesis:**

(7) Nonadiabatic Trajectory Calculations with *Ab initio* and Semiempirical Methods

E. Fabiano, Z. Lan, Y. Lu, W. Thiel, in *Conical Intersections: Theory Computation and Experiment (Adv. Ser. Phys. Chem. Vol. 17)* (Eds.: H. Köppel, W. Domcke, D. R. Yarkony), World Scientific, Singapore, **2011**, pp. 463-496.

*Own contribution: implementation of CASSCF nonadiabatic dynamics simulation and case study on  $CH_2NH_2^+$*

## Abstract

The main goal of this work was to probe a wide panorama of excited-state phenomena. The systems studied range from the small cation  $\text{CH}_2\text{NH}_2^+$  (6 atoms) via the medium-sized chromophore DMN (26 atoms) and the large fluorophore OVP5 (164 atoms) to solvated DNA oligomers ( $> 10^4$  atoms). Correspondingly, the applied computational methods covered *ab initio* theory, semiempirical multi-reference configuration interaction (MRCI), and hybrid quantum mechanical/molecular mechanical (QM/MM) approaches. One aspect of this work was to establish procedures for dealing with the dynamics of a wide variety of excited states, from small molecules in the gas phase toward macromolecules in the solvent phase. The QM/MM investigation of adenine in solvated DNA oligomers was among the most advanced attempts of performing nonadiabatic dynamics simulations for such large biological systems and helped to establish a reliable routine for simulating the photoinduced processes of such complex systems *in silico*.

The tasks in this work included the validation of methodology, the computation of vertical transitions and excited-state geometries, the identification of reaction paths, the simulation of decay dynamics, the search for conical intersections, the construction of potential energy surfaces (PESs), and the prediction of absorption and emission spectra. Major applications were the comprehensive studies of DMN and of adenine in DNA which led to the following results.

DMN was investigated in the gas phase at the semiempirical OM2/MRCI level using surface-hopping nonadiabatic dynamics simulations. A lifetime of 1.2 ps was predicted for the  $S_1$  state, in accordance with experimental observation. The reactive coordinate was found to be the C7=C8 double-bond twisting accompanied by pronounced pyramidalization at the C8 atom. The structures of conical intersections were located by full optimizations. The time-resolved fluorescence of DMN was simulated, which compared well with the experimental spectrum. The use of different active spaces in the OM2/MRCI calculations yielded similar results and thus demonstrated their internal consistency.

## Abstract

---

Adenine embedded in solvated DNA oligomers,  $(dA)_{10}$  and  $(dA)_{10} \cdot (dT)_{10}$ , was studied at the QM/MM (QM=OM2/MRCI) level using surface-hopping dynamics simulations. Both model systems were found to decay from the  $S_1$  to the  $S_0$  state via different monomeric channels, on account of the strong hydrogen-bonding interactions between the Watson-Crick pair in the double-stranded oligomer. Surprisingly the decay times ( $\sim 4-6$  ps) for the current models were ten times longer than those of  $9H$ -adenine in the gas or aqueous phase ( $\sim 0.4-0.5$  ps), while matching one of the time components observed experimentally. Possible reasons were identified for these longer decay times, with focus on the influence of MM environment on the QM adenine chromophore. Steady-state and time-dependent fluorescence spectra were computed to help understand the experimental observations.

## Zusammenfassung

Das Ziel dieser Arbeit war die theoretische Untersuchung elektronisch angeregter Zustände und photoinduzierter Prozesse. Die betrachteten Systeme reichen von dem kleinen Kation  $\text{CH}_2\text{NH}^+$  (6 Atome) über den mittelgroßen Chromophor DMN (26 Atome) und den großen Fluorophor OVP5 (164 Atome) bis hin zu solvatisierten DNA-Oligomeren ( $> 10^4$  Atome). Dementsprechend wurden unterschiedliche Rechenverfahren eingesetzt, angefangen von *ab initio* Methoden über semiempirische Multireferenz-Konfigurationswechselwirkungs-Verfahren (MRCI, multi-reference configuration interaction) bis hin zu kombinierten quantenmechanischen/molekülmechanischen (QM/MM) Methoden. Ein Aspekt dieser Arbeit betraf die Entwicklung zuverlässiger Prozeduren zur Behandlung der Dynamik angeregter Zustände, nicht nur bei kleinen Molekülen in der Gasphase, sondern auch bei Makromolekülen in Lösung. Die QM/MM-Untersuchung von Adenin in solvatisierten DNA Oligomeren gehört zu den ersten Versuchen, nichtadiabatische Simulationen für derartig große biologische Systeme durchzuführen; sie liefert ein zuverlässiges Protokoll für die *in silico* Simulation der photoinduzierten Prozesse in solchen komplexen Systemen.

Die hier beschriebenen Untersuchungen von angeregten Zuständen umfassten Methoden-Validierung, die Berechnung der vertikalen Übergänge und der Geometrien angeregter Zustände, die Identifizierung von Reaktionswegen, die Simulation der Zerfalldynamik, die Suche nach konischen Durchschneidungen, die Konstruktion von Potenzialflächen und die Vorhersage von Absorptions- und Emissionsspektren. Exemplarisch werden im Folgenden die Ergebnisse der umfangreichen Untersuchungen an DMN und an Adenin in DNA umrissen.

Die nichtadiabatische Dynamik von DMN in der Gasphase wurde mit der semiempirischen OM2/MRCI-Methode unter Verwendung von Surface-Hopping Simulationen untersucht. Dabei wurde eine Lebensdauer von 1,2 ps für den  $S_1$ -Zustand erhalten, im Einklang mit experimentellen Befunden. Als reaktive Koordinate stellte sich die Drehung um die C7=C8-Doppelbindung heraus, welche mit einer ausgeprägten Pyramidalisierung am C8-Atom einhergeht. Die Strukturen

## Zusammenfassung

---

der konischen Durchschneidungen wurden durch vollständige Optimierungen lokalisiert. Das simulierte zeitaufgelöste Fluoreszenzspektrum von DMN stimmt gut mit dem experimentellen Spektrum überein. Die Verwendung verschiedener aktiver Räume in den OM2/MRCI-Rechnungen ergab ähnliche Ergebnisse und bestätigte somit deren innere Konsistenz.

Adenin, eingebettet in solvatisierten DNA-Oligomeren,  $(dA)_{10}$  und  $(dA)_{10} \cdot (dT)_{10}$ , wurde auf QM/MM-Niveau (QM=OM2/MRCI) ebenfalls mittels Surface-Hopping Simulationen untersucht. Der nichtadiabatische Zerfall vom  $S_1$  zum  $S_0$  Zustand erfolgt bei beiden Modellsystemen über unterschiedliche monomere Kanäle, weil der im Einzelstrang bevorzugte Kanal wegen der starken Wasserstoffbrücken zwischen dem Watson-Crick-Paar in dem doppelsträngigen Oligomer blockiert ist. Überraschenderweise sind die Abklingzeiten (4-6 ps) für die Oligomere etwa zehn Mal länger als im Falle des *9H*-Adenins in der Gasphase oder wässrigen Phase (0,4-0,5 ps); sie liegen im Bereich einer der experimentell beobachteten Zeitkomponenten. Mögliche Gründe für diese längeren Abklingzeiten wurden identifiziert, insbesondere im Bezug auf den Einfluss der MM-Umgebung auf den QM-Adenin-Chromophor. Zudem wurden stationäre und zeitabhängige Fluoreszenzspektren berechnet, um ein besseres Verständnis der experimentellen Beobachtungen zu ermöglichen.

# Contents

List of figures .....	c
List of tables .....	e
List of abbreviations .....	g
Chapter 1 Introduction .....	1
Chapter 2 Research on excited states: Case studies .....	13
2.1 Semiempirical OM2 approach .....	14
2.2 Vertical transitions .....	16
2.3 Equilibrium geometries and adiabatic excitation energies .....	19
2.4 Photodissociation reactions.....	24
2.5 Nonadiabatic dynamics.....	29
Chapter 3 Excited state dynamics of DMN .....	33
3.1 Minima and conical intersections.....	34
3.2 Decay dynamics .....	37
3.3 Reaction paths.....	38
Chapter 4 Excited state dynamics of adenine .....	41
4.1 From single adenine to DNA strands.....	43
4.2 Absorption and fluorescence spectra.....	47
4.3 Decay dynamics .....	51
4.4 Influence of the environment.....	55
Chapter 5 Conclusion and outlook.....	61
References.....	63





## List of figures

<b>Figure 2.1</b>	Chemical structure of the OPV5 fluorophore.....	17
<b>Figure 2.2</b>	Calculated emission energies (eV) and fluorescence lifetime (ns) as function of the stretching force (nN).....	18
<b>Figure 2.3</b>	Comparison between a typical OVP5 fluorescence measurement and the AM1/MRCI calculation .....	19
<b>Figure 2.4</b>	Mean and standard deviations of the OM2/MRCI and TDB3LYP bond lengths .....	23
<b>Figure 2.5</b>	Mean and standard deviations of the OM2/MRCI and TDB3LYP bond angles .....	24
<b>Figure 2.6</b>	Mean and standard deviations of the OM2/MRCI, TDB3LYP, CASSCF, and CASPT2 adiabatic excitation energies .....	24
<b>Figure 2.7</b>	Chemical structures and atom numbering of benzaldehyde and acetophenone. ....	25
<b>Figure 2.8</b>	Optimized TS structures of the bond cleavage reactions in the $T_1$ state of benzaldehyde and acetophenone.....	27
<b>Figure 2.9</b>	Proposed photodissociation reaction mechanisms of benzaldehyde and acetophenone.....	29
<b>Figure 2.10</b>	Average occupations of the low-lying adiabatic states of gas-phase $\text{CH}_2\text{NH}_2^+$ .....	31
<b>Figure 2.11</b>	Two typical trajectories during the nonadiabatic dynamics of $\text{CH}_2\text{NH}_2^+$ .....	32
<b>Figure 3.1</b>	Conventions used for DMN in this work.....	34
<b>Figure 3.2</b>	Overlays of the optimized minima and CIs of DMN .....	36
<b>Figure 3.3</b>	Two-dimensional contour of the energy difference between the $S_0$ and $S_1$ PESs of DMN.....	39
<b>Figure 3.4</b>	Reaction paths obtained from linear interpolation in internal coordinates (LIIC).....	40
<b>Figure 4.1</b>	The systems investigated in the current work for (9 <i>H</i> -)adenine.....	47
<b>Figure 4.2</b>	Calculated absorption spectra of single adenine .....	48
<b>Figure 4.3</b>	Computed emission spectrum of single adenine in (dA) <sub>10</sub> .....	49

## List of Figures

---

<b>Figure 4.4</b>	Time-resolved emission spectrum of single adenine in (dA) <sub>10</sub> .....	50
<b>Figure 4.5</b>	Average occupation of the adenine low-lying electronic states during the nonadiabatic dynamics.....	53
<b>Figure 4.6</b>	Distribution of the dihedral angles (°) N1-C2-N3-C4 and N1-C5-C6-N6 of adenine at hops.....	54
<b>Figure 4.7</b>	Overlays of the hopping structures of DNA adenine .....	55
<b>Figure 4.8</b>	Components of the S <sub>1</sub> gradient perpendicular to the plane of solvated 9 <i>H</i> -adenine .....	56
<b>Figure 4.9</b>	Distribution of $\ \vec{g}'(\text{H2})\ $ versus $\ \vec{g}'(\text{N6})\ $ at the initial FC geometries of 9 <i>H</i> -adenine.....	57
<b>Figure 4.10</b>	Histogram of the minimum distance between N6 and the water hydrogen atoms at the initial FC geometries.....	57
<b>Figure 4.11</b>	Major environmental effects influencing the nonadiabatic dynamics .....	60

## List of tables

<b>Table 1.1</b>	Properties of theoretical methods for excited-state calculations.....	6
<b>Table 1.2</b>	Scaling of theoretical methods for excited-state calculations.....	7
<b>Table 4.1</b>	A summary of major time-resolved spectral experiments for DNA single strands. ....	44
<b>Table 4.2</b>	A summary of major time-resolved spectral experiments for DNA double strands. ....	44
<b>Table 4.3</b>	A summary of various pathways of DNA decay suggested by spectroscopists.....	46



## List of abbreviations

---

AS	active space
BOMD	Born-Oppenheimer molecular dynamics
CASPT2	complete active space with second-order perturbation theory
CASSCF	complete active space self-consistent field
CC	coupled-cluster
CI	conical intersection
CSF	configuration state function
DNA	deoxyribonucleic acid
FC	Franck-Condon
GA	genetic algorithm
GUGA	graphical unitary group approach
HF	Hartree-Fock
IC	internal conversion
LIIC	linear interpolation in internal coordinates
MCSCF	multi-configurational self-consistent field
MD	molecular dynamics
MO	molecular orbital
MRCI	multi-reference configuration interaction
NACME	nonadiabatic coupling matrix element
OM2	orthogonalization model 2
PES	potential energy surface
QM/MM	quantum mechanical/molecular mechanical
SCF	self-consistent field
SD	standard deviation
TDDFT	time-dependent density functional theory
TS	transition state
UV	ultraviolet
WC	Watson-Crick

---



# Chapter 1

## Introduction

“And God said, Let there be light: and there was light.” – It is the light that makes our planet alive and graceful. It converts inorganic materials into organic compounds, causes phototaxis of bacteria and plants, allows animals and human to see, but causes lesions as well. All the underlying changes behind these diverse phenomena are dominated by photochemical processes. From a quantum mechanical standpoint, the photon absorption with the injection of excess energy can promote an electron from an occupied orbital to a higher-lying unoccupied orbital, and through this transition the system leaves the electronic ground state and becomes an excited state. Therefore, studying excited states is central for understanding the essence of photoinduced processes. Molecules that undergo photochemical changes usually have characteristic spectral features, so that experimentalists are able to reveal their photochemical properties and to identify the underlying processes by spectroscopic means. A large variety of molecular spectroscopy techniques is available to investigate photoinduced reactions in all kinds of small and large molecules. Due to the renowned complexity of spectroscopy, powerful theoretical support is in great demand to interpret the spectral observations. [1] The boost of the computational sciences have made this possible *in silico*. Theoretical simulations can help to comprehend the spectra, to predict short-lived intermediates, and to identify reaction pathways. Many theoretical approaches, ranging from *ab initio*, time-dependent density functional and semiempirical methods to hybrid quantum mechanical/molecular mechanical (QM/MM) treatments, have been applied in the past decades to describe the excited states involved in photochemical processes. [2]

## Chapter 1 Introduction

---

On the part of theory, the quantum model of excited states is based on the time-dependent Schrödinger equation

$$i\hbar \frac{\partial}{\partial t} \Psi(\mathbf{Q}, \mathbf{q}, t) = \hat{H} \Psi(\mathbf{Q}, \mathbf{q}, t), \quad (1.1)$$

where the eigenfunction  $\Psi$  is dependent on the nuclear coordinates  $\mathbf{Q}$ , the electronic coordinates  $\mathbf{q}$ , and the time  $t$ . Since the nuclear motions are much slower than those of the electrons, we usually apply the Born-Oppenheimer (BO) approximation [3] and focus on the electronic motion. The easiest way to solve Eq. 1.1 under the BO approximation is to apply the time-dependent Hartree-Fock (TDHF) approximation, whose time-independent HF version can only give ground-state energies because it represents the wavefunction by a Slater determinant and does not allow for contributions from the virtual orbitals. However, in TDHF theory, the ground state is uncorrelated and the excited states are only partially correlated. The electron correlation is a consequence of the Coulomb repulsion which keeps the electrons apart (more so than in the mean-field HF treatment which only includes an average Coulomb repulsion and the Fermi correlation between electrons with the same spin). The correlation energy is defined as the difference between the exact solution of the nonrelativistic Schrödinger equation and the HF approximation.

There are several ways to describe electron correlation: one is to introduce the inter-electronic distance  $r_{12}$ , which leads to accurate solutions, but is still restricted to rather small systems. Another one is the configuration interaction approach [4] to the solution of the time-independent electronic Schrödinger equation

$$\hat{H} \Psi(\mathbf{q}) = E \Psi(\mathbf{q}). \quad (1.2)$$

Configuration interaction mixes the ground-state configuration with excited-state configurations. The electronic wavefunction is written as a linear combination

$$|\Psi_{\text{CI}}\rangle = C_0 |\Psi_0\rangle + C_S |S\rangle + C_D |D\rangle + \dots, \quad (1.3)$$

where  $|\Psi_0\rangle$  is the ground-state Slater determinant that is normally constructed from the HF molecular orbitals (MOs),  $|S\rangle$  denotes configurations generated by single excitations,  $|D\rangle$  denotes double excitations, and so on. When truncated at the single excitation term, the method becomes CI-S (configuration interaction with single excitations), [5] which normally overestimates excitation energies significantly. [6] Therefore, at least CI-SD (configuration interaction up to double excitations) is commonly used.



---

A linear combination of the excited configurations can alternatively be generated by having an excitation operator  $\hat{T}$  act on the ground-state Slater determinant. This strategy is used in coupled-cluster (CC) theory, which employs an exponential ansatz for the wavefunction:

$$|\Psi_{\text{CC}}\rangle = e^{\hat{T}} |\Psi_0\rangle. \quad (1.4)$$

Similar to configuration interaction, coupled-cluster theory can also be truncated at different levels. Sufficient accuracy is often obtained with CCSD [7] (coupled-cluster up to double excitations) where the wavefunction is expressed as

$$|\Psi_{\text{CCSD}}\rangle = e^{\hat{T}_1 + \hat{T}_2} |\Psi_0\rangle. \quad (1.5)$$

The CCSD(T) [8-11] method, with a perturbative treatment of triple excitations, is usually considered to be the “gold standard” of *ab initio* ground-state quantum chemistry. For excited states, linear response coupled-cluster treatments are normally applied. The coupled-cluster singles-and-doubles model CC2 [12-13] approaches the accuracy of CCSD at reduced computational costs. In the spirit of Møller-Plesset perturbation theory, a one-electron perturbation  $\hat{V}$  is added to the zeroth-order term  $\hat{F}$  (Fock operator) and the first-order contribution  $\hat{\Phi}$  (electron-electron fluctuation potential) in the Hamiltonian:

$$\hat{H} = \hat{H}_0 + \hat{H}_1 + \hat{V} = \hat{F} + \hat{\Phi} + \hat{V} \quad (1.6)$$

In practice, the resolution-of-the-identity (RI) technique [14-16] can be applied in CC2 and related methods to reduce the computational demands.

The *ab initio* methods outlined above, as well as variants such as EOM-CC (equation-of-motion coupled-cluster) and [17] SAC-CI (symmetry-adapted cluster CI), [18] are often successful in calculating excitation energies of closed-shell molecules. However, in general, complicated open-shell systems and excited states require multi-reference treatments that involve more reference functions than just  $|\Psi_0\rangle$ . The MRCI [19-20] (multi-reference configuration interaction) wavefunction is a linear combination of configuration state functions (CSFs) generated by excitations from a series of references  $|^I\Psi_0\rangle$ . Using  $a, b, c, \dots$  for occupied orbitals and  $i, j, k, \dots$  for unoccupied ones, it can be written as

$$|\Psi_{\text{MRCI}}\rangle = \sum_I c^I |\Phi_I\rangle + \sum_{ai} c_a^i |\Phi_a^i\rangle + \sum_{abij} c_{ab}^{ij} |\Phi_{ab}^{ij}\rangle. \quad (1.7)$$

The coefficients  $C$  are determined by the variational principle. [21] The introduction of multiple references allows more flexibility and, therefore, the recovery of a larger amount of

correlation energy. MRCI is thus potentially a very accurate method for excited states, but the computational effort grows sharply with the number of references.

In multi-configurational self-consistent field [22] (MCSCF) theory, the ansatz for the wavefunction is expressed as:

$$|\Psi_{\text{MCSCF}}\rangle = \sum_I c_I |\Psi_I\rangle = \sum_I c_I \left| \prod_i \psi_i \bar{\psi}_i \right\rangle, \quad (1.8)$$

with the MOs being represented as a linear combination of atomic orbitals,  $\psi_i = \sum_{\mu} C_{\mu i} \phi_{\mu}$

(in this thesis we always use  $\mu, \nu, \lambda, \sigma, \dots$  to denote atomic orbitals). The CSF coefficients  $c_I$  and the MO coefficients  $C_{\mu i}$  are both optimized until convergence is reached. A widely applied MCSCF approach is the complete-active-space self-consistent field (CASSCF) method, where the linear combination of CSFs corresponds to full configuration interaction (FCI) within a particular active space [AS, ( $m, n$ ) denotes  $m$  electrons in  $n$  orbitals]. The resulting CASSCF wavefunction is of multi-reference nature and can be used as the reference for MRCI calculations. CASSCF takes into account the so-called static correlation that is induced by the energetic degeneracy or near-degeneracy of different configurations. The missing dynamical correlation caused by instantaneous electronic motions can be computed using second-order perturbation theory, which results in the CASPT2 (complete active space with second-order perturbation theory) method. [23-24] CASPT2 is so far the most generally applicable and accurate method to compute all types of excited states in small and medium-sized molecules. [25-26] For first- and second-row compounds, CASPT2 gives bond lengths with errors of about 0.01 Å and bond energies with deviations of about 2-5 kcal·mol<sup>-1</sup>. [27]

Over the past decade, time-dependent density functional theory [28] (TDDFT) has become very popular. It allows first-principles excited-state calculations on relatively large molecules. Its accuracy depends on the chosen functional. Recent extensive benchmarks on a set of 28 medium-sized organic chromophores gave mean absolute deviations of about 0.2–0.5eV for the investigated functionals. [29] TDDFT is a fast and black-box method, but it cannot be systematically improved due to its DFT nature. It is a single-determinant method and is hence deficient in describing multi-reference situations. Moreover, standard TDDFT fails to give correct long-range properties, e.g., van der Waals and dispersion interactions or charge-transfer excitation energies. [30-31]

---

Two important properties of these first-principles methods are size-consistency and size-extensivity. Being size-consistent means that the energy of a system obtained from one single calculation at the dissociation limit should be equal to the energy sum of the two fragments. [32] A method is size-extensive when the computed energy of a system scales properly with the number of (either interacting or non-interacting) particles. [33] Truncated single-reference configuration interaction methods are neither size-consistent nor size-extensive. In principle, this also applies to truncated MRCI methods, which are however closer to being size-consistent and which normally yield reasonable dissociation curves. Coupled-cluster, CASSCF, and CASPT2 theories are all size-consistent. Some principal properties of first-principles methods are summarized in Table 1.1.

To be practical, a theoretical method needs to balance accuracy and efficiency. The computational demand of a method has a formal scaling with the system size, which is usually represented by the number of basis functions  $N$ .

## Chapter 1 Introduction

---

Table 1.2 lists the scaling of some mainstream methods for excited-state calculations. The scope of possible applications is limited by the computational cost, which often increases sharply upon enlargement of the system. High-level *ab initio* methods are expensive, and applications are feasible only for relatively small systems. TDDFT (hybrid,  $N^3$ ), CI-S, as well as CC (  $N^4$  ) scales much better and can thus handle larger systems, for example in Ref. [34-36], up to  $\sim 200$  second-row atoms. However, as mentioned above, standard TDDFT has to be used with caution due to its inherent deficiencies.

**Table 1.1** Properties of theoretical methods for excited-state calculations

	size-consistent	size-extensive	iterative	variational
TDDFT	no	no	yes	yes
CI-S, CI-SD, etc.	no	no	no	yes
CC	yes	yes	yes	no
CASSCF	yes	yes	no	yes
CASPT2	yes	nearly	yes	no
MRPT [37]	nearly	nearly	yes	no
MRCI (truncated)	nearly	nearly	yes	yes
FCI	yes	yes	no	yes

**Table 1.2** Scaling of theoretical methods for excited-state calculations:  $N$  is the number of basis functions, and  $2k$  is the number of active electrons in the MCSCF method.

method	scaling	size limit of system to apply
TDDFT	$N^3$	medium-large
CI-S	$N^4$	medium, 10-100 atoms
CCS	$N^4$	medium, 10-100 atoms
MCSCF	$16^k/k\pi$	small-medium, AS up to (14,14)
CC2	$N^5$	
CI-SD	$N^6$	
CCSD	$N^6$	
CCSD(T)	$N^7$	< 20
MRCI		small, AS $\leq$ (14,14)
MRMP $n$		small
MRCC/FCI		very small

Semiempirical quantum chemical methods have been developed for approximate calculations on large molecules. They employ drastic simplifications, which reduce the computation time by orders of magnitude compared with the first-principles methods. Here we briefly summarize their essential features. Formally, the standard semiempirical methods are formulated as HF methods that employ a minimal valence basis set and make use of a number of integral approximations such as the zero differential overlap (ZDO) approximation. [38] As a consequence, the overlap matrix  $\mathbf{S}$  is replaced in the secular equations ( $\mathbf{FC} = \mathbf{SCE}$ ) by the unit matrix, and in the construction of the Fock matrix  $\mathbf{F}$ , most of the two-electron integrals are neglected (e.g., all three-center and four-center terms). Using 1, 2, ... to denote electrons and  $A, B, C, D, \dots$  to denote atoms (centers), the two-electron integrals are defined as

$$\langle \mu\nu | \lambda\sigma \rangle = \iint \chi_\mu^A(1) \chi_\nu^B(2) \frac{1}{r_{12}} \chi_\lambda^C(1) \chi_\sigma^D(2) d\tau d\tau. \quad (1.9)$$

To reduce the computational costs, Eq. 1.9 is simplified in NDDO (neglect of diatomic differential overlap) approximation [39] as follows:

$$\langle \mu\nu | \lambda\sigma \rangle = \delta_{AB} \delta_{CD} \langle \mu^A \nu^B | \lambda^C \sigma^D \rangle. \quad (1.10)$$

Even more drastic approximations for the two-electron integrals are applied in earlier semiempirical approaches (e.g., CNDO: complete neglect of differential overlap; INDO, intermediate neglect of differential overlap). [39] For excited-state calculations, an INDO variant (INDO/S) has remained popular over the years, [40] but the modern semiempirical methods are generally based on the more refined NDDO approximation, for example MNDO (modified neglect of differential overlap), [41] PM3 (parameterized model), [42] and AM1 (Austin model 1). [43] Methods that go beyond the standard MNDO model include the

orthogonalization-corrected models OMX ( $X = 1, 2, 3$ ), [44-48] that are described in more detail in Section 2.1.

For calculating the excited-state properties of large molecules, it is practical to employ the semiempirical SCF (self-consistent-field) wavefunction as the starting point for a correlation treatment, e.g., configuration interaction. An efficient semiempirical MRCI implementation has been developed [49-50] on the basis of the graphical unitary group approach (GUGA), [51-52] which enables fast excited-state calculations. In a systematic benchmark study with high-level *ab initio* reference data, the OM2/MRCI and OM3/MRCI methods were found to give satisfactory results, being superior to the established MNDO-type methods – the mean absolute deviations were around 0.4-0.5 eV for the vertical excitation energies of the benchmark suite. [53] These methods are thus promising tools to study the excited states of large systems and to perform excited-state molecular dynamics (MD) simulations. Most investigations in this work have been conducted with the semiempirical MRCI approach, which will be further discussed in Section 2.1.

Even semiempirical excited-state calculations encounter practical limits in systems with several hundreds of atoms. For biomolecules and condensed-phase systems with thousands of atoms, there is thus currently no quantum method available that could capable perform a realistic excited-state simulation. A practical way out of this dilemma is to turn to hybrid QM/MM approaches. [54-55] Since photoinduced electronic transitions are normally localized in a small region of space, the system can be safely partitioned into two subdomains: the smaller QM part contains the chromophore and is treated at an appropriate quantum level (be it *ab initio*, TDDFT, or semiempirical); while the larger MM part comprises the remainder of the system and is treated classically by a force field. The complete QM/MM Hamiltonian has the form

$$\hat{H}_{\text{QM/MM}} = \hat{H}_{\text{QM}} + \hat{H}_{\text{MM}} + \hat{H}_{\text{QM-MM}}, \quad (1.11)$$

where  $\hat{H}_{\text{QM-MM}}$  is responsible for the bonded, van der Waals, and electrostatic interactions between the two layers. [54-55] For the electrostatic QM/MM interactions, there is a hierarchy of models available. [56] The most popular choice is electronic embedding, with a polarized QM part and a nonpolarized MM part. The QM wavefunction is calculated in the presence of the environment, by incorporating the MM point charges in the one-electron QM Hamiltonian, thus capturing its polarization by the surroundings.

---

By now, we have outlined the major computational methods for computing the electronic structure of excited states. Within the BO approximation, these methods are used to describe vertical excitation properties, minimum-energy structures, and potential energy surfaces (PESs) in the Franck-Condon (FC) region. In many systems, when following the nuclear motion along some particular coordinate, two or more PESs of different electronic states may approach and cross each other, i.e., their energies become near-degenerate or degenerate. In such regions, these electronic states are composed of highly mixed configurations, and they strongly couple with each other. The BO approximation breaks down in such a situation, thus necessitating a nonadiabatic description. The nuclear wave packet can propagate from one PES to another one via such a crossing, so that a nonadiabatic transition is induced. Such nonadiabatic transitions play a central role in many photoinduced processes including internal conversion, fluorescence quenching, nonradiative energy dissipation, and so on. [57-65]

Various theoretical models and computational techniques have been developed and applied for modeling nonadiabatic transitions. It is possible to locate the structures of conical intersections or minimum-energy crossing points (MECPs) using several algorithms. [66-75] The adiabatic routes connecting these optimized crossing structures with the FC geometry can be constructed by linearly interpolated paths. This gives access to the PES topology of the excited state(s), which provides much information about favorable mechanisms, transition states (TSs), energy barriers, and so forth. For a detailed understanding of the time evolution of the system, it is necessary to study its dynamics explicitly. A number of methods, from fully quantum to mixed quantum-classical, have been implemented to simulate the nonadiabatic molecular dynamics. The full quantum treatments solve the time-dependent Schrödinger equation, usually with approximations at different levels, and thus determine the quantal motion of the nuclei, e.g., by using the multi-configuration time-dependent Hartree [76-78] (MCTDH) or the *ab initio* multiple spawning [79-80] (AIMS) method. However, the application scope of these methods is still rather limited because of the steep scaling of the computational effort with system size and degrees of freedom.

Semiclassical methods handle the dynamics of nuclei in a classical manner while describing the electronic motion in a quantum framework. Representative approaches of this type include the mean-field Ehrenfest method, surface-hopping methods, quantum-classical Liouville descriptions, and mapping procedures. [81] The surface-hopping methods are among the most widely tested and successfully applied approaches. [82-87] They treat the nuclear motion by

classical dynamics on single adiabatic surface while allowing stochastic hops between surfaces. The relevant energies, gradients, and coupling terms are calculated on the fly. In the current work, we mainly focus on Tully’s trajectory surface hopping (TSH) method. [88-89] During the MD trajectories, the nuclear motions may bring the system into the vicinity of a conical intersection or a crossing seam, and the much increased interstate coupling then enables a nonadiabatic transition between the crossing states  $I$  and  $J$ . The instantaneous switch between these states is called a “hop”. The probability that a hopping event takes place is determined by

$$P^{IJ} = \frac{2 \int_t^{t+\Delta t} dt \operatorname{Re}(C_J^*(t)C_I(t)\dot{\mathbf{R}} \cdot \mathbf{d}^{IJ})}{|C_J(t)|^2}, \quad (1.12)$$

where  $\dot{\mathbf{R}}$  represents the nuclear velocity and  $\mathbf{d}^{IJ}$  is the nonadiabatic coupling matrix element (NACME). The quantum population  $|C_I(t)|^2$  is assumed to be constant during the small time interval  $\Delta t$ . [65] In TSH simulations, the quantum mechanical computation of the energies, gradients, and coupling terms is generally the rate-determining bottleneck. Therefore, TSH methods have been combined with semiempirical electronic structure methods [65,90-91] to reduce the computational cost. Semiempirical TSH approaches have been implemented both at the QM and QM/MM level [65,92-95] to enable explicit efficient simulations of nonadiabatic transitions in large systems. Excited-state lifetimes, decay channels, and time-dependent absorption and emission spectra can be determined from TSH trajectories. Coupled with conventional static quantum computations, TSH simulations serve as a powerful tool for studying excited states.

The research in this thesis covers a wide variety of excited-state calculations, including method validation and applications concerning vertical and adiabatic transition properties, equilibrium excited-state geometries, photoinduced reactions, and nonadiabatic dynamics. In Chapter 2, we address each of these topics by presenting an illustrative case study. This overview is followed by two comprehensive investigations. Chapter 3 addresses the nonadiabatic decay dynamics of the medium-sized benzylidene malononitrile derivative DMN (26 atoms) in the gas phase. This allows the identification of the favorable decay channel of the DMN chromophore in the  $S_1$  state. The computed absorption and emission spectra, as well as the fluorescence lifetime, are in good agreement with the experimental observations. The validity of the OM2/MRCI approach is also verified by achieving



---

consistent results with different ASs and at different excitation levels. Chapter 4 presents systematic studies on the decay dynamics of adenine – from the gas phase (15 atoms, QM) to the condensed phase ( $> 10^4$  atoms, QM/MM). The internal conversion of a single QM adenine embedded in solvated DNA oligomers is found to be ten times slower than in the gas phase or in water, matching one of the experimentally reported components. This deceleration is attributed to specific effects arising from the DNA environment. There are distinct decay pathways of adenine embedded in DNA single and double strands, which are governed by the hydrogen-bonding interaction between the Watson-Crick base pairs. These studies have led to reliable procedures for computing and simulating excited states in systems of different size, from small molecules to large biological systems.



## Chapter 2

# Research on excited states: case studies

Generally speaking, theoretical calculations are more difficult for electronically excited states than for ground states. On the one hand, this is due to the more complicated excited-state electronic structure and PES topology, with an interplay of several states, and on the other hand, to the wealth of excited-state phenomena to be modeled. Theoretical work on excited states thus involves many different tasks, including methodology development, the computation of steady-state absorption spectra (vertical excitation energies and oscillator strengths), the determination of excited-state equilibrium structures, the study of photochemical reactions, the simulation of excited-state dynamics, and the calculation of time-resolved emission spectra. This chapter addresses most of these topics. We first outline the semiempirical OM2 approach employed in the current work and the implementation of genetic algorithms for future reparametrizations (Section 2.1). [96] Thereafter we review semiempirical MRCI calculations on the vertical transitions of the fluorophore OPV5 (Section 2.2), [97] OM2/MRCI benchmarks for adiabatic properties (Section 2.3), [98] a CASPT2/CIPT2//CASSCF study on the photodissociation reactions of benzaldehyde and acetophenone (Section 2.4), [99] and an example of nonadiabatic dynamics at the CASSCF level (Section 2.5). [65]

## 2.1 Semiempirical OM2 approach

As introduced in Chapter 1, many computational methods have been developed to handle electronically excited states at different levels of accuracy. The semiempirical models are designed for high computational speed, without sacrificing too much accuracy. Here we present a brief introduction to the semiempirical OM2 approach that goes beyond the standard MNDO model by an explicit introduction of orthogonalization corrections.

The NDDO secular equation

$${}^{\text{NDDO}}\mathbf{F} {}^{\text{NDDO}}\mathbf{C} = {}^{\text{NDDO}}\mathbf{C}\mathbf{E} \quad (2.1)$$

has the same form as the Roothaan-Hall equation in an orthogonalized basis,

$$\mathbf{F}\mathbf{C} = \mathbf{S}\mathbf{C}\mathbf{E} \Rightarrow {}^\lambda\mathbf{F} {}^\lambda\mathbf{C} = {}^\lambda\mathbf{C}\mathbf{E}, \quad (2.2)$$

where  $\mathbf{F}$ ,  $\mathbf{C}$ ,  $\mathbf{S}$ , and  $\mathbf{E}$  represent the Fock matrix, the MO coefficient matrix, the overlap matrix, and the diagonal matrix of eigenvalues, respectively, and a superscript  $\lambda$  indicates an orthogonal basis. Assuming that

$${}^{\text{NDDO}}\mathbf{F} \approx {}^\lambda\mathbf{F} \quad (2.3)$$

we need to find a suitable semiempirical representation for  ${}^\lambda\mathbf{F}$  which is a sum of one- and two-electron parts,

$${}^\lambda\mathbf{F} = {}^\lambda\mathbf{H} + {}^\lambda\mathbf{G}. \quad (2.4)$$

At the *ab initio* level, the one-electron core Hamiltonian matrix is transformed from the original non-orthogonal basis to an orthogonal basis using

$${}^\lambda\mathbf{H} = \mathbf{S}^{-1/2}\mathbf{H}\mathbf{S}^{-1/2}. \quad (2.5)$$

The  $\mathbf{S}^{-1/2}$  matrix can be expanded in a binomial series

$$\mathbf{S}^{-1/2} = (1 + \mathbf{S}')^{-1/2} = 1 - \frac{1}{2}\mathbf{S}' + \frac{3}{8}\mathbf{S}'^2 - \frac{5}{16}\mathbf{S}'^3 + \dots, \quad (2.6)$$

so that the core Hamiltonian becomes

$$\begin{aligned} {}^\lambda\mathbf{H} &= \mathbf{S}^{-1/2}\mathbf{H}\mathbf{S}^{-1/2} \\ &= \mathbf{H} - \frac{1}{2}(\mathbf{S}'\mathbf{H} + \mathbf{H}\mathbf{S}') + \frac{3}{8}(\mathbf{S}'^2\mathbf{H} + \mathbf{H}\mathbf{S}'^2) + \frac{1}{4}\mathbf{S}'\mathbf{H}\mathbf{S}' + \mathbf{O}(\mathbf{S}'^3). \end{aligned} \quad (2.7)$$

Semiempirical one-electron orthogonalization corrections can be devised by considering the dominant terms in this expansion. This has led to a series of orthogonalization models (OMX,  $X = 1, 2, 3$ ). [44-48] In OM2, the core Hamiltonian matrix elements are chosen as

$$\begin{cases} H_{\mu\mu} = U_{\mu\mu} + \sum_B [Z_B \langle \mu\mu | ss \rangle^s + V_{\mu\mu,B}(\text{ORT}) + V_{\mu\mu,B}(\text{PEN}) + V_{\mu\mu,B}(\text{ECP})] \\ H_{\mu\nu} = \sum_B [Z_B \langle \mu\nu | ss \rangle^s + V_{\mu\nu,B}(\text{ORT}) + V_{\mu\nu,B}(\text{PEN}) + V_{\mu\nu,B}(\text{ECP})] \\ H_{\mu\lambda} = \beta_{\mu\lambda} + \sum_C V_{\mu\lambda,C}(\text{ORT}) \end{cases} \quad (2.8)$$

They contain orthogonalization corrections (ORT) to account for exchange repulsion, penetration integrals (PEN) for a refined treatment of electrostatics, and effective core potentials (ECP) to capture core-valence interactions. In these terms, there are parameters that can be adjusted against experimental and/or theoretical reference data. This also applies to the one-center one-electron energies  $U_{\mu\mu}$  in Eq. (2.8), and further parameters appear in the resonance integrals  $\beta_{\mu\lambda}$ .

Unlike *ab initio* methods, semiempirical approaches can be improved by reparametrization with different training sets to gain either a more balanced or a more case-specific performance. The parametrization is a many-dimensional global optimization problem. For example, in OM2, the commonly used first-row and second-row atoms H, C, N, and O have altogether 76 numerical parameters that need to be optimized. There are a number of strategies available for solving such mathematical optimization problems, among which genetic algorithms (GAs) are considered to offer a relatively large chance to find the global minimum. [100] GA-based optimization methods do not require any prior knowledge about the parameters, so that they have been applied by many researchers for optimizing purposes, especially also for parameterizing semiempirical methods. [101-106]

To prepare for a possible reparametrization of the OM2 method, specifically with regard to excited-state properties, GA-based methods have been implemented in the parametrization program PP99. [98,107] The open-source library PGAPack 1.1 [108] was incorporated. The fitness function that reflects the overall deviation of OM2/MRCI results from the reference data is chosen as

$$F_{\text{eval}} = \sum_p W_p \sqrt{\frac{\sum (P - P_{\text{ref}})^2}{N_p}}, \quad (2.9)$$

where  $W$  is the weight factor for a given excited-state property  $P$  which may e.g. be an excitation energy, a dipole moment, an oscillator strength, or a gradient. The proper working of the GA code has been tested and established for a range of different GA options. However, no serious reparametrization of the OM2 method has been attempted. The main reason was

the lack of reliable and comprehensive excited-state reference data at an early stage of the thesis. These reference data have later been generated in our group by systematic *ab initio* benchmarks for a representative set of organic chromophores. When this benchmark set had been completed, the focus of my work had shifted to the other topics described in this thesis. The reparametrization of OM2 and related methods is therefore still pending, but the implementation of the GA algorithms in the parametrization program has at least provided a working code for this task.

## 2.2 Vertical transitions

Because of the FC principle, molecular absorption and emission spectra are directly related to vertical transitions (either upward or downward). Computation of vertical transition properties thus plays a fundamental role in the interpretation and prediction of experimental spectra. Realistic theoretical modeling can be helpful in designing novel materials built from molecules that possess particular spectroscopic characteristics. In this context, we summarize the results of our semiempirical MRCI calculations on an oligoparaphenylenevinylene (OPV) derivative with unique spectral characteristics. [97]

OPVs constitute a class of fluorophores that feature tunable emission spectra when an external unidirectional force is imposed. [109-110] The particular derivative OPV5 is a large molecule with 164 atoms, consisting of a long conjugated backbone with repeated styryl units and four bulky alkyl side chains (see Figure 2.1). OPV5 has a very broad emission band that ranges from the red (555-645nm, 1.9-2.2 eV) to the green (478-555 nm, 2.2-2.6 eV) region. The fluorescence wavelength shifts upon applying an external mechanical force. When being mechanically stretched in a polyvinyl chloride (PVC) foil, OPV5 emits a significantly red-shifted fluorescence. Therefore, OPV5 has the potential to be used as an optical sensor for local mechanical forces.

To perform theoretical calculations and relate the observed spectroscopic changes to the underlying changes in the molecular properties, a proper method has to be chosen both with regard to speed and accuracy. For a molecule as large as OPV5, correlated *ab initio* calculations are not feasible. Even for TDDFT, the molecule is very big, and there are also well-documented TDDFT problems with such large conjugated systems. Therefore,

semiempirical methods appear to be the best option in this case. To evaluate the performance of different semiempirical methods, geometry optimizations and frequency analyses were carried out for three model compounds, *E*-stilbene, phenetole, and heptoxystilbene (see the supporting information of [97]). AM1 is among the methods whose results agree best with the *ab initio* results, and it has therefore been selected as the model Hamiltonian for the calculations on OPV5.

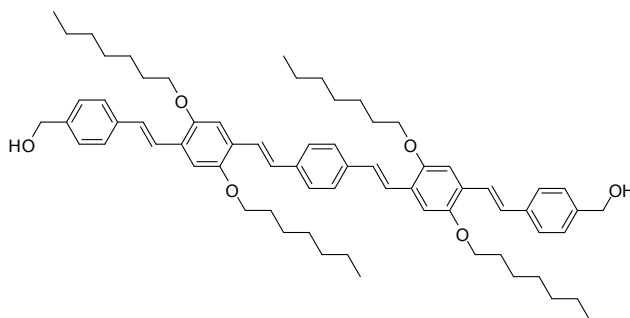


**Figure 2.1** Chemical structure of the OPV5 fluorophore

Full AM1/MRCI-SD optimizations employing a large (24,24) active space were performed for two conformers of OPV5 in  $C_2$  and  $C_i$  symmetry, respectively. Both conformers gave nearly identical results so that the following discussion only refers to the  $C_i$  conformer. The OPV5 emission energy and fluorescence lifetime are plotted as function of the stretching force in Figure 2.2. In these scans, the distance between the outermost ring carbon atoms of OPV5 was elongated (to 32.0 Å) starting from the optimized ground state minimum (29.2 Å), and all other coordinates of the molecule were fully relaxed. Forces were computed by analytical differentiation of a cubic-spline fit of the computed potential curves. No cleavage of any chemical bond was observed, even at the highest applied force (6.9 nN). This is consistent with reported rupture forces for C-C single bonds in the range of 2.3 to 13.4 nN [111] if one takes into account the higher stability of OPV5 due to the partial double bond character of its molecular backbone. The computed fluorescence energy goes up from 2.6 eV to 2.8 eV, while the estimated fluorescence lifetime is reduced from 1.2 ns to 1.0 ns. Here, the lifetime (in s) is given by

$$\tau = \frac{3}{2f_{10}\tilde{\nu}^2}, \quad (2.10)$$

where  $f_{10}$  is the  $S_1 \rightarrow S_0$  transition oscillator strength, and  $\tilde{\nu}$  is the corresponding transition

energy in  $\text{cm}^{-1}$ .

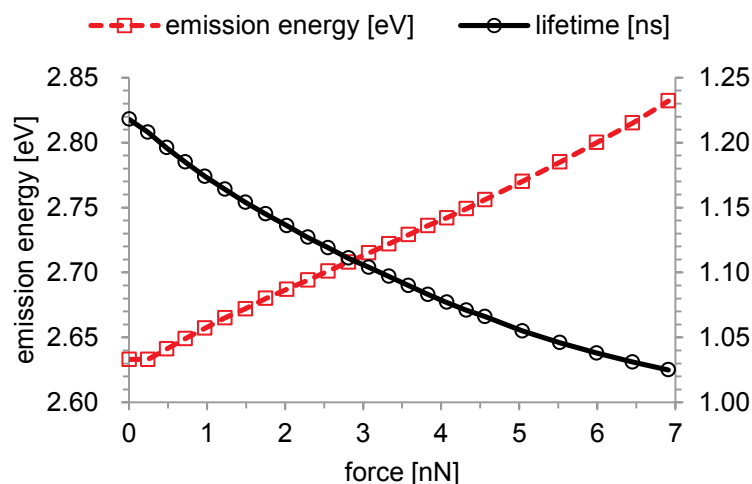


**Figure 2.2** Calculated emission energies (eV) and fluorescence lifetime (ns) as function of the stretching force (nN)

The experimental part of this collaborative work was done by researchers of the Heinrich-Heine-Universität Düsseldorf. They measured the fluorescence anisotropy and estimated the force acting on OPV5 in the foil. The fluorescence anisotropy was found to increase with the force, which indicates a reorientation of the fluorophores within the matrix. This can be explained by the corresponding conformational change in our theoretical calculations of the stretched OPV5. Experimentally, the fluorescence lifetime decreased by approximately 2.5% (~25 ps). In addition, there was an increase in the emission energy of about 0.2% (i.e., a blue shift of 1.2 nm). Comparing the experimental observations and the theoretical predictions, we find qualitative consistency both with regard to the reduction of the fluorescence lifetime and the direction of the blue shift (see Figure 2.3). A more quantitative comparison is not feasible, because the precise force on single OPV5 molecules in the PVC foil is not known experimentally. The experimental results seem to indicate an extremely efficient transfer of mechanical force onto the chromophore, that is, a force per molecule approximately two orders of magnitude higher than average. Therefore, a more realistic view of the process may also have to add lateral interactions of the polymer chains with the side chains of the chromophore to promote its unwinding.

In summary, our joint experimental and theoretical study proves the feasibility of fluorescence-based local force probes for polymers under tension. Improved optical sensors



of this type should in principle be able to monitor local mechanical stress in transparent samples down to the single-molecule level, which harbors promising applications in polymer science and nanotechnology.

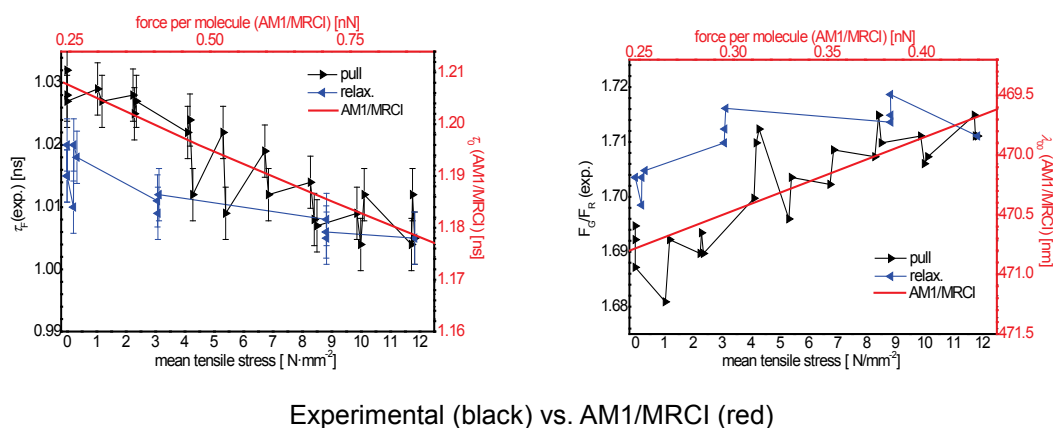


**Figure 2.3** Comparison between a typical OVP5 fluorescence measurement and the AM1/MRCI calculation: (a) lifetimes (ns) as function of the stretching force; (b) green to red shift ratio as function of the stretching force.

## 2.3 Equilibrium geometries and adiabatic excitation energies

A proper description of equilibrium geometries and adiabatic excitation energies is a key prerequisite in theoretical excited-state studies. While extensive benchmarks are available for vertical transitions, [53] there is much less validation on the performance of semiempirical MRCI methods for excited-state minima. Therefore we evaluated the excited-state equilibrium geometries and adiabatic excitation energies for the OM2 approach, which is among the most reliable semiempirical methods. [96] To be on the safe side with regard to correlation, we performed OM2/MRCISDTQ calculations (up to quadruple excitations).

106 electronically excited states in 32 organic molecules were covered in the benchmark set. The choice of these molecules and states was made on the basis of published CASSCF results, to allow for comparative statistical evaluations. The following 32 molecules were considered (with the point group specified in parenthesis): 9*H*-adenine ( $C_1$ ), acetaldehyde ( $C_1$ ), acetone

(C<sub>s</sub>), acetophenone (C<sub>s</sub>), acetylene (C<sub>2v</sub>, C<sub>2h</sub>), acrolein (C<sub>s</sub>), 2-amino-9-methylpurine (C<sub>1</sub>), aniline (C<sub>1</sub>), benzaldehyde (C<sub>s</sub>), *p*-benzoquinone (D<sub>2h</sub>), biphenylene (D<sub>2h</sub>), butadiene (C<sub>2v</sub>, C<sub>2h</sub>), cytosine (C<sub>1</sub>), diazomethane (C<sub>2v</sub>), dibenzo-*p*-dioxin (D<sub>2h</sub>), formaldehyde (C<sub>s</sub>), glyoxal (C<sub>2h</sub>), guanine (C<sub>1</sub>), 1-hydroxy-2-acetonaphthone (C<sub>s</sub>), indole (C<sub>s</sub>), maleimide (C<sub>2v</sub>), nitrosomethane (C<sub>s</sub>), propenoic acid anion (C<sub>s</sub>), pyridine (C<sub>2v</sub>, C<sub>s</sub>), pyrrole (C<sub>2v</sub>), C<sub>5</sub>H<sub>6</sub>NH<sub>2</sub><sup>+</sup> (Schiff base, C<sub>s</sub>), C<sub>10</sub>H<sub>12</sub>NH<sub>2</sub><sup>+</sup> (Schiff base, C<sub>s</sub>), *trans*-stilbene (C<sub>2</sub>), styrene (C<sub>s</sub>), *s*-tetrazine (D<sub>2h</sub>), thymine (C<sub>1</sub>), and uracil (C<sub>1</sub>). The symmetry constraints applied, as well as active spaces, are analogous to those of the CASSCF reference studies in the literature. [112-138] Only valence n→π\* and π→π\* excited states were included, while electronic states involving a dominant excitation from σ or to σ\* orbitals were not taken into account. Rydberg states were also excluded from our assessment because of the lack of Rydberg orbitals in the minimum basis set used by semiempirical methods.

The evaluation employed statistical comparisons with high-level reference data from the literature. The geometric parameters were compared to published CASSCF reference values. We evaluated the carbon-carbon (CC), carbon-hydrogen (CH), carbon-nitrogen (CN), carbon-oxygen (CO), and nitrogen-hydrogen (NH) bond lengths, i.e., those involving the elements currently available in OM2 (H, C, N, and O). In the data analysis, single and double bonds were not distinguished. TDDFT geometry optimizations were performed to supplement the OM2/MRCI results (B3LYP/TZVP using TurboMole 5.71 [139]). The adiabatic excitation energies obtained from OM2/MRCI, TDDFT, CASSCF, and CASPT2//CASSCF were compared to experimental gas-phase data from the literature. In the following we discuss the results for bond lengths, bond angles, and adiabatic excitation energies.

### ► Bond lengths

Figure 2.4 shows the bond length deviations from the CASSCF reference values obtained with OM2/MRCI and TDDFT. The results are sorted into groups consisting of n→π\*/π→π\* and singlet/triplet transitions. OM2/MRCI predicts CC and CN bond lengths about as well as TDDFT. In particular, the standard deviation for the CC bond lengths in the π→π\* and singlet states is almost 0.01 Å smaller in OM2/MRCI than in TDDFT, mainly due to the failure of TDDFT for the long retinal model Schiff base C<sub>10</sub>H<sub>12</sub>NH<sub>2</sub><sup>+</sup>, [140] where the maximum deviation given by the latter method (TDDFT) reaches -0.132 Å (-0.028 Å by OM2). Notably, the OM2/MRCI mean deviation for the CN bond lengths is only 0.003 Å. For the CH bond lengths, OM2/MRCI gives an average overestimation of 0.013 Å, somewhat worse

## 2.3 Equilibrium geometries and adiabatic excitation energies

---

than TDDFT. This deviation is caused by a systematic overestimation of the CH bond lengths adjacent to C=O double bonds (whose length is generally underestimated, see below) in carbonyl compounds. Likewise, the NH bond lengths are also systematically overestimated by 0.010~0.015 Å. In the statistics, the largest deviations are found for the CO bond lengths, which are underestimated in OM2/MRCI on average by -0.029 Å in the  $n \rightarrow \pi^*$  states, and the standard deviation is even less satisfactory (0.054 Å); similar values are found for TDDFT (-0.021 Å and 0.049 Å). These systematic deviations are probably at least partially due to the well-documented tendency of CASSCF to overestimate the CO bond distances (e.g., Ref. [141-143]). It would therefore be advisable to use other high-level *ab initio* reference data for the statistical evaluation (which are available in the literature to the same extent as CASSCF results).

### ► Bond angles

Considering the difficulty of defining subgroups, the 277 bond angles were treated as a single group in the statistics. The bond angles in the OM2/MRCI optimized excited-state structures are in very good agreement with the CASSCF reference values (see Figure 2.5), with mean and standard deviations of  $-0.2^\circ$  and  $3^\circ$ , respectively.

### ► Torsions

Bond torsions (characterized by dihedral angles) often play an important role in the dynamics of excited states. Here, we only note that most torsional features in the CASSCF geometries are qualitatively reproduced by OM2/MRCI and TDDFT. A quantitative assessment was not attempted. Generally speaking, the comparisons for bond lengths, bond angles, and dihedral angles show that OM2/MRCI gives reasonable excited-state geometries, which are overall similar to the published CASSCF structures of the reference molecules.

### ► Adiabatic excitation energy

Some previous OM2/MRCI studies have reported promising results for adiabatic excitation energies (e.g., [65,93-95,140,144-145]), but there has not yet been a systematic assessment. Here, we compare the OM2/MRCI results with accurate reference data from gas-phase experiments. Such experimental data are available for 53 out of the 106 excited states in our benchmark set – in the remaining cases, these experimental energies are not available, usually because of very low oscillator strengths or uncertainties in the spectroscopic assignments. All experimental reference energies refer to the 0-0 transition ( $T_{00}$ ). In addition to CASSCF energies, our statistics also incorporate CASPT2 single-point energies at CASSCF

equilibrium geometries (i.e., CASPT2//CASSCF), since this is in practice the most accurate level that is still affordable for medium-sized organic systems. Very few CAS-based energies in the literature include zero point energy (ZPE) corrections. For the sake of consistency, all our theoretical energies are therefore given in terms of electronic energies ( $T_e$ ). As a matter of fact, the inclusion of ZPE corrections typically lowers the adiabatic excitation energy by about 0.1-0.2 eV (e.g., Ref. [130]). Since these shifts are rather systematic and small, our comparisons below are statistically meaningful.

The statistical results are shown in Figure 2.6. Obviously OM2/MRCI gives fairly accurate adiabatic excitation energies. The mean and standard deviations from OM2/MRCI (-0.06 and 0.34 eV) are lower than those from TDDFT (-0.15 and 0.49 eV) or CASSCF (0.31 and 0.59 eV) and similar to those from CASPT2//CASSCF (-0.09 and 0.35 eV).

In summary, our statistical evaluation shows a sound performance of the OM2/MRCI approach in excited-state geometry optimizations. OM2/MRCI provides equilibrium geometries in good agreement with CASSCF. Judging from the mean and standard deviations relative to the CASSCF reference structures, OM2/MRCI and TDDFT give geometries of similar quality. Compared with accurate experimental data, the adiabatic excitation energies from OM2/MRCI are about as good as those from CASPT2//CASSCF and superior to those from CASSCF and TDDFT. This is especially encouraging in view of the fact that the semiempirical OM2/MRCI approach is computationally very fast in comparison with TDDFT and *ab initio* methods. [49] After proper individual validation, the OM2/MRCI approach is thus expected to be a powerful tool for investigating photoinduced processes, especially for large biomolecular systems. In the current work, OM2/MRCI is applied in Chapter 3 and Chapter 4.

## 2.3 Equilibrium geometries and adiabatic excitation energies

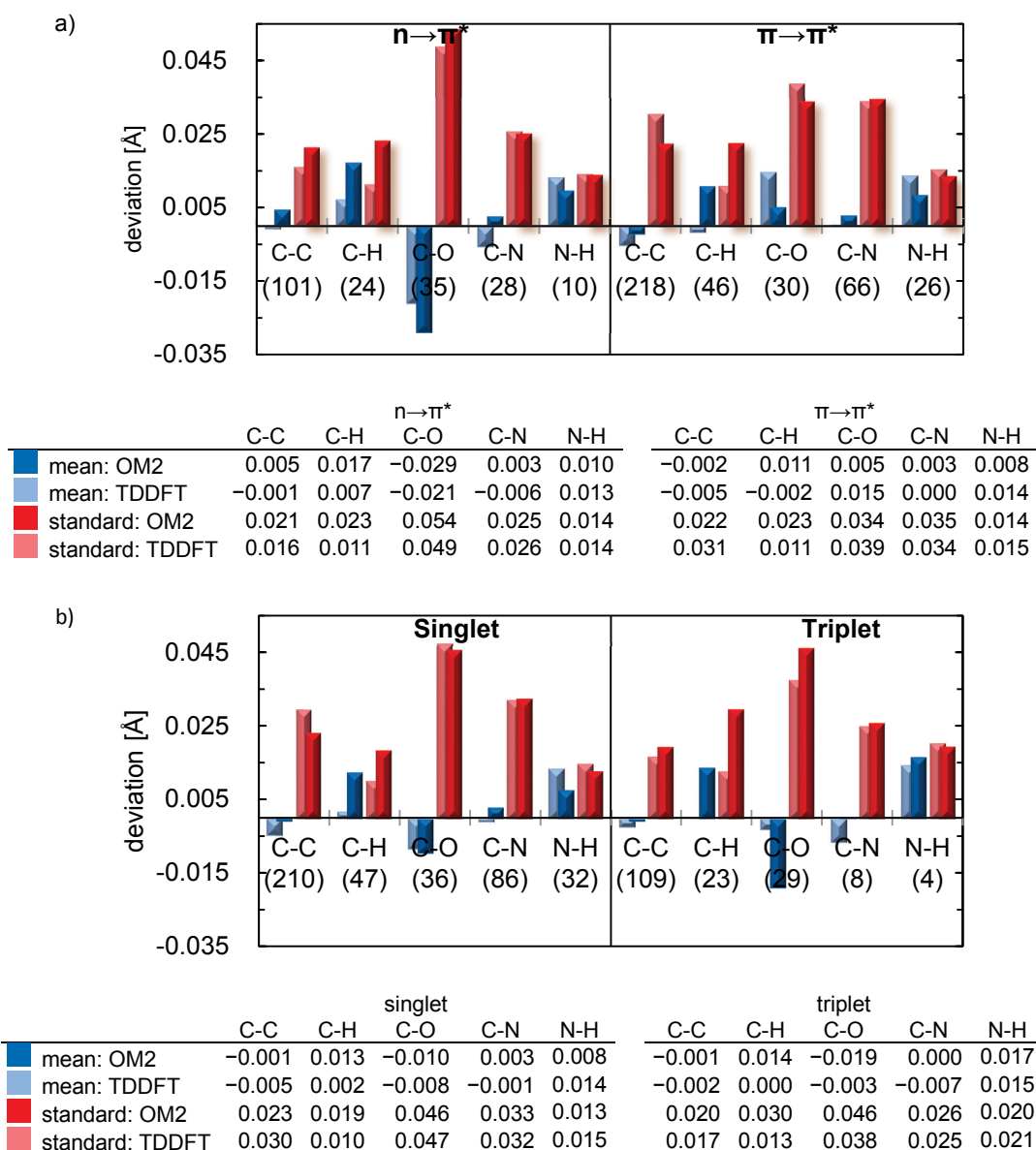


**Figure 2.4** Mean and standard deviations of the OM2/MRCI and TDB3LYP bond lengths for C-C, C-H, C-O, C-N, and N-H, compared with the CASSCF references (Å): (a) sorted into  $n \rightarrow \pi^*$  and  $\pi \rightarrow \pi^*$  excitations; (b) sorted into singlet and triplet excitations. The numbers in parentheses at the bottom indicate the number of comparisons for the OM2/MRCI method.

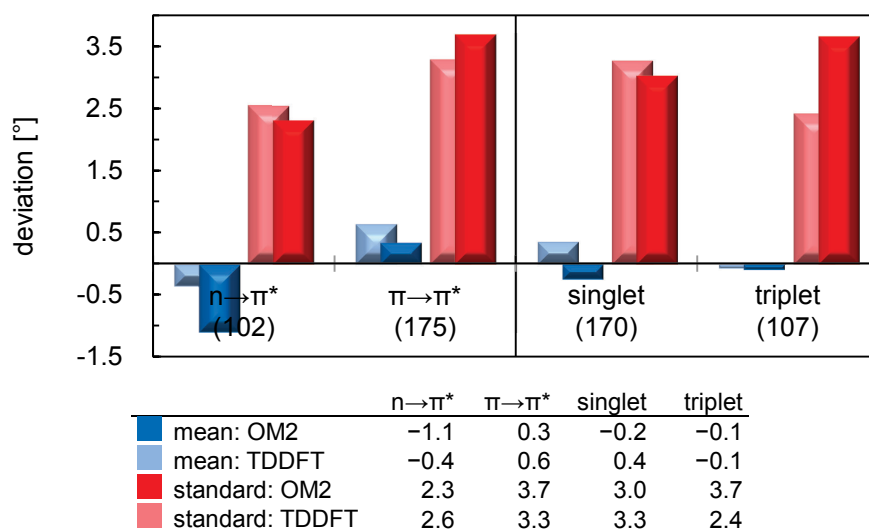


**Figure 2.5** Mean and standard deviations of the OM2/MRCI and TDDFT bond angles compared with the CASSCF references ( $^\circ$ ). The parenthesized numbers in the bottom indicate the populations of sampling for the OM2/MRCI method.

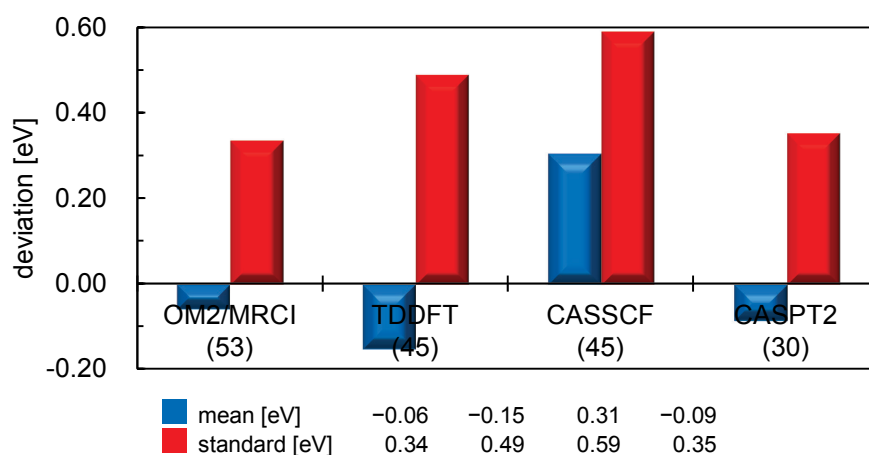


**Figure 2.6** Mean and standard deviations of the OM2/MRCI, TDDFT, CASSCF, and CASPT2 adiabatic excitation energies compared with the gas-phase experimental references (eV). These data were selected according to the availability of the results from the literature. The numbers in parentheses indicate the number of comparisons.

## 2.4 Photodissociation reactions

The photodissociation of carbonyl compounds is relevant to atmospheric chemistry, biology, and many other fields. [60] It has been widely studied over the past decades. [146-148]

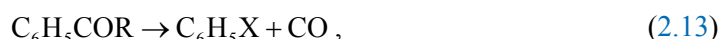
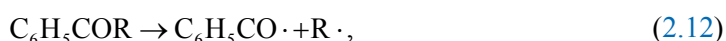
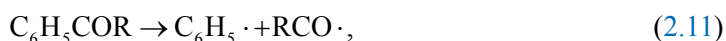
## 2.4 Photodissociation reactions

Aromatic carbonyl compounds differ from their aliphatic counterparts due to the  $\pi$ -electron conjugation between the aromatic and carbonyl groups, so that they exhibit unique photochemical reactivity and undergo photodissociation by special mechanisms. [147-151] Benzaldehyde ( $C_6H_5CHO$ , BA for short) and acetophenone ( $C_6H_5COCH_3$ , AP for short) (see Figure 2.7) are the most studied prototypical aromatic carbonyl compounds. [152-154] It is commonly accepted that their first and second singlet excited states ( $S_1$  and  $S_2$ ) arise from  $n \rightarrow \pi^*$  and  $\pi \rightarrow \pi^*$  transitions, and that two closely lying triplet states ( $T_1$  and  $T_2$ ) are below the  $S_1$  minimum. The decay dynamics of BA in the  $S_1$  state was reported to be orders of magnitude faster than that of noncarbonyl aromatic compounds due to presence of the  $n \rightarrow \pi^*$  state.



**Figure 2.7** Chemical structures and atom numbering of benzaldehyde and acetophenone.

Experimentally, there are three photodissociation reactions of BA and AP,



where ( $R = H, CH_3$ ). These reaction pathways play different roles in the two molecules. The HCO channel (cleavage between the phenyl and carbonyl groups) (Eq. 2.11) was found to be the major dissociation pathway of BA. [155] In contrast, for AP, the C1-C7 and C7-C9 bond fissions (Eqs. 2.11 and 2.12) are of comparable importance at higher excitation energies, while C7-C9 bond fission (Eq. 2.12) becomes dominant at lower energies. [156] The molecular channel (Eq. 2.13) is in both cases negligible. There are almost no theoretical studies on the dynamics of these photodissociations in the literature. [157] Here, we outline our high-level *ab initio* computations of these photodissociation mechanisms. [99]

We fully optimized the  $S_0$ ,  $S_1$ ,  $S_2$ ,  $T_1$ , and  $T_2$  equilibrium structures, transition states (TSs), and intersection geometries using state-averaged CASSCF/6-31+G\* calculations with equal weights. In the case of the C1-C7 and C7-C9 dissociation reactions of BA, we used the

highest-energy geometries on the path as approximate TS geometries. We chose a (10,8) AS for BA (containing one  $n$ , four  $\pi$ , and three  $\pi^*$  MOs) and a larger (12,11) AS for AP (with two extra  $\sigma$  electrons and three more MOs). The optimizations were followed by single-point calculations at the CIPT2/cc-pVDZ level (configuration interaction with second-order perturbation theory and the cc-pVDZ basis). [158] Comparative calculations were also carried out using the MS-CASSPT2/cc-pVDZ method (multi-state CASPT2). [159-160] Spin-orbit matrix elements for intersystem crossing (ISC) between the singlet and triplet states were computed at the CASSCF/cc-pVDZ level. [161] All CASSCF, CIPT2, and CASPT2 calculations were performed with the MOLPRO-2006 package. [162]

In view of the interlaced PESs of the low-lying singlet and triplet states of both BA and AP, we tried to find the corresponding crossing structures. For BA, the minimum-energy crossing point (MECP)  $CP_{S_1/T_2}(BA)$  between  $S_1$  and  $T_2$  and the minimum-energy conical intersection (MECI)  $CI_{T_1/T_2}(BA)$  between  $T_1$  and  $T_2$  were approximately located at the CASSCF level. At both optimized structures, there remained a small CASSCF energy gap between the two states, that is,  $1.2 \text{ kcal}\cdot\text{mol}^{-1}$  at  $CT_{S_1/T_2}(BA)$  and  $0.4 \text{ kcal}\cdot\text{mol}^{-1}$  at  $CI_{T_1/T_2}(BA)$ . These gaps remained very small at the CASPT2//CASSCF level ( $0.5$  and  $0.7 \text{ kcal}\cdot\text{mol}^{-1}$ , respectively). This confirms the existence of degenerate or near-degenerate states and corresponding crossing points in this region, even though we have not exactly located their geometries. In any event, the  $S_1$  energy of  $CT_{S_1/T_2}(BA)$  lies so closely above the  $S_1$  minimum  $MIN_{S_1}(BA)$ , by  $1.7$  (CASPT2) or  $1.6$  (CIPT2)  $\text{kcal}\cdot\text{mol}^{-1}$ , that  $CT_{S_1/T_2}(BA)$  can be reached easily after the initial photoexcitation to the  $S_1$  state.

The geometries of  $CT_{S_1/T_2}(BA)$  and  $CI_{T_1/T_2}(BA)$  are quite similar. For example, the C7-O8 bond lengths are  $1.338$  and  $1.301 \text{ \AA}$ , respectively; and the C1-C7 bond lengths are  $1.381$  and  $1.383 \text{ \AA}$ , respectively. Thus, the energies of these three states should be close (near-degenerate) to each other around  $CT_{S_1/T_2}(BA)$  and  $CI_{T_1/T_2}(BA)$ . Taking into account the similar energies of both structures at the CIPT2 (CASPT2) level, i.e.,  $79.2$  ( $83.0$ ) and  $79.8$  ( $80.1$ )  $\text{kcal}\cdot\text{mol}^{-1}$ , there should indeed exist an  $S_1/T_2/T_1$  three-state intersection *region* in their vicinity, even though we have not been able to locate a rigorous three-state crossing point. It should be pointed out that such three-state intersections have been reported for other aromatic carbonyl compounds. [146,149-150]

The  $S_1 \rightarrow T_1$  intersystem transition takes place efficiently in such an  $S_1/T_2/T_1$  three-state intersection region because of the so-called relay effect of the  $T_2$  state. According to the



## 2.4 Photodissociation reactions

El-Sayed rules, [163] the  $S_1 \rightarrow T_2$  intersystem crossing is rather facile since there is substantial spin-orbit coupling between the  $^1\pi \rightarrow \pi^*$  and  $^3n \rightarrow \pi^*$  states (which is allowed by symmetry). The lowest triplet  $T_1$  will then quickly be populated via a subsequent  $T_2 \rightarrow T_1$  internal conversion around the  $CI_{T_1/T_2}(BA)$  geometry. This kind of relay mechanism ( $S_1 \rightarrow T_2 \rightarrow T_1$ ) plays an essential role in its photodissociation dynamics [149-150] and explains the ultrafast  $S_1 \rightarrow T_1$  decay in BA. The situation in acetophenone is completely analogous both with regard to the geometries and relative energies, and the  $S_1/T_2/T_1$  three-state intersection region is again accessible both structurally and energetically.

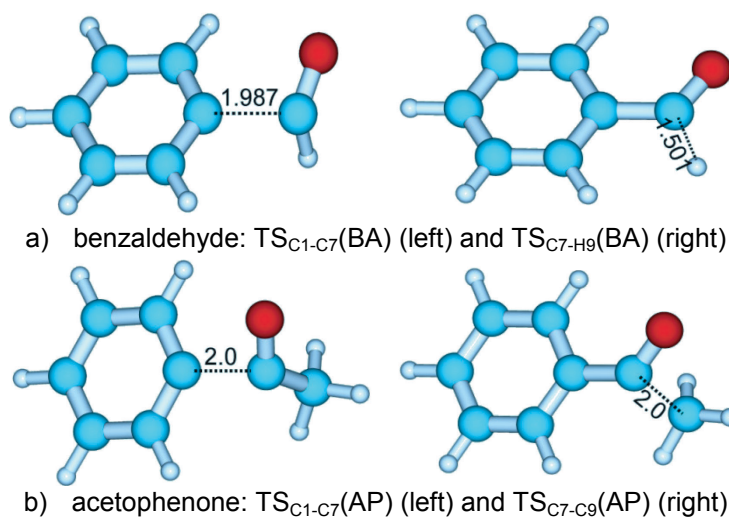


**Figure 2.8** Optimized TS structures of the bond cleavage reactions in the  $T_1$  state of benzaldehyde and acetophenone.

As discussed above, the  $S_1/T_2/T_1$  three-state intersection region can efficiently funnel electron population from  $S_1$  to  $T_1$  as a consequence of the relay effect of  $T_2$ . The  $T_1$  dissociation channels are experimentally known to be dominant at low excitation energies. Here we further discuss the mechanism of these reactions. The transition states,  $TS_{C1-C7}(BA)$  and  $TS_{C7-H9}(BA)$ , for C1-C7 and C7-H9 bond cleavage have been located in the  $T_1$  state of BA, respectively (see Figure 2.8a). Both are nonplanar with the dihedral angle O8-C7-C1-H9 being  $124.5^\circ$  and  $110.4^\circ$ , respectively. The bond lengths of C1-C7 and C7-H9 are found to be 1.987 Å in  $TS_{C1-C7}(BA)$  and 1.501 Å in  $TS_{C7-H9}(BA)$ , respectively, showing that the breaking bonds are quite elongated. The energies relative to  $MIN_{S_0}(BA)$  are computed to be 92.1 and 96.1 kcal·mol $^{-1}$ , respectively, corresponding to relative barriers of 20.3 and 24.3 kcal·mol $^{-1}$ . Hence C1-C7 bond fission is a bit more favorable than C7-H9 bond fission in the  $T_1$  state,

with the computed difference between both barriers being  $4.0 \text{ kcal}\cdot\text{mol}^{-1}$ . The preferred  $T_1$  channel should thus act as the main mechanism for forming ground-state phenyl and formyl radicals.

The transition states  $\text{TS}_{\text{C1-C7}}(\text{AP})$  and  $\text{TS}_{\text{C7-C9}}(\text{AP})$  for C1-C7 and C7-C9 bond cleavage in the  $T_1$  state of AP also possess nonplanar geometries (see Figure 2.8b). The dihedral angle O8-C7-C9-C1 is  $113.4^\circ$  and  $131.4^\circ$  in these transition states, respectively. The breaking bonds C1-C7 and C7-C9 are estimated to be stretched to  $2.0 \text{ \AA}$  in both cases. We note that these bonds lengths are  $1.498$  and  $1.512 \text{ \AA}$  in the ground state minimum  $\text{MIN}_0(\text{AP})$ , while in the  $T_1$  state minimum  $\text{MIN}_{T_1}(\text{AP})$  they become  $1.425$  and  $1.502 \text{ \AA}$ . Therefore the shorter C1-C7 bond is expected to be harder to cleave. This expectation is confirmed by the computed TS energies relative to  $\text{MIN}_{S_0}(\text{AP})$  that are  $99.0$  and  $82.5 \text{ kcal}\cdot\text{mol}^{-1}$  for  $\text{TS}_{\text{C1-C7}}(\text{AP})$  and  $\text{TS}_{\text{C7-C9}}(\text{AP})$ , respectively, corresponding to reaction barriers of  $26.5$  and  $10.0 \text{ kcal}\cdot\text{mol}^{-1}$ . Hence, C7-C9 bond cleavage in the  $T_1$  channel should be mainly responsible for the formation of ground-state  $\text{C}_6\text{H}_5\text{CO}\cdot$  and  $\text{CH}_3\cdot$  radicals.

On the basis of the above calculations, the photodissociation mechanism of BA can be summarized as follows (see Figure 2.9a). Upon photon absorption, BA is initially excited to the bright  $S_2$  state (the vertical excitation energy is  $104.9 \text{ kcal}\cdot\text{mol}^{-1}$ ), followed by an ultrafast  $S_2 \rightarrow S_1$  internal conversion and relaxation to the  $S_1$  minimum  $\text{MIN}_{S_1}(\text{BA})$  ( $77.6 \text{ kcal}\cdot\text{mol}^{-1}$ ). The dark  $S_1$  state could also be directly populated at the Franck-Condon geometry, but this is much less likely because this transition is forbidden by symmetry. Since the  $S_1/T_2/T_1$  three-state intersection is structurally and energetically similar to  $\text{MIN}_1(\text{BA})$ , the  $S_1 \rightarrow T_1$  intersystem crossing can occur efficiently, in analogy to other systems. [146,149-150,157] With the available excess energy, BA overcomes the barriers to C1-C7 and C7-H9 bond cleavage in the  $T_1$  state [ $\text{TS}_{\text{C1-C7}}(\text{BA})$  at  $92.1 \text{ kcal}\cdot\text{mol}^{-1}$  and  $\text{TS}_{\text{C7-H9}}(\text{BA})$  at  $96.1 \text{ kcal}\cdot\text{mol}^{-1}$ ] and forms the corresponding ground-state products. Given the rather small TS energy difference of only  $4 \text{ kcal}\cdot\text{mol}^{-1}$ , both dissociation channels are accessible, with a preference for C1-C7 cleavage that results in phenyl and formyl radical products. Generally speaking, the photodissociation mechanism of AP closely resembles that of BA (see Figure 2.9b), except for the final step where these two aromatic carbonyl compounds exhibit distinct dissociation behavior in the  $T_1$  state: in AP, C7-C9 bond cleavage dominates over the C1-C7 dissociation channel because of the much smaller barrier ( $10.0$  vs.  $26.5 \text{ kcal}\cdot\text{mol}^{-1}$ ), whereas C1-C7 bond fission is preferred by a small margin over C7-H9 bond fission in BA.

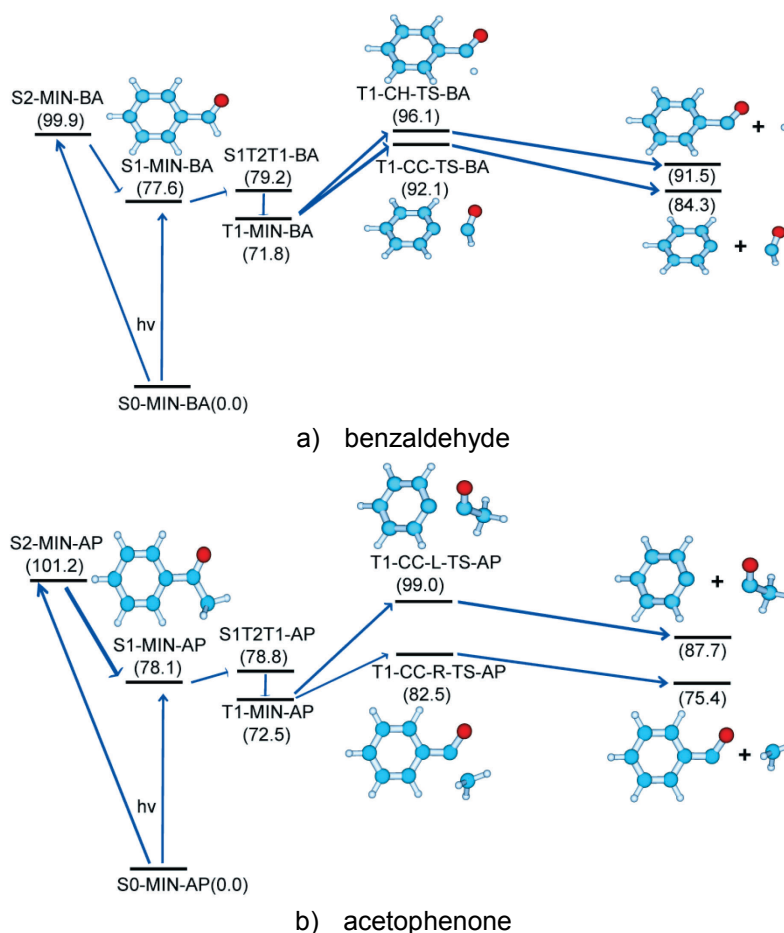


**Figure 2.9** Proposed photodissociation reaction mechanisms of benzaldehyde and acetophenone: relative energies ( $\text{kcal}\cdot\text{mol}^{-1}$ ) based on single-point CIPT2//CASSCF calculations are given in parentheses.

To conclude, photodissociation reactions are of great importance in photochemistry. Here, we have reported an *ab initio* study on the mechanistic photodissociation of benzaldehyde and acetophenone. On the basis of the current calculations, photodissociation mechanisms were proposed for both molecules, which are consistent with and explain the experimental observations. [155-156]

## 2.5 Nonadiabatic dynamics

In Chapter 1, we have introduced Tully's trajectory surface hopping (TSH) method [88-89], which describes the nonadiabatic dynamics reasonably well at relatively low computational

cost and has thus become one of the most popular tools for studying nonadiabatic phenomena in organic molecules. [65] In this method, the dynamics is simulated with independent classical trajectories and nonadiabatic effects are taken into account by allowing hopping between near-degenerate PESs. The electronic degrees of freedom are propagated along the trajectory according to the time-dependent Schrödinger equation (Eq. 1.1), while the nuclear degrees of freedom are described by classical equations of motion. The energies, gradients, and nonadiabatic couplings are calculated on the fly at each MD step during the trajectory. To maintain the self-consistency between the nuclear and the electronic time evolution, it is necessary to properly introduce nonadiabatic interactions by allowing instantaneous hops from one PES to another, with the hopping probability at each time being controlled by a stochastic switching algorithm. To account for the random nature of the switching algorithm, a swarm of trajectories must be considered for each initial configuration of the dynamics, and the final results are obtained as an average over a large number of trajectories. In current applications, *ab initio* TSH dynamics calculations are still restricted to small molecules when using accurate *ab initio* MRCI methods, while molecules of moderate size (up to about 20 atoms) can be handled at the CASSCF level. Due to its small size, the methaniminium cation ( $\text{CH}_2\text{NH}_2^+$ ) is often used for testing TSH implementations at different theoretical levels. [91,164-166] It serves as the smallest prototypical molecule for modeling the nonadiabatic dynamics of protonated Schiff bases. Here, we present a validation study on the CASSCF nonadiabatic dynamics [65] using our TSH implementation in the ChemShell package. [167]

Figure 2.10 shows the dynamics of the adiabatic population decay of  $\text{CH}_2\text{NH}_2^+$  as obtained at the CASSCF/6-31G\* level. After the initial population of the  $S_2$  state, an ultrafast  $S_2 \rightarrow S_1$  transfer occurs with a time constant of 11 fs, followed by a slower  $S_1 \rightarrow S_0$  internal conversion with a decay time of 63 fs. There are two major reaction coordinates for the internal conversion: C-N bond stretching and C-N bond torsion. We pick two typical trajectories propagated along these two coordinates and plot the relative energies evolving as function of simulation time in Figure 2.11. In both cases, a sudden elongation of the C-N bond is seen after the initial excitation. The  $S_2 \rightarrow S_1$  hopping occurs very quickly, as soon as the system reaches the  $S_2/S_1$  conical intersection with a planar structure. Motion along the torsional reaction coordinate leads towards an  $S_1/S_0$  conical intersection region characterized by C=N double bond twisting and pyramidalization, but with little bond elongation (see Figure 2.11a).

Following the second (stretching) type of reaction coordinate (see Figure 2.11b), there is instead a further increase of the CN distance, accompanied by bi-pyramidalization, which guides the system towards a different  $S_1/S_0$  conical intersection. On average, the two types of distortion contribute almost equally to the nonadiabatic dynamics of  $\text{CH}_2\text{NH}_2^+$  in the gas phase (according to CASSCF/6-31G\*).

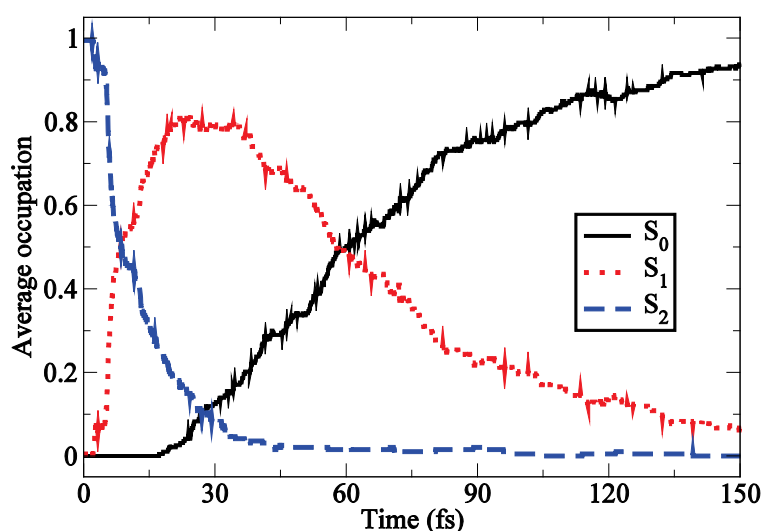


**Figure 2.10** Average occupations of the low-lying adiabatic states of gas-phase  $\text{CH}_2\text{NH}_2^+$  at the CASSCF/6-31G\* level.

Similar results have been found at the OM2/MRCI level. [91] In this case, the time constants of adiabatic population decay are 15 and 83 fs for the  $S_2$  and  $S_1$  state, respectively. The ratio between the torsional- and stretching-type trajectories is 7/3. The differences between the two approaches are small, suggesting again that the OM2/MRCI approach can indeed provide a reasonable description of the PESs and may be used to perform reliable dynamical simulations efficiently. In these gas-phase calculations of the nonadiabatic dynamics of  $\text{CH}_2\text{NH}_2^+$ , a single trajectory propagating to 150 fs (3000 steps of 0.05 fs) typically takes about five hours at the CASSCF level, and five minutes at the OM2/MRCI level.

Solvent effects can be studied by performing TSH simulations in a QM/MM framework. By fully solvating the  $\text{CH}_2\text{NH}_2^+$  molecule (QM) in a water droplet (MM, described by the TIP3P force field [168]), the nonadiabatic process was simulated in the condensed phase. The computed average decay times are slightly shorter than those in the gas phase, being 8 and 74 fs for the  $S_2$  and  $S_1$  state, respectively. Both the torsional- and stretching-type decay channels were also observed in aqueous solution where, however, almost 80% of the trajectories

decayed through the torsional-type channel. The observed changes of the decay behavior can be explained by the steric repulsion between  $\text{CH}_2\text{NH}_2^+$  and the surrounding water. Obviously, the solvent environment substantially affects the decay process. Such effects have also been observed in other studies (see Chapter 3 and Chapter 4). The emergence of the QM/MM TSH approach opens up the possibility to study the photoinduced processes of large systems in the condensed phase. Further comprehensive TSH simulations at the QM and QM/MM levels are described in the following chapters.

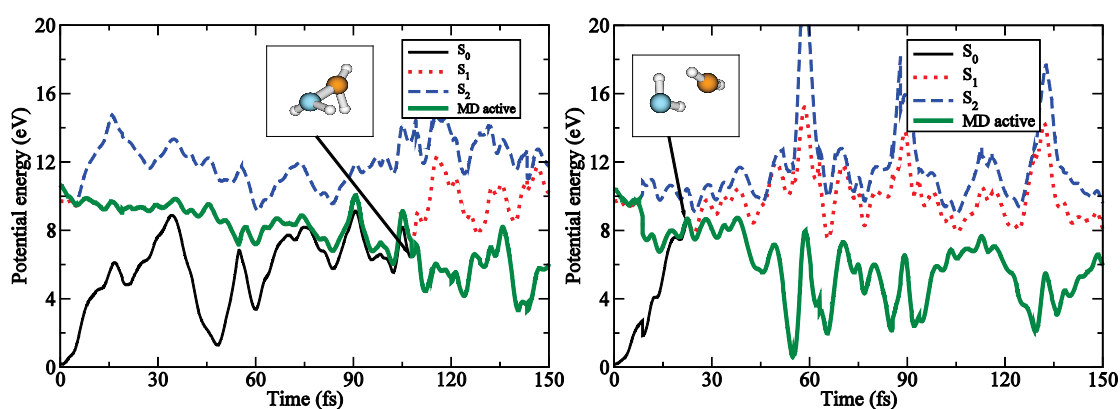


**Figure 2.11** Two typical trajectories during the nonadiabatic dynamics of  $\text{CH}_2\text{NH}_2^+$  with the relative energies of PESs evolving over the simulation time: schematic structures of the torsional-type (left) and stretching-type (right) crossings are shown.

## Chapter 3

# Excited state dynamics of DMN

Disubstituted benzenes having a “D(onor)-Ph-A(ceptor)” structure are interesting molecules because of their “push-pull” electronic properties. [169-174] Photoabsorption by such molecules leads to intramolecular charge-transfer (CT) excited states, which have been widely studied in recent years. Benzylidene malononitriles belong to this class of molecules. 2-[4-(dimethylamino)benzylidene]malononitrile (DMN, see Figure 3.1) has aroused much interest since it shows special features due to the interplay between the D→A transition and the solvents, which largely determines its fluorescence quantum yield. [169-172] Its fluorescence intensity becomes weaker with a decrease of the solution viscosity. [169,172] Therefore, DMN and its derivatives are often used to probe the polarity and micro-viscosity of solvents, polymers, ionic liquids, and biological media.

In spite of these broad applications, the mechanism of DMN excited-state dynamics is still unclear. It has been confirmed that fast  $S_1 \rightarrow S_0$  internal conversion is responsible for the fluorescence quenching and the non-radiative decay of these systems. [169-172] However, there are discrepancies between the mechanisms proposed by different researchers. Some suggest that twisting about the C1-N11 and/or C4-C7 bond(s) plays the key role in the internal conversion, as often in other twisted intramolecular charge transfer (TICT) chromophores. [175-179] Others favor a mechanism involving isomerization at the C7=C8 double bond. [175,180-181] And a third proposal combines all these motions. [169-172] On the theoretical side, the electronic structure of DMN in the  $S_1$  state at the FC region has been studied, and there have been two attempts to address the mechanism of the  $S_1 \rightarrow S_0$

decay. [169-170] They explained the internal conversion as a result of C7=C8 double-bond torsion that brings the system towards an  $S_0/S_1$  conical intersection.

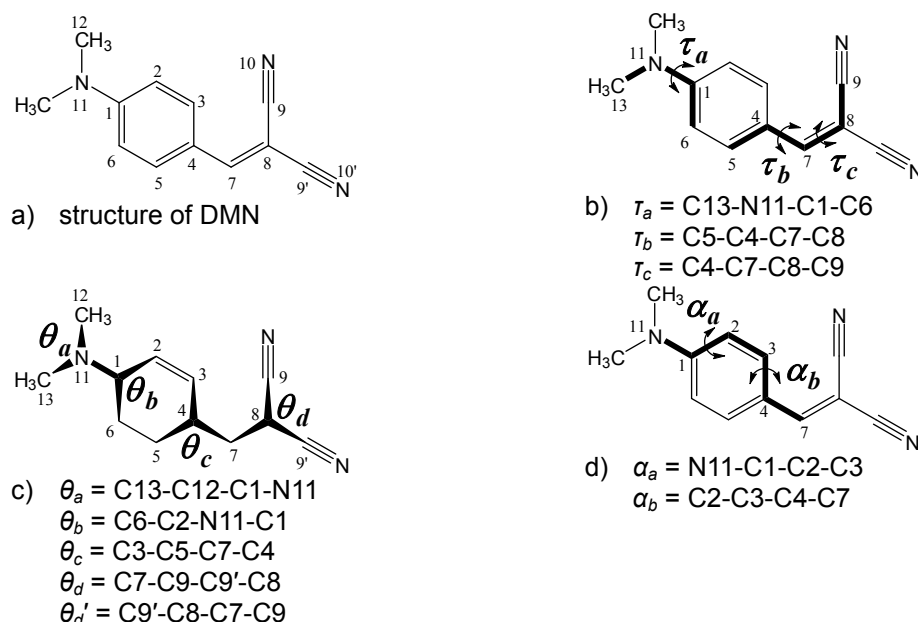


**Figure 3.1** Conventions used for DMN in this work: (a) chemical structure and atom numbering; (b) definition of dihedral angles  $\tau_a$ ,  $\tau_b$ , and  $\tau_c$  for bond twisting; (c) definition of dihedral angles  $\theta_a$ ,  $\theta_b$ ,  $\theta_c$ ,  $\theta_d$ , and  $\theta_{d'}$  for pyrimidalization; (d) definition of dihedral angles  $\alpha_a$  and  $\alpha_b$  for out-of-plane motion.

In this chapter, we summarize our study on the internal conversion mechanism of DMN in the gas phase, [145] which employed on nonadiabatic dynamics simulations. We chose OM2/MRCI as the quantum method, since the medium-sized DMN molecule with 26 atoms is beyond the limit of accurate *ab initio* simulations. Moreover, standard TDDFT neither treats the charge-transfer states properly nor describes the conical intersections reliably. In such a situation, the semiempirical OM2/MRCI approach appears to be the method of choice.

### 3.1 Minima and conical intersections

#### ► $\text{MIN}_{S_0}$

Unconstrained OM2/MRCI optimizations located the  $S_0$  minimum ( $\text{MIN}_{S_0}$ ) at an almost planar geometry (see Figure 3.2a). Calculations with different ASs, i.e., (12,10), (12,12), and



### 3.1 Minima and conical intersections

(14,14), gave similar minimum geometries. At the  $S_0$  minimum, the first singlet excited state  $S_1$  corresponds to the HOMO→LUMO ( $\pi\rightarrow\pi^*$ ) transition. The vertical excitation energy was computed to be 3.53-3.56 eV with the different ASs employed, reasonably close to the experimental value of  $3.38\pm 0.06$  eV and published theoretical values of 3.38-3.44 eV (RI-CC2). [169-172] Population analyses at the OM2/MRCI level show that the negative charge at the  $\text{CH}=\text{C}(\text{CN})_2$  moiety increases upon  $S_0\rightarrow S_1$  photoexcitation by about  $-0.4e$  (from  $-0.1e$  to  $-0.5e$ ). In contrast, the charges at the  $\text{N}(\text{CH}_3)_2$  and  $\text{C}_6\text{H}_4$  groups become more positive overall by about  $0.25e$  and  $0.15e$ , respectively. As a consequence, the  $S_1$  excited state has a much larger permanent dipole moment than the  $S_0$  ground state. We computed the increment as 9.1-9.8 D, compared with the experimental result of 8.8 D and theoretical values of 7.12-8.15 D (RI-CC2) and 3.75-4.54 D (TDDFT).

#### ► $\text{MIN}_{S_1}$

The optimized  $S_1$  geometry is slightly nonplanar (see Figure 3.2b). The geometric difference between the  $S_0$  and  $S_1$  minima is very small (root-mean-square deviation  $\sim 0.045$  Å) so that the  $S_1$  adiabatic excitation energy ( $T_a$ ) is lower than the vertical excitation energy ( $T_v$ ) by only 0.10-0.17 eV (with different ASs, same below). Similarly, the  $S_0$  energy at the optimized  $S_1$  minimum is only 0.09-0.18 eV relative to the ground-state minimum.

Besides, we have located several  $S_0/S_1$  conical intersections that are distinguished by different types of geometric distortions (see Figure 3.2c-f). Two of them are characterized by C4-C7 single-bond and C7=C8 double-bond twisting, denoted as  $\tau_c$  and  $\tau_b$ , respectively (see Figure 3.1). The other two display pronounced deformations of the benzene ring and out-of-plane displacements of the substituents.

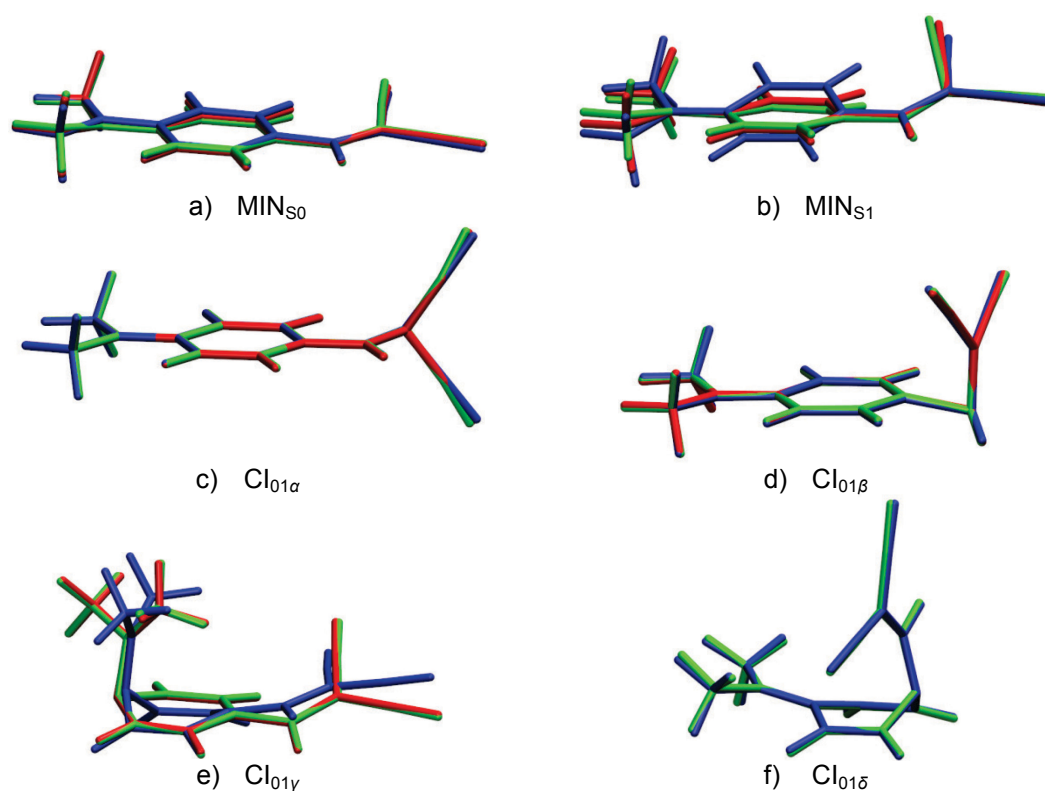


**Figure 3.2** Overlays of the optimized minima and CIs of DMN obtained with OM2/MRCI (12,10) (blue), MRCI-SDTQ(12,12) (red), and MRCI-SD(14,14) (green), respectively.

#### ► $CI_{01\alpha}$

With the (12,12) and (14,14) ASSs,  $CI_{01\alpha}$  was found at 2.55 and 2.51 eV (relative to  $MIN_{S0}$ ), respectively, while the relative energy is 2.76 eV with the (12,10) AS.  $CI_{01\alpha}$  shows strong twisting at the C7=C8 double bond ( $\tau_c \sim 120^\circ$ ) and pronounced pyramidalization at the C8 atom ( $\theta_d \sim 35^\circ$ ), as shown in Figure 3.2c. At the  $CI_{01\alpha}$  geometry, both C-C-N groups remain linear, and there is no internal rotation related to  $\tau_c$  or  $\tau_b$ . This conical intersection was also found in a CASSCF study. [169] This kind of conical intersections with twisted C=C double bond and pyramidalized CH=C(CN)<sub>2</sub> group are commonly seen in unsaturated molecules, e.g., in ethylene [182] or in xylene derivatives, where the pyramidalization is induced by the so-called “sudden polarization” effect. [183]

#### ► $CI_{01\beta}$

$CI_{01\beta}$  was located at 4.10/3.90/3.86 eV by OM2/MRCI using the (12,10)/(12,12)/(14,14) ASSs. It contains a significantly twisted C4-C7 bond ( $\tau_b \sim -103^\circ$ ), with the C7=C8 double bond being almost perpendicular to the benzene plane (see Figure 3.2d). Similar to  $CI_{01\alpha}$ ,  $CI_{01\beta}$  has

noticeable pyramidalization at the  $\text{CH}=\text{C}(\text{CN})_2$  moiety.

► **CI<sub>01γ</sub>**

The third  $S_0/S_1$  conical intersection  $\text{CI}_{01\gamma}$  (see Figure 3.2e) has two variants:  $\text{CI}_{01\gamma}(\text{a})$  obtained with (12,10) and  $\text{CI}_{01\gamma}(\text{b})$  obtained with (12,12) and (14,14). Both variants have the same type of distortion, that is, N11-C1 twist (characterized by  $\tau_a$ ), but differ by the direction of twisting ( $\tau_a \sim -19^\circ/10^\circ/12^\circ$ , with the three ASs, same below). Besides, strong out-of-plane deformation is seen in this type of conical intersection, so that the N11-C1 bond is nearly perpendicular to the ring plane ( $\alpha_a \sim 73^\circ/89^\circ/91^\circ$ ). Furthermore, the six-membered ring forms a boat-like conformation, with puckering at the C1 atom ( $\theta_b \sim -27^\circ/-35^\circ/-35^\circ$ ) and at the C4 atom ( $\theta_b \sim 8^\circ/4^\circ/5^\circ$ ). According to the three ASs employed, the relative energies of the three  $\text{CI}_{01\gamma}$  structures are 3.55, 4.40, and 4.48 eV, respectively. It should be pointed out that this  $\text{CI}_{01\gamma}$ -type conical intersection often plays an important role in the nonadiabatic decay of five- and six-membered ring systems. [184] However, the  $\text{CI}_{01\gamma}$  channel is not favored in the current DMN system (see discussion below in Section 3.3).

► **CI<sub>01δ</sub>**

At last, we found  $\text{CI}_{01\delta}$  at 3.71 eV with the (12,10) AS and at 3.47 eV with (14,14), but could not locate it with (12,12). Compared to  $\text{CI}_{01\gamma}$ , it is also boat-like but to the opposite direction: with slight puckering at the C1 atom ( $\theta_b = -5^\circ/-5^\circ$ ) and intense puckering at the C4 atom ( $\theta_b \sim 30^\circ/30^\circ$ ). As a consequence, the C4-C7 bond becomes nearly perpendicular to the ring plane ( $\tau_b \sim 158^\circ/157^\circ$ ) (see Figure 3.2f), while  $\text{N}(\text{CH}_3)_2$  group nearly remains in the ring plane.

## 3.2 Decay dynamics

We performed surface-hopping simulations at the OM2/MRCI level to explore the decay dynamics of DMN. Different ASs, i.e., (12,10), (14,14), and (16,14), were employed to show the internal consistency of our approach. Very similar decay behavior was indeed found when using these ASs, indicating that the simulated dynamics is rather stable to the selection of the AS. In these simulations, DMN is initially excited to the bright  $S_1$  state. Up to 400 fs, less than 5% trajectories have decayed to the  $S_0$  state. Thereafter, most trajectories have reached the crossing region between the  $S_0$  and  $S_1$  states, and the system starts to continuously repopulate to the  $S_0$  state. After 2.0 ps, the fractional occupation of  $S_0$  has grown to over 90%

and the decay is basically complete. When using the (12,12) AS, the results differ somewhat: the decay is slightly slower so that there remains almost ~30%  $S_1$  population after 2.0 ps.

To derive the  $S_1$  time constant, we used an exponential decay function to fit the time-dependent fractional occupations:

$$p(t) = \exp\left(-\frac{t-t_0}{\tau}\right), \quad (3.1)$$

where  $t_0$  is the starting time for the  $S_1$  population decay and  $\tau$  is the time constant for the subsequent decay. The initial plateau phase (without significant repopulation of the ground state) suggests a  $t_0$  value of about 400 fs. Combining the data calculated with the ASs (12,10), (14,14), and (16,14), the fitting gives  $t_0 = 468$  fs and  $\tau = 770$  fs. Thus the computed time constant of the  $S_1$  state is

$$t_0 + \tau = 1.24 \text{ ps}. \quad (3.2)$$

The use of the AS(14,14) results in slightly slower dynamics, with  $t_0$  around 400 fs and a total lifetime of ~1.6 ps.

For comparison, there is a recent theoretical estimate of the  $S_1$  lifetime of DMN in acetonitrile of 1.1 ps (referring to the decay time of the fluorescence intensity to  $1/e$  of its initial value), reported by Swalina and Maroncelli. [169] They employed a drastically simplified model: DMN was modeled as two rigid bodies connected by the C7=C8 double bond and interacting with the acetonitrile solvent molecules via Lennard-Jones and electrostatic forces, and the spectral dynamics was simulated by following the motion of this model system in a one-dimensional torsional potential around the C7=C8 bond derived from *ab initio* energies. Even so, their model apparently still captures some of the essential physics, since it yields a lifetime close to the one from our surface-hopping simulations. The experimental fluorescence lifetime in solution varies from ~0.7 ps in nonpolar solvents (n-hexane, etc.) to ~1.4 ps in polar solvents (acetonitrile, etc.). [172] Our computed gas-phase value falls into this range.

### 3.3 Reaction paths

To identify the favorable decay channel of the nonadiabatic dynamics, we analyzed the

### 3.3 Reaction paths

hopping structures extracted from the simulations. As plotted in Figure 3.3, the hopping events cluster in a small area with  $\tau_c \sim 110\text{-}130^\circ$  and  $\theta'_d \sim 80\text{-}110^\circ$ ; these two dihedral angles represent the C7=C8 double-bond twisting and CH=C(CN)<sub>2</sub> pyramidalization, respectively, and their values at the hopping geometries are close to those at the optimized structure of the conical intersection  $\text{CI}_{01\alpha}$ . This clearly indicates that all trajectories decay to the  $S_0$  state via the  $\text{CI}_{01\alpha}$  channel. We have confirmed this conclusion by plotting histogram distributions for all relevant dihedral angles defined in Figure 3.1 (see Ref. [145]). Again, the calculations with the different ASs, (12,10), (14,14), and (16,14), lead to the same conclusion: they all favor nonadiabatic decay via  $\text{CI}_{01\alpha}$ . This mechanism is also supported by Allen et al., [170] Jee et al., [171] and the Maroncelli group. [169,172]

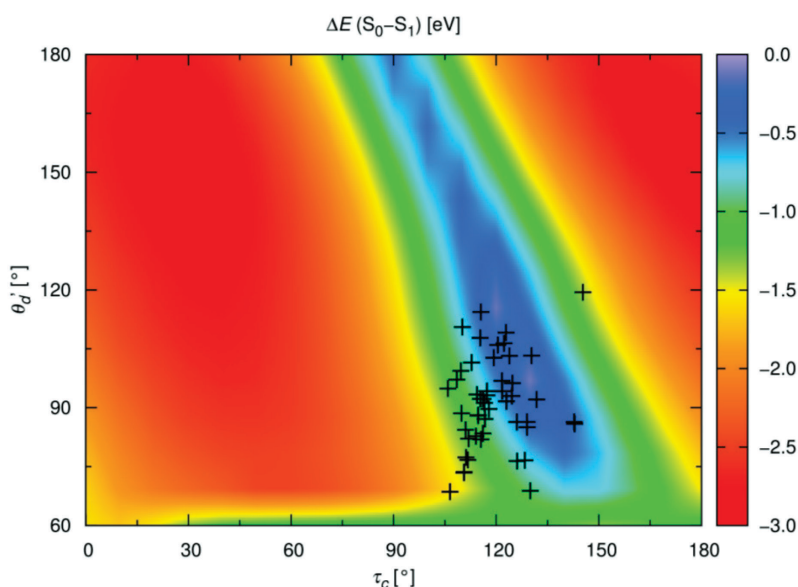


**Figure 3.3** Two-dimensional contour of the energy difference between the  $S_0$  and  $S_1$  PESs of DMN, as function of  $\tau_c$  and  $\theta'_d$  (dihedral C9'C8C7C9). The scan is based on 248 OM2/MRCI-SDTQ(12,12) single-point calculations, with the remaining geometric parameters taken from the optimized  $\text{CI}_{01\alpha}$  structure. The blue/violet area indicates the crossing seam. The  $S_1 \rightarrow S_0$  hopping events simulated using OM2/MRCI-SD(12,12) are marked by black crosses.

We also computed the  $S_0$  and  $S_1$  energies using a grid covering the two relevant reaction coordinates  $\tau_c$  ( $0\text{-}180^\circ$ ) and  $\theta'_d$  ( $60\text{-}180^\circ$ ). 248 single-point calculations were performed on this grid with OM2/MRCI-SDTQ(12,12). In this way we visualized the PES topology around the  $\text{CI}_{01\alpha}$  conical intersection, as shown in Figure 3.3. We found a seam-like region which starts at  $\tau_c \sim 80^\circ / \theta'_d \sim 180^\circ$  and ends at  $\tau_c \sim 150^\circ / \theta'_d \sim 70^\circ$ . The optimized MECI, i.e.,  $\text{CI}_{01\alpha}$ , is

located at  $\tau_c \sim 121^\circ$  and  $\theta'_d \sim 119^\circ$ . We see from Figure 3.3 that most hopping events are found in the bottom section of the seam where  $\theta'_d$  is less than  $120^\circ$ , i.e., before the trajectories arrive at the MECI.

To check the character of the other competing channels, we computed linearly interpolated reaction paths between the optimized  $S_0$  minimum and the MECIs, with 21 points calculated at the OM2/MRCI-SDTQ/(12,12) level for each path. In the case of  $CI_{01\alpha}$ , the resulting energy curve is essentially flat on the first half of the path and then drops off gradually to reach the lower-lying conical intersection, while in the other cases ( $CI_{01\beta}$  and  $CI_{01\gamma}$ ) we found sizable barriers and overall uphill profiles (see Figure 3.4). This suggests that only  $CI_{01\alpha}$  will be easily accessible during the dynamics.

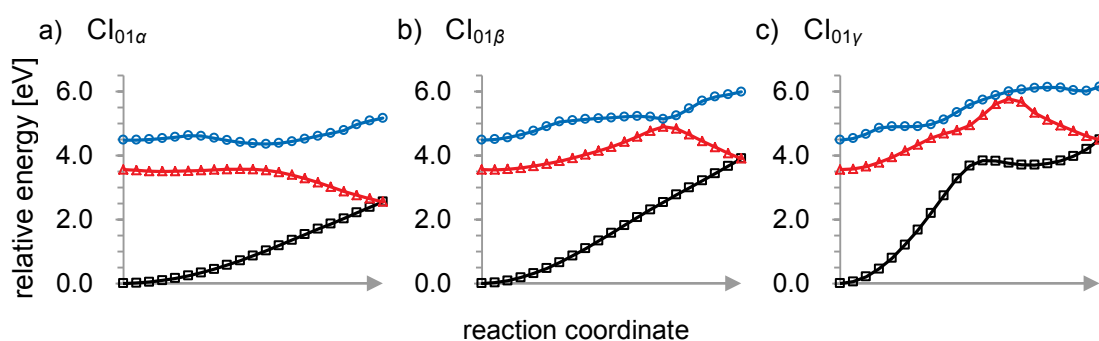


**Figure 3.4** Reaction paths obtained from linear interpolation in internal coordinates (LIIC) between the optimized  $S_0$  minimum and the minimum-energy conical intersections (MECIs). For each path 21 single-point calculations were performed at the MRCI-SDTQ(12,12) level. Three lowest electronic states are recorded:  $S_0$  (black square),  $S_1$  (red triangle), and  $S_0$  (blue circle).

To summarize this chapter, we studied the nonadiabatic decay dynamics of DMN, a 26-atom push-pull system, with OM2/MRCI surface hopping. We located several MECI structures and found  $CI_{01\alpha}$  to be the dynamically relevant conical intersection. The reaction coordinate involves twisting around the  $C7=C8$  double bond and pyramidalization at the  $CH=C(CN)_2$  group. We showed that the  $CI_{01\alpha}$  channel is energetically most favored among the competing alternatives. Further studies on charge-transfer systems are planned for the prototypical case of DMABN (4,4-dimethylaminobenzonitrile).

## Chapter 4

# Excited state dynamics of adenine

The excited states of DNA are of vital significance because they are directly linked to human health. It is known that ultraviolet (UV) photon absorption causes electronic excitation of nucleobase chromophores, which can induce direct DNA damage [185] by dimerizing pyrimidines or indirect DNA damage [186] by other bimolecular reactions. As a matter of fact, only  $< 0.1\%$  photons result in harmful lesions (that may still be fatal), while the large majority of the absorbed excitation energy is quenched by the nucleobases through efficient photoprotection mechanisms. [185] In these photoinduced processes, ultrafast internal conversion plays a decisive role, which usually takes place in less than a picosecond and transforms most of the harmful excitation energy into kinetic energy (heat). [187-189] However, the detailed photodynamics of both DNA damage and photoprotection is still poorly known. By contrast, with the help of the time-resolved spectroscopic techniques, there is much well-established experimental knowledge about the excited-state dynamics in single nucleobases. [190-192] Being the prototypical photoinduced process in DNA bases, the photodynamical behavior of single bases is essential for understanding the photostability of DNA strands. In particular, *9H*-adenine is one of the most studied nucleobases, and its excited-state properties are relatively well known. [193-204] The absorption maximum of *9H*-adenine at 252 nm (4.92 eV) is assigned to two closely-lying  $\pi \rightarrow \pi^*$  states, which are labeled as  $L_a$  and  $L_b$ . [205-207] Another singlet state of  $n \rightarrow \pi^*$  character, located only 0.073 eV below the  $\pi \rightarrow \pi^*$  state, may be involved in the photoexcitation as a dark state. [207] Biexponential fitting of the time-resolved spectra in the gas phase gives time constants for a

## Chapter 4 Excited state dynamics of adenine

---

short component of 40-100 fs and a longer component of 0.75-1 ps. [197-198,200-202,208] These sub-picosecond time scales are considered fingerprints of intramolecular internal conversions.

A number of computational investigations of 9*H*-adenine have also been conducted, and several minimum-energy crossing points or conical intersections (MECPs or MECIs) connecting the PESs of the low-lying singlet states have been located. [112,184,209-216] Two conical intersections,  $^2E$  and  $^6S_1$  (see Section 4.3), are considered energetically favorable, being characterized by strong out-of-plane deformation at the C2-H2 and C6-N6 moieties, respectively. On the basis of these computational results, several principal reaction paths in the gas phase have been suggested. For example, based on their linear interpolation in internal coordinates (LIIC) at the CASPT2//CASSCF (16,12)/6-31G\* level, Barbatti and Lischka [184] find barrierless paths to both  $^2E$  and  $^6S_1$  conical intersections. Their findings agree with the report by Perun et al. at the level of CASPT2//CASSCF (12,10)/ANO-L. [112] Hassan et al. [215], in their MRCI//CASSCF (8,8)/6-31++G\* calculations, report an ultrafast  $L_a \rightarrow n\pi^*$  conversion that is followed by a steep LIIC path down to the  $^6S_1$  conical intersection, whereas the route toward the  $^2E$  conical intersection needs an activation energy of 0.21 eV. By contrast, Conti et al. [216] find the  $^6S_1$  conical intersection at the CASPT2//CASSCF (16,12)/6-31+G\* level to lie 0.42 eV above the  $n\pi^*$  minimum. Semiempirical MRCI surface-hopping dynamics simulations performed by Fabiano and Thiel [144] indicate a two-step nonadiabatic relaxation consisting of a  $\sim 15$ -fs  $S_2 \rightarrow S_1$  deactivation and a  $\sim 560$ -fs exponential repopulation of the  $S_0$  ground state, fairly analogous to the *ab initio* MRCI-S excited-state dynamics [184] except that the second step mainly proceeds via the  $^6S_1$  channel (OM2/MRCI) rather than the  $^2E$  channel (MRCI-S). To summarize, these studies agree on some general qualitative features of gas-phase 9*H*-adenine, for example, the presence of three closely coupling excited states around 5 eV ( $n \rightarrow \pi^*$ ,  $L_a \pi \rightarrow \pi^*$ , and  $L_b \pi \rightarrow \pi^*$ ), the existence of several competing nonradiative decay channels (e.g.,  $^6S_1$  vs.  $^2E$ ), and the distorted geometries at the corresponding conical intersections, while differing in various mechanistic details. These investigations have laid the foundation for the further exploration of real DNA systems. In this chapter, we review the systematic investigation of solvated 9*H*-adenine [93] and adenine embedded in solvated DNA strands. [94-95]



## 4.1 From single adenine to DNA strands

Numerous experimental studies employing various time-resolved spectroscopic techniques have been published on solvated DNA models in the past decade. As the simplest model in the condensed phase, solvated *9H*-adenine or adenosine was determined to exhibit decay time constants of 180-670 fs in water, slightly shorter than in the gas phase. [188-189,217-221] Regarding the much more complicated DNA photophysics and photochemistry, the spectroscopists have reported multiexponential behavior with time constants ranging from hundreds of femtoseconds to hundreds of picoseconds (see Table 4.1 and Table 4.2). [222] Considering the much longer components compared to isolated (gas-phase or solvated) nucleobases, it has been suggested that the photodynamics in DNA may be composed of multiple decay channels involving localized and/or delocalized states and processes. A variety of decay models have been proposed to explain the puzzling observations, for example:

- ▶ The Kohler group [223-225] [(dA)<sub>18</sub> and (dA)<sub>18</sub>·(dT)<sub>18</sub>] and the Fiebig group [226-227] [(dA)<sub>2-18</sub> and (dA)<sub>12/18</sub>·(dT)<sub>12/18</sub>] conducted femtosecond pump-probe experiments and came to similar conclusions, namely that singlet excited states of single or “badly” stacked bases relax to the hot ground state by ultrafast internal conversion within 1 ps, while initial excitons delocalized over several bases rapidly (sub-picosecond) trap to “localized” (on two bases) exciplexes or charge-transfer (CT) states that survive longer than 100 ps.
- ▶ Markovitsi and coworkers [228-231] [(dA)<sub>20</sub>, (dA)<sub>20</sub>·(dT)<sub>20</sub>, and double-stranded polymers (dA)<sub>*n*</sub>·(dT)<sub>*n*</sub>] also detected multiexponential components [0.3-0.85 ps, 1.6-3.9 ps, and up to 187 ps] with transient absorption up-conversion techniques that are able to map the temporal behavior of photoluminescence. They interpreted their findings as Frenkel and/or CT excitons [232-234] extending over several bases, which give rise to the longer components after ultrafast (<100 fs) intraband scattering. They suggested that the decay of  $\pi \rightarrow \pi^*$  and/or  $n \rightarrow \pi^*$  states of thymine/adenine single bases corresponds to the shorter components.
- ▶ Using a tri-exponential decay function, Schwalb and Temps [235] reported similar fitting results with time constants of 0.52-0.63 ps, 2.6-5.8 ps, and 16.2-97.0 ps for their up-conversion experiments on (dA)<sub>20</sub> and (dA)<sub>20</sub>·(dT)<sub>20</sub>.

## Chapter 4 Excited state dynamics of adenine

- Phillips and coworkers [236] reported Kerr-gated fluorescence spectra of solvated (dA)<sub>20</sub> and proposed a decay mechanism, in which all components originate from monomeric adenine excitation, but embark on different decay paths including radiationless internal conversion (IC, ~0.39 ps) and the formation of two excimers E<sub>1</sub> (~4.3 ps) and E<sub>2</sub> (~182 ps).

**Table 4.1** A summary of major time-resolved spectral experiments for DNA single strands.

group	sample	$\tau_1$	$\tau_2$	$\tau_3$	excitation		decay		technique	Ref.
					mn	en	mn	em		
Fiebig	(dA) <sub>2-18</sub>	0.2	8-10	>100	yes	yes	yes	yes	pump-probe	[226]
Kohler	(dA) <sub>18</sub>		2.02	126	yes	yes	yes	yes	pump-probe	[222-223]
Markovitsi	(dA) <sub>20</sub>	0.3	1.6		yes	yes	yes	no	up-conversion	[237]
Phillips	(dA) <sub>20</sub>	0.39	4.3	182	yes	no	yes	yes	Kerr-gated	[236]
Temps	(dA) <sub>20</sub>	0.63	5.8	97.0		yes		yes	up-conversion	[235]

mn=monomer; en=exciton; em=excimer.

**Table 4.2** A summary of major time-resolved spectral experiments for DNA double strands.

group	sample	$\tau_1$	$\tau_2$	$\tau_3$	excitation		decay		technique	Ref.
					mn	en	mn	em		
Fiebig	(dA) <sub>12/18</sub> ·(dT) <sub>12/18</sub>	<1	8-10	>100	yes	yes	yes	yes	pump-probe	[226]
Kohler	(dA) <sub>18</sub> ·(dT) <sub>18</sub>		2.46	101	yes	yes	yes	yes	pump-probe	[222-223]
Markovitsi	(dA) <sub>20</sub> ·(dT) <sub>20</sub>	0.4	2.4		yes	yes	yes	no	up-conversion	[237]
		0.46	2.80							
	(dA) <sub>n</sub> ·(dT) <sub>n</sub>	0.85	3.9	187						[229]
Temps	(dA) <sub>20</sub> ·(dT) <sub>20</sub>	0.52	2.6	16.2		yes		yes	up-conversion	[235]

mn=monomer; en=exciton; em=excimer.

The major mechanisms from the literature are summarized in Table 4.3. This brief review shows that, although a number of interpretations emerged to rationalize the experimental observations, there is still a long way from a firm consensus on the DNA excited-state dynamics. Controversial issues include the localized and/or delocalized character of the excited states and the effects of environments (solvents and DNA strands).

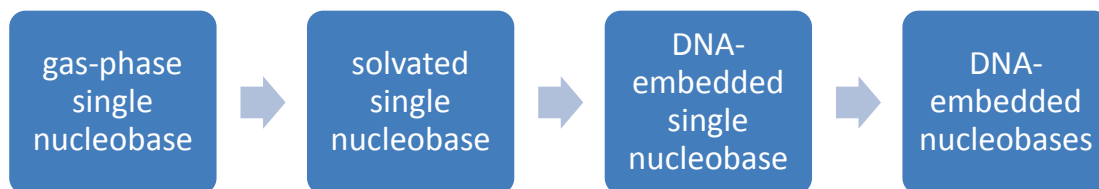
The enigma of DNA photochemistry has also aroused much interest on the theoretical side. There have been many efforts to establish sound theoretical models and to explain the experimental observations. The simplest models, stacked base dimers (as well as trimers) and base pairs, have been studied most. DFT, CASSCF, and configuration interaction approaches have been applied to model virtually every aspect of DNA photochemistry, including energetics, [238-239]  $\pi$ -stacking and/or base-pairing, [240-242] electrostatic interactions, [243] damage and repair reactions, [244-245] <sup>excited-state</sup> delocalization (charge transfer, <sup>excimer/exciple</sup>, <sup>exciton</sup>), [246-249] and decay dynamics. [250] Various methods have been applied to investigate the

## 4.1 From single adenine to DNA strands

solvent effects in DNA photodynamics, for example: the continuum solvation models [251], the reference interaction site model self-consistent field (RISM-SCF) method, [252] the sequential Monte Carlo/CASPT2 approach with a simple point charge (SPC) model, [253] and the polarizable continuum model [254-262] (PCM). Unfortunately, such calculations quickly become much more costly when going to larger systems like polynucleotides.

In such cases, semiempirical methods are attractive because of their efficiency and still acceptable accuracy. The INDO/S [40,263-265] method has given reasonable results for the excitation energies of DNA strands. [238,266-267] A recent direct semiclassical simulation studies on DNA fragments has also been performed at the semiempirical level. [90,268] However, even semiempirical methods meet difficulties when dealing with large molecules in the condensed phase, e.g., solvated DNA. For such systems, QM/MM [54-55] becomes a practical choice. The QM/MM approach (as introduced in Chapter 1) allows a realistic description of the chromophore in its native environment, accounting for the effects of steric repulsion, transient hydrogen bonding, van der Waals (vdW) interactions, etc., and it thus enables full-scale atomistic simulations. Some successful QM/MM studies on DNA excited states, including nonadiabatic dynamics simulations, have already been presented. [92,269-270]

To our knowledge, none of the currently available theoretical approaches is yet quantitatively reliable in modeling a system as large as solvated DNA. The simulation of the nonadiabatic dynamics in the condensed phase is especially challenging because of the need to realistically describe both the electronic structure of all relevant excited states under the influence of the environment and the dynamics of the entire system. In our work, we followed the strategy to start from a single isolated nucleobase and then successively increase the complexity towards DNA using the semiempirical OM2/MRCI [44-45,49,53] method. We thus set a logical road map to step from a simple gas-phase model toward fully atomistic simulations of DNA:



Here we focus on steps 2 and 3 of this road map, namely *9H*-adenine solvated in water and single *9H*-adenine embedded in DNA strands.

## Chapter 4 Excited state dynamics of adenine

**Table 4.3** A summary of various pathways of DNA decay suggested by spectroscopists.

group	scheme suggested	Ref.
Fiebig	<ul style="list-style-type: none"> <li>▶ exciton of 3-4 (or more) bases <math>\xrightarrow{\sim\text{several ps}}</math> “localized” exciplex</li> <li>    dimer <math>\xrightarrow{\sim\text{several } 100 \text{ ps}}</math></li> <li>▶ single base <math>\xrightarrow{\sim 200 \text{ fs}}</math> <math>S'_0</math> (hot ground state)</li> </ul>	[227]
Kohler	<ul style="list-style-type: none"> <li>▶ locally excited Franck-Condon of stacked bases <math>\xrightarrow{&lt;0.4 \text{ ps}}</math></li> <li>    excimer <math>\xrightarrow{&gt;100 \text{ ps}}</math></li> <li>▶ unstacked bases <math>\xrightarrow{&lt;1 \text{ ps}}</math> <math>S'_0</math> (hot ground state) <math>\xrightarrow{2 \text{ ps}}</math> <math>S_0</math> (by vibrational cooling)</li> <li>▶ initial excitons <math>\xrightarrow{\text{several ps}}</math> <math>\xrightarrow{&lt;1 \text{ ps}}</math> “localized” exciplexes or charge-transfer states <math>\xrightarrow{&gt;100 \text{ ps}}</math></li> </ul>	[223]
Markovitsi	<ul style="list-style-type: none"> <li>▶ Frenkel and/or CT exciton of 2-6 (or more) bases <math>\xrightarrow{&lt;100 \text{ fs}}</math></li> <li>    intraband scattering <math>\xrightarrow{\text{longer component}}</math> emission</li> <li>▶ <math>\pi\pi^*</math> of thymine (and/or adenine) single bases <math>\xrightarrow{\text{shorter component}}</math> emission</li> <li>▶ <math>n\pi^*</math> states <math>\rightarrow</math> emission</li> <li>▶ no excimer/exciple</li> </ul>	[229-230]
Phillips	<ul style="list-style-type: none"> <li>▶ single adenine <math>\xrightarrow{\sim 0.39 \text{ ps}}</math> irradiative internal conversion</li> <li>▶ single adenine <math>\xrightarrow{\text{ultrafast}}</math> <math>E_1</math>-excimer <math>\xrightarrow{\sim 4.3 \text{ ps}}</math> emission</li> <li>▶ single adenine <math>\xrightarrow{\text{ultrafast}}</math> <math>E_2</math>-excimer <math>\xrightarrow{\sim 182 \text{ ps}}</math> emission</li> </ul>	[236]
Temps	<ul style="list-style-type: none"> <li>▶ exciton or exciplex (with charge transfer) <math>\xrightarrow{&lt;100 \text{ ps}}</math></li> </ul>	[235]

Three nucleobase models were constructed at the QM/MM level in this work: *9H*-adenine solvated in water (Figure 4.1b) and adenine embedded in two *B*-type oligonucleotides (dA)<sub>10</sub> and (dA)<sub>10</sub>·(dT)<sub>10</sub> (Figure 4.1c and d). They were entirely solvated in spherical water droplets with a diameter of about 40 Å for *9H*-adenine in water and 60 Å for adenine in DNA strands. Overall, 3333, 12457, and 12515 atoms were included in the models, respectively. We have performed 2-ps Born-Oppenheimer molecular dynamics (BOMD) simulations at 300 K for generating the initial states, geometries, and velocities for the subsequent 1.5-ps surface-hopping dynamics simulations.

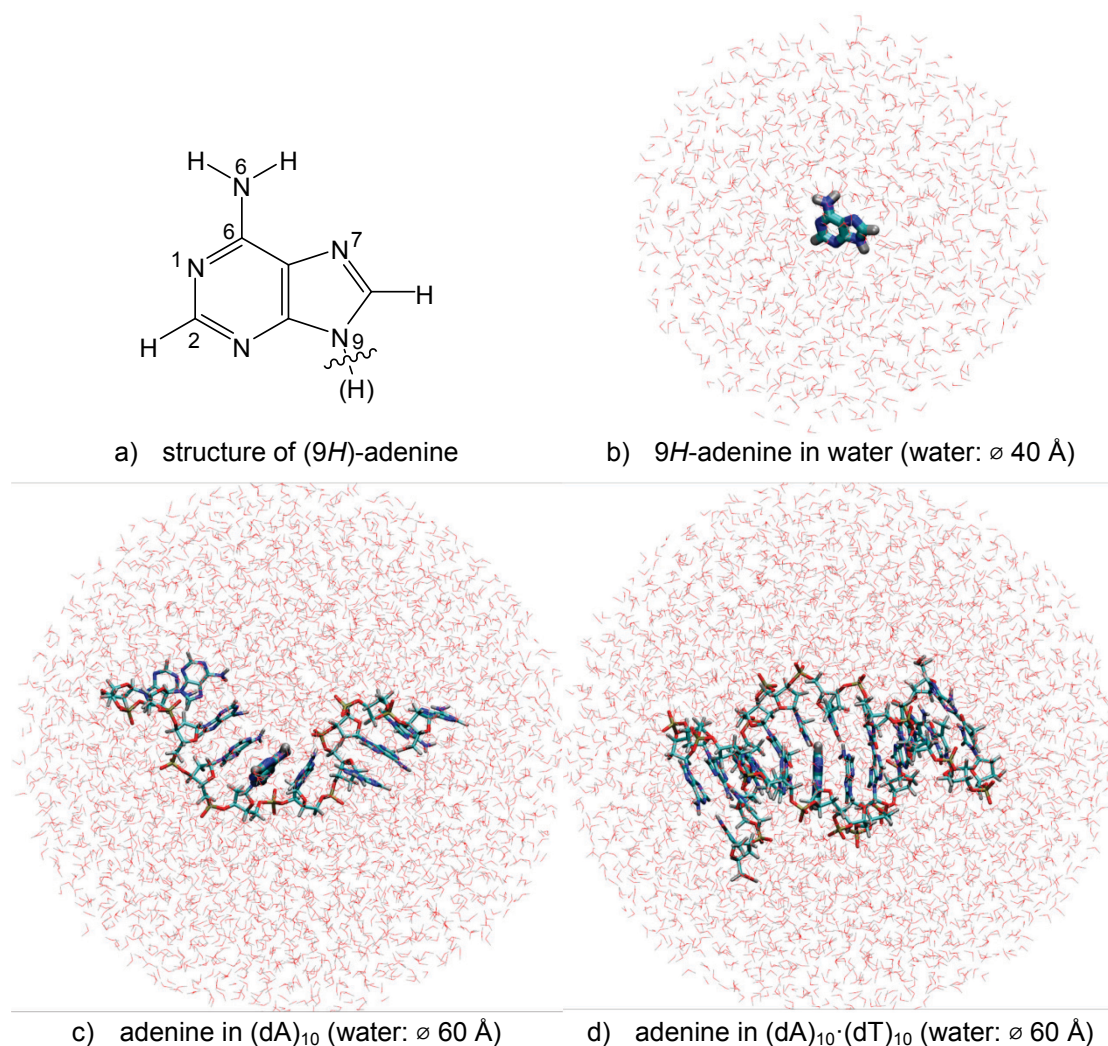


**Figure 4.1** The systems investigated in the current work for (9*H*)-adenine. the QM part is shown in bold-licorice

## 4.2 Absorption and fluorescence spectra

We first compare the calculated absorption spectra of single adenine in the gas phase, [144] in the aqueous phase, [93] and in oligonucleotides. [94-95] The steady-state absorption spectra were derived from snapshots taken from ground-state BOMD simulations (to ensure proper sampling) by superimposing Gaussian-broadened absorption profiles obtained from the computed vertical excitation energies and oscillator strengths ( $S_0$  to  $S_1$ ,  $S_2$ , and so on). The simulated spectra are shown in Figure 4.2 for (9*H*)-adenine surrounded by four environments.

## Chapter 4 Excited state dynamics of adenine

We note that there is a small red shift (0.06 eV) when going from the gas phase (QM) to aqueous solution (QM/MM), and a small blue shift (0.09-0.17 eV) when going from the latter to the DNA strands (QM/MM). For single adenine in DNA strands, the first absorption band, with a maximum of 4.71 eV in (dA)<sub>10</sub> and 4.78 eV in (dA)<sub>10</sub>·(dT)<sub>10</sub>, can be decomposed into three overlapping transitions at 4.60, 4.80, and 4.93 eV in (dA)<sub>10</sub> and at 4.66, 4.91, and 4.99 eV in (dA)<sub>10</sub>·(dT)<sub>10</sub>, respectively (see Figure 4.2c and d).

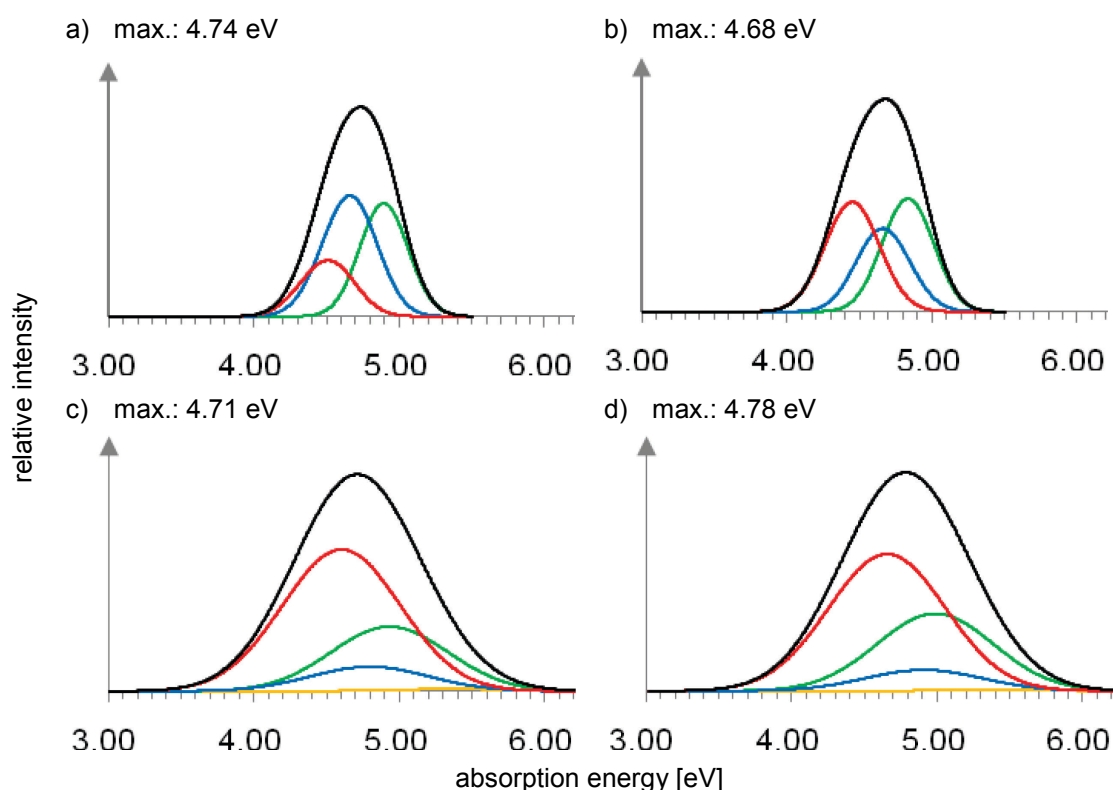


**Figure 4.2** Calculated absorption spectra of single adenine using the QM or QM/MM (QM=OM2/MRCI) approach and snapshots from ground-state BOMD simulations (with Gaussian broadening): (a) in vacuo, (b) in water, (c) in (dA)<sub>10</sub>, and (d) in (dA)<sub>10</sub>·(dT)<sub>10</sub>. The overall bands (black) can be decomposed into contributions from the lowest-energy transitions: S<sub>1</sub> (red), S<sub>2</sub> (blue), S<sub>3</sub> (green), and S<sub>4</sub> (yellow).

Various experimental spectra show similar red shifts [222,272-274] (0.14-0.31 eV) and blue shifts [228,231,275] (0.01-0.07 eV). These shifts are induced by the complex electrostatic and steric environment in the condensed phase. Due to the monomeric nature of the current models of single adenine in DNA strands, the calculated absorption bands exclude contributions from delocalized excimer and exciton states, which are reported to be present in the experimental spectra. [222-230,237] In spite of this inherent limitation, the QM/MM



## 4.2 Absorption and fluorescence spectra

results for a single QM adenine compare reasonably well with the experimental spectra, which have their absorption maximum at 4.82 eV for single-stranded (dA)<sub>20</sub> [275] and at 4.78 eV [or 4.84 eV] for double-stranded (dA)<sub>20</sub>·(dT)<sub>20</sub> [or (dA)<sub>n</sub>·(dT)<sub>n</sub>]. [231] The deviations of the computed monomeric band maxima from experiment are quite uniform (red shift) in the gas phase, in water, and in DNA. They are well within the usual error margin of OM2/MRCI. [53]

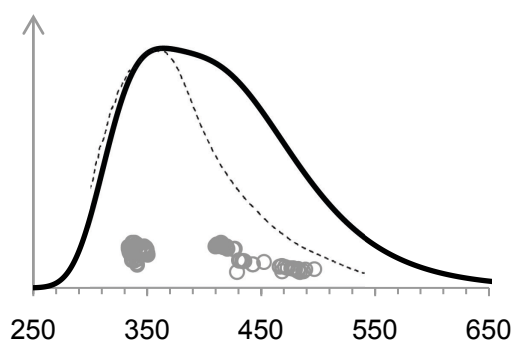


**Figure 4.3** Computed emission spectrum of single adenine in (dA)<sub>10</sub> (black line) with envelope of  $E_{\text{emission}}(S_1 \rightarrow S_0)$  based on 121 optimized  $S_1$  structures (grey circles). The experimental steady-state fluorescence of (dA)<sub>20</sub> from Ref. [236] is shown as dashed line.

Our calculated spectra can be compared with the QM/MM [QM=MSPT2//CASSCF(12,10)] results for single adenine in (dA)<sub>10</sub>·(dT)<sub>10</sub> by Conti et al., who report excitations at 4.83 eV, 5.04 eV, and 5.49 eV and assign them to  $L_a$  ( $\pi \rightarrow \pi^*$ ),  $L_b$  ( $\pi \rightarrow \pi^*$ ), and  $n \rightarrow \pi^*$ , respectively. [270] Consistently, OM2/MRCI also finds the lowest excitation to be bright for single adenine in DNA, which, to a large extent, displays  $L_a$  ( $\pi \rightarrow \pi^*$ ) character. Similar agreement is seen for  $S_2$  which also involves a  $\pi \rightarrow \pi^*$  transition (assigned as  $L_b$  by Conti et al.), while the dark  $S_3$  state lies at a higher energy at the MSPT2//CASSCF level. [270] Nevertheless, it is important to note that the simple diabatic picture breaks down here because there is generally a rather strong mixing between the lowest singlet states. The character of the electronic states often changes during the MD trajectory at the distorted geometries where the MOs are also mixed. Accordingly, it is inappropriate to label the PESs of these states in terms of  $L_a$ ,  $L_b$ , or  $n \rightarrow \pi^*$ . Therefore we only discuss the excited states in adiabatic language, i.e.,  $S_1$  and  $S_2$  states.

To estimate the steady-state emission of single adenine in (dA)<sub>10</sub>, we optimized the  $S_1$

excited-state geometries for all trajectories and reached convergence for 121 out of 200 snapshots. As indicated in Figure 4.3, there are two groups of optimized structures, which show emission with relatively large oscillator strengths ( $\sim 0.08$ - $0.10$ ), at energies around 410 nm (3.0 eV, mostly  $\pi \leftarrow \pi^*$ ) and 340 nm (3.6 eV, mixed  $\pi \leftarrow \pi^*$  and  $n \leftarrow \pi^*$  character). Experimentally, the steady-state fluorescence spectrum of the oligonucleotide (dA)<sub>20</sub> has a broad emission maximum at  $\sim 360$  nm ( $\sim 3.4$  eV) that envelops our predicted peaks. [236] We expect that dynamic effects can mix the emissions arising from the optimized excited-state local minima.

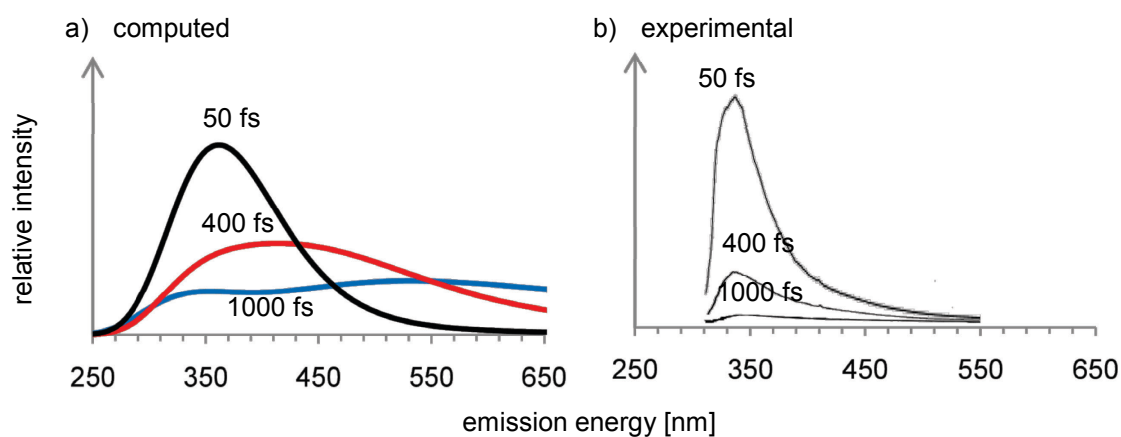


**Figure 4.4** Time-resolved emission spectrum of single adenine in (dA)<sub>10</sub> computed at the QM/MM (QM=OM2/MRCI) level by averaging over the nonadiabatic dynamics simulations (with Gaussian broadening), recorded at 50 fs (black), 400 fs (red), and 1000 fs (blue), respectively. The experimental time-resolved fluorescence spectrum of (dA)<sub>20</sub> from Ref. [236] is shown on the right.

Figure 4.4 shows the calculated temporal evolution of emission derived from the nonadiabatic dynamics simulations of single adenine in (dA)<sub>10</sub>, where three MD snapshots spanning 20 fs (to simulate the experimental resolution) were broadened over all trajectories for each recorded time (50, 400, and 1000 fs). This calculation predicts spectral shapes that are compatible with the experimental time-resolved fluorescence spectra of the adenine oligomer. [236] Both the calculated and experimental contours possess prominent tails extending to longer wavelengths. In the calculated emission spectra, these tails arise from a progressive red shift of the monomeric emission as time goes on. There is an accompanying attenuation of the fluorescence intensity over time, as also reported in the experimental work. [236] However, the computed red shift is more pronounced than the observed one (see Figure 4.4). We note again in this context that the calculated emission spectra refer to a single



QM adenine and thus do not account for delocalized excimer/exciple states that are believed to be indispensable, [223] which will cause some systematic errors. For the purpose of documentation, we also simulated the time-resolved fluorescence spectrum for single adenine in (dA)<sub>20</sub>·(dT)<sub>20</sub> without further discussion (see Ref. [95]). This computed spectrum cannot be directly compared to the experimental spectra, [230,276-277] since the actual emission process may involve the other nucleobase (thymine) and various delocalized electronic states.

### 4.3 Decay dynamics

Due to the mixed character of the vertical transitions during the BOMD simulation, a minor portion [12% for adenine in (dA)<sub>10</sub> and 19% in (dA)<sub>10</sub>·(dT)<sub>10</sub>] of nonadiabatic dynamics trajectories start from the S<sub>2</sub> state. The corresponding S<sub>2</sub>→S<sub>1</sub> internal conversion is found to take place extremely rapidly, with a mean time constant of only ~7 fs (see Figure 4.5c and d). This process is faster than in the gas phase or in water. This computed ultrafast S<sub>2</sub>→S<sub>1</sub> decay reflects the strong mixing of different electronic configurations. Our exponential fitting for the S<sub>1</sub> state gives mean time constants of 5.7 ps and 4.1 ps for adenine in (dA)<sub>10</sub> and (dA)<sub>10</sub>·(dT)<sub>10</sub>, respectively (see Figure 4.5c and d). Unexpectedly, these values are larger than those in the gas phase (~0.5 ps) and in water (~0.4 ps) by an order of magnitude. This means that the decay dynamics of a single adenine is much slowed down when it is embedded in DNA helices. As discussed in Section 4.1, time-resolved spectroscopic studies have reported that the fluorescence is of multiexponential character and may involve monomeric nucleobases. [222-225,227,229-230,235-236,271] The simulations of our model system provide computational evidence that monomeric nonradiative processes may contribute to the observed decay component with time constants of several picoseconds in DNA strands. We have analyzed the conformational changes during all trajectories and found that the decay process takes place in two stages: in stage I, the geometric preparation is done that is required to reach the conical intersection region; and in stage II, the trajectories fluctuate on the S<sub>1</sub> surface near the conical intersection until the internal conversion occurs. The reason for the much longer decay times will be analyzed in Section 4.4.

Despite the fact that the adenine units in DNA single and double strands are computed to have similar time constants for the S<sub>1</sub>→S<sub>0</sub> internal conversion, they decay by very different

mechanisms. 26% of the 73 simulated trajectories for adenine in (dA)<sub>10</sub> hop to the S<sub>0</sub> surface within the simulation time. The dihedral angle  $|\angle(\text{N1C5C6N6})|$  in 11 of these trajectories is less than 145° at the S<sub>1</sub>→S<sub>0</sub> hopping event (Figure 4.6c), indicating a decay channel via an S<sub>0</sub>/S<sub>1</sub> conical intersection that is characterized by out-of-plane deformation of the amino group and ring puckering at the C6 atom (Figure 4.7a). The same reaction channel is also found to be the dominant one for 9*H*-adenine in vacuo and in water (Figure 4.6a and b). According to the Cremer-Pople-Boeyens classification, this type of distorted conformation is denoted as <sup>6</sup>S<sub>1</sub> [or more explicitly as CI(<sup>6</sup>S<sub>1</sub>)]. [278-279] In three trajectories, the nonradiative decay occurs via another conical intersection that exhibits puckering of the six-membered ring at the C2 atom and bending of the C2H2 moiety (see Figure 4.6c and Figure 4.7b). This conical intersection is denoted as the <sup>2</sup>E channel. The remaining five trajectories undergo diverse side reactions, including ring decomposition and C2-H2 or C8-H8 cleavage, before hopping to the ground state. To summarize, the primary decay mechanism of single adenine in vacuo, in water, and in (dA)<sub>10</sub> is identified to be dominated by the same <sup>6</sup>S<sub>1</sub> type of conical intersection.

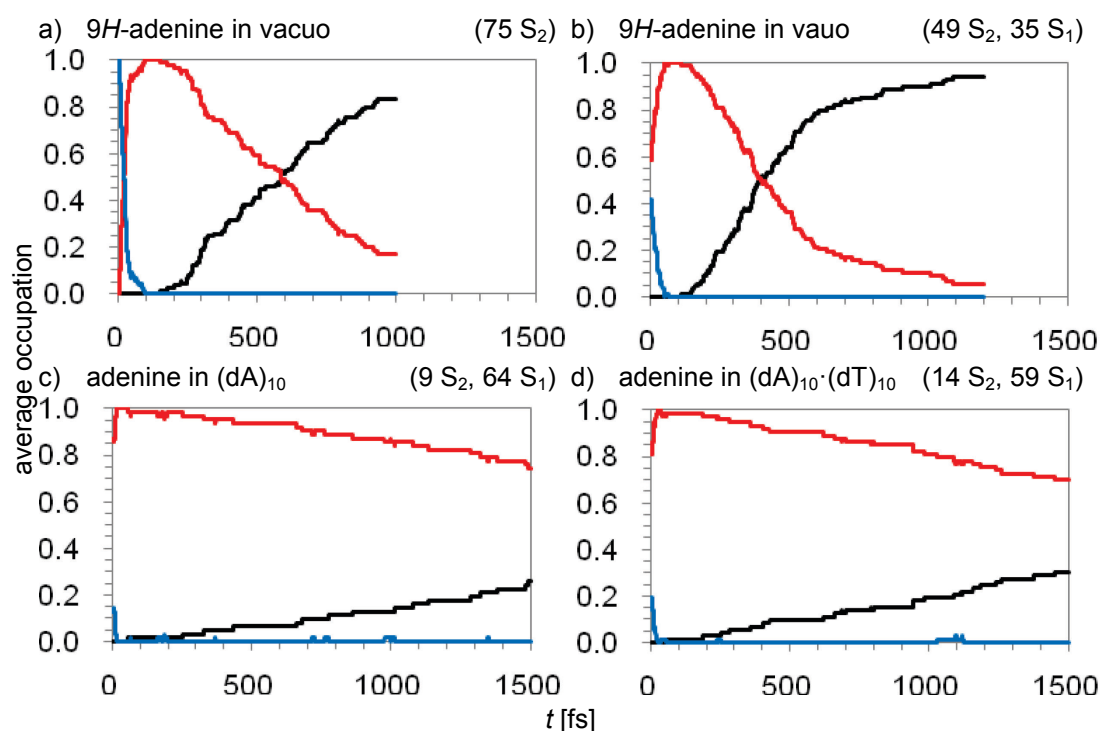


**Figure 4.5** Average occupation of the adenine low-lying electronic states during the nonadiabatic dynamics:  $S_0$  (black)  $S_1$  (red), and  $S_2$  (blue). The number of trajectories starting from  $S_1$  and  $S_2$  are specified in parentheses, respectively.

Within the 1.5 ps of simulation time for adenine in the  $(dA)_{10} \cdot (dT)_{10}$ , 29% of the 73 trajectories decay to the ground state. 14 trajectories of them proceed via the  ${}^2E$  conical intersection which acts as the minor pathway for adenine in single-stranded DNA, with dihedral angles  $|\angle(N1C2N3C4)|$  of  $60\text{--}80^\circ$  at the hops (see Figure 4.6d and Figure 4.7c). Four trajectories decay to the ground state via a conical intersection where the annelated rings fold along the bridging C4-C5 bond and the six-membered ring puckers at N3 to form a screw-boat structure. This  ${}^4S_3$  type conformation has been reported in Ref. [184] (see Figure 4.7d). Again, the remaining four trajectories return to the ground state through diverse side reactions. Notably, no trajectory of adenine in  $(dA)_{10} \cdot (dT)_{10}$  decays to  $S_0$  by the  ${}^6S_1$  mechanism.

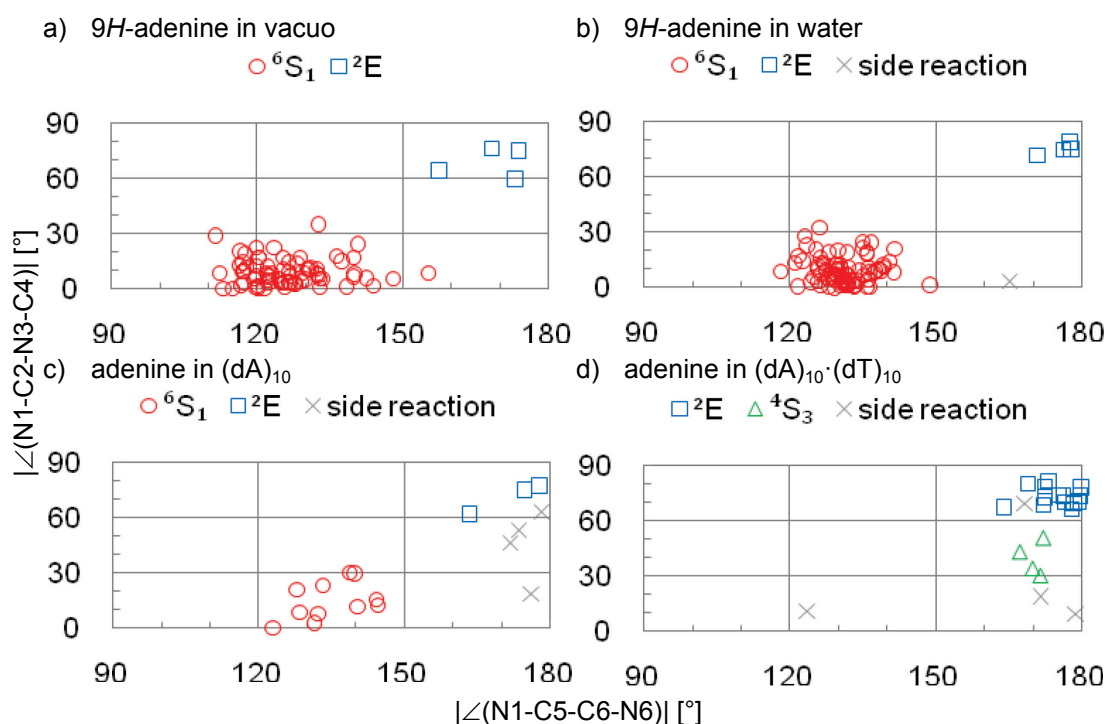


**Figure 4.6** Distribution of the dihedral angles ( $^{\circ}$ ) N1-C2-N3-C4 and N1-C5-C6-N6 of adenine at hops: the hopping channels are distinguished by different symbols.

In contrast to the dominance of a single decay channel for *9H*-adenine in vacuo and in water, where over 90% of the trajectories pass CI( $^6S_1$ ) and only less than 10% decay via CI( $^2E$ ), the decay of single adenine within  $(dA)_{10}$  is of mixed character (60%  $^6S_1$  and 16%  $^2E$ ). In the duplex DNA model, each adenine is bound to a thymine counterpart by two strong hydrogen bonds,  $N6H^A \dots O2^T$  and  $N1^A \dots H3^T$ , forming a Watson-Crick base pair. Since the hydrogen bonding provides significant stabilization, the out-of-plane motion of the amino group will be completely impeded. In all 22 trajectories that exhibit a nonadiabatic transition, the  $N6H^A \dots O2^T$  hydrogen bond is well retained, with  $N6H^A \dots O2^T$  distances varying between 2.8 and 3.6 Å during the simulation time. In the nonradiative decay of adenine in  $(dA)_{10} \cdot (dT)_{10}$ , the  $^6S_1$  channel is thus completely suppressed, and the  $^2E$  channel becomes dominant. This clearly demonstrates that the mechanism for the internal conversion of adenine to the electronic ground state is controlled by the biological environment.

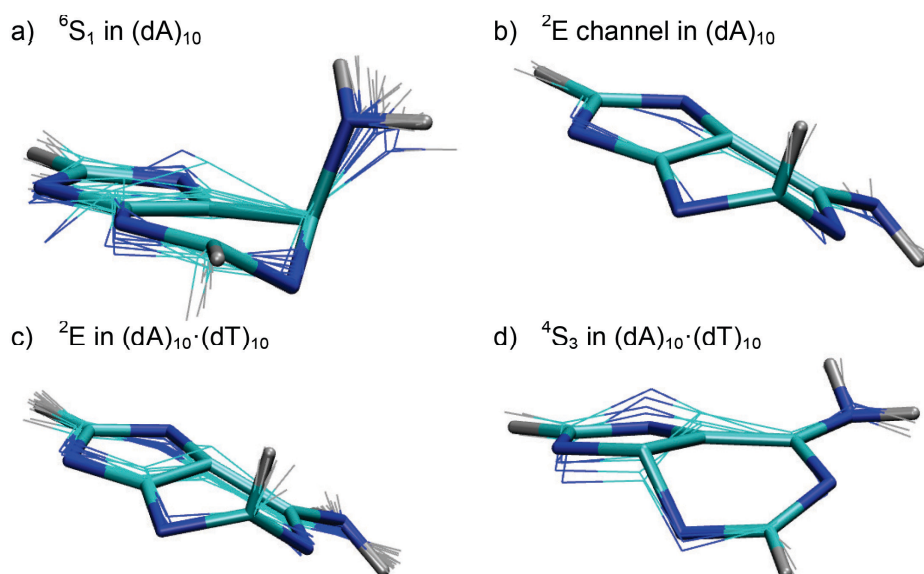


**Figure 4.7** Overlays of the hopping structures of DNA adenine: (a)  ${}^6S_1$  channel in  $(dA)_{10}$ ; (b)  ${}^2E$  channel in  $(dA)_{10}$ ; (c)  ${}^2E$  channel in  $(dA)_{10}\cdot(dT)_{10}$ ; and (d) screw-boat channel in  $(dA)_{10}\cdot(dT)_{10}$ . The structures represented in bold-licorice are the minimum-energy crossing points from Ref. [184], and the structures drawn in the line representation show the hopping geometries from our current simulations.

## 4.4 Influence of the environment

### ► Hydrogen bonding in aqueous solution

The nonadiabatic decay dynamics of *9H*-adenine in solution [93] is similar to that in the gas phase, [144] since the  $CI({}^6S_1)$  channel is favored over the  $CI({}^2E)$  channel in both cases. The decay process in water is found to be even slightly faster than in vacuo. This can be traced back to the solvent effect arising from the aqueous environment. The two competing decay mechanisms ( ${}^6S_1$  and  ${}^2E$ ) involve substantial out-of-plane motions at the N6 and H2 atoms. Hence we analyzed the  $S_1$  gradients at these two atoms at the FC geometries, denoted as  $\vec{g}_{S_1}(N6)$  and  $\vec{g}_{S_1}(H2)$ , and compared the norms of their components perpendicular to the ring plane (plane N1C5C6 and N1C2N3, respectively), i.e.,  $\|\vec{g}'_{S_1}(N6)\|$  and  $\|\vec{g}'_{S_1}(H2)\|$  (see Figure 4.8). We found that  $\|\vec{g}'_{S_1}(N6)\|$  is generally larger than  $\|\vec{g}'_{S_1}(H2)\|$  (see Figure 4.9). In the FC region, the  $S_1$  gradient thus drives the C6-N6 moiety to bend out of the plane, much more so than the C2-H2 moiety, towards geometries where the  $S_1$  state exhibits diminishing

$\pi \rightarrow \pi^*$  and increasing  $n \rightarrow \pi^*$  character. The reaction path leading to CI( ${}^6S_1$ ) with an out-of-plane amino group is therefore dynamically favored over the  ${}^2E$  channel that involves out-of-plane motion of the H2 atom.

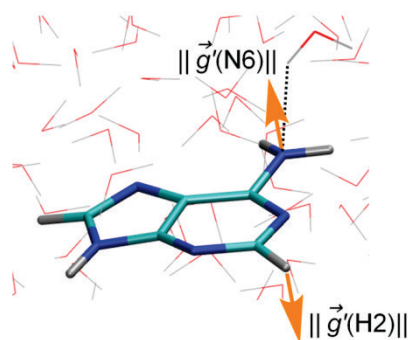


**Figure 4.8** Components of the  $S_1$  gradient perpendicular to the plane of solvated  $9H$ -adenine:  $\|\vec{g}'(\text{H2})\|$  at H2 and  $\|\vec{g}'(\text{N6})\|$  at N6. The latter benefits from hydrogen bonding (see text).

When comparing with the situation in the gas phase (see Figure 4.9), we clearly see that, in the FC region, the norm  $\|\vec{g}'_{S_1}(\text{N6})\|$  tends to be larger in water than in vacuo, and hence there is a more pronounced tendency for the out-of-plane motion of the amino group in the dominant CI( ${}^6S_1$ ) channel. This rationalizes the slightly faster decay dynamics of  $9H$ -adenine in water compared with the gas phase.

To figure out why  $\|\vec{g}'_{S_1}(\text{N6})\|$  is larger than  $\|\vec{g}'_{S_1}(\text{H2})\|$ , we analyzed the hydrogen bonding between the N6 atom and solvent water molecules. A histogram distribution of the distance between N6 and the nearest hydrogen from solvent water at the FC geometries is plotted in Figure 4.10. A favorable distance (1.9-2.1Å) for an N6...H<sup>water</sup> hydrogen bond is found in almost 50% of the snapshots. Hence, hydrogen bonding is present and appears to accelerate the decay of adenine in water through the  ${}^6S_1$  conical intersection, since the direction of the gradient at N6 correlates with the position of the nearest hydrogen-bonding water molecule.

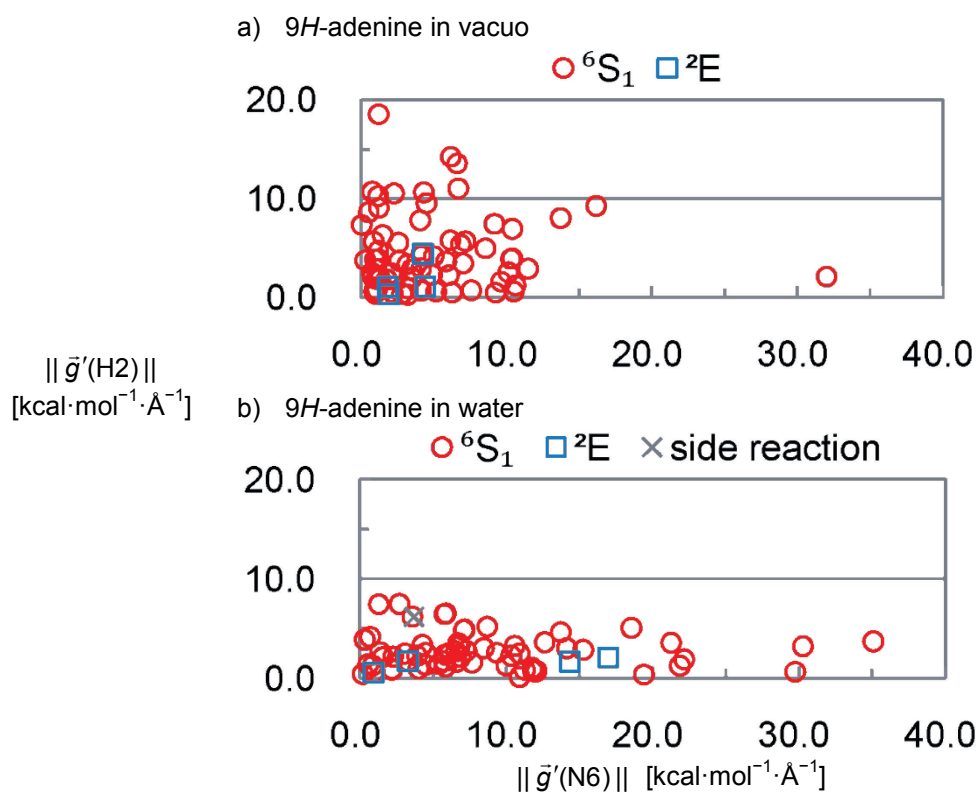


**Figure 4.9** Distribution of  $\|\vec{g}'(\text{H2})\|$  versus  $\|\vec{g}'(\text{N6})\|$  at the initial FC geometries of 9H-adenine: (a) in vacuo [144] and (b) in water. [93]  $\|\vec{g}'(\text{H2})\|$  and  $\|\vec{g}'(\text{N6})\|$  denote the norms of the S<sub>1</sub> gradient components perpendicular to the planes (N1C5C6) and (N1C2N3), respectively.

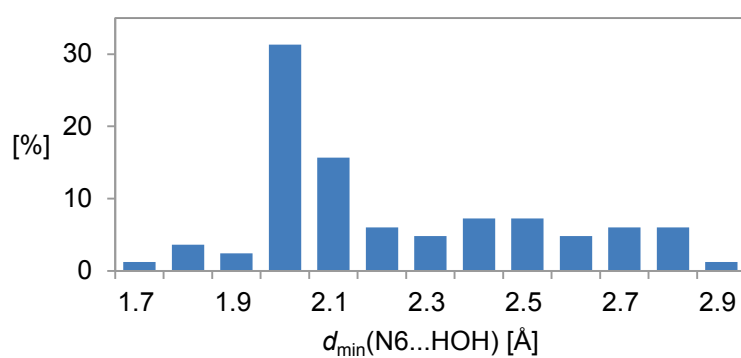


**Figure 4.10** Histogram of the minimum distance between N6 and the water hydrogen atoms at the initial FC geometries

### ► Steric hindrance in the DNA models

The  ${}^6S_1$  channel requires pronounced out-of-plane motion of the amino group, which in the rather rigid DNA environment may be affected by steric effects of the environment. Assuming that the vdW force between two atoms is attractive (repulsive) when the distance between them is greater (smaller) than the sum of their vdW radii (i.e., the vdW contact distance), [280] we assessed the vdW interactions between the QM adenine embedded in single-stranded DNA and the nearest MM bases along the stacking direction, by monitoring the real-time change of the minimum distance between the QM adenine A and the nearest MM adenine A' or A'' during the nonadiabatic dynamics trajectories. We found significant instantaneous vdW repulsions in all trajectories between the following atom pairs: amino H<sup>A</sup> and amino N<sup>A'/A''</sup>, amino H<sup>A</sup> and ring N<sup>A'/A''</sup>, amino H<sup>A</sup> and ring C<sup>A'/A''</sup>, and amino N<sup>A</sup> and ring C<sup>A'/A''</sup>. In these cases the minimum distance is frequently below the vdW contact distance.

These repulsions between adjacent adenine moieties in close contact are expected to cause steric hindrance and to impede the out-of-plane deformation that is required to reach the  ${}^6S_1$  conical intersection region. When adenine is embedded in (dA)<sub>10</sub>, the bending motion of the amino group is seen in our simulations only after ~350 fs due to such steric hindrance. [94-95] By contrast, during all trajectories in vacuo and in water, this bending motion appears already after ~150 fs and quickly leads to favorable conformations for hopping. [93] Hence, the initial stage I needs more time in the DNA environment than in vacuo or water. Conti et al. also interpret the slower component of the DNA decay as the result of steric hindrance (barrier ~0.2 eV) in their *ab initio* QM/MM study. [270]

### ► Electronic effects in the DNA models

Steric effects are probably not the only reason for observed longer decay components in DNA oligomers. [225] In our simulations in vacuo and in water, most trajectories started the  $S_1 \rightarrow S_0$  hopping process as soon as the conformational preparation of stage I was finished after ~150 fs. The simulations of the DNA models showed a different behavior: After entering stage II at ~350 fs, the trajectories remained longer in the  $S_1$  state with less hopping events taking place. To rationalize this low hopping rate, we examined the electronic probability of nonadiabatic hopping, see Eq. 1.12. [65] Considering that the velocity  $\dot{\mathbf{R}}$  should be similar in different environments (at a given temperature) and that its direction is arbitrary, we compared the interstate NACME for the  $S_0$  and  $S_1$  states in the different models



$$d_R^{01}(\mathbf{R}) = {}^{\text{Cl}}d_R^{01}(\mathbf{R}) + {}^{\text{SCF}}d_R^{01}(\mathbf{R}) = \frac{h_R^{01}(\mathbf{R})}{\Delta E_{10}} + \sum_{i,j} \gamma_{ij}^{01} \left\langle \phi_i(\mathbf{r}; \mathbf{R}) \left| \frac{\partial \phi_j(\mathbf{r}; \mathbf{R})}{\partial R} \right. \right\rangle, \quad (4.1)$$

which was approximated by the dominant first term in our calculations. We found that the norm  $\|\mathbf{h}^{01}\|$  of the  $S_0/S_1$  interstate coupling vector of adenine in DNA is significantly smaller than that of 9H-adenine in the gas phase or in water, by a factor of about 2. Hence, the biological environment of adenine in DNA lowers the nonadiabatic  $S_1 \rightarrow S_0$  hopping probability, and the low hopping rate is also partly due to electronic effects exerted by the environment.

#### ► Energy gap in the DNA models

According to Eq. 4.1, the hopping probability is also dependent on the energy gap  $\Delta E_{10}$  between the  $S_1$  and  $S_0$  states. We also compared this term between the simulated models: in the gas phase and in water,  $\Delta E_{10}$  quickly approached zero and most hops occurred with a small  $\Delta E_{10}$ ; by contrast, the gap remained sizable for most trajectories in  $(\text{dA})_{10}$  during stage II. This observation clearly indicates that, compared to the gas-phase or aqueous-phase environment, the surrounding DNA strand does not allow adenine to reach appropriate conformations with a small energy gap. At the QM/MM level of theory, two factors determine this energy gap: firstly, the external MM point charges in the well-ordered DNA strand polarize the QM adenine and thus affect the energies; secondly, the energy gap is directly related to the molecular conformation.

#### ► Summary

Our preceding analysis shows that solvent (water) and environment (DNA) effects strongly influence the nonadiabatic decay dynamics of adenine. The situation is rather complicated since there are several such effects which may influence each other. For a chromophore in the condensed phase modeled by QM/MM nonadiabatic dynamics simulations, the hopping probability between two electronic states depends on a number of factors, as illustrated in Figure 4.11. The environment affects the conformational preferences of the chromophore and the accessible conformational space, for example through steric repulsion and specific hydrogen bonding. It also determines the temperature of the system and hence the nuclear velocities that enter the nonadiabatic coupling term; moreover, when fluorescence emission is quenched by internal conversion (surface hopping), the excess energy obtained from photoexcitation is converted into vibrational energy and finally dissipated to the environment

via vibrational cooling. [189,221] The electronic effects of the environment directly influence the nonadiabatic coupling matrix elements (NACME) and the energy gaps, through the polarization of the QM wavefunction, and they do so also indirectly via their influence on the conformation of the chromophore.

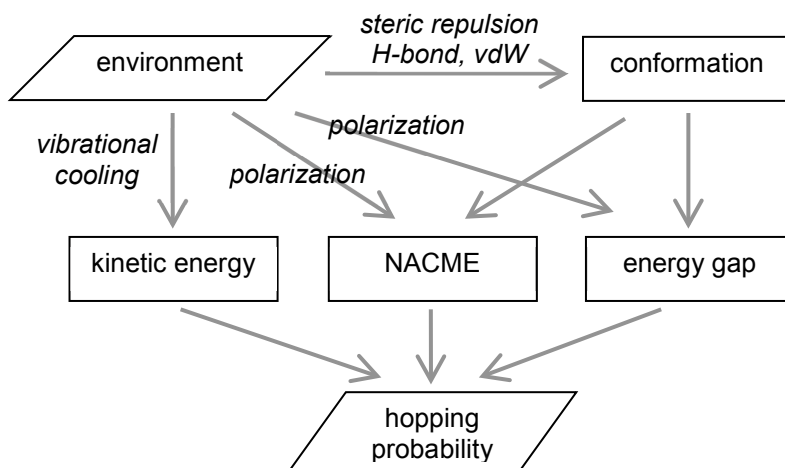


**Figure 4.11** Major environmental effects influencing the nonadiabatic dynamics

To summarize, we have advanced two steps in the research strategy outlined in Section 4.1, by investigating solvated *9H*-adenine and single adenine in solvated DNA strands. While our simulations explain at least part of the experimental observations, it should be stressed again that the present DNA studies are inherently limited to monomeric processes by having only a single QM adenine. The next step will be to remove this restriction and enlarge the QM region to at least two adenine units in order to study the behavior of delocalized states.

## Chapter 5

# Conclusion and outlook

We have presented in this work a wide panorama of theoretical studies on electronically excited states, encompassing validation of methodology, vertical transitions, excited-state equilibrium geometries, photochemical reactions, and nonadiabatic photoinduced process. In these studies, we have tried to be comprehensive and systematic. More specifically, we have reviewed the major theoretical methods for treating excited states and employed them in various applications; we have evaluated the performance of the semiempirical OM2/MRCI approach and implemented genetic algorithms for future reparametrizations; we have applied the semiempirical AM1/MRCI method to predict the fluorescence properties of the fluorophore OVP5; we have identified the photodissociation mechanisms of benzaldehyde and acetophenone at the *ab initio* CASPT2//CASSCF level; and finally, we have established a computational protocol for performing surface-hopping simulations of complex systems and applied it to study the excited-state dynamics of the charge-transfer molecule DMN and of the DNA nucleobase adenine in different environments.

The surface-hopping nonadiabatic dynamics simulations of DMN in the gas phase have been performed at the OM2/MRCI level. A decay lifetime of 1.2 ps was obtained for the  $S_1$  state, which falls into the range of the experimental observations. The reactive coordinate leading to conical intersection  $CI_{01\alpha}$  was found to be the C7=C8 double-bond twisting accompanied by pronounced pyramidalization at the C8 atom. The structures of several conical intersections were located by full optimizations, and their accessibility was checked by computing linearly interpolated reaction paths, which confirmed the preference for the  $CI_{01\alpha}$  channel. The

## Chapter 5 Conclusion and outlook

---

absorption and steady-state fluorescence spectra were calculated, and the time-resolved fluorescence of DMN was simulated, which compared well with the experimental spectrum and gave a fluorescence lifetime of  $\sim 1.0$  ps. The use of different active spaces in the OM2/MRCI calculations yielded similar results and thus demonstrated their internal consistency. Analogous investigations of the decay dynamics of the prototypical DMABN charge-transfer system are planned.

9*H*-adenine in the aqueous phase and embedded in solvated DNA oligomers, (dA)<sub>10</sub> and (dA)<sub>10</sub>·(dT)<sub>10</sub>, was studied at the QM/MM (QM=OM2/MRCI) level using surface-hopping dynamics simulations. 9*H*-adenine in water was found to decay mainly via a conical intersection with strong out-of-plane deformation of the amino group (<sup>6</sup>S<sub>1</sub>), consistent with the previously reported results for gas-phase 9*H*-adenine. The two DNA model systems decayed from S<sub>1</sub> to S<sub>0</sub> via different monomeric channels (<sup>6</sup>S<sub>1</sub> and <sup>2</sup>E, respectively), on account of the strong hydrogen-bonding interactions between the Watson-Crick pair in the double-stranded oligomer. The S<sub>1</sub>→S<sub>0</sub> decay time constant of 9*H*-adenine was slightly shorter in water than in vacuo ( $\sim 0.4$  ps vs.  $\sim 0.5$  ps). Surprisingly, the time constants for both DNA models ( $\sim 4$ -6 ps) were about ten times longer than those of 9*H*-adenine in vacuo or water, while matching one of the time components observed experimentally. Possible reasons were identified for these longer decay times, and the influence of MM environment on the QM adenine chromophore was analyzed in detail. Steady-state and time-dependent fluorescence spectra were computed to help understand the experimental observations. As a next step toward more complete models, QM/MM simulations are planned with larger QM regions containing two stacked (adenine...adenine) or paired (adenine...thymine) nucleobases to account for delocalization effects (excitons, excimers).

The current applications have covered systems of different size, ranging from the small CH<sub>2</sub>NH<sub>2</sub><sup>+</sup> cation (6 atoms) via the medium-sized DMN chromophore (26 atoms) and the large OVP5 fluorophore (164 atoms) to solvated DNA oligomers (containing over ten thousand atoms). The QM/MM investigation of adenine in solvated DNA models is among the most advanced attempts of performing nonadiabatic dynamics simulations for such large biological systems. It has led to a reliable routine for simulating the photoinduced processes of such macromolecules *in silico*.

## References

- [1] S. Grimme, *Rev. Comput. Chem.* **2004**, *20*, 153-218.
- [2] A. Dreuw, *ChemPhysChem* **2006**, *7*, 2259-2274.
- [3] M. Born, R. Oppenheimer, *Ann. Phys.* **1927**, *84*, 457-484.
- [4] A. Szabo, N. S. Ostlund, *Modern Quantum Chemistry*, Dover Publications, Inc., Mineola, **1996**.
- [5] J. B. Foresman, M. Head-Gordon, J. A. Pople, M. J. Frisch, *J. Phys. Chem.* **1992**, *96*, 135-149.
- [6] R. E. Stratmann, G. E. Scuseria, M. J. Frisch, *J. Chem. Phys.* **1998**, *109*, 8128-8224.
- [7] H. Koch, O. Christiansen, R. Kobayashi, P. Jørgensen, T. Helgaker, *Chem. Phys. Lett.* **1994**, *228*, 233-238.
- [8] K. Raghavachari, G. W. Trucks, J. A. Pople, M. Head-Gordon, *Chem. Phys. Lett.* **1989**, *157*, 479-483.
- [9] R. J. Bartlett, J. D. Watts, S. A. Kucharski, J. Noga, *Chem. Phys. Lett.* **1990**, *165*, 513-522.
- [10] G. E. Scuseria, T. J. Lee, *J. Chem. Phys.* **1990**, *93*, 5851-5855.
- [11] T. D. Crawford, J. F. Stanton, *Int. J. Quantum Chem.* **1998**, *70*, 601-611.
- [12] O. Christiansen, H. Koch, P. Jørgensen, *Chem. Phys. Lett.* **1995**, *243*, 409-418.
- [13] O. Christiansen, H. Koch, P. Jørgensen, T. Helgaker, *Chem. Phys. Lett.* **1996**, *263*, 530-539.
- [14] C. Hättig, F. Weigend, *J. Chem. Phys.* **2000**, *113*, 5154-5161.
- [15] C. Hättig, K. Hald, *Phys. Chem. Chem. Phys.* **2002**, *4*, 2111-2118.
- [16] C. Hättig, A. Köhn, *J. Chem. Phys.* **2002**, *117*, 6939-6951.

## References

---

- [17] J. F. Stanton, R. J. Bartlett, *J. Chem. Phys.* **1993**, *98*, 7029-7039.
- [18] H. Nakatsuji, *Chem. Phys. Lett.* **1979**, *67*, 329-333.
- [19] R. J. Buenker, S. D. Peyerimhoff, W. Butcher, *Mol. Phys.* **1978**, *35*, 771-791.
- [20] P. J. Knowles, H.-J. Werner, *Theor. Chim. Acta* **1992**, *84*, 95-103.
- [21] I. Shavitt, in *Methods of Electronic Structure Theory* (Ed.: H. F. Schaefer III), Plenum, New York, **1977**, p. 189.
- [22] B. O. Roos, *Adv. Chem. Phys.* **1987**, *69*, 399-446.
- [23] K. Andersson, P.-Å. Malmqvist, B. O. Roos, *J. Chem. Phys.* **1992**, *96*, 1218-1226.
- [24] K. Andersson, P.-Å. Malmqvist, B. O. Roos, A. J. Sadlej, K. Wolinski, *J. Phys. Chem.* **1990**, *94*, 5483-5488.
- [25] B. O. Roos, M. P. Fülscher, P.-Å. Malmqvist, M. Merchán, L. Serrano-Andrés, in *Quantum Mechanical Electronic Structure Calculations with Chemical Accuracy* (Ed.: S. R. Langhoff), Kluwer Academic Publishers, Dordrecht, **1995**, p. 357.
- [26] B. O. Roos, K. Andersson, M. P. Fülscher, P.-Å. Malmqvist, L. Serrano-Andrés, K. Pierloot, M. Merchán, in *New Methods in Computational Quantum Mechanics (Adv. Chem. Phys. Vol. XCIII)* (Eds.: I. Prigogine, S. A. Rice), John Wiley & Sons, New York, **1996**, p. 219.
- [27] K. Andersson, B. O. Roos, *Int. J. Quantum Chem.* **1993**, *45*, 591-607.
- [28] F. Furche, R. Ahlrichs, *J. Chem. Phys.* **2002**, *117*, 7433-7447.
- [29] M. R. Silva-Junior, M. Schreiber, S. P. A. Sauer, W. Thiel, *J. Chem. Phys.* **2008**, *129*, 104103.
- [30] A. Dreuw, M. Head-Gordon, *J. Am. Chem. Soc.* **2004**, *126*, 4007-4016.
- [31] T. Yanai, D. P. Tew, N. C. Handy, *Chem. Phys. Lett.* **2004**, *393*, 51-57.
- [32] P. R. Taylor, *Lecture Notes in Quantum Chemistry: European Summer School*, Springer-Verlag, Berlin, **1994**.
- [33] R. J. Bartlett, *Ann. Rev. Phys. Chem.* **1981**, *32*, 359-401.
- [34] D. Sundholm, *Chem. Phys. Lett.* **1999**, *302*, 480-484.
- [35] F. Furche, R. Ahlrichs, C. Wachsmann, E. Weber, A. Sobanski, F. Vogtle, S. Grimme, *J. Am. Chem. Soc.* **2000**, *122*, 1717-1724.
- [36] A. Dreuw, B. D. Dunietz, M. Head-Gordon, *J. Am. Chem. Soc.* **2002**, *124*,

- 
- 12070-12071.
- [37] J. M. Rintelman, I. Adamovic, S. Varganov, M. S. Gordon, *J. Chem. Phys.* **2005**, *122*, 044105.
- [38] F. Jensen, *Introduction to Computational Chemistry*, John Wiley & Sons, Chichester, **1999**.
- [39] J. Pople, D. Beveridge, *Approximate Molecular Orbital Theory*, McGraw-Hill, New York, **1970**.
- [40] M. C. Zerner, in *Reviews of Computational Chemistry* (Eds.: K. B. Lipkowitz, D. B. Boyd), VCH Publishers, New York, **1991**, pp. 313-365.
- [41] M. J. S. Dewar, W. Thiel, *J. Am. Chem. Soc.* **1977**, *99*, 4899-4907.
- [42] J. J. P. Stewart, *J. Comput. Chem.* **1989**, *10*, 209-220.
- [43] M. J. S. Dewar, E. G. Zoebisch, E. F. Healy, J. J. P. Stewart, *J. Am. Chem. Soc.* **1985**, *107*, 3902-3909.
- [44] W. Weber, Ph.D. thesis, Universität Zürich (Switzerland) **1996**.
- [45] W. Weber, W. Thiel, *Theor. Chem. Acc.* **2000**, *103*, 495-506.
- [46] M. Kolb, Ph.D. thesis, Universität Wuppertal (Germany) **1991**.
- [47] M. Kolb, W. Thiel, *J. Comput. Chem.* **1993**, *14*, 775-789.
- [48] R. S. Kohler, Ph.D. thesis, Universität Zürich (Switzerland) **2003**.
- [49] A. Koslowski, M. E. Beck, W. Thiel, *J. Comput. Chem.* **2003**, *24*, 714-726.
- [50] A. Koslowski, S. Patchkovskii, W. Thiel, *Theor. Chem. Acc.* **2005**, *114*, 84-89.
- [51] I. Shavitt, *Int. J. Quantum Chem.* **1977**, *11*, 131-148.
- [52] I. Shavitt, in *The Unitary Group for the Evaluation of Electronic Energy Matrix Elements (Lecture Notes in Chemistry Vol. 22)* (Ed.: J. Hinze), Springer, Warrington, **1981**, p. 51.
- [53] M. R. Silva-Junior, W. Thiel, *J. Chem. Theor. Comput.* **2010**, *6*, 1546-1564.
- [54] H.-M. Senn, W. Thiel, *Top. Curr. Chem.* **2007**, *268*, 173-290.
- [55] H.-M. Senn, W. Thiel, *Angew. Chem.* **2009**, *121*, 1220-1254; *Angew. Chem. Int. Ed.* **2009**, *48*, 1198-1229.
- [56] D. Bakowies, W. Thiel, *J. Phys. Chem.* **1996**, *100*, 10580-10594.
- [57] J. Michl, *Top. Curr. Chem.* **1974**, *46*, 1-59.

## References

---

- [58] M. Klessinger, J. Michl, *Excited States and Photochemistry of Organic Molecules*, VCH Publishers, New York, **1995**.
- [59] H. Köppel, W. Domcke, L. S. Cederbaum, *Adv. Chem. Phys.* **1984**, *57*, 59-246.
- [60] W. Domcke, D. R. Yarkony, H. Köppel (Eds.), *Book Conical Intersections: Electronic Structure, Dynamics and Spectroscopy (Adv. Ser. Phys. Chem. Vol. 15)*, World Scientific, Singapore, **2004**.
- [61] M. Baer, *Beyond Born-Oppenheimer: Electronic Nonadiabatic Coupling Terms and Conical Intersections*, John Wiley & Sons, Hoboken, **2006**.
- [62] W. Domcke, G. Stock, *Adv. Chem. Phys.* **1997**, *100*, 1-169.
- [63] A. G. Worth, L. S. Cederbaum, *Ann. Rev. Phys. Chem.* **2004**, *55*, 127-158.
- [64] M. K. Shukla, J. Leszczynski (Eds.), *Book Radiation Induced Molecular Phenomena in Nucleic Acids (Chall. Adv. Comput. Chem. Phys. Vol. 5)*, Springer, Amsterdam, **2008**.
- [65] E. Fabiano, Z. Lan, Y. Lu, W. Thiel, in *Conical Intersections: Theory Computation and Experiment (Adv. Ser. Phys. Chem. Vol. 17)* (Eds.: H. Köppel, W. Domcke, D. R. Yarkony), World Scientific, Singapore, **2011**, pp. 463-496.
- [66] D. R. Yarkony, *Rev. Mod. Phys.* **1996**, *68*, 985-1013.
- [67] D. R. Yarkony, *Acc. Chem. Res.* **1998**, *31*, 511-518.
- [68] M. J. Bearpark, M. A. Robb, H. B. Schlegel, *Chem. Phys. Lett.* **1994**, *223*, 269-274.
- [69] F. Bernardi, M. Olivucci, M. A. Robb, *Chem. Soc. Rev.* **1996**, *25*, 321-347.
- [70] C. Ciminelli, G. Granucci, M. Persico, *Chem. Eur. J.* **2004**, *10*, 2327-2341.
- [71] T. W. Keal, A. Koslowski, W. Thiel, *Theor. Chem. Acc.* **2007**, *118*, 837-844.
- [72] D. R. Yarkony, *J. Chem. Phys.* **2005**, *123*, 204101
- [73] M. J. Paterson, M. J. Bearpark, M. A. Robb, L. Blancafort, *J. Chem. Phys.* **2004**, *121*, 11562-11571
- [74] M. A. Robb, L. Blancafort, A. D. DeBellis, *J. Phys. Chem. A* **2005**, *109*, 7527-7537.
- [75] I. Gómez, M. Reguero, M. Boggio-Pasqua, M. A. Robb, *J. Am. Chem. Soc.* **2005**, *127*, 7119-7129.
- [76] H.-D. Meyer, U. Manthe, L. S. Cederbaum, *Chem. Phys. Lett.* **1990**, *165*, 73-78.
- [77] U. Manthe, H.-D. Meyer, L. S. Cederbaum, *J. Chem. Phys.* **1992**, *97*, 3199-3213.



- 
- [78] M. H. Beck, A. Jäckle, G. A. Worth, H.-D. Meyer, *Phys. Rep.* **2000**, *324*, 1-105.
- [79] M. Ben-Nun, J. Quenneville, T. J. Martínez, *J. Phys. Chem. A* **2000**, *104*, 5161-5175.
- [80] M. Ben-Nun, T. J. Martínez, *J. Chem. Phys.* **1998**, *108*, 7244-7257.
- [81] G. Stock, M. Thoss, in *Conical Intersections: Electronic Structure, Dynamics and Spectroscopy (Adv. Ser. Phys. Chem. Vol. 15)* (Eds.: W. Domcke, D. R. Yarkony, H. Köppel), World Scientific, Singapore, **2004**, pp. 619-698.
- [82] A. Bjerre, E. E. Nikitin, *Chem. Phys. Lett.* **1967**, *1*, 179-181.
- [83] J. C. Tully, R. K. Preston, *J. Chem. Phys.* **1971**, *55*, 562-572.
- [84] R. K. Preston, J. C. Tully, *J. Chem. Phys.* **1971**, *54*, 4297-4304.
- [85] N. C. Blais, D. G. Truhlar, *J. Chem. Phys.* **1983**, *79*, 1334-1342.
- [86] F. Webster, P. J. Rossky, R. A. Friesner, *Comput. Phys. Commun.* **1991**, *63*, 494-522.
- [87] S. Chapman, *Adv. Chem. Phys.* **1992**, *82*, 423-483.
- [88] S. Hammes-Schiffer, J. C. Tully, *J. Chem. Phys.* **1994**, *101*, 4657-4667.
- [89] J. C. Tully, *J. Chem. Phys.* **1990**, *93*, 1061-1071.
- [90] G. Granucci, M. Persico, A. Toniolo, *J. Chem. Phys.* **2001**, *114*, 10608-10615.
- [91] E. Fabiano, T. W. Keal, W. Thiel, *Chem. Phys.* **2008**, *349*, 334-347.
- [92] G. Groenhof, L. V. Schäfer, M. Boggio-Pasqua, M. Goette, H. Grubmüller, M. A. Robb, *J. Am. Chem. Soc.* **2007**, *129*, 6812-6819.
- [93] Z. Lan, Y. Lu, E. Fabiano, W. Thiel, *ChemPhysChem* **2011**, *12*, 1989-1998.
- [94] Y. Lu, Z. Lan, W. Thiel, *Angew. Chem.* **2011**, *123*, 6996-6999; Y. Lu, Z. Lan, W. Thiel, *Angew. Chem. Int. Ed.* **2011**, *50*, 6864-6867.
- [95] Y. Lu, Z. Lan, W. Thiel, *J. Comput. Chem.* **2011**, submitted.
- [96] Y. Lu, W. Thiel, in preparation.
- [97] S. Marawske, D. Dörr, D. Schmitz, A. Koslowski, Y. Lu, H. Ritter, W. Thiel, C. A. M. Seidel, R. Kühnemuth, *ChemPhysChem* **2009**, *10*, 2041-2048.
- [98] Y. Lu, W. Thiel, in preparation.
- [99] G. Cui, Y. Lu, W. Thiel, *Chem. Phys. Lett.* **2011**, submitted.
- [100] M. Mitchell, *An Introduction To Genetic Algorithms*, MIT Press, Cambridge, MA, **1996**.
- [101] J. Y. Mane, M. Klobukowski, *Chem. Phys. Lett.* **2010**, *500*, 140-143.

## References

---

- [102] K. Sastry, D. D. Johnson, A. Thompson, D. E. Goldberg, T. J. Martinez, J. Leiding, J. Owens, *Mat. Manu. Proc.* **2007**, *22*, 553-561.
- [103] E. N. Brothers, K. M. Merz, Jr., *J. Phys. Chem. B* **2002**, *106*, 2779-2785.
- [104] T. R. Cundari, J. Deng, W. Fu, *Int. J. Quantum Chem.* **2000**, *77*, 421-432.
- [105] I. Rossi, D. G. Truhlar, *Chem. Phys. Lett.* **1995**, *233*, 231-236.
- [106] M. C. Hutter, J. R. Reimers, N. S. Hush, *J. Phys. Chem. B* **1998**, *102*, 8080-8090.
- [107] W. Thiel, PP99, Max-Planck-Institut für Kohlenforschung, Mülheim an der Ruhr.
- [108] D. Levine, P. Hallstrom, D. Noelle, G. Reeder, B. Walenz, PGAPack version 1.1, Mathematics and Computer Science Division at Argonne National Laboratory, Argonne, IL. <ftp://ftp.mcs.anl.gov>.
- [109] U. F. Röhrig, U. Troppmann, I. Frank, *Chem. Phys. Lett.* **2003**, *289*, 381-388.
- [110] S. Tretiak, A. Saxena, R. L. Martin, A. R. Bishop, *Phys. Rev. Lett.* **2002**, *89*, 097402.
- [111] J. A. Odell, A. Keller, *J. Polym. Sci. Pt. B-Polym. Phys.* **1986**, *24*, 1889-1916.
- [112] S. Perun, A. L. Sobolewski, W. Domcke, *J. Am. Chem. Soc.* **2005**, *127*, 6257-6265.
- [113] C. Angeli, S. Borini, L. Ferrighi, R. Cimiraglia, *J. Mol. Struct. (Theochem)* **2005**, *718*, 55-69.
- [114] Y.-W. Wang, H.-Y. He, W.-H. Fang, *J. Mol. Struct. (Theochem)* **2003**, *634*, 281-287.
- [115] K. Malsch, R. Rebentisch, P. Swiderek, G. Hohlneicher, *Theor. Chim. Acta* **1998**, *100*, 171-182.
- [116] W.-H. Fang, *J. Am. Chem. Soc.* **1999**, *121*, 8376-8384.
- [117] E. L. Rachofsky, J. B. A. Ross, M. Krauss, R. Osman, *J. Phys. Chem. A* **2001**, *105*, 190-197.
- [118] T. Pino, S. Douin, N. Boudin, P. Bréchnignac, *Chem. Phys. Lett.* **2006**, *419*, 356-361.
- [119] X.-J. Hou, P. Quan, T. Höltzl, T. Veszprémi, M. T. Nguyen, *J. Phys. Chem. A* **2005**, *109*, 10396-10402.
- [120] J. Weber, K. Malsch, G. Hohlneicher, *Chem. Phys.* **2001**, *264*, 275-318.
- [121] M. E. Beck, R. Rebentisch, G. Hohlneicher, M. P. Fülcher, L. Serrano-Andrés, B. O. Roos, *J. Chem. Phys.* **1997**, *107*, 9464-9474.
- [122] N. Nakayama, H. Nakano, K. Hirao, *Int. J. Quantum Chem.* **1998**, *66*, 157-175.

- 
- [123] N. Ismail, L. Blancafort, M. Olivucci, B. Kohler, M. A. Robb, *J. Am. Chem. Soc.* **2002**, *124*, 6818-6819.
- [124] J. F. Arenas, I. López-Tocón, J. C. Otero, J. Soto, *J. Am. Chem. Soc.* **2002**, *124*, 1728-1735.
- [125] I. Ljubić, A. Sabljčić, *J. Phys. Chem. A* **2005**, *109*, 8209-8217.
- [126] T. Nakajima, S. Kato, *J. Phys. Chem. A* **2001**, *105*, 10657-10663.
- [127] H. Chen, S. Li, *J. Phys. Chem. A* **2006**, *110*, 12360-12362.
- [128] A. V. Szeghalmi, V. Engel, M. Z. Zgierski, J. Popp, M. Schimitt, *J. Raman Spectrosc.* **2006**, *37*, 148-160
- [129] L. Serrano-Andrés, B. O. Roos, *J. Am. Chem. Soc.* **1996**, *118*, 185-195.
- [130] T. Climent, R. González-Luque, M. Merchán, *J. Phys. Chem. A* **2003**, *107*, 6995-7003.
- [131] E. K. Dolgov, V. A. Bataev, V. I. Pupyshev, I. A. Godunov, *Int. J. Quantum Chem.* **2004**, *96*, 589-597.
- [132] C. S. Page, M. Olivucci, *J. Comput. Chem.* **2002**, *24*, 298-309.
- [133] Z.-L. Cai, J. R. Reimers, *J. Phys. Chem. A* **2000**, *104*, 8389-8408.
- [134] V. Molina, M. Merchán, B. O. Roos, *Spectrochimica Acta A* **1999**, *55*, 433-446.
- [135] V. Molina, B. R. Smith, M. Merchán, *Chem. Phys. Lett.* **1999**, *309*, 486-494.
- [136] M. Schütz, J. Hutter, H. P. Lüthi, *J. Chem. Phys.* **1995**, *103*, 7048-7057.
- [137] S. Perun, A. Sobolewski, W. Domcke, *J. Phys. Chem A* **2006**, *110*, 13238-13244.
- [138] M. Merchán, R. González-Luque, T. Climent, L. Serrano-Andrés, E. Rodríguez, M. Reguero, D. Peláez, *J. Phys. Chem. B* **2006**, *110*, 26471-26476.
- [139] R. Ahlrichs, Bär. M., H.-P. Baron, R. Bauernschmitt, S. Böcker, M. Ehrig, K. Eichkorn, S. Elliott, F. Haase, M. Häser, H. Horn, C. Huber, U. Huniar, M. Kattannek, C. Kölmel, M. Kollwitz, C. Ochsenfeld, H. Öhm, A. Schäfer, U. Schneider, O. Treutler, M. von Arnim, F. Weigend, P. Weis, H. Weiss, version 5.71, Quant Chem Group TURBOMOLE; University of Karlsruhe, Karlsruhe, Germany, since 1988.
- [140] M. Wanko, M. Hoffmann, P. Strodet, A. Koslowski, W. Thiel, F. Neese, T. Frauenheim, M. Elstner, *J. Phy. Chem. B* **2005**, *109*, 3606-3615.

## References

---

- [141] V. A. Bataev, V. I. Pupyshev, I. A. Godunov, *J. Mol. Struct. (Theochem)* **1999**, 480-481, 263-267.
- [142] T. Nakajima, S. Kato, *J. Chem. Phys.* **1996**, 105, 5927-5938.
- [143] M. Dallos, T. Muller, H. Lischka, R. Shepard, *J. Chem. Phys.* **2001**, 114, 746-757.
- [144] E. Fabiano, W. Thiel, *J. Phys. Chem. A* **2008**, 112, 6859-6863.
- [145] Z. Lan, Y. Lu, O. Weingart, W. Thiel, *J. Phys. Chem. A* **2011**, submitted.
- [146] W.-H. Fang, *Acc. Chem. Res.* **2008**, 41, 452-457.
- [147] S. De Feyter, E. W.-G. Diau, A. H. Zewail, *Angew. Chem. Int. Ed.* **2000**, 39, 260-263.
- [148] L. J. Butler, *Annu. Rev. Phys. Chem.* **1998**, 49, 125-171.
- [149] W.-H. Fang, D. L. Phillips, *ChemPhysChem* **2002**, 3, 889-892.
- [150] J. Li, F. Zhang, W.-H. Fang, *J. Phys. Chem. A* **2005**, 109, 7718-7724.
- [151] Q. Fang, Y. J. Liu, *J. Phys. Chem. A* **2010**, 114, 680-684.
- [152] M. Berger, I. L. Goldblatt, C. Steel, *J. Am. Chem. Soc.* **1973**, 95, 1717-1725.
- [153] S.-H. Lee, K.-C. Tang, I.-C. Chen, M. Schmitt, J. P. Shaffer, T. Schultz, J. G. Underwood, M. Z. Zgierski, A. Stolow, *J. Phys. Chem. A* **2002**, 106, 8979-8991.
- [154] B. Xiang, C. Z. Zhu, L. Zhu, *Chem. Phys. Lett.* **2009**, 474, 74-78.
- [155] L. Zhu, T. J. Cronin, *Chem. Phys. Lett.* **2000**, 317, 227-231.
- [156] H. Q. Zhao, Y. S. Cheung, C. L. Liao, C. X. Liao, C. Y. Ng, W. K. Li, *J. Chem. Phys.* **1997**, 107, 7230-7241.
- [157] H. Y. Xiao, Y. J. Liu, W.-H. Fang, *J. Mol. Struct. (Theochem)* **2007**, 802, 99-103.
- [158] P. Celani, H. Stoll, H.-J. Werner, *Mol. Phys.* **2004**, 102, 2369-2379.
- [159] H.-J. Werner, *Mol. Phys.* **1996**, 89, 645-661.
- [160] P. Celani, H.-J. Werner, *J. Chem. Phys.* **2000**, 112, 5546-5557.
- [161] T. H. Dunning, Jr., *J. Chem. Phys.* **1989**, 90, 1007-1023.
- [162] H. J. Werner, P. J. Knowles, R. Lindh, F. R. Manby, M. Schütz, P. Celani, T. Korona, G. Rauhut, R. D. Amos, A. Bernhardsson, A. Berning, D. L. Cooper, M. J. O. Deegan, A. J. Dobbyn, F. Eckert, C. Hampel, G. Hetzer, A. W. Lloyd, S. J. McNicholas, W. Meyer, M. E. Mura, A. Nicklass, P. Palmieri, R. Pitzer, U. Schumann, H. Stoll, A. J. Stone, R. Tarroni, T. Thorsteinsson, MOLPRO

- 
- version 2006.6, a package of ab initio programs 2006. See <http://www.molpro.net>.
- [163] H. A. Bethe, M. A. El-Sayed, *Quantum Mechanics of One- and Two-Electron Systems*, Springer-Verlag, Berlin, **1957**.
- [164] M. Barbatti, G. Granucci, M. Persico, M. Ruckebauer, M. Vazdar, E. Eckert-Maksić, *J. Photochem. Photobiol. A* **2007**, *190*, 228-240.
- [165] I. Tavernelli, E. Tapavicza, U. Rothlisberger, *J. Mol. Struct. (Theochem)* **2009**, *914*, 22-29.
- [166] M. Barbatti, A. J. A. Aquino, H. Lischka, *Mol. Phys.*, *104*, 1053-1060.
- [167] P. Sherwood, M. S. de Vries, M. F. Guest, G. Schreckenbach, C. R. A. Catlow, S. A. French, A. A. Sokol, S. T. Bromley, W. Thiel, A. J. Turner, S. Billeter, F. Terstegen, S. Thiel, J. Kendrick, S. C. Rogers, J. Casci, M. Watson, F. King, E. Karlsen, M. Sjøvoll, A. Fahmi, A. Schäfer, C. Lennartz, *J. Mol. Struct. (Theochem)* **2003**, *632*, 1-28.
- [168] W. L. Jorgensen, J. Chandrasekhar, J. D. Madura, R. W. Impey, M. L. Klein, *J. Chem. Phys.* **1982**, *79*, 926-935.
- [169] C. Swalina, M. Maroncelli, *J. Phys. Chem. C* **2010**, *114*, 5602-5610.
- [170] B. D. Allen, A. C. Benniston, A. Harriman, S. A. Rostron, C. Yu, *Phys. Chem. Chem. Phys.* **2005**, *7*, 3035-3040.
- [171] A.-Y. Jee, E. Bae, M. Lee, *J. Phys. Chem. B* **2009**, *113*, 16508-16512.
- [172] H.; Jin, M.; Liang, S.; Arzhantsev, X.; Li, M. Maroncelli, *J. Phys. Chem. B* **2010**, *114*, 7565-7578.
- [173] B. Mennucci, C. Cappelli, C. A. Guido, R. Cammi, J. Tomasi, *J. Phys. Chem. A* **2009**, *113*, 3009-3020.
- [174] B. Mennucci, C. Cappelli, R. Cammi, J. Tomasi, *Theor. Chem. Acc.* **2007**, *117*, 1029-1039.
- [175] J. C. Hooker, J. M. Torkelson, *Macromolecules* **1995**, *28*, 7683-7692.
- [176] Z. A. Dreger, J. O. White, H. G. Drickamer, *Chem. Phys. Lett.* **1998**, *290*, 399-404.
- [177] K. I. Gutkowski, M. L. Japas, P. F. Aramendia, *Chem. Phys. Lett.* **2006**, *426*, 329-333.
- [178] M. A. Haidekker, E. A. Theodorakis, *Org. Biomol. Chem.* **2007**, *5*, 1669-1678.
- [179] A. Paul, A. Samanta, *J. Phys. Chem. B* **2008**, *112*, 16626-16632.

## References

---

- [180] S. Mqadmi, A. Pollet, *J. Photochem. Photobiol. A* **1990**, *53*, 275-281.
- [181] A. Safarzadeh-Amiri, *Chem. Phys. Lett.* **1986**, *129*, 225-230.
- [182] M. Ben-Nun, T. J. Martínez, *J. Chem. Phys.* **2000**, *259*, 237-248.
- [183] B. G. Levine, T. J. Martínez, *Annu. Rev. Phys. Chem.* **2007**, *58*, 613-634.
- [184] M. Barbatti, H. Lischka, *J. Am. Chem. Soc.* **2008**, *130*, 6831-6839.
- [185] J. A. Parrish, K. F. Jaenicke, R. R. Anderson, *Photochem. Photobiol.* **1982**, *36*, 187-191.
- [186] A. Cantrell, D. J. McGarvey, in *Sun Protection in Man (Comprehensive Series in Photosciences Vol. 3)* (Ed.: P. U. Giacomoni), Elsevier, Amsterdam, **2001**.
- [187] M. Daniels, W. Hauswirth, *Science* **1971**, *171*, 675-677.
- [188] J.-M. L. Pecourt, J. Peon, B. Kohler, *J. Am. Chem. Soc.* **2000**, *122*, 9348-9349.
- [189] J.-M. L. Pecourt, J. Peon, B. Kohler, *J. Am. Chem. Soc.* **2001**, *123*, 10370-10378.
- [190] P. R. Callis, *Annu. Rev. Phys. Chem.* **1983**, *34*, 329-357.
- [191] C. E. Crespo-Hernández, B. Cohen, P. M. Hare, B. Kohler, *Chem. Rev.* **2004**, *104*, 1977-2019.
- [192] H. Saigusa, *J. Photochem. Photobiol. C* **2006**, *7*, 197-210.
- [193] N. J. Kim, G. Jeong, Y. S. Kim, J. Sung, S. K. Kim, Y. D. Park, *J. Chem. Phys.* **2000**, *113*, 10051-10055.
- [194] H. Kang, K. T. Lee, B. Jung, Y. J. Ko, S. K. Kim, *J. Am. Chem. Soc.* **2002**, *124*, 12958-12959.
- [195] H. Kang, B. Jung, S. K. Kim, *J. Chem. Phys.* **2003**, *118*, 6717-6719.
- [196] I. Hünig, C. Plützer, K. A. Seefeld, D. Löwenich, M. Nispel, K. Kleinermanns, *ChemPhysChem* **2004**, *5*, 1427-1431.
- [197] S. Ullrich, T. Schultz, M. Z. Zgierski, A. Stolow, *J. Am. Chem. Soc.* **2004**, *126*, 2262-2263.
- [198] S. Ullrich, T. Schultz, M. Z. Zgierski, A. Stolow, *Phys. Chem. Chem. Phys.* **2004**, *6*, 2796-2801.
- [199] M. Zierhut, W. Roth, I. Fischer, *Phys. Chem. Chem. Phys.* **2004**, *6*, 5178-5183.
- [200] C. Canuel, M. Mons, F. Piuze, B. Tardivel, I. Dimicoli, M. Elhanine, *J. Chem. Phys.* **2005**, *122*, 074316.

- 
- [201] H.-H. Ritze, H. Lippert, E. Samoylova, V. R. Smith, I. V. Hertel, W. Radloff, T. Schultz, *J. Chem. Phys.* **2005**, *122*, 224320.
- [202] H. Satzger, D. Townsend, M. Z. Zgierski, S. Patchkovskii, S. Ullrich, A. Stolow, *Proc. Natl. Acad. Sci. USA* **2006**, *103*, 10196-10201.
- [203] M. G. D. Nix, A. L. Devine, B. Cronin, M. N. R. Ashfold, *J. Chem. Phys.* **2007**, *126*, 124312.
- [204] C. Z. Bisgaard, H. Satzger, S. Ullrich, A. Stolow, *ChemPhysChem* **2009**, *10*, 101-110.
- [205] L. B. Clark, I. Tinoco, *J. Am. Chem. Soc.* **1965**, *87*, 11-15.
- [206] W. Voelter, R. Records, E. Bunnenberg, C. Djerassi, *J. Am. Chem. Soc.* **1968**, *90*, 6163-6170.
- [207] A. F. Fucaloro, L. S. Forster, *J. Am. Chem. Soc.* **1971**, *93*, 6443-6448.
- [208] E. Samoylova, H. Lippert, S. Ullrich, I. V. Hertel, W. Radloff, T. Shultz, *J. Am. Chem. Soc.* **2005**, *127*, 1782-1786.
- [209] C. M. Marian, *J. Chem. Phys.* **2005**, *122*, 104314.
- [210] H. Chen, S. Li, *J. Phys. Chem. A* **2005**, *109*, 8443-8446.
- [211] S. B. Nielsen, T. I. Sølling, *ChemPhysChem* **2005**, *6*, 1276-1281.
- [212] L. Serrano-Andrés, M. Merchán, A. C. Borin, *Chem. Eur. J.* **2006**, *12*, 6559-6571.
- [213] L. Serrano-Andrés, M. Merchán, A. C. Borin, *Proc. Natl. Acad. Sci. U.S.A.* **2006**, *103*, 8691-8696.
- [214] L. Blancafort, *J. Am. Chem. Soc.* **2006**, *128*, 210-291.
- [215] W. H. I. Hassan, W. C. Chung, N. Shimakura, S. Koseki, H. Kono, Y. Fujimura, *Phys. Chem. Chem. Phys.* **2010**, *12*, 5317-5328.
- [216] I. Conti, M. Garavelli, G. Orlandi, *J. Am. Chem. Soc.* **2009**, *131*, 16108-16118.
- [217] T. Gustavsson, A. Sharonov, D. Onidas, D. Markovitsi, *Chem. Phys. Lett.* **2002**, *356*, 49-54.
- [218] B. Cohen, P. M. Hare, B. Kohler, *J. Am. Chem. Soc.* **2003**, *125*, 13594-13601.
- [219] T. Pancur, N. K. Schwalb, F. Renth, F. Temps, *Chem. Phys. Lett.* **2005**, *313*, 199-212.
- [220] T. Gustavsson, N. Sarkar, E. Lazzarotto, D. Markovitsi, R. Improta, *Chem. Phys. Lett.* **2006**, *429*, 551-557.
- [221] C. T. Middleton, B. Cohen, B. Kohler, *J. Phys. Chem. A* **2007**, *111*, 10460-10467.

## References

---

- [222] C. T. Middleton, K. de La Harpe, C. Su, Y. K. Law, C. E. Crespo-Hernández, B. Kohler, *Annu. Rev. Phys. Chem.* **2009**, *60*, 217-239.
- [223] C. E. Crespo-Hernández, B. Cohen, B. Kohler, *Nature* **2005**, *436*, 1141-1144.
- [224] T. Takaya, C. Su, K. de La Harpe, C. E. Crespo-Hernández, B. Kohler, *Proc. Natl. Acad. Sci. U.S.A.* **2008**, *105*, 10285-10290.
- [225] B. Kohler, *J. Phys. Chem. Lett.* **2010**, *1*, 2047-2053.
- [226] I. Buchvarov, Q. Wang, M. Raytchev, A. Trifonov, T. Fiebig, *Proc. Natl. Acad. Sci. U.S.A.* **2007**, *104*, 4794-4797.
- [227] T. Fiebig, *J. Phys. Chem. B* **2009**, *113*, 9348-9349.
- [228] B. Bouvier, J. P. Dognon, R. Lavery, D. Markovitsi, P. Millié, D. Onidas, K. Zakrzewska, *J. Phys. Chem. B* **2003**, *107*, 13512-13522.
- [229] D. Markovitsi, T. Gustavsson, F. Talbot, *Photochem. Photobiol. Sci.* **2007**, *6*, 717-724.
- [230] D. Onidas, T. Gustavsson, E. Lazzarotto, D. Markovitsi, *J. Phys. Chem. B* **2007**, *111*, 9644-9650.
- [231] D. Markovitsi, T. Gustavsson, A. Banyasz, *Mutat. Res. Rev.* **2010**, *704*, 21-28.
- [232] J. Frenkel, *Phys. Rev.* **1931**, *37*, 1276-1294.
- [233] E. I. Rashbah, M. D. Sturge, *Excitons*, North-Holland, Amsterdam, **1982**.
- [234] A. S. Davydov, *Theory of Molecular Excitons*, Plenum Press, New York, **1971**.
- [235] N. Schwalb, F. Temps, *Science* **2008**, *322*, 243-245.
- [236] W.-M. Kwok, C. Ma, D. L. Phillips, *J. Am. Chem. Soc.* **2006**, *128*, 11894-11905.
- [237] D. Markovitsi, A. Sharonov, D. Onidas, T. Gustavsson, *ChemPhysChem* **2003**, *4*, 303-305.
- [238] W. C. Chung, Z. Lan, Y. Ohtsuki, N. Shimakura, W. Domcke, Y. Fujimura, *Phys. Chem. Chem. Phys.* **2007**, *9*, 2075-2084.
- [239] L. Jensen, N. Govind, *J. Phys. Chem. A* **2009**, *113*, 9761-9765.
- [240] P. Jurečka, J. Šponer, J. Černý, P. Hobza, *Phys. Chem. Chem. Phys.* **2006**, *8*, 1985-1993.
- [241] K. B. Bravaya, O. Kostko, M. Ahmed, A. Krylov, *Phys. Chem. Chem. Phys.* **2010**, *12*, 2292-2307.



- 
- [242] A. Abo-Riziq, L. Grace, E. Nir, M. Kabelac, P. Hobza, M. S. de Vries, *Proc. Natl. Acad. Sci. U.S.A.* **2005**, *102*, 20-23.
- [243] D. Nachtigallová, P. Hobza, H.-H. Ritze, *Phys. Chem. Chem. Phys.* **2008**, *10*, 5689-5697.
- [244] H. Tachikawa, H. Kawabata, *Chem. Phys. Lett.* **2008**, *462*, 321-326.
- [245] J. J. Serrano-Pérez, I. González-Ramírez, P. B. Coto, M. Merchán, L. Serrano-Andrés, *J. Phys. Chem. B* **2008**, *112*, 14096-14098.
- [246] E. Emanuele, D. Markovitsi, P. Millié, K. Zakrzewska, *ChemPhysChem* **2005**, *6*, 1387-1393.
- [247] E. R. Bittner, *J. Chem. Phys.* **2006**, *125*, 094909.
- [248] S. Tonzani, G. C. Schatz, *J. Am. Chem. Soc.* **2008**, *130*, 7607-7612.
- [249] G. Olaso-González, M. Merchán, L. Serrano-Andrés, *J. Am. Chem. Soc.* **2009**, *131*, 4368-4377.
- [250] D. Nachtigallová, T. Zelený, M. Ruckebauer, T. Müller, M. Barbatti, P. Hobza, H. Lischka, *J. Am. Chem. Soc.* **2010**, *132*, 8261-8263.
- [251] B. Mennucci, A. Toniolo, J. Tomasi, *J. Phys. Chem. A* **2001**, *105*, 4749-4757.
- [252] S. Yamazaki, S. Kato, *J. Am. Chem. Soc.* **2007**, *129*, 2901-2909.
- [253] V. Ludwig, Z. M. da Costa, M. S. do Amaral, A. C. Borin, S. Canuto, L. Serrano-Andrés, *Chem. Phys. Lett.* **2010**, *492*, 164-169.
- [254] S. Miertus, E. Scrocco, J. Tomasi, *Chem. Phys. Lett.* **1981**, *55*, 117-129.
- [255] J. Tomasi, B. Mennucci, R. Cammi, *Chem. Rev.* **2005**, *105*, 2999-3094.
- [256] M. Cossi, N. Rega, G. Scalmani, V. Barone, *J. Chem. Phys.* **2001**, *114*, 5691-5701.
- [257] F. Santoro, V. Barone, R. Improta, *Proc. Natl. Acad. Sci. U.S.A.* **2007**, *104*, 9931-9936.
- [258] R. Improta, *Phys. Chem. Chem. Phys.* **2008**, *10*, 2656-2664.
- [259] R. Improta, F. Santoro, V. Barone, A. Lami, *J. Phys. Chem. A* **2009**, 15346-15354.
- [260] F. Santoro, V. Barone, A. Lami, R. Improta, *Phys. Chem. Chem. Phys.* **2010**, *12*, 4934-4948.
- [261] R. Improta, V. Barone, *Angew. Chem. Int. Ed.* **2011**, DOI: 10.1002/anie.201104382.
- [262] F. Santoro, V. Barone, R. Improta, *ChemPhysChem* **2008**, *9*, 2531-2537.

## References

---

- [263] J. E. Ridley, M. C. Zerner, *Theor. Chim. Acta* **1973**, *32*, 111-134.
- [264] M. C. Zerner, G. H. Lowe, R. F. Kirchner, U. T. Mueller-Westerhoff, *J. Am. Chem. Soc.* **1980**, *102*, 589-599.
- [265] M. C. Zerner, P. C. de Mello, M. Hehenberger, *Int. J. Quantum Chem.* **1982**, *21*, 251-257.
- [266] E. B. Starikov, G. Cuniberti, S. Tanaka, *J. Phys. Chem. B* **2009**, *113*, 10428-10435.
- [267] A. A. Voityuk, *Phys. Chem. Chem. Phys.* **2008**, *12*, 7403-7408.
- [268] A. N. Alexandrova, J. C. Tully, G. Granucci, *J. Phys. Chem. B* **2010**, *114*, 12116-12128.
- [269] A. W. Lange, J. M. Herbert, *J. Am. Chem. Soc.* **2009**, *131*, 3913-3922.
- [270] I. Conti, P. Altoè, M. Stenta, M. Garavelli, G. Orlandi, *Phys. Chem. Chem. Phys.* **2010**, *12*, 5016-5023.
- [271] D. Markovitsi, T. Gustavsson, I. Vayá, *J. Phys. Chem. Lett.* **2010**, *1*, 3271-3276.
- [272] L. B. Clark, G. G. Peschel, Jr. Tinoco, I., *J. Phys. Chem.* **1965**, *69*, 3615-3618.
- [273] L. Li, D. M. Lubman, *Anal. Chem.* **1987**, *59*, 2538-2541.
- [274] H. Du, R.-C. A. Fuh, J. Li, L. A. Corkan, J. S. Lindsey, *Photochem. Photobiol. Sci.* **1998**, *68*, 141-142.
- [275] L. Hu, Y. Zhao, F. Wang, G. Chen, C. Ma, W.-M. Kwok, D. L. Phillips, *J. Phys. Chem. B* **2007**, *111*, 11812-11816.
- [276] G. Ge, S. Georghiou, *Photochem. Photobiol. Sci.* **1991**, *54*, 477-480.
- [277] I. Vayá, T. Gustavsson, F.-A. Miannay, T. Douki, D. Markovitsi, *J. Am. Chem. Soc.* **2010**, *132*, 11834-11835.
- [278] J. C. A. Boeyens, *J. Chem. Crystallogr.* **1978**, *8*, 317-320.
- [279] D. Cremer, J. A. Pople, *J. Am. Chem. Soc.* **1975**, *97*, 1354-1358.
- [280] A. Bondi, *J. Phys. Chem.* **1964**, *68*, 441-451.





paper (1)

***Fluorophores as Optical Sensors for Local Forces***

S. Marawske, D. Dörr, D. Schmitz, A. Koslowski, Y. Lu, H. Ritter, W.  
Thiel, C. A. M. Seidel, and R. Kühnemuth

*ChemPhysChem* **2009**, *10*, 2041-2048.



# Fluorophores as Optical Sensors for Local Forces\*\*

Stefan Marawske,<sup>[a]</sup> Denis Dörr,<sup>[a]</sup> Daniel Schmitz,<sup>[b]</sup> Axel Koslowski,<sup>[c]</sup> You Lu,<sup>[c]</sup>  
Helmut Ritter,<sup>\*[b]</sup> Walter Thiel,<sup>\*[c]</sup> Claus A. M. Seidel,<sup>\*[a]</sup> and Ralf Kühnemuth<sup>\*[a]</sup>

The main aim of this study is to investigate correlations between the impact of an external mechanical force on the molecular framework of fluorophores and the resultant changes in their fluorescence properties. Taking into account previous theoretical studies, we designed a suitable custom-tailored oligoparaphenylenevinylene derivative (OPV5) with a twisted molecular backbone. Thin foils made of PVC doped with 100 nm OPV were prepared. By applying uniaxial force, the foils were stretched and three major optical effects were observed simultaneously. First, the fluorescence anisotropy increased, which indicates a reorientation of the fluorophores within the matrix. Second, the fluorescence lifetime decreased by approximately 2.5% (25 ps). Finally, we observed an increase in the emission energy of about 0.2% (corresponding to a blue-shift of 1.2 nm). In addition, analogous measurements with Rhodamine 123 as an inert reference dye showed only minor effects,

which can be attributed to matrix effects due to refractive index changes. To relate the observed spectroscopic changes to the underlying changes in molecular properties, quantum-chemical calculations were also performed. Semiempirical methods had to be used because of the size of the OPV5 chromophore. Two conformers of OPV5 ( $C_2$  and  $C_i$  symmetry) were considered and both gave very similar results. Both the observed blue-shift of fluorescence and the reduced lifetime of OPV5 under tensile stress are consistent with the results of the semiempirical calculations. Our study proves the feasibility of fluorescence-based local force probes for polymers under tension. Improved optical sensors of this type should in principle be able to monitor local mechanical stress in transparent samples down to the single-molecule level, which harbors promising applications in polymer science and nanotechnology.

## 1. Introduction

Synthetic polymers are increasingly used in mechanically demanding applications. These products show residual stresses which can lead to deformation, fracture or even complete breakage of the material if exposed to, for example, strong variations of temperature or effective mechanical forces. Therefore, a detailed understanding of these residual stresses is essential for quality assessment and further development and improvement of polymers. To test the material properties, local probing can be achieved by doping with fluorophores that are sensitive to the environment and forces. Several studies are already available that describe optical properties of low-molecular-weight fluorophores physically mixed with polymeric matrices. Observed effects like spectral shifts have been related to mechanical manipulation in the case of simple distance sensors based on force-induced excimer formation and dissociation<sup>[1]</sup> or charge-transfer probes.<sup>[2]</sup> Fluorescence lifetime changes have been proposed to monitor local stress in polymer films.<sup>[3]</sup> Dissolved dyes have been used to probe orientation and alignment of polymer matrices.<sup>[4]</sup> Specific mechanical manipulation of optically induced *cis*–*trans* transitions in polyazobenzenes with DMSO as solvent has been demonstrated on the single-molecule level.<sup>[5]</sup>

According to simulations it is expected that conjugation in distorted or twisted fluorophores, with sterically hindered ground states, can be improved by applying an external unidirectional force.<sup>[6]</sup> One class of these fluorophores consists of oligoparaphenylenevinylene derivatives (OPVs).<sup>[6,7]</sup> OPVs have been investigated extensively as they are model systems for

the corresponding polymers (polyparaphenylenevinylene, PPV),<sup>[8]</sup> which are of great technological interest for applications in optoelectronic devices such as organic light-emitting diodes. Optical properties of PPVs<sup>[9,10]</sup> and OPVs<sup>[11]</sup> are partially governed by the conjugation length of the individual chromophoric unit that is a result of its local chemical environment and deformation. The effect of relative molecular alignment in aggregates and oriented thin films on intermolecular coupling

[a] S. Marawske, D. Dörr, Prof. Dr. C. A. M. Seidel, Dr. R. Kühnemuth  
Lehrstuhl für Molekulare Physikalische Chemie  
Heinrich-Heine-Universität, Universitätsstr. 1  
40225 Düsseldorf (Germany)  
Fax: (+49) 211-81-12803  
E-mail: ralf.kuehnemuth@uni-duesseldorf.de  
cseidel@gwdg.de

[b] D. Schmitz, Prof. Dr. H. Ritter  
Lehrstuhl für Präparative Polymerchemie  
Heinrich-Heine-Universität, Universitätsstr. 1  
40225 Düsseldorf (Germany)  
Fax: (+49) 211-81-15840  
E-mail: h.ritter@uni-duesseldorf.de

[c] Dr. A. Koslowski, Y. Lu, Prof. Dr. W. Thiel  
Max-Planck-Institut für Kohlenforschung  
Kaiser-Wilhelm-Platz 1  
45470 Mülheim an der Ruhr (Germany)  
Fax: (+49) 208-306-2996  
E-mail: thiel@mpi-muelheim.mpg.de

[\*\*] S. Marawske and D. Dörr contributed equally to this work.

Supporting information for this article is available on the WWW under <http://dx.doi.org/10.1002/cphc.200900240>.

and energy transfer as prominent optical processes in the condensed phases of these chromophores has been studied in detail.<sup>[12,13]</sup> However, in order to avoid fluorophore interactions we reduced the probe concentration to levels approaching the single-molecule regime. Moreover, none of the previous spectroscopic studies could present a complete characterization of the optical properties of a fluorescent probe including lifetime, anisotropy and spectral shifts as a function of the tensile stress in conjunction with a detailed theoretical analysis. The quantitative correlation of these techniques is a prerequisite to understand the underlying fundamental processes and to optimize specialized fluorophores. Herein, we designed a custom-tailored endgroup-functionalized OPV as a model compound which, based on the available information provided in the earlier reports,<sup>[1–4,6,7,11]</sup> is expected to show a significant change in the fluorescence properties if an external force is applied.

## 2. Results and Discussion

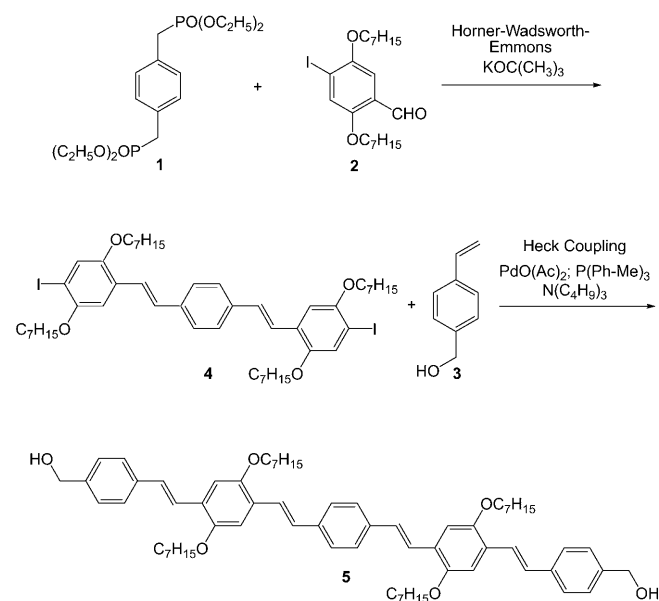
### 2.1. Synthesis

An OPV-type fluorophore **5** (OPV5) with sterically demanding *n*-heptyloxy side-chains and hydroxyl end-groups was synthesized in a stepwise procedure shown in Scheme 1.

In a first step, the double Horner–Wadsworth–Emmons reaction of *p*-xylylen-bis(diethylphosphonate) **1** and 4-formyl-1-iodo-2,5-bis(heptyloxy)-benzene **2** gave the styrylstilbene derivative **4**, which was subsequently reacted with 4-vinylbenzyl alcohol **3** in terms of a Heck reaction to form the wanted OPV5 diol **5**.<sup>[14–18]</sup>

### 2.2. Fluorescence Properties of OPV5

The fluorescence properties of OPV5 were investigated by measuring steady-state absorption and emission spectra, aniso-



Scheme 1. Synthesis of the 5-ring oligo(paraphenylenevinylene) OPV5 diol.

tropy, fluorescence lifetime, and quantum yield in THF (Table 1). The normalized absorption and fluorescence spectra and a typical result for the fluorescence decay of OPV5 dis-

Table 1. Spectral properties of OPV5 in different environments.

Solvent	$\lambda_{\text{ex}}$ [nm] <sup>[a]</sup>	$\lambda_{\text{f}}$ [nm] <sup>[b]</sup>	$\tau_1$ [ns] <sup>[c]</sup>	$\tau_2$ [ns] <sup>[c]</sup>	$\tau_{\text{av}}$ [ns] <sup>[d]</sup>	$\Phi_{\text{f}}$ <sup>[e]</sup>
THF	432	485	0.83 (0.77)	0.52 (0.23)	0.78	0.53
PVC	445	492	0.97 (0.97)	<sup>[f]</sup>	1.03	0.81

[a] Absorption maximum. [b] Fluorescence maximum. [c] Fluorescence lifetime components,  $\tau_i$  (amplitudes,  $A_i$ ). [d] Fluorescence weighted average lifetime  $\tau_{\text{av}} = (A_1\tau_1^2 + A_2\tau_2^2)/(A_1\tau_1 + A_2\tau_2)$ . [e] Fluorescence quantum yields, measured in THF and extrapolated by correcting for refractive index in case of PVC (for details, see the Supporting Information, Section 2). [f] Typically a minor component of  $\sim 2.2$  ns was observed, probably due to background fluorescence of the polymer matrix or distorted OPVs. Lifetimes in PVC were determined from *p*-polarized fluorescence in the green spectral window to maximize signal-to-noise ratio.

solved in PVC are shown in Figure 1. To recover the fluorescence lifetimes from the data by nonlinear regression analysis, the background contribution was determined from the baseline before the laser pulse and a double-exponential decay model was applied, taking into account repetitive excitation.<sup>[19]</sup> Double and triple exponential decays of OPVs have been described in literature before, with the origin of the two longer lifetimes assigned to *cis*–*trans* isomers. A very fast component of 20–50 ps was related to excited state dynamics of the chromophore.<sup>[20]</sup> Within the time resolution of our bulk setup we also observe a double exponential fluorescence decay with two significant components in THF (see Table 1).

However, in a PVC foil the fluorescence decay shows a single dominant lifetime component (97%) of 0.97 ns. The decay contains also a minor (3–5%) contribution of a longer second fluorescence lifetime of 2.2 ns, which may be attributed to background fluorescence of the polymer matrix or distorted OPVs.

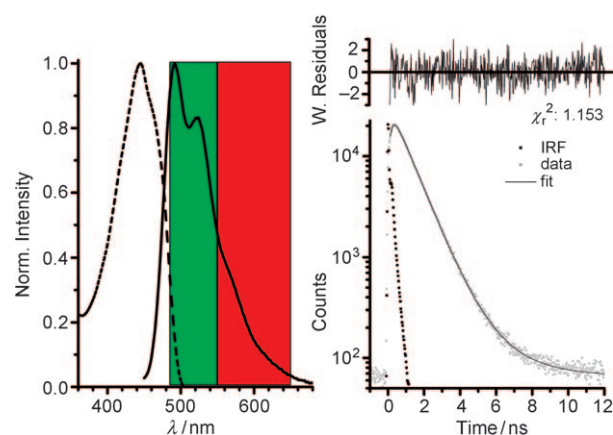


Figure 1. OPV5 in PVC: left: absorption (----) and fluorescence (—) spectra with detection windows for green (478–555 nm) and red (555–645 nm); right: decay histogram with double-exponential fit and residuals of OPV5  $F(t) = \text{IRF} \otimes [A_1 \exp(-t/\tau_1) + A_2 \exp(-t/\tau_2)] + B$ ; where IRF is the instrumental response function,  $A_i$  is the particular of the particular lifetime component  $\tau_i$  and  $B$  is the background (results listed in Table 1).



Moreover, OPV5 in the foil is brighter than in THF, as indicated by an increase in the fluorescence lifetime and quantum yield (Table 1). As the number of photons in our experiment was limited due to photobleaching, the two different lifetime components were difficult to separate. Therefore, the fluorescence weighted average lifetime (Table 1) of OPV5 was found to be a stable parameter for further fluorescence lifetime analysis. Typical spectral properties of OPV5 in different environments are listed in Table 1.

### 2.3. Quantum-Chemical Calculations

To relate the observed spectroscopic changes to the underlying changes in the molecular properties, quantum-chemical calculations were performed using semiempirical methods because of the size of the OPV5 chromophore. The theoretical study involved the selection of a suitable semiempirical approach (AM1) through comparison with higher-level results for small model compounds, computation of ground-state potential curves (AM1/SCF) for elongation of the chromophore, reoptimization of the resulting geometries in the first excited singlet state, and calculation of its spectral properties using multi-reference configuration interaction (AM1/MRCI) methods (for details see the Supporting Information, Section 3).

Two conformers of OPV5 ( $C_2$  and  $C_i$  symmetry) were considered, which both gave very similar results, as shown in Figure 2. Scheme 2 shows the  $C_2$  geometries of the ground

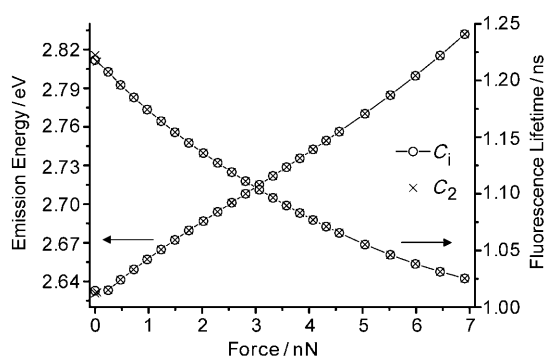
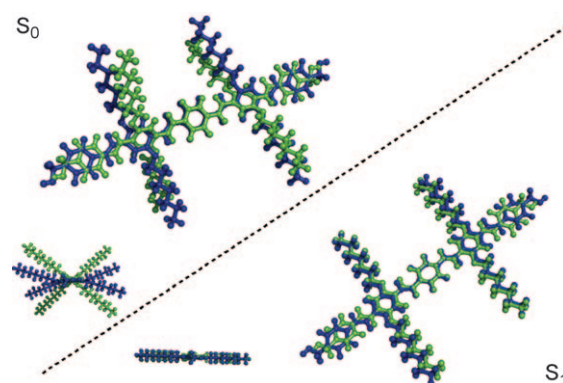


**Figure 2.** Calculated emission energies and fluorescence lifetimes dependent on the applied force per molecule. Results are shown for two different conformers, one in  $C_2$  symmetry ( $\times$ ) and one in  $C_i$  symmetry ( $\circ$ ) with the nearly identical results superimposed on top of each other.

and the first excited state without (green) and with (blue) applied force. The distance of the outermost ring carbon atoms of the chromophore was varied and all other coordinates of the molecule were then allowed to relax. Forces were computed by analytical differentiation of a cubic-spline fit of the computed potential curves. No breakage of any chemical bond was observed, even at the highest applied force (6.9 nN). This is consistent with reported rupture forces for C–C single bonds in the range of 2.3 to 13.4 nN<sup>[21]</sup> taking into account the higher stability of OPV5 due to the partial double bond character of its molecular backbone. In the ground state (Scheme 2, left) an unwinding of the molecular backbone under stress is ob-



**Scheme 2.** Simulation of the conformational change in the molecular geometry of OPV5 under  $C_2$  symmetry in the ground state (left) and in the first excited state (right), green: no force applied, blue: 6.9 nN per molecule.

served, whereas the first excited singlet state  $S_1$  (Scheme 2, right) remains almost planar throughout. For the range of forces considered (up to 6.9 nN), the AM1/MRCI calculations give a notable increase in the fluorescence energies (wavenumber  $\tilde{\nu}$  in  $\text{cm}^{-1}$ ) upon stretching as shown in Figure 2, and also an initial increase in the oscillator strengths  $f$  (for forces up to 4 nN). The resulting fluorescence lifetimes<sup>[22]</sup>  $\tau_r = 3/(2f\tilde{\nu}^2)$  as derived from the Einstein coefficients decrease monotonically (up to 16% for the maximum force of 6.9 nN) which is indicated by the declining curve in Figure 2. The calculations thus predict a blue-shift of fluorescence and reduced radiative lifetimes upon stretching OPV5 (see also Figure 2) along the conjugated chain.

### 2.4. Combined Force and Fluorescence Experiments

In order to investigate the impact of force on the fluorophores, thin foils ( $\sim 50 \mu\text{m}$ ) made of technical atactic PVC doped with OPV5 (ca. 100 nM) have been prepared. By applying uniaxial force the foil is stretched. As the foil is comparatively thin and the concentration of the dye is low, reabsorption is negligible in our experiments. In order to minimize surface effects, great care was taken to keep the laser focus centered in the PVC foil throughout the whole experiment. In this way the observation volume was at least  $20 \mu\text{m}$  away from any surface. At each data point of the fluorescence analysis a  $xy$ -scan using a piezo-scanner was performed in order to minimize photobleaching and to be more independent of local heterogeneities of the foil which might occur in the preparation process.

Three major optical effects can be observed simultaneously (Figure 3). First, the fluorescence anisotropy increases (top panel), which indicates a reorientation of the fluorophores within the matrix. Second, the fluorescence lifetime decreases (middle panel) by approximately 2.5% ( $\Delta\tau = -25 \pm 2.5$  ps). Finally, we observe a blue-shift in the emission spectrum by about 1.2 nm (bottom panel), as indicated by an increased background-corrected fluorescence ratio,  $F_G/F_R$ , in the green and red spectral detection windows (Figure 1, left). In the next sections we discuss all three effects in detail. As a negative control measurement we also prepared foils doped with Rhod-

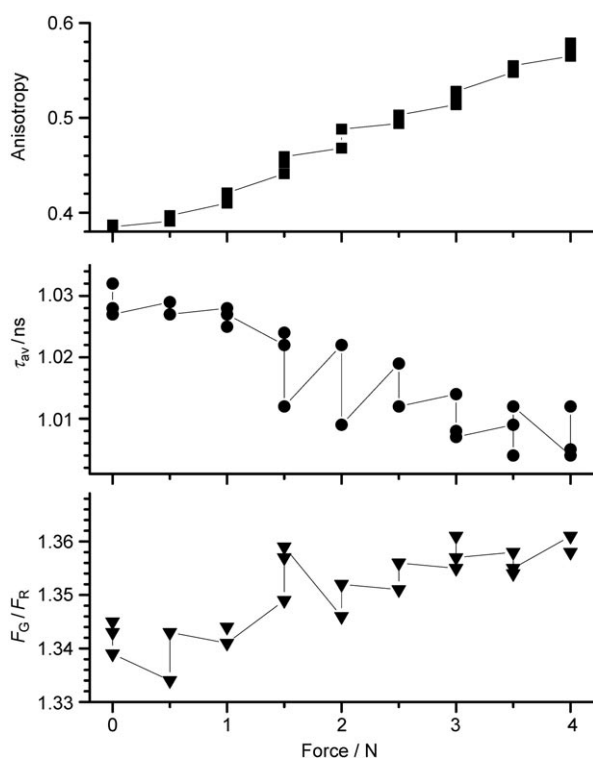


**Figure 3.** Increasing fluorescence anisotropy (top panel, ■), decreasing fluorescence lifetime (middle panel, ●) and increasing green-to-red fluorescence ratio (bottom panel, ▼) of OPV5 within the PVC foil versus the applied force.

amine 123 (Rh123) under the same conditions. The Rh123 is a rather spherical dye with no pronounced long axis, as is OPV5. Moreover Rh123 has a rigid molecular backbone, so it should be quite insensitive to external forces.

#### 2.4.1. Fluorescence Anisotropy

In the force experiment, the polarization of the exciting laser light and the pulling direction were chosen to be parallel to maximize excitation probability. As the transition dipole moments of OPVs are oriented almost parallel to their molecular backbones,<sup>[13,23]</sup> the increase in fluorescence intensity as well as in anisotropy while the foil is stretched shows that the fluorophores change the orientation of their long axis towards the direction of tension. This fluorescence increase and the irreversibility of this effect prove that the molecular rotation of OPV5 in PVC is negligible, making it an ideal marker to probe local orientations of suitable polymer matrices. This is in accordance with stretch orientation studies of different OPV derivatives dissolved in polyethylene or polystyrene foils.<sup>[24]</sup> For a quantitative evaluation of the experiments it is necessary to take the individual sample cross-sections  $S_i$  ( $S = \text{thickness} \times \text{width}$ ) of the foil for each point of the measurement into account by calculating the applied mean tensile stresses using Equation (1):

$$F_i/S_i = F_i / \{S_S - (S_S - S_E) [\Delta L_i / (L_E - L_S)]\} \quad (1)$$

where  $F_i$  is the applied force,  $S_S$  and  $S_E$  the cross sections at the start and the end of the experiment and  $[\Delta L_i / (L_E - L_S)]$  the rela-

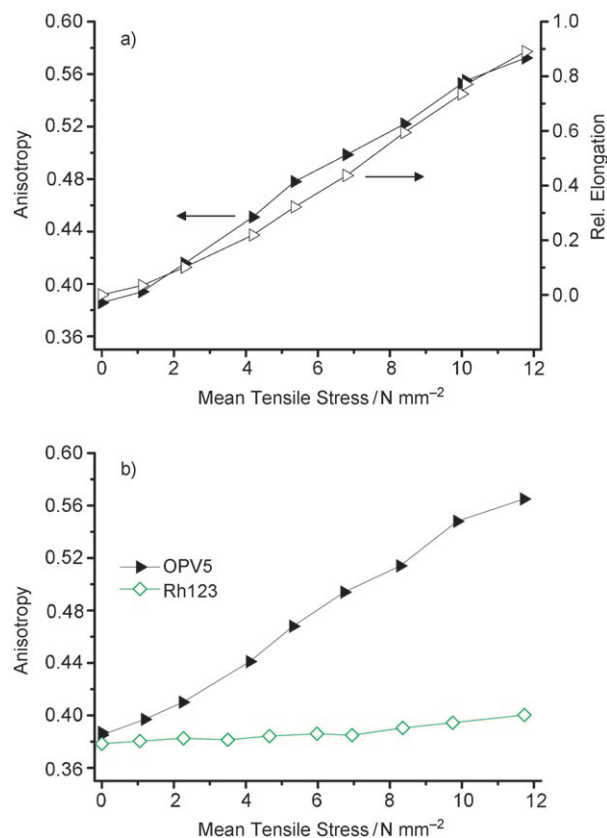


**Figure 4.** a) Relative elongation of the PVC foil ( $\Delta$ ) and the fluorescence anisotropy of OPV5 ( $\blacktriangle$ ) versus mean tensile stress. b) Comparison of the anisotropy between OPV5 (black) and Rh123 (green). With increasing tensile stress the OPV5 fluorophore shows a distinct reorientation whereas in case of Rh123 the effect is remarkably smaller.

tive elongation. Figure 4a illustrates the strict correlation between the elongation of the foil ( $\Delta$ ) and the change in the fluorescence anisotropy ( $\blacktriangle$ ) dependent on the mean tensile stress. Orientation of the polymer matrix was also confirmed using a polarization microscope. The unstretched unstained foil does not show any preferred direction, whereas the stretched foil clearly exhibits birefringence as expected (not shown).<sup>[25]</sup> This indicates that the macroscopic pre-alignment of the polymer chains in the unstretched foils is negligible.

If we compare the change in anisotropy between OPV5 (black) and the control dye Rh123 (green) as shown in Figure 4b it is clearly visible that the anisotropy very sensitively reflects the reorientation of OPV5 whereas in case of Rh123, only the expected small change is observed.

#### 2.4.2. Fluorescence Lifetime

For the analysis of the fluorescence lifetime in our combined force and fluorescence experiments we exclusively used data recorded by an ultra-fast single-photon-sensitive detector [Micro Photon Devices (MPD), instrumental response function (IRF)  $\approx 30$  ps, also see the Experimental Section]. The results of a detailed analysis of the fluorescence decay time of OPV5 as a function of the mean tensile stress is displayed in Figure 5a. The black curve shows the first part of the experiment (pulling)

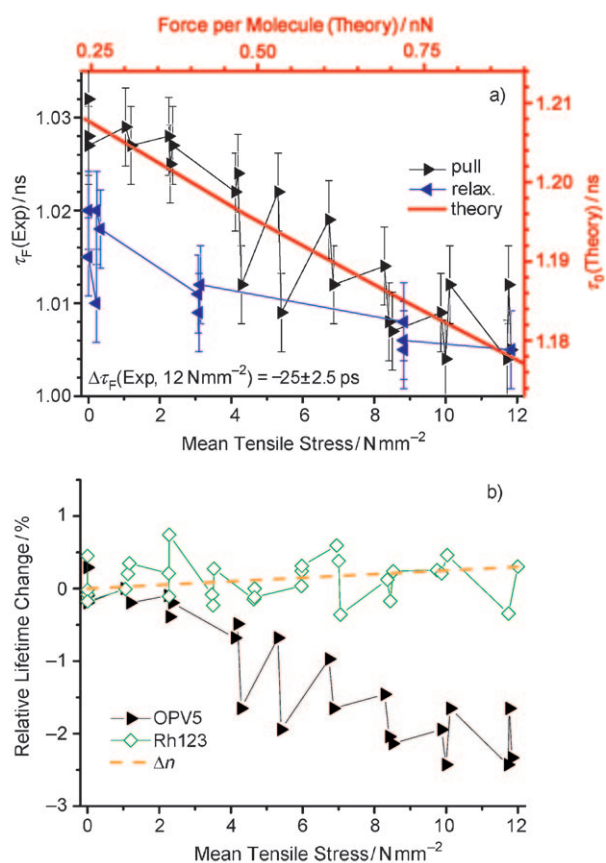


**Figure 5.** a) Comparison between a typical fluorescence lifetime measurement (black axes) and theory (AM1/MRCI, red): The PVC foil is stretched (black) and subsequently relaxed (blue). The error bars represent the shot-noise-limited uncertainty of the lifetime fits of about 4 ps. Both ordinates are scaled to an equal relative range of lifetimes. b) Comparison of the relative fluorescence lifetime change between OPV5 (black) and Rh123 (green). Upon stress the fluorescence lifetime of the OPV5 fluorophore decreases up to 2.5% at a maximum tensile stress of around  $12 \text{ N mm}^{-2}$  whereas Rh123 only shows a slight increase close to the noise level which is consistent with expected changes due to refractive index changes of the matrix ( $\Delta n$ , dashed orange).

while the blue curve describes the second step (relaxation). With increasing stress, the fluorescence lifetime is decreasing down to  $\Delta\tau = 25 \pm 2.5 \text{ ps}$  at the highest applicable stress of  $12 \text{ N mm}^{-2}$ . The effect is not completely reversible upon relaxation: in the presented experiment the final lifetime at  $0 \text{ N}$  is lower than the initial value at  $0 \text{ N}$  by about 10 ps. In a second extension relaxation cycle with the same sample the observed hysteresis was significantly smaller (not shown).

We also performed measurements in which the fluorescence lifetime returned to the starting value within the first cycle, indicating slight variations in the local static interactions of fluoro-

phore and matrix for different samples. With different samples we observed changes between 20 and 45 ps in the fluorescence lifetime. The average effect is around  $-26 \pm 5 \text{ ps}$  for applied tensile stresses of  $12 \text{ N mm}^{-2}$ . Foils with less plasticizer exhibited a similar, approximately linear dependence of lifetime on the tensile stress only after an offset of up to  $10 \text{ N mm}^{-2}$  (Supporting Information, Section 2.5). An alignment is achieved much faster in soft and flexible samples. This indicates the necessity for at least partial molecular alignment to couple solutes with external forces. Rates of radiative transitions depend on the environment of the chromophore, in particular on the local index of refraction. Two independent effects can cause the refractive index of PVC to change upon stretching (for details see Table 2 and the Supporting Information, Section 2.3): 1) From reported density changes<sup>[26]</sup> the Lorentz-Lorenz equation<sup>[27]</sup> predicts index variations of the order of  $\Delta n \approx 4.6 \times 10^{-4}$  for relative elongations of 100%. 2) The observed birefringence due to polymer chain orientation was reported to be around one order of magnitude stronger, ranging up to  $\Delta n \approx 3.1 \times 10^{-3}$ .<sup>[26, 28–32]</sup>

By applying a modified Strickler–Berg approach, different cavity models have been developed, which should be taken into account to estimate the influence of refractive index changes on the fluorescence lifetime.<sup>[33]</sup> As the solvent is expelled from the volume occupied by the fluorescent molecule, a cavity is created in which the fluorophore is located. In the approximation and depending on the guest molecule's shape, the empty spherical cavity model (ESC) or the empty ellipsoidal cavity model (EEC) can be used to describe the appropriate boundaries. The OPV5 fluorophore probably is described best by an ellipsoidal model. In case of Rh123 we believe that the empty spherical cavity model more realistically reflects the molecular shape. Corresponding changes in the fluorescence lifetime as estimated using these empty cavity models are expected to be smaller than ca. 3 ps, which is a relative change of less than 0.5% (Table 2).<sup>[33]</sup>

This is almost an order of magnitude smaller than the lifetime effect we observe. To further characterize the static matrix effect, we also performed measurements with the rigid dye Rh123 dissolved in PVC. We could not observe any significant change in the fluorescence lifetime  $\tau_f$ . At a fluorescence life-

**Table 2.** Influence of the matrix due to refractive index changes on the fluorescence properties of OPV5 and Rh123. Effects on the fluorescence lifetime assumed by an empty spherical cavity model (ESC) and an empty ellipsoidal cavity model (EEC). Effects on solvatochromic shifts of the emission spectra by applying Onsager theory.

		$\Delta\tau_f$ ESC [ps] <sup>[a]</sup>	$\Delta\tau_f$ EEC [ps] <sup>[a]</sup>	$\Delta\tau_f$ ESC [ps] <sup>[b]</sup>	$\Delta\tau_f$ EEC [ps] <sup>[b]</sup>	$\Delta\lambda$ <sup>[c]</sup> [nm]
OPV5	Estimate (density) <sup>[d]</sup>	−0.64 (0.05%)	−0.38 (0.03%)	−0.42 (0.04%)	−0.25 (0.02%)	0.022
	Estimate (biref.) <sup>[e]</sup>	−4.36 (0.34%)	−2.56 (0.20%)	−2.87 (0.28%)	−1.69 (0.16%)	0.146
	Experiment		−25 ± 2.5 (2.5%)			−1.2 ± 0.2
Rh123	Estimate (density) <sup>[d]</sup>	−1.59 (0.05%)	–	−1.47 (0.05%)	–	0.063
	Estimate (biref.) <sup>[e]</sup>	−10.71 (0.33%)	–	−9.92 (0.32%)	–	0.420
	Experiment		6 ± 10 (≈0.3%)			0.4 ± 0.2

[a] Change in radiative lifetime. [b] Change in fluorescence lifetime. [c] Solvatochromic shift. [d]  $\Delta n = 4.6 \times 10^{-4}$  from density changes. [e]  $\Delta n = 3.1 \times 10^{-3}$  from birefringence (see Supporting Information).

time of about 3.1 ns we found a change of  $\Delta\tau_F = 4 \pm 8$  ps at  $12 \text{ Nmm}^{-2}$ . Within a statistical error of around 8 ps, the relative change is smaller than 0.3%, which agrees well with expected refractive index effects of up to 10 ps (Table 2). In Figure 5b the relative lifetime changes for OPV5 (black) and Rh123 (green) are shown. In the case of Rh123, the changes can be attributed to the discussed refractive index changes alone, as indicated by the dashed orange curve, whereas the fluorescence lifetime of OPV5 shows a clear decrease up to 2.5%, about an order of magnitude larger than would be predicted by  $\Delta n$  (further details can be found in Table 2 and in the Supporting Information, Section 2.3). The fluorescence lifetimes from the semiempirical AM1/MRCI calculations are also included in Figure 5a (red part of the graph). They show an almost linear dependence on the applied force, being consistent with the experimental observations. The absolute values of the fluorescence lifetimes differ between theory and experiment, partly because of refractive index effects and nonradiative processes ( $\Phi_F < 1$ ) in the PVC matrix which were not taken into account in the simulations. Moreover, theory directly relates the force exerted on a single molecule to a change in radiative lifetime of  $S_1$ , whereas the only experimentally accessible information is the macroscopic mean tensile stress to which the whole foil is exposed. The force per molecule exerted in the foils can be estimated by using the mean molecular cross section of PVC molecules of about  $0.3 \text{ nm}^2$ . It is around 4 pN per molecule for the maximum force in Figure 6a (also see the Supporting Information, Section 2.2). This is only a mean value assuming a homogeneous force distribution in the substrate. Forces on individual molecules might locally be higher and can approach the realm where covalent chemical bonds may break (2.3 to 13.4 nN).<sup>[21,34]</sup> Our measured values as indicated by comparison of theory and experiment are within these limits. Thus, elongation induces a change of an apparent local mechanical force of ca. 0.6 nN per molecule (Figure 5a).

### 2.4.3. Spectral Blue-Shift of Fluorescence

Simultaneously with the changes in anisotropy and lifetime there is a spectral shift of the fluorescence upon stretching, which was detected by monitoring the intensity ratio of the two spectral bands in the emission region ("green" and "red", Figure 1, left). The results of this analysis are shown in Figure 6a. The black curve describes the results of the pulling step, in blue the subsequent relaxation step is shown and in red the results of the theoretical calculations are given. With increasing tensile stress the green-to-red fluorescence ratio  $F_G/F_R$  is increasing, indicating a blue shift of the spectra. Using the spectral shape as determined by steady-state measurements of the unstrained foil, the observed change in the ratio  $F_G/F_R$  for tensile stresses up to  $12 \text{ Nmm}^{-2}$  translates into a blue-shift of about  $1.2 \pm 0.2 \text{ nm}$ , as determined by linear regression analysis.

According to the AM1/MRCI calculations, this shift would be consistent with a change of an applied local mechanical force of ca. 0.18 nN per molecule. Using the spectral positions given in Table 1 and applying Onsager theory<sup>[35]</sup> we expect red-shifts in the force experiment due to refractive index changes small-

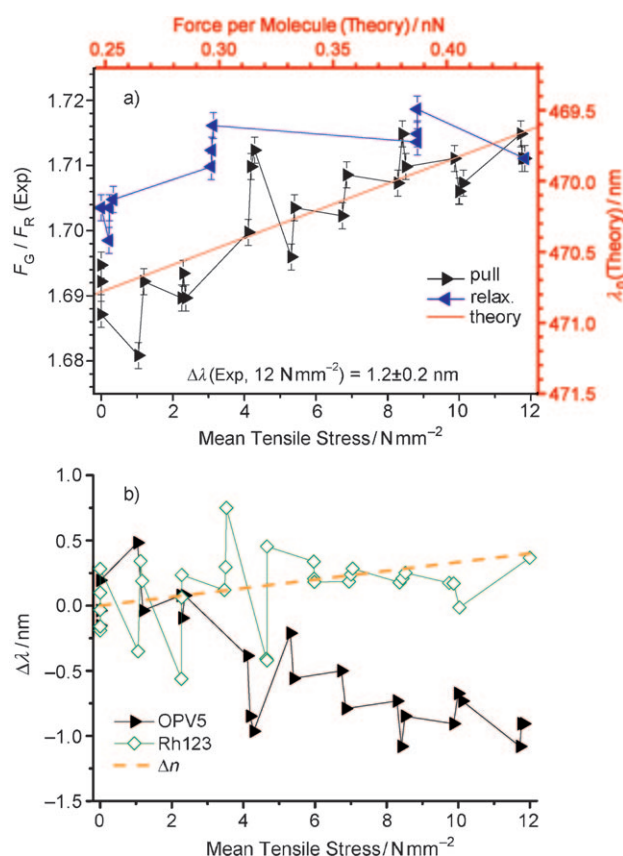


**Figure 6.** a) Green-to-red fluorescence ratio  $F_G/F_R$  from the experiment (black axes) in Figure 5a versus mean tensile stress. The PVC foil is stretched (black) and subsequently relaxed (blue). Also shown is the calculated (AM1/MRCI, red) spectral shift as function of the force applied on a single molecule. Both ordinates are scaled to equal relative spectral range. The error bars represent shot-noise. The real error is larger probably due to chromatic aberrations caused by a mismatch of refractive index of PVC foil ( $n = 1.53$ ) and objective design (corrected for  $n = 1.33$ ). The aberrations depend strongly on the focus position inside the foil and change upon stretching. b) Comparison of the relative spectral shifts of OPV5 (black) and Rh123 (green). At the maximum tensile stress of around  $12 \text{ Nmm}^{-2}$ , the spectrum of OPV5 features a blue-shift of 1.2 nm whereas the spectrum of Rh123 reveals a small red-shift consistent with estimations of the influence of the matrix alone due to refractive index changes (dashed orange).

er than  $\Delta\lambda \approx 0.15 \text{ nm}$  in case of OPV5. Corresponding reference measurements with Rh123 showed a spectral red-shift of  $\Delta\lambda = 0.31 \pm 0.14 \text{ nm}$  at  $12 \text{ Nmm}^{-2}$ , which is within the expected range for refractive-index-induced changes of up to 0.4 nm for this dye. In Figure 6b, the relative changes of the emission maxima are given for OPV5 (black) and Rh123 (green). A red-shift in case of Rh123 can be assigned to changes due to refractive index as discussed and shown by the dashed orange curve. However, for OPV5 a clear blue-shift of around 1.2 nm is observed (see also Table 2 and the Supporting Information, Section 2).

### 2.5. Overall Discussion

The observed force dependences of the lifetime and the measured spectral shift are significantly higher than would be ex-



pected from the matrix due to changes in the refractive index,  $\Delta n$ , alone.<sup>[36,37]</sup> Taking matrix effects due to changes in  $\Delta n$  into account (see Table 2), only a small increase in  $\Delta\tau_F$  by up to 12% and a reduction in  $\Delta\lambda$  by up to 14% is expected. Thus, a net effect of  $\Delta\tau_F = -22$  ps and  $\Delta\lambda = 1.25$  nm can be unambiguously attributed to force. In comparison with theory, these shifts then translate into an apparent mean local force on a single chromophore in the range of ca. 0.2–0.55 nN (see Figure 2). The uncertainty lies within the expected accuracy level of the semi-empirical computations.

Due to the visco-elastic properties of the PVC matrix its extension shows only a faint reversibility with the applied force, which suggests that the local environment of the fluorophores does not depend on force, but on extension. This is corroborated by the orientation of the fluorophores as indicated by anisotropy, which is largely dependant on extension of the foil only. However, the observed changes of fluorescence lifetime as well as the spectral shift are mainly reversible with the applied force. Altogether, this indicates only a marginal influence of the matrix on the fluorescence lifetime as well as the emission spectrum of the fluorophore. This clearly proves the concept of a fluorescent probe as a sensor for local forces.

The blue-shift of fluorescence and the reduced lifetime of OPV5 under tensile stress are qualitatively consistent with the results from semiempirical calculations. A more quantitative comparison is not feasible, as the force on single OPV5 molecules is not known precisely in the experiment (apparently less than 1 nN). The experimental results seem to indicate an extremely efficient transfer of mechanical force onto the chromophore, that is, a force per molecule approximately two orders of magnitude higher than average. Therefore, a more realistic view of the process may also have to add lateral interactions of the polymer chains with the side chains of the chromophore to promote its unwinding. Unwinding of the ground state as observed in the simulated experiments for uniaxial forces can also be achieved by applying torsional forces to the side-chains. For both mechanisms we expect qualitatively similar spectroscopic effects. The presence of an additional mechanism is supported by experiments using modified OPV5 carrying polymer chains attached to the hydroxyl endgroups as possible handles to enhance coupling of external forces from the matrix to the fluorophores (not shown). No difference in the force-dependent effects was observed between OPV5 and the modified OPV5.

### 3. Conclusions

In summary, we have explored possible applications of fluorophores as optical sensors for local mechanical forces. To that end, a custom-tailored chromophore consisting of an aromatic backbone strained by sterically demanding alkyloxy side-chains was synthesized. A flexible PVC matrix served to align the fluorophores by stretching. Transfer of mechanical strain from the matrix induced a geometrical change in the chromophore. Consistent with the results of semiempirical calculations on the same system, this caused a decrease in the fluorescence lifetime by 2.5% (25 ps) and an increase of the emission energy

by 0.2% which corresponds to a blue-shift of 1.2 nm at tensile stresses of  $12 \text{ N mm}^{-2}$ . From a different point of view the force of 0.2–0.55 nN acting on a single molecule can be interpreted as an equivalent energy difference of 0.15–0.8 kcal mol<sup>-1</sup> (Supporting Information, Table 8).

Our study proves the feasibility of fluorescence-based local force probes for polymers under tension. Necessary improvements can be achieved by developing more sensitive fluorophores and possibly by increasing the efficiency of force transmission from the matrix to the probe, that is, by using modified end-groups to attach additional polymer chains as handles. Improved optical sensors of this type should in principle be able to monitor local mechanical stress in transparent samples down to the single-molecule level, which can be used for reliability studies of the materials and also harbor promising further applications in polymer science and nanotechnology.

### Experimental Section

**OPV5:** The yellow crystalline solid was purified by column chromatography using a 95:5 mixture of chloroform and acetone as an eluent. Yield: 45% (see the Supporting Information, Section 1 for the synthesis). <sup>1</sup>H NMR (500 MHz, [D<sub>8</sub>]THF, 25 °C, TMS):  $\delta = 0.81$  (m, 12H, CH<sub>3</sub>), 1.27–1.34 (m, 16H, CH<sub>2</sub>), 1.48 (m, 8H, CH<sub>2</sub>), 1.78 (m, 8H, CH<sub>2</sub>), 3.99 (m, 8H, CH<sub>2</sub>), 4.06 (m, 2H, OH), 4.46 (d, 4H, CH<sub>2</sub>), 7.11–7.22 (m, 12H, CH), 7.38–7.46 (m, 12H, CH); MALDI-TOF MS:  $m/z$ : 1003 M<sup>+</sup>

**PVC Foil:** PVC (0.3 g, Aldrich, CAS# 9002-86-2, Mn: 47000) was dissolved in THF (5 mL, Prolabo, CAS# 109-99-9, AnalaR NORMAPUR) together with hexamoll® (0.045 g, BASF Ludwigshafen, CAS# 166412-78-8), a plasticizer which is necessary to make the foil flexible enough to be stretched. This solution was then cleaned with activated charcoal which was afterwards removed by centrifugation. To the polymer solution (5 mL) OPV5 (21.5 ng, 21.4 pmol, the concentration is far below excimer formation<sup>[38]</sup>) was added and filled into a petri dish. THF was evaporated at room temperature until the foil gained its solid state. Finally, the foil was dried for 5 h under high-vacuum conditions, yielding substrates with a glass-temperature of 46 °C. The resulting foil showed a thickness of around 50  $\mu\text{m}$ , the exact value being determined by a z-scan of the laser focus through the sample prior and after each experiment. The effective cross section of each foil was calculated from its thickness and the width as measured by a calliper-gauge.

**Fluorescence Spectroscopy:** The fluorescence and absorption spectra were measured with FluoroLog-3 (Jobin Yvon Horiba) and Cary-300 Bio (Varian), respectively. Time-correlated single-photon counting (TCSPC) measurements were performed using a 5000 U (IBH) with a pulsed diode laser source at 471 nm (Picoquant). The combined force and fluorescence measurements were performed on a home-built setup.<sup>[39]</sup> Linearly polarized and pulsed light from a diode laser (Picoquant) at 468 nm and a repetition rate of 50 MHz is coupled into an inverted epifluorescent confocal microscope (Olympus, IX71) at a mean intensity of  $I_0/2 \approx 2.5 \text{ kW cm}^{-2}$  in a near-diffraction-limited focus. The fluorescence was then separated with respect to polarization parallel and perpendicular to the laser light. These two components were further split by a dichroic beamsplitter (AHF, BS560) in a "green" fraction 487–548 nm (AHF, HQ 520/66) and a "red" fraction 548–644 nm (AHF, HQ 580/130) and finally focused on single-photon avalanche diodes [Micro Photon Devices PDM 50CT (green), Perkin-Elmer SPCM-AQR-14 (red)]. The signals

of the detectors were recorded by two synchronized time-correlated single photon counting pc-boards (Becker & Hickl, SPC-150). In order to minimize photobleaching, for each data point a *xy*-scan of  $98 \times 98 \mu\text{m}^2$  was performed with a piezo-scanner (PI, P-527). Taking into account an average number of ca. 360 dye molecules in the confocal detection volume element, pixel intensity distributions within each scan were shot-noise limited and gave no indication of additional heterogeneity (see the Supporting Information, Section 2.7). The self-made PVC foils were stretched by a tensile stage (Deben, MTEST 200) which was mounted upside down on the inverted microscope.

Calculations: In view of the size of the OPV5 chromophore, its fluorescence lifetime was computed using semiempirical methods.<sup>[40]</sup> Geometry optimizations were performed on two conformers of OPV5 in the ground state at the AM1/SCF level,<sup>[41]</sup> one in  $C_2$  symmetry (with the  $C_2$  axis perpendicular to the central aromatic ring) and the other one in  $C_i$  symmetry. Spectral properties were computed at the AM1/MRCI level at the optimized (nearly planar) excited-state geometries, in particular the radiative lifetime  $\tau_r$  of the first excited singlet state.

## Acknowledgements

This work was financially supported by the Deutsche Forschungsgemeinschaft (SFB 663, Projects B4 and C4) and is printed at its instigation with financial support provided by the Deutsche Forschungsgemeinschaft. The authors thank Dr. S. Kalinin and Dr. S. Felekyan.

**Keywords:** analytical methods • fluorescence spectroscopy • molecular modelling • optical properties • organic chemistry

- [1] C. Löwe, C. Weder, *Adv. Mater.* **2002**, *14*, 1625–1629.
- [2] J. W. Hofstraat, J. Veurink, B. Gebben, H. J. Verheij, J. W. Verhoeven, *J. Fluoresc.* **1998**, *8*, 335–342.
- [3] T. Ikawa, T. Shiga, A. Okada, *J. Appl. Polym. Sci.* **2002**, *83*, 2600–2603.
- [4] H. Springer, R. Neuert, F. D. Müller, G. Hinrichsen, *Colloid Polym. Sci.* **1983**, *261*, 800–804.
- [5] T. Hugel, N. B. Holland, A. Cattani, L. Moroder, M. Seitz, H. E. Gaub, *Science* **2002**, *296*, 1103–1106.
- [6] U. F. Röhrig, U. Troppmann, I. Frank, *Chem. Phys.* **2003**, *289*, 381–388.
- [7] S. Tretiak, A. Saxena, R. L. Martin, A. R. Bishop, *Phys. Rev. Lett.* **2002**, *89*, 097402.
- [8] H. Meier, U. Stalmach, H. Kolshorn, *Acta Polym.* **1997**, *48*, 379–384.
- [9] F. Schindler, J. M. Lupton, J. Feldmann, U. Scherf, *Proc. Natl. Acad. Sci. USA* **2004**, *101*, 14695–14700.

- [10] D. A. Vanden Bout, W. T. Yip, D. Hu, D. K. Fu, T. M. Swager, P. F. Barbara, *Science* **1997**, *277*, 1074–1077.
- [11] K. Becker, E. Da Como, J. Feldmann, F. Scheliga, E. Thorn Csányi, S. Tretiak, J. M. Lupton, *J. Phys. Chem. B.* **2008**, *112*, 4859–4864.
- [12] H.-J. Egelhaaf, J. Gierschner, D. Oelkrug, *Synth. Met.* **1996**, *83*, 221–226.
- [13] J. Gierschner, M. Ehni, H.-J. Egelhaaf, B. M. Medina, D. Beljonne, H. Benmansour, G. C. Bazan, *J. Chem. Phys.* **2005**, *123*, 144914.
- [14] M. Bothe, G. Schmidt-Naake, *Macromol. Rapid Commun.* **2003**, *24*, 609–613.
- [15] R. A. W. Johnstone, M. E. Rose, *Tetrahedron* **1979**, *35*, 2169–2173.
- [16] Z. Bao, Y. Chen, R. Cai, L. Yu, *Macromolecules* **1993**, *26*, 5281–5286.
- [17] D. A. M. Egbe, C. P. Roll, E. Bircckner, U. W. Grummt, R. Stockmann, E. Klemm, *Macromolecules* **2002**, *35*, 3825–3837.
- [18] T. Maddux, W. J. Li, L. P. Yu, *J. Am. Chem. Soc.* **1997**, *119*, 844–845.
- [19] J. R. Fries, L. Brand, C. Eggeling, M. Köllner, C. A. M. Seidel, *J. Phys. Chem. A* **1998**, *102*, 6601–6613.
- [20] R. E. Di Paolo, J. S. de Melo, J. Pina, H. D. Burrows, J. Morgado, A. L. Macanita, *ChemPhysChem* **2007**, *8*, 2657–2664.
- [21] J. A. Odell, A. Keller, *J. Polym. Sci. Pt. B-Polym. Phys.* **1986**, *24*, 1889–1916.
- [22] M. Klessinger, J. Michl, *Lichtabsorption und Photochemie organischer Moleküle*, VCH, Weinheim, **1989**.
- [23] F. C. Spano, *J. Chem. Phys.* **2002**, *116*, 5877–5891.
- [24] T. Damerau, M. Hennecke, *J. Chem. Phys.* **1995**, *103*, 6232–6240.
- [25] J. G. Rider, E. Hargreaves, *J. Phys. D* **1970**, *3*, 993–1008.
- [26] S. A. Jabarin, *Polym. Eng. Sci.* **1991**, *31*, 638–643.
- [27] L. Horner, *J. Makromol. Chem.* **1943**, *1*, 234–246.
- [28] A. Ajji, M. C. Renaud, *J. Appl. Polym. Sci.* **1991**, *42*, 335–345.
- [29] Y. Shindo, B. E. Read, R. S. Stein, *Makromol. Chem.* **1968**, *118*, 272–312.
- [30] B. Yalcin, M. Cakmak, *J. Polym. Sci. Pol. Phys.* **2005**, *43*, 724–742.
- [31] M. E. R. Robinson, D. I. Bower, W. F. Maddams, *J. Polym. Sci. Pol. Phys.* **1978**, *16*, 2115–2138.
- [32] H. S. Özkan, T. Oskay, H. Y. Guney, H. Dirim, *J. Polym. Sci. Pol. Phys.* **1994**, *32*, 631–640.
- [33] D. Toptygin, *J. Fluoresc.* **2003**, *13*, 201–219.
- [34] M. Grandbois, M. Beyer, M. Rief, H. Clausen-Schaumann, H. E. Gaub, *Science* **1999**, *283*, 1727–1730.
- [35] L. Onsager, *J. Am. Chem. Soc.* **1936**, *58*, 1486–1493.
- [36] C. N. R. Rao, S. Singh, V. P. Senthilnathan, *Chem. Soc. Rev.* **1976**, *5*, 297–316.
- [37] J. Gierschner, H. G. Mack, L. Lüer, D. Oelkrug, *J. Chem. Phys.* **2002**, *116*, 8596–8609.
- [38] B. R. Crenshaw, C. Weder, *Adv. Mater.* **2005**, *17*, 1471–1476.
- [39] J. Widengren, V. Kudryavtsev, M. Antonik, S. Berger, M. Gerken, C. A. M. Seidel, *Anal. Chem.* **2006**, *78*, 2039–2050.
- [40] A. Koslowski, M. E. Beck, W. Thiel, *J. Comput. Chem.* **2003**, *24*, 714–726.
- [41] M. J. S. Dewar, E. G. Zoebisch, E. F. Healy, J. J. P. Stewart, *J. Am. Chem. Soc.* **1985**, *107*, 3902–3909.

Received: March 26, 2009

Published online on May 26, 2009

paper (2)

***QM/MM Nonadiabatic Decay Dynamics of 9H-Adenine  
in Aqueous Solution***

Z. Lan, Y. Lu, E. Fabiano, and W. Thiel

*ChemPhysChem* **2011**, *12*, 1989-1998.





# QM/MM Nonadiabatic Decay Dynamics of 9H-Adenine in Aqueous Solution

Zhenggang Lan,<sup>\*,[a]</sup> You Lu,<sup>[a]</sup> Eduardo Fabiano,<sup>[b]</sup> and Walter Thiel<sup>[a]</sup>

*Dedicated to Professor Karl Kleinermanns on the occasion of his 60th birthday*

The photoinduced nonadiabatic decay dynamics of 9H-adenine (hereafter, adenine) in aqueous solution were investigated by surface-hopping simulations within a quantum mechanical/molecular mechanical (QM/MM) framework. The QM subsystem (adenine) was treated at the semiempirical OM2/MRCI level, whereas the MM solvent (water) was described by the TIP3P force field model. Classical molecular dynamics (MD) simulations were used to generate snapshots with different solvent configurations and geometries. For a representative number of these snapshots, the energy minima of the lowest electronic

states and the most important conical intersections were located by QM/MM geometry optimization. Surface-hopping QM/MM MD simulations were performed for all selected snapshots to study the nonadiabatic dynamics after photoexcitation, including the two lowest excited singlet states, which are both populated in the initial photoexcitation due to strong vibronic coupling in the Franck–Condon region. The simulations yield ultrafast  $S_2$ – $S_1$  decay within 40 fs and  $S_1$ – $S_0$  internal conversion to the ground state within 410 fs, which is consistent with recent experimental results from time-resolved spectroscopy.

## 1. Introduction

In recent years, the nonadiabatic decay dynamics of 9H-adenine (hereafter, adenine) has been widely investigated because it represents the prototypical photoinduced process in DNA bases.<sup>[1–5]</sup> The mechanism of the radiationless decay of isolated adenine in the gas phase is reasonably well understood.<sup>[6–37]</sup> Experimentally, the excited-state lifetime of isolated adenine is extremely short.<sup>[6–16,23]</sup> Time-resolved pump–probe experiments on gas-phase adenine indicated the existence of two decay components with different timescales (less than 200 fs and less than 1 ps).<sup>[10–14,16]</sup> In theoretical studies, several conical intersections ( $\pi\pi^*/n\pi^*$ ,  $\pi\pi^*/\pi\sigma^*$ ,  $n\pi^*/gs$ ,  $\pi\pi^*/gs$ ,  $\pi\sigma^*/gs$ ) were located that are relevant for the nonadiabatic decay of adenine.<sup>[17–36]</sup> Minimum-energy reaction paths connecting the Franck–Condon (FC) region and different conical intersections were constructed to explore possible radiationless decay pathways.<sup>[18–22,24–31,35,36]</sup> Furthermore, direct on-the-fly dynamic simulations were performed<sup>[32–34,37]</sup> to assess the relative importance of different decay channels and to compare the corresponding decay times with those measured in time-resolved pump–probe experiments. On the basis of this work, it was possible to identify three main decay paths in gas-phase adenine. For excitation energies close to the center of the main absorption band ( $\approx 250$  nm), there are two competing mechanisms that involve two distinctly different conical intersections, namely,  $\pi\pi^* \rightarrow gs$ <sup>[19–22,26,28,29,32,34–36]</sup> and  $\pi\pi^* \rightarrow n\pi^* \rightarrow gs$ .<sup>[10–14,19,20,24,25,30,33,34,36]</sup> According to our previous semiempirical OM2/MRCI surface-hopping study on gas-phase adenine, the  $\pi\pi^* \rightarrow n\pi^*$  and partially also the  $\pi\pi^* \rightarrow gs$  channels are responsible for the ultrafast decay component, whereas the  $n\pi^* \rightarrow gs$  decay mainly contributes to the slower sub-picosecond decay.<sup>[33]</sup> At different excitation energies ( $< 233$  nm and  $\approx 267$  nm) there is also a  $\pi\pi^* \rightarrow \pi\sigma^* \rightarrow gs$  channel,<sup>[15,18,21,23,35,36]</sup>

which is accessed through a Rydberg-type  $\pi\sigma^*$  excitation and leads to hydrogen dissociation.

Compared with detailed knowledge about radiationless decay dynamics in the gas phase, the photophysical behavior of adenine in solution or in a DNA environment is much less understood. Experimentally, the excited-state lifetime of adenine in solution was found to be even shorter than in the gas phase, with published values ranging from 180 to 670 fs.<sup>[38–46]</sup> In these experimental studies, it was difficult to identify the dominant decay mechanisms or details of the dynamics. On the theoretical side, vertical excitation energies and conical intersections between low-lying electronic states were computed by using continuum solvation models<sup>[47]</sup> and the reference interaction site model self-consistent field method.<sup>[48]</sup> A sequential Monte Carlo/CASPT2 study on the photophysics of adenine in aqueous solution addressed the solvent effects on gas-phase minimum-energy paths in the two lowest excited states by using the simple point charge (SPC) model to describe the surrounding water molecules.<sup>[49]</sup>

The simulation of the nonadiabatic dynamics in the condensed phase is a challenging task because of the need to realistically describe both the electronic structure of all relevant excited states under the influence of the environment and the

[a] Dr. Z. Lan, Y. Lu, Prof. Dr. W. Thiel  
Max-Planck-Institut für Kohlenforschung,  
Kaiser-Wilhelm-Platz 1, D-45470 Mülheim an der Ruhr (Germany)  
Fax: (+49) 208-306-2996  
E-mail: lan@mpi-muelheim.mpg.de

[b] Dr. E. Fabiano  
National Nanotechnology Laboratory  
Istituto di Nanoscienze del CNR  
Via per Arnesano, I-73100 Lecce (Italy)

dynamics of the entire system, including the environment. This will generally require an explicit representation of the environment. Continuum models, such as the polarizable continuum model (PCM)<sup>[50–54]</sup> and the conductor-like screening model (COSMO)<sup>[55,56]</sup> are expected to be less suitable, even in the seemingly isotropic case of a solvated molecule, since nonadiabatic transitions between different electronic states may cause ultrafast changes in the electronic density of the solute molecule, which in turn may trigger a strong anisotropic perturbation of the solvent. The resulting reorganization of the solvent may have a non-negligible influence on the time evolution of the system. Hybrid QM/MM schemes<sup>[57,58]</sup> provide a convenient way to combine an accurate quantum description of the solute with an explicit and efficient atomistic model of the solvent environment at the force field level. In recent years, the QM/MM approach has been successfully used in combination with surface-hopping methods to study nonadiabatic dynamics in condensed-phase systems, both in solution and in biological environments.<sup>[48,59–69]</sup> A purely QM surface-hopping simulation has recently been reported for microsolvated adenine, taking into account the first solvation shell (26 water molecules) and treating the entire system by the time-dependent density functional tight-binding (TD-DFTB) method.<sup>[70]</sup>

Herein, we study the nonadiabatic dynamics of adenine in aqueous solution by surface-hopping QM/MM simulations. The electronic structure in the ground state and the excited states of adenine is described quantum mechanically by using the OM2/GUGA-Cl approach,<sup>[71–75]</sup> while the solvent water molecules are represented by a classical force field model. The OM2/GUGA-Cl method provides a good compromise between computational cost and accuracy. It has been applied successfully in recent investigations of the gas-phase relaxation dynamics of isolated DNA bases.<sup>[33,76,77]</sup> Herein, we characterize the relevant potential-energy surfaces and report the results of surface-hopping simulations for adenine in water. We analyze the effects of solvation on the photoinduced nonadiabatic dynamics of adenine, by comparing the results in the gas phase and in aqueous solution, and we also comment on accuracy issues.

## Computational Details

A model of adenine in aqueous solution was constructed by placing adenine (Figure 1) at the center of a pre-optimized TIP3P water sphere<sup>[78]</sup> with a radius of 37 Å.

The system was then relaxed and equilibrated by running classical molecular dynamics (MD) simulations with a quartic boundary potential using the CHARMM program.<sup>[79]</sup> Thereafter, all water molecules beyond a cutoff radius of 20 Å were deleted. The resulting structure was the starting point for a ground-state Born–Oppenheimer QM/MM MD simulation, during which all water molecules further than 16 Å from the center were kept fixed. A sample of 200 snapshots was extracted from this MD run to provide starting geometries for subsequent QM/MM excited-state calculations and surface-hopping dynamics.

Hybrid QM/MM calculations employed the development version of the ChemShell package<sup>[80,81]</sup> by using a specifically adapted inter-

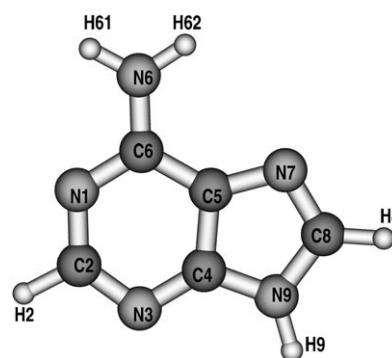


Figure 1. Molecular structure and atom numbering of 9H-adenine.

face to the MNDO code.<sup>[82]</sup> The QM part (adenine) was described by the semiempirical orthogonalization model 2 (OM2) Hamiltonian<sup>[71,72]</sup> using the restricted open-shell Hartree–Fock (ROHF) formalism in the self-consistent field (SCF) procedure. Excited states were calculated at the multireference configuration interaction (MRCI) level in the graphical unitary group approach (GUGA) formalism, with analytical evaluation of the OM2/MRCI gradients and nonadiabatic couplings.<sup>[73–75]</sup> The active CI space consisted of 12 electrons in 10 orbitals, that is, the six highest occupied orbitals and the four lowest unoccupied orbitals. The MRCI treatment employed four reference configurations corresponding to the leading configurations of the four lowest singlet states of adenine:  $g_s$  (closed-shell ground state),  $n\pi^*$  ( $n \rightarrow \pi^*$ ),  $L_a$  (HOMO–LUMO  $\pi \rightarrow \pi^*$ ), and  $L_b$  ( $\pi \rightarrow \pi^*$ ).<sup>[18–22,27,28,31,33]</sup> The present OM2/MRCI calculations were thus carried out in exactly the same manner as in our previous study on gas-phase adenine.<sup>[33]</sup> The MM part (solvent) was described by using the TIP3P water model.<sup>[78]</sup> An electrostatic embedding approach was adopted to model the interactions between adenine and water: the MM charges were incorporated into the one-electron part of the QM Hamiltonian and the QM/MM electrostatic interactions were evaluated from the QM electrostatic potential and the MM partial charges. It should be noted that water is unpolarizable in the fixed-charge TIP3P representation and that dynamic solvent effects due to fast electronic rearrangements in the solvent molecules can thus not be captured in this model.

Geometry optimizations of energy minima and conical intersections were performed with the DL-FIND optimizer<sup>[83]</sup> in ChemShell, using the Newton–Raphson and Lagrange–Newton algorithms, respectively. For an isolated gas-phase adenine molecule, the corresponding optimized geometries are well-defined and unique. In contrast, for adenine in aqueous solution, there are many of such geometries for each energy minimum or conical intersection because the solvent environment can adopt many different configurations. To investigate the influence of different solvent arrangements and to assess the fluctuations caused by different solvent configurations, geometry optimizations were carried out for a number of snapshots taken from the initial ground-state QM/MM MD run (see above). The following procedure was adopted: 1) 20 different snapshots were optimized to locate their  $S_0$  ground-state minima. At each optimized geometry, the vertical excitation energies of the low-lying excited states were calculated. Thereafter, the average vertical excitation energy was determined for each state. 2) Starting from these optimized  $S_0$  geometries, geometry optimizations were carried out for the  $S_1$  minimum, the  $S_2$  minimum, and the  $S_1$ – $S_2$  conical intersection, assuming that these species can be reached directly from the FC geometry. 3) The  $S_0$ – $S_1$  conical intersections were not accessible in this manner. They could be located,

however, by optimizations that started from the corresponding hopping geometries encountered during excited-state dynamics (see below). 4) The resulting geometries of the two  $S_0$ - $S_1$  conical intersections were taken as the starting points for optimizations on the  $S_0$  ground-state surface. These optimizations always led to the respective initial  $S_0$  minimum and thus established a one-to-one correspondence for a given snapshot.

The surface-hopping MD method<sup>[84–86]</sup> was implemented in a development version of the ChemShell package. This involved the integration of the surface-hopping dynamics module into the QM/MM framework and the adaptation of the ChemShell-MNDO interface. The present QM/MM implementation is analogous to the original MNDO implementation,<sup>[86]</sup> with a few additional features: parts of the system can now be kept fixed during excited-state dynamics (to allow for a frozen outer solvent shell), and the nonadiabatic coupling terms can also be computed in the presence of the MM charges. For QM/MM simulations of the nonadiabatic dynamics of adenine in water, the nuclear degrees of freedom were propagated on classical trajectories for 1.2 ps with a time step of 0.2 fs, by using the velocity Verlet algorithm. The time evolution of the quantum amplitudes along these trajectories was calculated by using a unitary propagator and a time step 200 times smaller. The fewest switching algorithm<sup>[85]</sup> was employed to compute the hopping probabilities. All simulations were performed in the adiabatic representation and final results were obtained by averaging over 90 trajectories. The selection of initial configurations was guided by the concept of obtaining an adequate approximate sampling of the center of the absorption band,<sup>[87]</sup> which was achieved by applying the same procedure as in our previous gas-phase study of adenine,<sup>[33]</sup> with the number of trajectories starting from a given snapshot and excited state determined from the corresponding oscillator strength. Further technical details about the surface-hopping calculations are documented in references [86] and [87].

## 2. Results

### 2.1. Potential Energy Surfaces

For adenine in water, the ground-state minimizations at the OM2/MRCI level led to snapshot geometries with planar aromatic rings and a slight pyrimidization of the amino group, see Figure 2, similar to that found at the ab initio level.<sup>[47,48]</sup>

Table 1 lists OM2/MRCI results obtained at 10 such optimized snapshot geometries, for the vertical excitation energies, the oscillator strengths, and the weights of the leading configurations in the corresponding CI wavefunctions. The vertical excitation energies of the three lowest singlet excited states,  $S_1$ ,  $S_2$ , and  $S_3$ , lie between 4.45–4.69, 4.67–4.90, and 4.86–4.95 eV, respectively, and thus vary over a range of about 0.1–0.2 eV. In 9 out of 10 cases, the  $S_1$  state is separated from the  $S_2$  state by 0.22–0.32 eV, while the  $S_2$  and  $S_3$  states lie within 0.1 eV.

Given these small energy gaps, one may expect heavy mixing between the leading configurations and a strong variation of this mixing between different snapshots, which is indeed confirmed by inspection of the CI wavefunctions (see Table 1). In the first excited state ( $S_1$ ), the  $\pi\pi^*$  (HOMO–LUMO,  $L_a$ ) configuration contributes most in 7 out of 10 cases, with weights in the CI wavefunction that are typically around 50% and always above 30%, while the contributions from the  $\pi\pi^*$

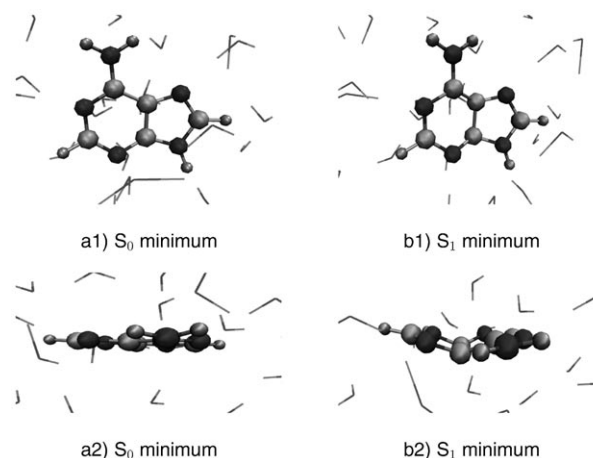


**Figure 2.** Typical molecular geometries of adenine in water at the a)  $S_0$  and b)  $S_1$  minima. Upper panel: top view; lower panel: side view.

( $L_b$ ) configuration are always smaller (but not negligible) and those from the  $n\pi^*$  configuration vary substantially between different snapshots (highest in 3 cases, lowest in 6 cases). The  $n\pi^*$  excitation dominates the second excited state ( $S_2$ ) in 4 snapshots and the third excited state ( $S_3$ ) in 3 snapshots, with weights of more than 50%, whereas these states are mostly of mixed  $L_a$  and  $L_b$   $\pi\pi^*$  character in the other cases. The  $\pi\pi^*$  excitation to the  $L_a$  configuration carries most of the oscillator strength, and therefore, the transitions to  $S_1$  and to either  $S_2$  or  $S_3$  are computed to be reasonably intense in the individual snapshots. In an overall assessment of the data in Table 1, it is clear that the lowest three singlet excited states of adenine in water are closely spaced and that their electronic character thus depends strongly on the solvent configuration at each individually optimized snapshot geometry. Hence, sampling over snapshots appears to be necessary to account for solvent fluctuations and to arrive at realistic theoretical predictions.

Experimentally, the absorption band maximum of adenine in aqueous solution is located at 4.77 eV (260 nm) compared with 4.92 eV (252 nm) in the gas phase,<sup>[88,89]</sup> which corresponds to a redshift of 0.15 eV (8 nm). According to OM2/MRCI, the vertical excitation energies of gas-phase adenine are 4.58, 4.66, and 4.97 eV for the  $n\pi^*$ ,  $L_a$ , and  $L_b$  states, respectively, with most of the oscillator strength being carried by the  $L_a$  transition.<sup>[33]</sup> Although there is much mixing in the excited states of adenine in water (see above), the most pronounced  $L_a$  character is found in the  $S_1$  state, which is on average redshifted by about 0.1 eV relative to the gas phase (see Table 1), in qualitative agreement with experiment. By the same token, the  $n\pi^*$  transition is blueshifted by about 0.1–0.3 eV, whereas the changes for the  $L_b$  transition are small. For a more direct comparison with experiment, we have simulated the first absorption band of adenine in the gas phase (QM) and in aqueous solution (QM/MM) by selecting 200 snapshots from ground-state MD runs at 300 K and performing single-point OM2/MRCI calculations for the excitation energies and oscillator strengths of the three lowest singlet excited states, which were then used to generate theoretical spectra following established proce-

**Table 1.** Adenine in water: vertical excitation energies [eV], oscillator strengths, and weights [%] of the leading configurations in the OM2/MRCI wavefunctions of the lowest three singlet excited states for 10 selected snapshots, with oscillator strengths given in parentheses and weights in square brackets.

Snapshot	Excitation	$S_1$	$S_2$	$S_3$
1	$n \rightarrow \pi^*$	4.69 (0.099)	4.77 (0.057)	4.86 (0.157)
	$\pi \rightarrow \pi^* (L_a)$	[34]	[50]	[<1]
	$\pi \rightarrow \pi^* (L_b)$	[30]	[14]	[37]
2	$n \rightarrow \pi^*$	4.56 (0.102)	4.88 (0.055)	4.91 (0.165)
	$\pi \rightarrow \pi^* (L_a)$	[41]	[1]	[37]
	$\pi \rightarrow \pi^* (L_b)$	[37]	[11]	[32]
3	$n \rightarrow \pi^*$	4.58 (0.177)	4.90 (0.165)	4.91 (0.010)
	$\pi \rightarrow \pi^* (L_a)$	[8]	[5]	[62]
	$\pi \rightarrow \pi^* (L_b)$	[49]	[32]	[<1]
4	$n \rightarrow \pi^*$	4.58 (0.178)	4.89 (0.142)	4.91 (0.032)
	$\pi \rightarrow \pi^* (L_a)$	[26]	[38]	[2]
	$\pi \rightarrow \pi^* (L_b)$	[24]	[40]	[<1]
5	$n \rightarrow \pi^*$	4.57 (0.193)	4.87 (0.031)	4.92 (0.142)
	$\pi \rightarrow \pi^* (L_a)$	[8]	[71]	[<1]
	$\pi \rightarrow \pi^* (L_b)$	[50]	[5]	[26]
6	$n \rightarrow \pi^*$	4.61 (0.161)	4.89 (0.164)	4.95 (0.021)
	$\pi \rightarrow \pi^* (L_a)$	[24]	[<1]	[41]
	$\pi \rightarrow \pi^* (L_b)$	[1]	[18]	[62]
7	$n \rightarrow \pi^*$	4.64 (0.079)	4.79 (0.083)	4.89 (0.160)
	$\pi \rightarrow \pi^* (L_a)$	[44]	[34]	[4]
	$\pi \rightarrow \pi^* (L_b)$	[32]	[30]	[6]
8	$n \rightarrow \pi^*$	4.64 (0.079)	4.79 (0.083)	4.89 (0.160)
	$\pi \rightarrow \pi^* (L_a)$	[59]	[16]	[14]
	$\pi \rightarrow \pi^* (L_b)$	[28]	[18]	[36]
9	$n \rightarrow \pi^*$	4.54 (0.164)	4.81 (0.020)	4.89 (0.178)
	$\pi \rightarrow \pi^* (L_a)$	[1]	[34]	[23]
	$\pi \rightarrow \pi^* (L_b)$	[21]	[40]	[21]
10	$n \rightarrow \pi^*$	4.45 (0.236)	4.67 (0.008)	4.89 (0.137)
	$\pi \rightarrow \pi^* (L_a)$	[56]	[22]	[22]
	$\pi \rightarrow \pi^* (L_b)$	[20]	[<1]	[45]
10	$n \rightarrow \pi^*$	4.56 (0.189)	4.88 (0.082)	4.89 (0.088)
	$\pi \rightarrow \pi^* (L_a)$	[8]	[64]	[5]
	$\pi \rightarrow \pi^* (L_b)$	[50]	[15]	[17]

dures.<sup>[90]</sup> This yields band maxima of 4.73 and 4.67 eV in the gas phase and in aqueous solution, that is, 0.19 and 0.10 eV below the experimental values, respectively. The computed redshift of 0.06 eV is in the right direction, but smaller than that observed experimentally (0.15 eV, see above).

A detailed comparison of the present results with previous ab initio calculations<sup>[47,48]</sup> is not possible because the latter disregarded the fluctuations arising from different solvent configurations. However, concerning the ordering of the excited states, there is qualitative agreement: the ab initio calculations also predicted that the  $n\pi^*$  state is the lowest excited singlet state of adenine in the gas phase, but not in water where it is above at least one of the  $\pi\pi^*$  states.<sup>[47,48]</sup>

Geometry optimizations on the  $S_1$  surface were attempted for all 20 snapshots that had been optimized in the ground state. Starting from the corresponding  $S_0$  minima, these opti-

mizations reached an excited-state minimum in five cases (25%). These minima are characterized by moderate ring distortions and out-of-plane displacements of the C4 and C5 atoms (for a typical example see Figure 2, right panel). Compared with the ground state, the C2–N3 and C5–C6 bonds are lengthened by around 0.03 and 0.06 Å, whereas the N3–C4 and C5–N7 bonds are shortened by around 0.01 and 0.04 Å, respectively, in agreement with ab initio results.<sup>[47]</sup> These minima lie 3.6–4.2 eV above the corresponding  $S_0$  minima and 2.2–2.4 eV above the  $S_0$  ground-state energy at these geometries (see Table 2). The computed oscillator strengths for emis-

**Table 2.** Adenine in water: relative energies [eV] of the lowest singlet states at the optimized geometry of the  $S_1$  minimum, for the snapshots where this minimum could be located (see text). For a given snapshot, the energy of the corresponding  $S_0$  minimum is set to zero.

	Snapshot				
	1	2	3	4	5
$S_0$	1.93	1.48	1.40	1.46	1.34
$S_1$	4.18	3.68	3.60	3.87	3.77
$S_2$	5.49	4.93	4.86	4.97	4.75
$S_3$	5.56	5.09	5.21	5.33	5.25

sion are rather low (between 0.026 and 0.031), so that these  $S_1$  minima are best viewed as dark  $n\pi^*$  states. In previous ab initio CASSCF calculations for adenine in water, the lowest  $n\pi^*$  minimum was found 4.31 eV above the  $S_0$  minimum.<sup>[48]</sup> The remaining OM2/MRCI optimizations on the  $S_1$  surface (15 cases, 75%) led to a  $S_0$ – $S_1$  conical intersection with a strong out-of-plane distortion of the amino group (see below).

It was not possible to locate any  $S_2$  minimum by geometry optimizations on the  $S_2$  surface. Starting from the available  $S_0$  minima, all optimizations ended up at an  $S_1$ – $S_2$  conical intersection ( $CI_{12}$ ) very close to the FC region that is characterized by small ring distortions and a slight pyramidalization of the amino group (for a typical example, see Figure 3, left panel). It lies at 4.47–5.17 eV (see Table 3) and has  $n\pi^*/L_o$  character. At

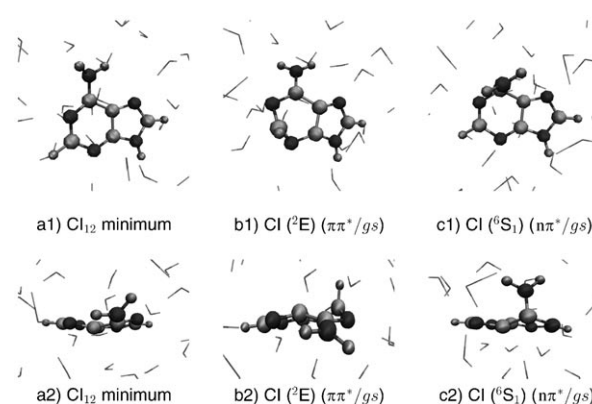


**Figure 3.** Typical molecular geometries of adenine in water at the a)  $CI_{12}$ , b)  ${}^2E$ , and c)  ${}^6S_1$  conical intersections. Upper panel: top view; lower panel: side view.



**Table 3.** Adenine in water: relative energies [eV] of the  $Cl_{12}$  conical intersection for five selected snapshots. In each case, the energy of the corresponding  $S_0$  minimum is set to zero.

	Snapshot				
	1	2	3	4	5
energy [eV]	4.93	4.47	4.89	4.57	5.17

the OM2/MRCI level, there is another  $S_1$ – $S_2$  conical intersection with  $L_a/L_b$  character and small out-of-plane distortions (at C4, C5, and H2), similar to the one identified in a CASSCF study of adenine in water,<sup>[48]</sup> however, this conical intersection plays no role in the deexcitation dynamics (see below).

Consistent with previous ab initio studies,<sup>[48]</sup> two  $S_0$ – $S_1$  conical intersections could be located for each of the snapshots. The first one is of  $L_a/g_s$  character and lies 3.95–4.33 eV above the corresponding  $S_0$  minimum (and hence in each case below the lowest vertical excitation energy at the  $S_0$  minimum). The optimized geometries of this conical intersection are quite similar in all five snapshots. There is a moderate out-of-plane displacement of the C4 and C5 atoms, a small pyramidalization of the amino group, and a strong out-of-plane displacement of the C2 and H2 atoms: the C2–H2 bond is almost perpendicular to the ring, with dihedral angles  $|\chi(N1C2N3C4)|$  ranging from 77.9 to 80.7° and  $|\chi(H2C2N3C4)|$  from 81.5 to 85.9° (see Figure 3 central panel and Table 4). This type of conical intersection has been assigned<sup>[32]</sup> as  ${}^2E$  for adenine in the gas phase according to the Cremer–Pople–Boeyens classification.<sup>[91,92]</sup>

**Table 4.** Adenine in water: relative energies [eV] and characteristic internal coordinates of the  ${}^2E$  conical intersection for 5 selected snapshots. In each case, the energy of the corresponding  $S_0$  minimum is set to zero.

	Snapshot				
	1	2	3	4	5
energy [eV]	4.33	3.95	4.11	3.96	4.12
$\chi(H2-C2-C5)$ [°]	109.6	107.7	106.6	106.2	106.5
$\chi(H2-C2-N3-C4)$ [°]	84.1	81.5	–85.9	82.1	83.1
$\chi(N1-C2-N3-C4)$ [°]	–80.7	–80.1	77.9	–79.1	–78.4

The second  $S_0$ – $S_1$  conical intersection is labeled as  ${}^6S_1$ .<sup>[32]</sup> It is characterized in all snapshots by a pronounced out-of-plane distortion of the C6 atom and the amino group, such that the C6–N6 bond is almost perpendicular to the ring, with dihedral angles  $|\chi(N1C5C6N6)|$  between 123.8 and 129.3° and  $|\chi(C2N1C6N6)|$  between 73.6 and 81.8° (see Figure 3 right panel and Table 5). The OM2/MRCI wavefunction indicates strong configurational mixing at this  ${}^6S_1$  conical intersection, but it is still possible to assign a predominant  $n\pi^*/g_s$  character. The  ${}^6S_1$  energy varies rather strongly (3.38–4.33 eV relative to the ground-state energy of the respective snapshot, see Table 5) such that it lies above the  ${}^2E$  energy in two cases, and below in three cases (see Table 4).

Generally speaking, the types and geometries found for the conical intersections of adenine in water are quite similar to

**Table 5.** Adenine in water: relative energies [eV] and characteristic internal coordinates of the  ${}^6S_1$  conical intersection for 5 selected snapshots. In each case, the energy of the corresponding  $S_0$  minimum is set to zero.

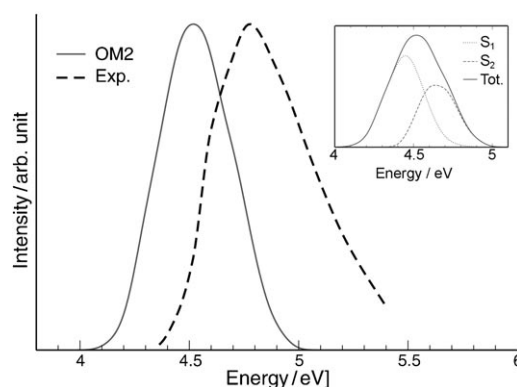
	Snapshot				
	1	2	3	4	5
energy [eV]	4.28	4.26	4.33	3.73	3.38
$\chi(N3-C6-N6)$ [°]	103.4	100.6	101.3	99.0	100.5
$\chi(C2-N1-C6-N6)$ [°]	–81.8	75.1	–78.3	–73.6	75.9
$\chi(N1-C5-C6-N6)$ [°]	125.7	–129.3	127.7	126.1	–123.8

those in the gas phase. This is true not only for comparisons with OM2/MRCI gas-phase results,<sup>[33]</sup> but also with regard to ab initio studies.<sup>[19–22,24–28,31,32]</sup> The qualitative topology of the computed potential-energy surfaces thus seems to be rather robust when going from the gas phase to aqueous solution. On the other hand, the OM2/MRCI relative energies show larger variations that indicate a significant influence of the solvent environment. One common feature for all five snapshots is that the energies of the  ${}^2E$  and  ${}^6S_1$  conical intersections are always below the lowest vertical excitation energy at the  $S_0$  minimum. It is thus energetically possible that they can be quickly reached after vertical excitation, provided that a direct downhill path exists. The geometry optimizations on the  $S_1$  potential-energy surface indicate that this is indeed the case, since they directly accessed the  ${}^6S_1$  conical intersection for most of the snapshots (75%).

## 2.2. Nonadiabatic Dynamics

The selection of the initial configurations for the surface-hopping trajectories was governed by the idea to simulate photoexcitation near the center of the absorption band of solvated adenine (263 nm). The resulting simulated absorption band is shown in Figure 4 and compared with the experimental spectrum.<sup>[42]</sup>

Apart from a redshift of 0.25 eV, the curve calculated at the OM2/MRCI level agrees very well with the experimental one, indicating that the sampling procedure was adequate. The OM2/MRCI calculations show that the absorption band con-

**Figure 4.** Simulated and experimental absorption bands of solvated adenine. The inset shows the contributions of the  $S_1$  and  $S_2$  states to the total absorption band. The experimental data are taken from reference [42].

tains significant contributions from both the  $S_1$  and  $S_2$  states (see inset of Figure 4), which are close in energy and show significant configurational mixing in the FC region. Consequently, initial sampling yields 51 trajectories (57%) starting on the  $S_1$  potential-energy surface and 39 (43%) starting on the  $S_2$  potential-energy surface.

The average occupation of the adiabatic states as a function of time is illustrated in Figure 5. In the early stage of the dynamics, the strong electronic mixing causes an ultrafast  $S_2 \rightarrow S_1$

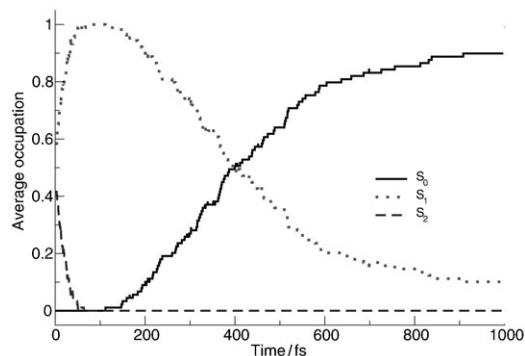


**Figure 5.** Time-dependent average occupation of the low-lying adiabatic states of solvated adenine.

population transfer with a time constant of 40 fs. After 80 fs, no more trajectories are evolving on the  $S_2$  potential-energy surface and the average occupation of the  $S_1$  state reaches its maximum. After around 100 fs, the decay of the  $S_1$  population starts and internal conversion to the  $S_0$  state occurs with a time constant of 410 fs.

Because of the strongly mixed character of the electronic states involved in the nonadiabatic dynamics of solvated adenine, it is difficult to make clear assignments of these processes within the adiabatic representation used in the simulations. Nevertheless, some information about the character of these states and the different decay paths followed can be inferred from an analysis of the  $S_0$ - $S_1$  conical intersections that are accessed during the decay dynamics. These intersections,  ${}^2E$  ( $L_a/g_s$ ) and  ${}^6S_1$  ( $n\pi^*/g_s$ ), are characterized by strong ring puckering at the atoms C2 and C6, which induces large out-of-plane displacements of the H2 atom and the amino group, respectively. They can be easily identified by monitoring the dihedral angles  $|\chi(N1C2N3C4)|$  and  $|\chi(N1C5C6N6)|$ . The values of these two dihedral angles at the hopping points are shown in Figure 6 for all trajectories computed in the gas phase<sup>[33]</sup> and in water.

It is evident from Figure 6 that there are two distinct decay paths. The vast majority of the trajectories (95%) decay to the ground state through the  ${}^6S_1$  conical intersection, indicating that the  $S_1$  state acquires a predominant  $n\pi^*$  character far from the FC (and  $Cl_{12}$ ) region. In a few trajectories (5%), the  $S_1$  state is apparently of  $\pi\pi^*$  character and decays via the  ${}^2E$  conical intersection. We also note that the decay route of a trajectory is independent of whether it started in the  $S_1$  or  $S_2$  state, suggesting that the system leaves the FC (and  $Cl_{12}$ ) region

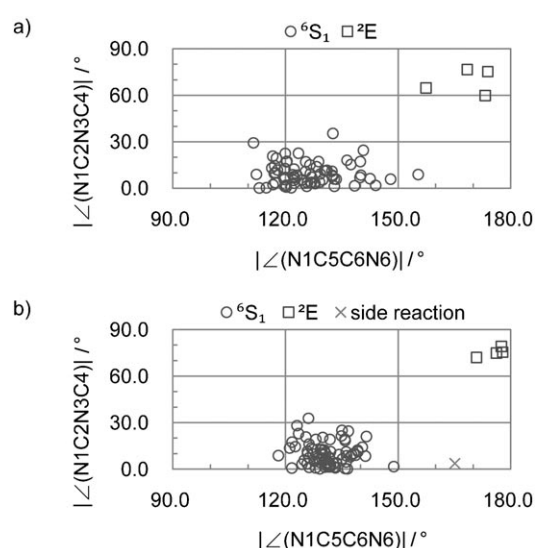


**Figure 6.** Dihedral angles  $|\chi(N1C5C6N6)|$  and  $|\chi(N1C2N3C4)|$  that characterize the  ${}^2E$  and  ${}^6S_1$  conical intersections at the  $S_1 \rightarrow S_0$  hopping events: a) adenine in vacuo;<sup>[33]</sup> b) adenine in water (this work).

with no memory of its previous dynamics, which is lost because of the strong nonadiabatic interactions. A similar observation was also made for adenine and aminopyrimidine in the gas phase.<sup>[33,93]</sup>

Simulation of the nonadiabatic dynamics of solvated adenine yields two decay constants, corresponding to the ultrafast decay of the  $S_2$  state (40 fs) and to the slower decay of the  $S_1$  state (410 fs). The ultrafast decay reflects the strong nonadiabatic coupling experienced by the excited states in the FC region. The  $S_1$  decay time results from two distinct relaxation paths. The main contribution comes from trajectories passing through the  ${}^6S_1$  conical intersection, where hopping occurs from 200 to 600 fs after the beginning of the dynamics. The overall decay time is then slightly reduced by a small contribution from the trajectories that return to the ground state via the  ${}^2E$  conical intersection within 180 fs.

The present QM(OM2/MRCI)/MM surface-hopping results for solvated adenine (1111 MM water molecules) are qualitatively consistent with the QM(TD-DFTB) surface-hopping simulations for microsolvated adenine (16 QM water molecules), which also gives a two-step nonradiative decay involving the ultrafast relaxation of the initially excited  $S_2$  state with a lifetime of 16 fs and the subsequent transition to the ground state within 200 fs.<sup>[70]</sup>

A direct comparison of the experimentally measured decay times with those obtained from our simulations is not straightforward because the surface-hopping calculations have been performed in the adiabatic representation, whereas experiments essentially probe the global decay behavior. Nevertheless, we note that the computed decay time for the  $S_1$  state is consistent with available experimental data.<sup>[38–44,46]</sup> It compares particularly well with the decay constant obtained from recent fluorescence up-conversion experiments, which led to a lifetime of 300–500 fs for excitations around the center of the absorption band of solvated adenine.<sup>[44]</sup> Experimental time con-

stants have not yet been reported for the ultrafast decay of the  $S_2$  state (computed:  $\tau \approx 40$  fs).

### 3. Discussion

#### 3.1. Solvent Effects

In this section, we compare the present results for adenine in water with those obtained previously in the gas phase.<sup>[33]</sup> The optimized ground-state geometry of adenine is completely planar in the gas phase, whereas there is a slight pyramidalization of the amino group in water. For the computed vertical excitation energies, solvation causes a redshift of about 0.1 eV for the  $\pi\pi^*$   $L_a$  state and a blueshift of 0.1–0.3 eV for the  $n\pi^*$  state, in good agreement with CASSCF calculations<sup>[48]</sup> and experimental data.<sup>[88,89]</sup> As a consequence of these shifts, the two lowest excited states of solvated adenine are strongly mixed in the FC region, so that two transitions contribute to the absorption band (see inset of Figure 4). This is in contrast to the gas phase where the absorption band is essentially due to excitations into the  $S_2$  ( $\pi\pi^*$   $L_a$ ) state, according to the OM2/MRCI calculations.<sup>[33]</sup>

In our standard procedure, excited-state geometry optimizations start from an optimized ground-state structure. In the gas phase, this leads to an  $S_1$  ( $n\pi^*$ ) minimum of adenine with rather small ring distortions.<sup>[33]</sup> In water, the optimizations on the  $S_1$  surface either directly reach the  ${}^6S_1$  conical intersection (see above) or yield an  $S_1$  minimum with notable ring distortions at the C4 and C5 atoms. On the other hand, an  $S_2$  minimum cannot be located in this manner, neither in the gas phase nor in water, because geometry optimizations always directly lead to an  $S_1$ – $S_2$  conical intersection of  $n\pi^*/L_a$  character. Finally, there are two  $S_0$ – $S_1$  conical intersections, namely,  ${}^2E$  and  ${}^6S_1$ , that connect the ground state with the  $L_a$  and  $n\pi^*$  states, respectively; these are found both in the gas phase and in water, with very similar structures.

As already mentioned, the OM2/MRCI electronic structure of the two lowest excited states of adenine is different in the gas phase and in aqueous solution, which might also suggest different nonadiabatic dynamics. According to the gas-phase OM2/MRCI results, the initial excitation populates almost exclusively the bright  $S_2$  ( $\pi\pi^*$ ) state and the deexcitation proceeds mainly through a two-step  $\pi\pi^* \rightarrow n\pi^* \rightarrow \text{gs}$  pathway. In water, due to strong mixing, the bright  $L_a$  transition populates both the  $S_1$  and  $S_2$  states with almost the same probability; the  ${}^2E$  and  ${}^6S_1$  conical intersections lie close to each other energetically and one might thus expect that these two decay paths are of similar importance. However, the OM2/MRCI surface-hopping simulations show that this is not the case: the deexcitation dynamics in solution is similar to that in the gas phase, since the  $\pi\pi^* \rightarrow n\pi^* \rightarrow \text{gs}$  decay path is again clearly favored, even more so than in the gas phase.

This can be attributed to the topology of the  $S_1$  surface of adenine in water: inside the FC region, the N6 atom normally has a larger  $S_1$  gradient component perpendicular to the ring than H2, as can be seen from the norm of these gradient components plotted in Figure 7 for all trajectories. The  $S_1$  gradient

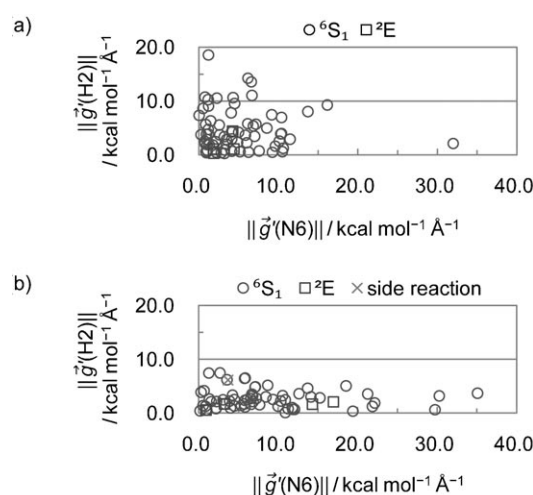


**Figure 7.** Norms of  $S_1$  gradient components perpendicular to the (N1C5C6) and (N1C2N3) planes ( $\|\vec{g}\|$ ) at atoms N6 and H2, respectively, evaluated for each trajectory at the initial FC geometry. a) Adenine in vacuo (ref. [33]) and b) adenine in water (this work).

thus drives adenine towards geometries with an out-of-plane amino group, rather than H2, with diminishing  $\pi\pi^*$  and increasing  $n\pi^*$  character. As a consequence, the approach to the  ${}^6S_1$  ( $n\pi^*/\text{gs}$ ) conical intersection with an out-of-plane amino group is dynamically favored over the out-of-plane motion of the H2 atom that would lead to the  ${}^2E$  ( $\pi\pi^*/\text{gs}$ ) conical intersection. When comparing with the situation in the gas phase (see Figure 7a) it is clear that, in the FC region, adenine has a larger out-of-plane gradient norm at N6 in water and hence a more pronounced tendency for the out-of-plane motion of the amino group towards the dominant  ${}^6S_1$  ( $n\pi^*/\text{gs}$ ) conical intersection. This explains the somewhat faster decay dynamics of adenine in water than in the gas phase. Furthermore, in the FC region, the  $S_1$  gradient at N6 in water generally points towards the side of adenine with the most favorable hydrogen-bonding interactions between N6 and nearby solvent water molecules, and large  $S_1$  gradient norms at N6 tend to be associated with short such hydrogen bonds—at the FC geometry, about 50% of the snapshots have N6...H hydrogen-bonds of 2.1 Å or less. Hence, hydrogen bonding appears to accelerate the decay of adenine in water through the  ${}^6S_1$  ( $n\pi^*/\text{gs}$ ) conical intersection.

We recall in this context that 75% of the geometry optimizations on the  $S_1$  surface reach the  ${}^6S_1$  conical intersection, indicating the existence of a direct path connecting the FC region and this intersection. Figure 8 shows an example for such a path that has been followed during one of the energy minimizations on the  $S_1$  surface. Clearly the availability of such barrierless pathways is consistent with the predominance of trajectories heading towards the  ${}^6S_1$  conical intersection.

#### 3.2. Accuracy Issues

In this section we offer some cautionary comments on the accuracy and reliability of excited-state calculations in general and of our semiempirical OM2/MRCI approach in particular.

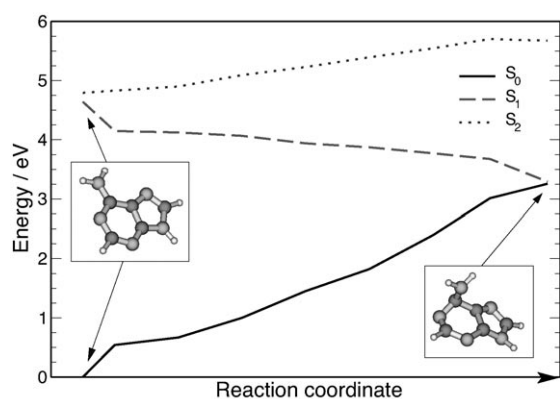


**Figure 8.** Adenine in water: energy profile of the  $S_0$ ,  $S_1$ , and  $S_2$  states along a path connecting the FC region and the  ${}^6S_1$  conical intersection (see text). The reaction coordinate corresponds to the out-of-plane displacement of the amino group.

We have recently performed extensive benchmarks on electronically excited states,<sup>[94–99]</sup> which covered 28 medium-sized organic chromophores and a total of 223 excitations. It is clear from this work that it is extremely difficult, even for rather small molecules, to obtain accurate (converged) ab initio results for electronically excited states. For larger molecules, such as adenine, state-of-the-art ab initio studies usually employ state-averaged CASSCF calculations (with a suitable active space and a moderate basis set) and then include dynamic correlation by perturbation theory (CASPT2) or by an MRCI treatment. The uncertainties of such an approach can be assessed, for example, by comparisons with the theoretical best estimates for vertical excitation energies of 104 singlet excited states that have been derived in our benchmarks.<sup>[94,99]</sup> The corresponding mean absolute deviations (MAD) are very large for the CASSCF results as a result of neglecting dynamic correlation; they are 0.33 eV for CASPT2 results from the literature and 0.10 eV for our own MS-CASPT2/TZVP results (see ref. [94] for detailed data), and an extension of the basis set from TZVP to aug-cc-pVTZ leads to mean absolute changes in the CASPT2 energies of 0.16 eV.<sup>[99]</sup> Given this situation, one can hardly expect an a priori accuracy of better than 0.2 eV in state-of-the-art CASPT2 (or other ab initio) calculations on molecules of the size of adenine. The semiempirical OM2/MRCI approach applied presently is several orders of magnitude faster than CASPT2 and it is thus not surprising that it is generally less accurate, with a MAD value of 0.50 eV in our singlet benchmark set.<sup>[98]</sup> It is thus important to gauge its reliability for any given target molecule. This was done in our initial investigation on the excited-state dynamics of gas-phase adenine<sup>[33]</sup> by demonstrating that the OM2/MRCI excitation energies and optimized geometries were in reasonable agreement with those from the high-level calculations then available.

To update these comparisons,<sup>[33]</sup> we now consider the results from three recent ab initio studies of gas-phase adenine,<sup>[32,35,36]</sup> which report geometry optimizations and reaction path calculations performed at the following levels: CASPT2//CASSCF-(16,12)/6-31G\*,<sup>[32]</sup> CASPT2//CASSCF(16,12)/6-31 + G\*,<sup>[35]</sup> and

MRCI//CASSCF(8,8)/6-31 + G\*.<sup>[36]</sup> These studies (as well as previous ones and OM2/MRCI) agree on some general qualitative features, for example, the presence of three closely spaced excited states around 5 eV ( $n\pi^*$ ,  $\pi\pi^*$   $L_a$ , and  $\pi\pi^*$   $L_b$ ), the existence of several competing nonradiative decay channels, and the type of distorted geometries at the corresponding conical intersections, especially for the low-energy  ${}^6S_1$  and  ${}^2E$  species. However, there are significant differences in the computed energies and consequently also in the favored decay mechanisms. For example, relative to the ground-state  $S_0$  minimum, the  ${}^6S_1$  conical intersection is reported at 4.33,<sup>[32]</sup> 4.86,<sup>[35]</sup> and 3.74 eV,<sup>[36]</sup> covering a wide range of more than 1 eV (OM2/MRCI: 4.08 eV). Likewise, the  ${}^2E$  conical intersection is located at 3.98<sup>[32]</sup> and 3.50 eV<sup>[36]</sup> (OM2/MRCI: 4.11 eV, not reported in ref. [35]). Ab initio MRCIS excited-state dynamics simulations indicate a two-step nonadiabatic relaxation in gas-phase adenine consisting of an ultrashort deactivation to  $S_1$  and a longer subpicosecond exponential decay to the  $S_0$  ground state,<sup>[32]</sup> fairly analogous to the OM2/MRCI excited-state dynamics<sup>[33]</sup> except that the second step mainly proceeds by the  ${}^2E$  channel (MRCIS) rather than the  ${}^6S_1$  channel (OM2/MRCI). One of the recent ab initio pathway calculations<sup>[36]</sup> arrives at a similar mechanistic scenario with several participating excited states, whereas another one<sup>[35]</sup> proposes a different interpretation of the observed biexponential decay that involves only the bright  $L_a$  state, with ultrafast initial relaxation to an energy plateau followed by a slower direct conversion to the ground state. Furthermore, the computed energy profiles along linearly interpolated internal coordinate (LIIC) pathways between the initially generated FC geometry and the relevant conical intersections differ in that some are barrierless (as in OM2/MRCI), while others are associated with small or sizable barriers. For example, in their comprehensive CASPT2 study of conical intersections, Barbatti and Lischka find a “practically barrierless” LIIC path to the  ${}^2E$  conical intersection, and the same applies to the  ${}^6S_1$  channel (see their Figure 3).<sup>[32]</sup> Hassan et al. report a two-step  $n\pi^*$  pathway with an ultrafast conversion from the initially populated  $L_a$  to the  $n\pi^*$  state and a subsequent “downhill” LIIC path on the  $n\pi^*$  surface to the  ${}^6S_1$  conical intersection, while the direct  $\pi\pi^*$  pathway goes through a minimum and then over a transition state (with a barrier of 0.21 eV) on the route toward the  ${}^2E$  conical intersection.<sup>[36]</sup> In contrast, Conti et al.<sup>[35]</sup> located the  ${}^6S_1$  conical intersection at a much higher energy (0.42 eV above the  $n\pi^*$  minimum) than the two other recent ab initio studies,<sup>[32,36]</sup> and therefore, they ruled out the  ${}^6S_1$  channel and favored the direct  $\pi\pi^*$  pathway. Generally speaking, it is clear that the topology of the underlying potential-energy surfaces will largely govern the excited-state dynamics, and thus, also the preferred nonadiabatic decay mechanisms. In this sense, one should generally view the results from dynamics simulations with some caution, be it in the gas phase<sup>[32–34]</sup> or in solution (this work), while recognizing that they offer much more detailed insight into photoinduced processes than static explorations of potential-energy surfaces.

In summary, it seems fair to state that the best available ab initio studies on gas-phase adenine agree on general qualitative features of the excited-state potential-energy surfaces, but



there are still substantial discrepancies with regard to quantitative aspects and the characterization of the decay mechanisms. Our OM2/MRCI results are generally within the range of the published ab initio results; they are more consistent with some of them than with others. Given this situation, it seems justified to exploit the computational efficiency of OM2/MRCI for investigating the excited-state dynamics of adenine. This allows us to perform an extensive sampling of phase space by running many trajectories with sufficiently long simulation times, so that dynamical aspects are well treated, both at the QM and QM/MM levels. OM2/MRCI simulations are thus expected to be realistic enough to provide useful insight into the effects of the environment.

#### 4. Conclusions

We have reported a QM/MM study of the nonadiabatic dynamics of adenine in aqueous solution, with the QM part (adenine) treated at the OM2/MRCI level and the MM part (solvent) described by the TIP3P water model. For a number of snapshots from an initial ground-state MD simulation, the relevant potential-energy surfaces were characterized by locating energy minima and conical intersections. The optimized geometries turned out to be quite similar to those in the gas phase, especially in the case of the conical intersections, whereas the relative energies showed larger fluctuations that reflect different arrangements of the solvent molecules around the adenine.

Due to the strong vibronic coupling in the FC region, both the  $S_1$  and  $S_2$  states could be populated by photoexcitation. Surface-hopping QM/MM dynamics simulations predicted an ultrafast  $S_2$ - $S_1$  decay with a time constant of less than 40 fs, whereas the  $S_1$ - $S_0$  conversion to the ground state was computed to be somewhat slower, with a time constant of 410 fs that agreed well with the available experimental data. Most trajectories (>90%) returned to the ground state via the  ${}^6S_1$  ( $n\pi^*/gs$ ) conical intersection, while only a few (<10%) passed through the  ${}^2E$  ( $\pi\pi^*/gs$ ) conical intersection. The topology of the  $S_1$  surface favored paths leading towards  ${}^6S_1$  because the necessary out-of-plane motion of the amino group was induced by large corresponding  $S_1$  gradient components in the FC region. These out-of-plane gradient components generally tended to be larger for adenine in water than in vacuo, which led to faster  $S_1$  decay in water. Overall, however, the nonadiabatic dynamics of adenine was found to be similar in the gas phase and in water, with regard to the crucial conical intersections and the dominant relaxation paths, irrespective of the solvent-induced changes in the electronic structure of the two lowest singlet excited states.

We believe that the present surface-hopping QM/MM approach provides a realistic description of the photoinduced nonradiative relaxation of adenine in aqueous solution. The use of the semiempirical OM2/GUGA-CI method for the QM part was essential to make this study feasible in terms of computational costs, considering that around 100 trajectories (6000 time steps each) had to be calculated for each snapshot. Clearly, this efficient approach can also be employed in analogous surface-hopping studies of other complex systems, for

example, DNA bases in a biological environment. Applications of this kind are in progress.

#### Acknowledgements

We thank Dr. M. Barbatti and Dr. T. W. Keal for helpful discussions. This work was supported by the Deutsche Forschungsgemeinschaft (SFB 663, project C4). Partial funding was also provided by the ERC-Starting Grant FP7-Project, DEDOM, Grant agreement no. 207441.

**Keywords:** adenine • computational chemistry • gas-phase reactions • photochemistry • semiempirical calculations

- [1] P. R. Callis, *Annu. Rev. Phys. Chem.* **1983**, *34*, 329–357.
- [2] C. E. Crespo-Hernández, B. Cohen, P. M. Hare, B. Kohler, *Chem. Rev.* **2004**, *104*, 1977–2020.
- [3] H. Saigusa, *J. Photochem. Photobiol. C* **2006**, *7*, 197–210.
- [4] M. K. Shukla, J. Leszczynski, *J. Biomol. Struct. Dyn.* **2007**, *25*, 93–118.
- [5] C. T. Middleton, K. de La Harpe, C. Su, Y. K. Law, C. E. Crespo-Hernández, B. Kohler, *Annu. Rev. Phys. Chem.* **2009**, *60*, 217–239.
- [6] N. J. Kim, G. Jeong, Y. S. Kim, J. Sung, S. K. Kim, Y. D. Park, *J. Chem. Phys.* **2000**, *113*, 10051–10055.
- [7] H. Kang, K. T. Lee, B. Jung, Y. J. Ko, S. K. Kim, *J. Am. Chem. Soc.* **2002**, *124*, 12958–12959.
- [8] H. Kang, B. Jung, S. K. Kim, *J. Chem. Phys.* **2003**, *118*, 6717–6719.
- [9] I. Hünig, C. Plützer, K. A. Seefeld, D. Löwenich, M. Nispel, K. Kleiner-manns, *ChemPhysChem* **2004**, *5*, 1427–1431.
- [10] S. Ullrich, T. Schultz, M. Z. Zgierski, A. Stolow, *J. Am. Chem. Soc.* **2004**, *126*, 2262–2263.
- [11] S. Ullrich, T. Schultz, M. Z. Zgierski, A. Stolow, *Phys. Chem. Chem. Phys.* **2004**, *6*, 2796–2801.
- [12] M. Zierhut, W. Roth, I. Fischer, *Phys. Chem. Chem. Phys.* **2004**, *6*, 5178–5183.
- [13] C. Canuel, M. Mons, F. Piuze, B. Tardivel, I. Dimicoli, M. Elhanine, *J. Chem. Phys.* **2005**, *122*, 074316.
- [14] H. Satzger, D. Townsend, M. Z. Zgierski, S. Patchkovskii, S. Ullrich, A. Stolow, *Proc. Natl. Acad. Sci. USA* **2006**, *103*, 10196–10201.
- [15] M. G. D. Nix, A. L. Devine, B. Cronin, M. N. R. Ashfold, *J. Chem. Phys.* **2007**, *126*, 124312.
- [16] C. Z. Bisgaard, H. Satzger, S. Ullrich, A. Stolow, *ChemPhysChem* **2009**, *10*, 101–110.
- [17] B. O. R. M. P. Fülcher, L. Serrano-Andrés, *J. Am. Chem. Soc.* **1997**, *119*, 6168–6176.
- [18] A. L. Sobolewski, W. Domcke, C. Dedonder-Lardeux, C. Jouvet, *Phys. Chem. Chem. Phys.* **2002**, *4*, 1093–1100.
- [19] C. M. Marian, *J. Chem. Phys.* **2005**, *122*, 104314.
- [20] S. Perun, A. L. Sobolewski, W. Domcke, *J. Am. Chem. Soc.* **2005**, *127*, 6257–6265.
- [21] S. Perun, A. L. Sobolewski, W. Domcke, *Chem. Phys.* **2005**, *313*, 107–112.
- [22] H. Chen, S. Li, *J. Phys. Chem. A* **2005**, *109*, 8443–8446.
- [23] H.-H. Ritze, H. Lippert, E. Samoylova, V. R. Smith, I. V. Hertel, W. Radloff, T. Schultz, *J. Chem. Phys.* **2005**, *122*, 224320.
- [24] M. Z. Zgierski, S. Patchkovskii, T. Fujiwara, E. C. Lim, *J. Phys. Chem. A* **2005**, *109*, 9384–9387.
- [25] M. Z. Zgierski, S. Patchkovskii, E. C. Lim, *J. Chem. Phys.* **2005**, *123*, 081101.
- [26] S. Brønsted Nielsen, T. I. Sølling, *ChemPhysChem* **2005**, *6*, 1276–1281.
- [27] L. Blancafort, *J. Am. Chem. Soc.* **2006**, *128*, 210–219.
- [28] L. Serrano-Andrés, M. Merchán, A. C. Borin, *Proc. Natl. Acad. Sci. USA* **2006**, *103*, 8691–8696.
- [29] L. Serrano-Andrés, M. Merchán, A. C. Borin, *Chem. Eur. J.* **2006**, *12*, 6559–6571.
- [30] W. Credo Chung, Z. Lan, Y. Ohtsuki, N. Shimakura, W. Domcke, Y. Fujimura, *Phys. Chem. Chem. Phys.* **2007**, *9*, 2075–2084.

- [31] M. Z. Zgierski, T. Fujiwara, E. C. Lim, *Chem. Phys. Lett.* **2008**, *463*, 289–299.
- [32] M. Barbatti, H. Lischka, *J. Am. Chem. Soc.* **2008**, *130*, 6831–6839.
- [33] E. Fabiano, W. Thiel, *J. Phys. Chem. A* **2008**, *112*, 6859–6863.
- [34] Y. Lei, S. Yuan, Y. Dou, Y. Wang, Z. Wen, *J. Phys. Chem. A* **2008**, *112*, 8497–8504.
- [35] I. Conti, M. Garavelli, G. Orlandi, *J. Am. Chem. Soc.* **2009**, *131*, 16108–16118.
- [36] W. H. I. Hassan, W. C. Chung, N. Shimakura, S. Koseki, H. Kono, Y. Fujimura, *Phys. Chem. Chem. Phys.* **2010**, *12*, 5317–5328.
- [37] A. N. Alexandrova, J. C. Tully, G. Granucci, *J. Phys. Chem. B* **2010**, *114*, 12116–12128.
- [38] J.-M. L. Pecourt, J. Peon, B. Kohler, *J. Am. Chem. Soc.* **2000**, *122*, 9348–9349.
- [39] J.-M. L. Pecourt, J. Peon, B. Kohler, *J. Am. Chem. Soc.* **2001**, *123*, 5166.
- [40] J.-M. L. Pecourt, J. Peon, B. Kohler, *J. Am. Chem. Soc.* **2001**, *123*, 10370–10378.
- [41] T. Gustavsson, A. Sharonov, D. Onidas, D. Markovitsi, *Chem. Phys. Lett.* **2002**, *356*, 49–54.
- [42] B. Cohen, P. M. Hare, B. Kohler, *J. Am. Chem. Soc.* **2003**, *125*, 13594–13601.
- [43] B. Cohen, C. E. Crespo-Hernández, B. Kohler, *Faraday Discuss.* **2004**, *127*, 137–147.
- [44] T. Pancur, N. K. Schwalb, F. Renth, F. Temps, *Chem. Phys.* **2005**, *313*, 199–212.
- [45] T. Gustavsson, N. Sarkar, E. Lazzarotto, D. Markovitsi, R. Improta, *Chem. Phys. Lett.* **2006**, *429*, 551–557.
- [46] C. T. Middleton, B. Cohen, B. Kohler, *J. Phys. Chem. A* **2007**, *111*, 10460–10467.
- [47] B. Mennucci, A. Toniolo, J. Tomasi, *J. Phys. Chem. A* **2001**, *105*, 4749–4757.
- [48] S. Yamazaki, Kato, *J. Am. Chem. Soc.* **2007**, *129*, 2901–2909.
- [49] V. Ludwig, Z. M. da Costa, M. S. do Amaral, A. C. Borin, S. Canuto, L. Serano-Andrés, *Chem. Phys. Lett.* **2010**, *492*, 164–169.
- [50] M. Cossi, V. Barone, *J. Chem. Phys.* **2001**, *115*, 4708–4717.
- [51] R. Cammi, S. Corni, B. Mennucci, J. Tomasi, *J. Chem. Phys.* **2005**, *122*, 104513.
- [52] S. Corni, R. Cammi, B. Mennucci, J. Tomasi, *J. Chem. Phys.* **2005**, *123*, 134512.
- [53] R. Improta, V. Barone, G. Scalmani, M. J. Frisch, *J. Chem. Phys.* **2006**, *125*, 054103.
- [54] R. Improta, G. Scalmani, M. J. Frisch, V. Barone, *J. Chem. Phys.* **2007**, *127*, 074504.
- [55] A. Klamt, *J. Phys. Chem.* **1996**, *100*, 3349–3353.
- [56] S. A. do Monte, T. Müller, M. Dallos, H. Lischka, M. Diedenhofen, A. Klamt, *Theor. Chem. Acc.* **2004**, *111*, 78–89.
- [57] H. M. Senn, W. Thiel, *Top. Curr. Chem.* **2007**, *268*, 173–290.
- [58] H. M. Senn, W. Thiel, *Angew. Chem.* **2009**, *121*, 1220–1254; *Angew. Chem. Int. Ed.* **2009**, *48*, 1198–1229.
- [59] P. Cattaneo, M. Persico, A. Tani, *Chem. Phys.* **1999**, *246*, 315.
- [60] S. Inglese, G. Granucci, T. Laino, M. Persico, *J. Phys. Chem. B* **2005**, *109*, 7941–7947.
- [61] G. Groenhof, L. V. Schäfer, M. Boggio-Pasqua, M. Goette, H. Grubmüller, M. A. Robb, *J. Am. Chem. Soc.* **2007**, *129*, 6812–6819.
- [62] L. M. Frutos, T. Andrzejewski, F. Santoro, N. Ferré, M. Olivucci, *Proc. Natl. Acad. Sci. USA* **2007**, *104*, 7764–7769.
- [63] G. Groenhof, L. V. Schäfer, M. Boggio-Pasqua, H. Grubmüller, M. A. Robb, *J. Am. Chem. Soc.* **2008**, *130*, 3250–3251.
- [64] M. Persico, G. Granucci, S. Inglese, T. Laino, A. Toniolo, *THEOCHEM* **2003**, *621*, 119–126.
- [65] A. Toniolo, C. Ciminelli, G. Granucci, T. Laino, M. Persico, *Theor. Chem. Acc.* **2004**, *93*, 270–279.
- [66] C. Ciminelli, G. Granucci, M. Persico, *J. Chem. Phys.* **2005**, *123*, 174317.
- [67] M. Persico, G. Granucci in *Continuum Solvation Models in Chemical Physics: From Theory to Applications* (Eds.: R. Cammi, B. Mennucci), Wiley, New York, **2007**, pp. 450–470.
- [68] C. Ciminelli, G. Granucci, M. Persico, *Chem. Phys.* **2008**, *349*, 325–333.
- [69] M. Böckmann, N. L. Doltsinis, D. Marx, *J. Phys. Chem. A* **2010**, *114*, 745–754.
- [70] R. Mitrić, U. Werner, M. Wohlgemuth, G. Seifert, V. Bonačić-Koutecký, *J. Phys. Chem. A* **2009**, *113*, 12700–12705.
- [71] W. Weber, Ph.D. thesis, Universität Zürich (Switzerland), **1996**.
- [72] W. Weber, W. Thiel, *Theor. Chem. Acc.* **2000**, *103*, 495–506.
- [73] A. Koslowski, M. E. Beck, W. Thiel, *J. Comput. Chem.* **2003**, *24*, 714–726.
- [74] S. Patchkovskii, A. Koslowski, W. Thiel, *Theor. Chem. Acc.* **2005**, *114*, 84–89.
- [75] T. W. Keal, A. Koslowski, W. Thiel, *Theor. Chem. Acc.* **2007**, *118*, 837–844.
- [76] Z. Lan, E. Fabiano, W. Thiel, *J. Phys. Chem. B* **2009**, *113*, 3548–3555.
- [77] Z. Lan, E. Fabiano, W. Thiel, *ChemPhysChem* **2009**, *10*, 1225–1229.
- [78] W. L. Jorgensen, J. Chandrasekhar, J. D. Madura, R. W. Impey, M. L. Klein, *J. Chem. Phys.* **1983**, *79*, 926–935.
- [79] B. R. Brooks, R. E. Bruccoleri, B. D. Olafson, D. J. States, S. Swaminathan, M. Karplus, *J. Comput. Chem.* **1983**, *4*, 187–217.
- [80] P. Sherwood, A. H. de Vries, M. F. Guest, G. Schreckenbach, C. R. A. Catlow, S. A. French, A. A. Sokol, S. T. Bromley, W. Thiel, A. J. Turner, S. Billeter, F. Terstegen, S. Thiel, J. Kendrick, S. C. Rogers, J. Casci, M. Watson, F. King, E. Karlsen, M. Sjøvoll, A. Fahmi, *THEOCHEM* **2003**, *632*, 1–32.
- [81] <http://www.chemshell.org>.
- [82] MNDO Program (Version 6.1), W. Thiel, Max-Planck-Institut für Kohlenforschung, Mülheim an der Ruhr, Germany, **2007**.
- [83] J. Kästner, J. M. Carr, T. W. Keal, W. Thiel, A. Wander, P. Sherwood, *J. Phys. Chem. A* **2009**, *113*, 11856–11865.
- [84] J. C. Tully, *J. Chem. Phys.* **1990**, *93*, 1061–1071.
- [85] S. Hammes-Schiffer, J. C. Tully, *J. Chem. Phys.* **1994**, *101*, 4657–4667.
- [86] E. Fabiano, T. W. Keal, W. Thiel, *Chem. Phys.* **2008**, *349*, 334–347.
- [87] M. Barbatti, G. Granucci, M. Persico, M. Ruckebauer, M. Vazdar, M. Eckert-Maksić, H. Lischka, *J. Photochem. Photobiol. A* **2007**, *190*, 228–240.
- [88] L. B. Clark, G. G. Peschel, I. Tinoco, Jr., *J. Phys. Chem.* **1965**, *69*, 3615–3618.
- [89] D. Voet, W. B. Gratzner, R. A. Cox, P. Doty, *Biopolymers* **1963**, *1*, 193–208.
- [90] M. Parac, M. Doerr, C. M. Marian, W. Thiel, *J. Comput. Chem.* **2010**, *31*, 90–106.
- [91] D. Cremer, J. A. Pople, *J. Am. Chem. Soc.* **1975**, *97*, 1354–1358.
- [92] J. C. A. Boeyens, *J. Cryst. Mol. Struct.* **1978**, *8*, 317–320.
- [93] M. Barbatti, H. Lischka, *J. Phys. Chem. A* **2007**, *111*, 2852–2858.
- [94] M. Schreiber, M. R. Silva-Junior, S. P. A. Sauer, W. Thiel, *J. Chem. Phys.* **2008**, *128*, 134110.
- [95] M. R. Silva-Junior, M. Schreiber, S. P. A. Sauer, W. Thiel, *J. Chem. Phys.* **2008**, *129*, 104103.
- [96] S. P. A. Sauer, M. Schreiber, M. R. Silva-Junior, W. Thiel, *J. Chem. Theory Comput.* **2009**, *5*, 555–564.
- [97] M. R. Silva-Junior, S. P. A. Sauer, M. Schreiber, W. Thiel, *Mol. Phys.* **2010**, *108*, 453–465.
- [98] M. R. Silva-Junior, W. Thiel, *J. Chem. Theory Comput.* **2010**, *6*, 1546–1564.
- [99] M. R. Silva-Junior, M. Schreiber, S. P. A. Sauer, W. Thiel, *J. Chem. Phys.* **2010**, *133*, 174318.

Received: December 17, 2010

Revised: April 8, 2011

Published online on June 14, 2011

paper (3)

***Hydrogen Bonding Regulates the Monomeric  
Nonradiative Decay of Adenine in DNA Strands***

Y. Lu, Z. Lan, and W. Thiel

*Angew. Chem.* **2011**, *123*, 6996-6999;

*Angew. Chem. Int. Ed.* **2011**, *50*, 6864-6867.



# Hydrogen Bonding Regulates the Monomeric Nonradiative Decay of Adenine in DNA Strands\*\*

You Lu, Zhenggang Lan,\* and Walter Thiel\*

It has been suggested in ultrafast spectroscopic studies that excited states localized on single nucleobases as well as delocalized exciton or excimer/exciple states contribute towards the nonradiative decay of DNA helices.<sup>[1–11]</sup> Unlike the situation in the gas phase and in water, where the internal conversions through conical intersections (CIs) are reasonably well understood,<sup>[12,13]</sup> little is known about the decay mechanisms of single nucleobases in DNA. Experimentally, it is difficult to identify the different decay channels,<sup>[9]</sup> and the excited-state decay of DNA model systems is extremely complex, being wavelength dependent and showing multi-exponential behavior, with time constants ranging from the sub-ps regime to 100 ps and beyond.<sup>[2–11,14,15]</sup> There are several recent computational studies on this topic,<sup>[1,16–26]</sup> but one central question is still unanswered: how is the mechanism of radiationless decay on an individual nucleobase affected by the biological environment of DNA?

Herein, we study the nonradiative decay dynamics of a single adenine embedded within solvated oligonucleotides by QM/MM<sup>[27,28]</sup> calculations. The dynamics were simulated in silico by on-the-fly surface-hopping calculations.<sup>[29,30]</sup> To mimic DNA single and double strands, two B-type oligomer models (dA)<sub>10</sub> and (dA)<sub>10</sub>·(dT)<sub>10</sub> were constructed by using Maestro 7.5.<sup>[31]</sup> They were solvated in spherical water droplets described by the TIP3P model.<sup>[32]</sup> The DNA charges were neutralized with Na<sup>+</sup> ions using SYBYL 8.0.<sup>[33]</sup> For either model, the QM region contained 14 atoms from an adenine located near the center of the system, while the MM region consisted of all remaining atoms.

After setting up the models, QM/MM simulations were carried out using a development version of the ChemShell package.<sup>[34–36]</sup> The QM subsystem (QM adenine) was treated by the OM2/MRCI approach<sup>[37–40]</sup> (semiempirical orthogonalization model 2 combined with multireference configuration interaction) using a (12,10) active space (12 electrons in 10 orbitals).<sup>[41,42]</sup> The MM part was handled by the DL\_POLY package<sup>[43]</sup> applying the CHARMM27 force field.<sup>[44]</sup> Born–Oppenheimer molecular dynamics (BOMD) simulations at

300 K were performed for both oligonucleotides in their electronic ground state, for initial sampling and for computing electronic absorption spectra. Thereafter, surface-hopping simulations involving the three lowest adiabatic states (S<sub>0</sub>, S<sub>1</sub>, and S<sub>2</sub>) were run up to 1.5 ps. Details of the computational procedures are given in the Supporting Information.

The choice of the computational model (a single QM adenine in an MM environment) restricts the present study to monomeric excitation and decay processes. Hence we do not consider excitons (delocalized over stacked bases)<sup>[2–5,11,16,17,45]</sup> or excimer/exciple states,<sup>[6–13]</sup> nor do we treat electron- or proton-transfer processes among hydrogen-bonded nucleobases,<sup>[19,46–49]</sup> in spite of their important role in DNA. Another limitation is the use of a semiempirical QM/MM approach, which is dictated by the need for computational efficiency<sup>[36]</sup> and limits the accuracy that can be attained. OM2/MRCI has recently been applied successfully to study the excited-state dynamics of nucleobases,<sup>[41,42,50,51]</sup> and we refer the readers to the work on adenine in the gas phase<sup>[41]</sup> and in aqueous solution<sup>[42]</sup> for a detailed discussion of accuracy issues, including comparisons with high-level ab initio results for gas-phase adenine. On this basis the current QM/MM approach is expected to provide realistic results, especially with regard to the influence of the environment on the photophysics of adenine.

Figure 1 shows the Gaussian-broadened absorption bands relevant to the three lowest-lying excited states (S<sub>1</sub>, S<sub>2</sub>, and S<sub>3</sub>) of adenine in (dA)<sub>10</sub> and (dA)<sub>10</sub>·(dT)<sub>10</sub>. The S<sub>1</sub> state is found to be bright in the both helices. The absorption maximum occurs at 4.71 eV for adenine in (dA)<sub>10</sub>, somewhat lower than the experimental value<sup>[20]</sup> of 4.82 eV for (dA)<sub>20</sub>. Analogous results are found for (dA)<sub>10</sub>·(dT)<sub>10</sub> whose calculated absorption maximum is at 4.78 eV, again close to or slightly lower than the experimental values of 4.78 eV for (dA)<sub>20</sub>·(dT)<sub>20</sub> and

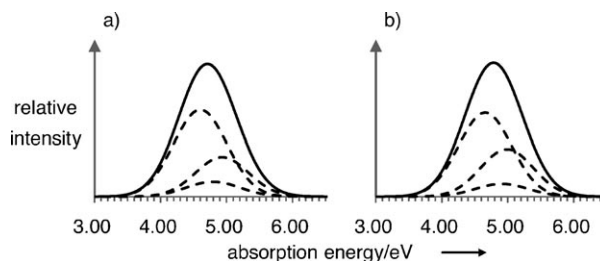


**Figure 1.** Absorption spectrum calculated by the QM/MM (QM = OM2/MRCI) approach for 200 snapshots from ground-state BOMD simulations (with Gaussian broadening). a) (dA)<sub>10</sub>, maximum at 4.71 eV; b) (dA)<sub>10</sub>·(dT)<sub>10</sub>, maximum at 4.78 eV. The overall bands (solid) can be decomposed into contributions from the three lowest-energy transitions (shown as dashed lines).

[\*] Y. Lu, Dr. Z. Lan, Prof. Dr. W. Thiel  
Max-Planck-Institut für Kohlenforschung  
Kaiser-Wilhelm-Platz 1, 45470 Mülheim an der Ruhr (Germany)  
Fax: (+49) 208-306-2996  
E-mail: lan@mpi-muelheim.mpg.de  
thiel@mpi-muelheim.mpg.de

[\*\*] We are grateful to Dr. Mario Barbatti and Dr. Eduardo Fabiano for valuable discussions and to Dr. Tell Tuttle for his help in setting up the QM/MM calculations.

Supporting information for this article is available on the WWW under <http://dx.doi.org/10.1002/anie.201008146>.

4.84 eV for  $(dA)_n \cdot (dT)_n$ .<sup>[17,45]</sup> The current QM/MM computations thus tend to underestimate the first absorption maximum in DNA strands by up to 0.11 eV, in analogy to the situation in the gas phase (0.19 eV) and in aqueous solution (0.10 eV).<sup>[41,42]</sup> We note in this context that Frenkel excitons (not covered presently) should cause a blue shift of the absorption compared with the monomers.<sup>[1,16,17,21,45]</sup>

During the initial BOMD ground-state sampling, the  $S_1$  and  $S_2$  states are populated according to their oscillator strengths. This leads to a minority of trajectories [12% for adenine in  $(dA)_{10}$  and 19% in  $(dA)_{10} \cdot (dT)_{10}$ ] that start from the  $S_2$  state. For these trajectories, the  $S_2 \rightarrow S_1$  decay takes place extremely rapidly (mean lifetime ca. 7 fs, see Figure 2),

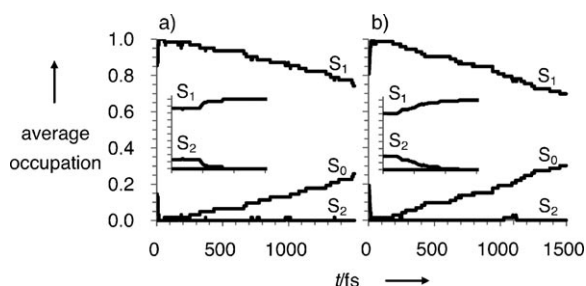


**Figure 2.** Average occupations of adenine. a)  $(dA)_{10}$ , 64 trajectories starting from  $S_1$  and 9 from  $S_2$ ; b)  $(dA)_{10} \cdot (dT)_{10}$ , 59 trajectories starting from  $S_1$  and 14 from  $S_2$ . Dynamics within the initial 30 fs are shown in the insets.

distinctly faster than in the gas phase or in water.<sup>[41,42]</sup> Thereafter, the  $S_1$  state undergoes nonradiative decay through the  $S_0/S_1$  CIs on the timescale of several picoseconds. Exponential fitting gives mean  $S_1$  lifetimes of 5.7 ps and 4.1 ps for adenine in  $(dA)_{10}$  and  $(dA)_{10} \cdot (dT)_{10}$ , respectively.

Compared with the results in the gas phase and in water,<sup>[41,42]</sup> the decay dynamics of an individual adenine is thus slowed down (by an order of magnitude) when it is embedded in DNA helices. Several factors are responsible for this deceleration. First, the biological environment in DNA lowers the interstate coupling and thus reduces the electronic hopping probability (see the Supporting Information). Second, the  $S_0/S_1$  CIs are generally characterized by strong out-of-plane distortions (see below), and the motion towards such a CI is impeded for steric reasons since it brings the bending atom or functional group close to the adjacent nucleobase. Finally, there is another  $S_1$  minimum of adenine close to the dominant  $S_0/S_1$  CI, which is more pronounced in DNA than in the gas phase and may thus further delay the hopping by acting as a trap for the trajectories (see the Supporting Information). Experimental studies<sup>[2–11,14,15]</sup> have reported time constants from multi-exponential fits of spectroscopic data in DNA base multimers that typically cluster in three ranges (0.2–0.6 ps, 2–6 ps, and 100–200 ps), which have been associated with monomeric/internal conversion,<sup>[2–11]</sup> vibrational cooling<sup>[6,11]</sup> or exciton/excimer processes,<sup>[7–11]</sup> and the decay of delocalized states,<sup>[2–11,15]</sup> respectively. The current calculations indicate monomeric decay in the low ps range. This suggests that in this range monomeric nonradiative processes may also contribute to the experi-

mentally observed decay in DNA strands,<sup>[2–11,14,15]</sup> without ruling out other decay channels in the complex electrostatic and steric environment of DNA.<sup>[6,7,52–54]</sup>

In spite of the fact that the computed time constants for the  $S_1 \rightarrow S_0$  nonradiative decay of adenine are similar in DNA single and double strands, the decay channels are found to be quite different. Considering the  $(dA)_{10}$  single strand first, 19 of a total of 73 trajectories (26%) hop to the  $S_0$  surface within 1.5 ps. In 11 of these, the dihedral angle  $|\angle(N_1C_5C_6N_6)|$  (Figure 3d) is less than  $145^\circ$  at the  $S_1 \rightarrow S_0$  hopping events

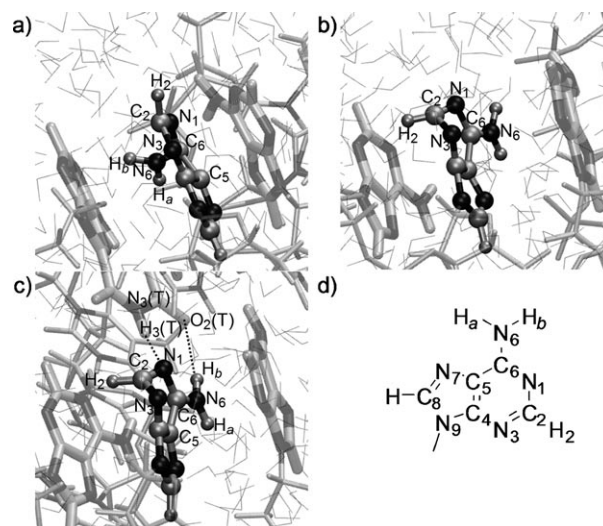


**Figure 3.** Typical structures at conical intersections of adenine: a)  ${}^6S_1$  channel in  $(dA)_{10}$ ; b)  ${}^2E$  channel in  $(dA)_{10}$ ; c)  ${}^2E$  channel in  $(dA)_{10} \cdot (dT)_{10}$ ; d) chemical structure of adenine. In these VMD<sup>[66]</sup> pictures, the QM adenines are drawn as ball-and-stick representations, and the adjacent bases are drawn as bold-licorice representations. The A–T hydrogen bonds are highlighted in (c).

(Figure 4a), indicating a decay via the  $S_0/S_1$  CI that is characterized by an out-of-plane deformation of the amino group and a ring puckering at the  $C_6$  atom (Figure 3a).<sup>[55–58]</sup> According to the Cremer–Pople–Boeyens classification,<sup>[59,60]</sup>

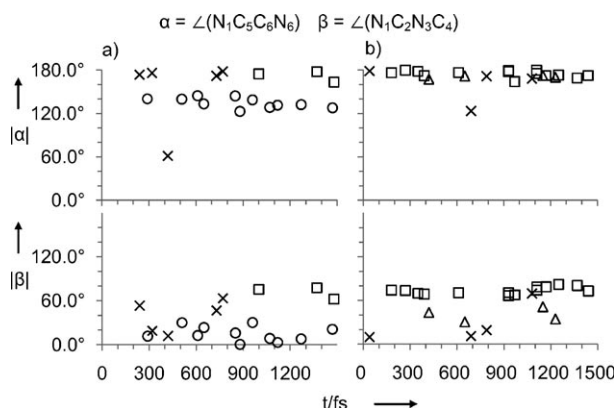


**Figure 4.** Scatter plots of some key geometric parameters at the  $S_1 \rightarrow S_0$  hopping events for adenine in: a)  $(dA)_{10}$  and b)  $(dA)_{10} \cdot (dT)_{10}$ . Hops occur via the  ${}^6S_1$  channel ( $\circ$ ), the  ${}^2E$  channel ( $\square$ ), the screw-boat channel ( $\triangle$ ), and side reactions ( $\times$ ), see text for details.



this type of CI has been assigned<sup>[58]</sup> as  ${}^6S_1$  for adenine in the gas phase (see the Supporting Information for details). In three trajectories, the nonradiative decay occurs via the  $S_0/{}^1L_a$  CI that is identified by the puckering of the six-membered ring at the  $C_2$  atom and the bending of the  $H_2$  atom (see Figure 3b and Figure 4a)<sup>[55–58]</sup> and is labeled<sup>[58]</sup> as the  ${}^2E$  channel. The remaining five trajectories follow diverse pathways before  $S_1 \rightarrow S_0$  hopping events, including ring decomposition and  $C_2-H_2$  or  $C_8-H_8$  cleavage, which may be considered as side reactions. For adenine in  $(dA)_{10}$ , the  ${}^6S_1$  channel thus represents the primary monomer pathway for returning to the ground state.

Turning to adenine in the  $(dA)_{10} \cdot (dT)_{10}$  double strand, 22 of 73 trajectories (29%) show  $S_1 \rightarrow S_0$  nonradiative decay within 1.5 ps. The majority of these (14) proceed via the  ${}^2E$  CI by means of  $C_2$ -puckering and  $H_2$ -bending (see Figure 3c), with dihedral angles  $|\chi(N_1C_2N_3C_4)|$  of typically  $60-80^\circ$  at the hops (see Figure 3d and Figure 4b), exactly as for the  ${}^2E$  channel in  $(dA)_{10}$ . Four trajectories hop to  $S_0$  when the molecular plane folds along the  $C_4-C_5$  axis and the six-membered ring puckers at  $N_3$  to yield a screw-boat structure, similar to the  ${}^4S_3$  conformation reported in reference [58] (see Figure 4b and the Supporting Information). The remaining four trajectories return to the ground state through side reactions such as the breaking of the five-membered ring, H-migration from  $C_2$  to  $N_3$ , or  $C_8-H_8$  cleavage. Most notably, no trajectory of adenine in  $(dA)_{10} \cdot (dT)_{10}$  decays to  $S_0$  by the  ${}^6S_1$  mechanism.

Our previous studies at the same semiempirical OM2/MRCI level have shown that the  ${}^6S_1$  CI plays a dominant role in the nonradiative decay of adenine in vacuo and in water,<sup>[41,42]</sup> where more than 90% of the trajectories pass the  ${}^6S_1$  CI and only less than 10% decay via the  ${}^2E$  channel. When adenine is surrounded by single-strand DNA in water, the  ${}^6S_1$  channel is still dominant (ca. 60%), even though the  ${}^2E$  channel and others become more important. For adenine in duplex DNA, two hydrogen bonds,  $N_6H^A \cdots O_2^T$  and  $N_1^A \cdots H_3^T$ , are formed in each Watson–Crick adenine–thymine base pair (see Figure 3c). Since the amino group of adenine is involved in the first hydrogen bond, its out-of-plane motion will be restrained. In all 22 trajectories that show a nonadiabatic transition, the  $N_6H^A \cdots O_2^T$  hydrogen bond is retained, with  $N_6H^A \cdots O_2^T$  distances ranging between 2.8 and 3.6 Å during the 1.5 ps simulation time (see the Supporting Information); the corresponding value in the crystal structure is 2.80 Å.<sup>[61]</sup> In the nonradiative decay of adenine in  $(dA)_{10} \cdot (dT)_{10}$ , the  ${}^6S_1$  channel is thus completely suppressed, and the  ${}^2E$  channel becomes dominant. This clearly demonstrates that the mechanism for the internal conversion of adenine to the electronic ground state is controlled by the biological environment.

Generally speaking, the results from excited-state dynamics are largely governed by the topology of the underlying potential energy surfaces. In adenine, there is not yet consensus on some of these features among different theoretical approaches.<sup>[42]</sup> For example, in the gas phase, the path to the  ${}^6S_1$  CI is essentially barrierless in some studies,<sup>[41,58,62]</sup> but not in others,<sup>[56,63,64]</sup> which will clearly affect the dynamical preferences. Hence, the outcome of dynamics studies should

be viewed with caution and in the context of other theoretical work. Based on ab initio QM/MM reaction path calculations, Conti et al.<sup>[25]</sup> propose the  ${}^2E$  channel as the leading pathway for the nonradiative decay of adenine in  $(dA)_{10} \cdot (dT)_{10}$  (in accord with the present work), but they also favor this channel in the gas phase (as opposed to the  ${}^6S_1$  channel in OM2/MRCI<sup>[41]</sup>). A recent ab initio QM/MM dynamics study<sup>[65]</sup> on a stacked trimer model (4-aminopyrimidine between two methyl guanine molecules) reports analogous decay mechanisms in isolated and stacked 4-aminopyrimidine (via similarly distorted CIs), a slight increase in the lifetime, and a notable dynamical influence of hydrogen bonding; such features are also apparent in our present work.

To summarize, we performed QM/MM surface-hopping simulations to investigate the nonradiative decay dynamics of adenine embedded within solvated DNA strands. For an individual adenine unit in  $(dA)_{10}$  and  $(dA)_{10} \cdot (dT)_{10}$ , the time constants for internal conversion to the electronic ground state were computed to be 5.7 ps and 4.1 ps, respectively. They are about ten times longer than in vacuo or in water. Our simulations indicate that the  ${}^6S_1$  ( $C_6$ -puckering and amino-bending) channel plays a leading role in the nonradiative decay of a single adenine in  $(dA)_{10}$ , while the  ${}^2E$  ( $C_2$ -puckering and  $H_2$ -bending) channel coexists. By contrast, for adenine in  $(dA)_{10} \cdot (dT)_{10}$ , the  ${}^6S_1$  mechanism is completely suppressed by hydrogen bonding between adenine and thymine, and the  ${}^2E$  channel becomes dominant. We regard this surface-hopping study on an individual adenine unit in a realistic environment of nucleotides as an initial step towards more complete simulations of the complex excited-state dynamics in DNA. Being reasonably efficient and realistic, the current QM/MM (QM = OM2/MRCI) approach should be a useful tool for such theoretical investigations into DNA photochemistry.

Received: December 23, 2010

Revised: May 12, 2011

Published online: June 9, 2011

**Keywords:** DNA · hydrogen bonds · molecular dynamics · photochemistry · semiempirical calculations

- [1] E. Emanuele, K. Zakrzewska, D. Markovitsi, R. Lavery, P. Millié, *J. Phys. Chem. B* **2005**, *109*, 16109–16118.
- [2] D. Onidas, T. Gustavsson, E. Lazzarotto, D. Markovitsi, *J. Phys. Chem. B* **2007**, *111*, 9644–9650.
- [3] D. Onidas, T. Gustavsson, E. Lazzarotto, D. Markovitsi, *Phys. Chem. Chem. Phys.* **2007**, *9*, 5143–5148.
- [4] D. Markovitsi, T. Gustavsson, F. Talbot, *Photochem. Photobiol. Sci.* **2007**, *6*, 717–724.
- [5] D. Markovitsi, T. Gustavsson, I. Vayá, *J. Phys. Chem. Lett.* **2010**, *1*, 3271–3276.
- [6] T. Takaya, C. Su, K. de La Harpe, C. E. Crespo-Hernández, B. Kohler, *Proc. Natl. Acad. Sci. USA* **2008**, *105*, 10285–10290.
- [7] C. T. Middleton, K. de La Harpe, C. Su, Y. K. Law, C. E. Crespo-Hernández, B. Kohler, *Annu. Rev. Phys. Chem.* **2009**, *60*, 217–239.
- [8] C. E. Crespo-Hernández, B. Cohen, B. Kohler, *Nature* **2005**, *436*, 1141–1144.
- [9] B. Kohler, *J. Phys. Chem. Lett.* **2010**, *1*, 2047–2053.

- [10] W.-M. Kwok, C. Ma, D. L. Phillips, *J. Am. Chem. Soc.* **2006**, *128*, 11894–11905.
- [11] I. Buchvarov, Q. Wang, M. Raytchev, A. Trifonov, T. Fiebzig, *Proc. Natl. Acad. Sci. USA* **2007**, *104*, 4794–4797.
- [12] C. E. Crespo-Hernández, B. Cohen, M. H. Patrick, B. Kohler, *Chem. Rev.* **2004**, *104*, 1977–2020.
- [13] C. E. Crespo-Hernández, B. Kohler, *J. Phys. Chem. B* **2004**, *108*, 11182–11188.
- [14] D. Markovitsi, A. Sharonov, D. Onidas, T. Gustavsson, *ChemPhysChem* **2003**, *4*, 303–305.
- [15] N. Schwalb, F. Temps, *Science* **2008**, *322*, 243–245.
- [16] B. Bouvier, T. Gustavsson, D. Markovitsi, P. Millié, *Chem. Phys.* **2002**, *275*, 75–92.
- [17] B. Bouvier, J. P. Dognon, R. Lavery, D. Markovitsi, P. Millié, D. Onidas, K. Zakrzewska, *J. Phys. Chem. B* **2003**, *107*, 13512–13522.
- [18] E. R. Bittner, *J. Chem. Phys.* **2006**, *125*, 094909.
- [19] G. Groenhof, L. V. Schäfer, M. Boggio-Pasqua, M. Goette, H. Grubmüller, M. A. Robb, *J. Am. Chem. Soc.* **2007**, *129*, 6812–6819.
- [20] L. Hu, Y. Zhao, F. Wang, G. Chen, C. Ma, W.-M. Kwok, D. L. Phillips, *J. Phys. Chem. B* **2007**, *111*, 11812–11816.
- [21] R. Improta, *Phys. Chem. Chem. Phys.* **2008**, *10*, 2656–2664.
- [22] S. Tonzani, G. C. Schatz, *J. Am. Chem. Soc.* **2008**, *130*, 7607–7612.
- [23] A. W. Lange, J. M. Herbert, *J. Am. Chem. Soc.* **2009**, *131*, 3913–3922.
- [24] E. B. Starikov, G. Cuniberti, S. Tanaka, *J. Phys. Chem. B* **2009**, *113*, 10428–10435.
- [25] I. Conti, P. Altoè, M. Stenta, M. Garavelli, G. Orlandi, *Phys. Chem. Chem. Phys.* **2010**, *12*, 5016–5023.
- [26] A. N. Alexandrova, J. C. Tully, G. Granucci, *J. Phys. Chem. B* **2010**, *114*, 12116–12128.
- [27] H.-M. Senn, W. Thiel, *Top. Curr. Chem.* **2007**, *268*, 173–290.
- [28] H.-M. Senn, W. Thiel, *Angew. Chem.* **2009**, *121*, 1220–1254; *Angew. Chem. Int. Ed.* **2009**, *48*, 1198–1229.
- [29] J. C. Tully, *J. Chem. Phys.* **1990**, *93*, 1061–1071.
- [30] S. Hammes-Schiffer, J. C. Tully, *J. Chem. Phys.* **1994**, *101*, 4657–4667.
- [31] Maestro, version 7.5, Schrödinger, LLC, New York, NY, **2005**.
- [32] W. L. Jorgensen, J. Chandrasekhar, J. D. Madura, R. W. Impey, M. L. Klein, *J. Chem. Phys.* **1982**, *79*, 926–935.
- [33] SYBYL 8.0, Tripos International, 1699 South Hanley Rd., St. Louis, Missouri, 63144, USA.
- [34] P. Sherwood, A. H. de Vries, M. F. Guest, G. Schreckenbach, C. R. A. Catlow, S. A. French, A. A. Sokol, S. T. Bromley, W. Thiel, A. J. Turner, S. Billeter, F. Terstegen, S. Thiel, J. Kendrick, S. C. Rogers, J. Casci, M. Watson, F. King, E. Karlsen, M. Sjøvoll, A. Fahmi, A. Schäfer, C. Lennartz, *J. Mol. Struct. (Theochem)* **2003**, *632*, 1.
- [35] <http://www.chemshell.org>.
- [36] E. Fabiano, Z. Lan, Y. Lu, W. Thiel in *Conical Intersections: Theory, Computation and Experiment (Adv. Ser. Phys. Chem. Vol. 17)* (Eds.: H. Köppel, W. Domcke, D. R. Yarkony), World Scientific, Singapore, **2011**, in press.
- [37] W. Weber, PhD thesis, Universität Zürich (Switzerland), **1996**.
- [38] W. Weber, W. Thiel, *Theor. Chem. Acc.* **2000**, *103*, 495–506.
- [39] A. Koslowski, M. E. Beck, W. Thiel, *J. Comput. Chem.* **2003**, *24*, 714–726.
- [40] M. R. Silva-Junior, W. Thiel, *J. Chem. Theory Comput.* **2010**, *6*, 1546–1564.
- [41] E. Fabiano, W. Thiel, *J. Phys. Chem. A* **2008**, *112*, 6859–6863.
- [42] Z. Lan, Y. Lu, E. Fabiano, W. Thiel, *ChemPhysChem*, DOI: 10.1002/cphc.20101054.
- [43] W. Smith (Guest Editor), *Molecular Simulation*, **2006**, *32*, 933–1121.
- [44] a) A. D. MacKerell, N. K. Banavali, *J. Comput. Chem.* **2000**, *21*, 105–120; b) N. Foloppe, A. D. MacKerell, *J. Comput. Chem.* **2000**, *21*, 86–104.
- [45] D. Markovitsi, T. Gustavsson, A. Banyasz, *Mutat. Res. Rev.* **2010**, *704*, 21–28.
- [46] A. Abo-Riziq, L. Grace, E. Nir, M. Kabelac, P. Hobza, M. S. de Vries, *Proc. Natl. Acad. Sci. USA* **2005**, *102*, 20–23.
- [47] A. L. Sobolewski, W. Domcke, C. Hättig, *Proc. Natl. Acad. Sci. USA* **2005**, *102*, 17903–17906.
- [48] P. R. L. Markwick, N. L. Doltsinis, *J. Chem. Phys.* **2007**, *126*, 175102.
- [49] N. K. Schwalb, F. Temps, *J. Am. Chem. Soc.* **2007**, *129*, 9272–9273.
- [50] Z. Lan, E. Fabiano, W. Thiel, *J. Phys. Chem. B* **2009**, *113*, 3548–3555.
- [51] Z. Lan, E. Fabiano, W. Thiel, *ChemPhysChem* **2009**, *10*, 1225–1229.
- [52] D. Markovitsi, F. Talbot, T. Gustavsson, D. Onidas, E. Lazzarotto, S. Marguet, *Nature* **2006**, *441*, E7.
- [53] F. Santoro, V. Barone, R. Improta, *Proc. Natl. Acad. Sci. USA* **2007**, *104*, 9931–9936.
- [54] F. Santoro, V. Barone, R. Improta, *J. Am. Chem. Soc.* **2009**, *131*, 15232–15245.
- [55] S. Perun, A. L. Sobolewski, W. Domcke, *J. Am. Chem. Soc.* **2005**, *127*, 6257–6265.
- [56] L. Serrano-Andrés, M. Merchán, A. C. Borin, *Chem. Eur. J.* **2006**, *12*, 6559–6571.
- [57] S. Yamazaki, S. Kato, *J. Am. Chem. Soc.* **2007**, *129*, 2901–2909.
- [58] M. Barbatti, H. Lischka, *J. Am. Chem. Soc.* **2008**, *130*, 6831–6839.
- [59] D. Cremer, J. A. Pople, *J. Am. Chem. Soc.* **1975**, *97*, 1354–1358.
- [60] J. C. A. Boeyens, *J. Chem. Crystallogr.* **1978**, *8*, 317–320.
- [61] J. D. Watson, F. H. C. Crick, *Nature* **1953**, *171*, 964–967.
- [62] W. H. I. Hassan, W. C. Chung, N. Shimakura, S. Koseki, H. Kono, Y. Fujimura, *Phys. Chem. Chem. Phys.* **2010**, *12*, 5317–5328.
- [63] L. Blancafort, *J. Am. Chem. Soc.* **2006**, *128*, 210–219.
- [64] I. Conti, M. Garavelli, G. Orlandi, *J. Am. Chem. Soc.* **2009**, *131*, 16108–16118.
- [65] D. Nachtigallová, T. Zelený, M. Ruckebauer, T. Müller, M. Barbatti, P. Hobza, H. Lischka, *J. Am. Chem. Soc.* **2010**, *132*, 8261–8263.
- [66] W. Humphrey, A. Dalke, K. Schulten, *J. Mol. Graph.* **1996**, *14*, 33–38.



paper (4)

***Monomeric Adenine Decay Dynamics Influenced by  
DNA Environment***

Y. Lu, Z. Lan, and W. Thiel

*J. Comput. Chem.*, **2011**, 33, 1225-1235.



# Monomeric Adenine Decay Dynamics Influenced by the DNA Environment

You Lu,<sup>[a]</sup> Zhenggang Lan,<sup>[b]</sup> and Walter Thiel<sup>\*,[a]</sup>

We report on-the-fly surface-hopping dynamics simulations of single adenine embedded in solvated DNA oligomers, (dA)<sub>10</sub> and (dA)<sub>10</sub>·(dT)<sub>10</sub>. Both model systems are found to decay from the S<sub>1</sub> to the S<sub>0</sub> state via distinct monomeric channels, on account of the strong hydrogen-bonding interactions between the Watson–Crick pair in the double-stranded oligomer. Surprisingly, the decay times (several picoseconds) for the current models are 10 times longer than those of adenine in the gas or aqueous phase, while matching one of the time constants observed experimentally. We discuss possible reasons for these longer decay times, including steric

hindrance in the DNA strands, electronic effects of the environment, and the presence of other local excited-state minima. We present optimized geometries and relative energies for representative S<sub>0</sub> and S<sub>1</sub> minima as well as conical intersections related to the hopping events. We have also computed steady-state and time-dependent fluorescence spectra that may help understand the experimental observations. © 2012 Wiley Periodicals, Inc.

DOI: 10.1002/jcc.22952

## Introduction

Numerous experimental studies using time-resolved spectroscopic techniques have been published on DNA models in the past decade. They have uncovered the complicated multiexponential character of DNA photophysics and photochemistry, with time constants ranging from hundreds of femtoseconds to hundreds of picoseconds.<sup>[1]</sup> Hence, it has been suggested that the photoinduced processes in DNA may be composed of multiple components involving localized and/or delocalized states and processes. In an attempt to explain their often puzzling observations, spectroscopists have proposed a variety of decay models. The Kohler group<sup>[2–4]</sup> [(dA)<sub>18</sub> and (dA)<sub>18</sub>·(dT)<sub>18</sub>] and the Fiebig group<sup>[5,6]</sup> [(dA)<sub>2–18</sub> and (dA)<sub>12/18</sub>·(dT)<sub>12/18</sub>] conducted femtosecond pump-probe experiments and came to similar conclusions: singlet excited states of single or unstacked bases relax to the hot ground state by ultrafast internal conversion (IC) within 1 ps, whereas initial excitons delocalized over several bases rapidly (within several ps) trap to ‘localized’ exciplexes or charge-transfer (CT) states that survive longer than 100 ps. Transient absorption up-conversion techniques can be used to map the temporal behavior of photoluminescence. With the help of such techniques, Markovitsi and coworkers<sup>[7,8]</sup> [(dA)<sub>20</sub>, (dA)<sub>20</sub>·(dT)<sub>20</sub>, and (dA)<sub>n</sub>·(dT)<sub>n</sub>] also detected multiexponential components [0.3–0.85 ps, 1.6–3.9 ps, and up to 187 ps], which they interpreted as follows: Frenkel and/or CT excitons<sup>[9]</sup> extending over several bases give rise to the longer components after ultrafast (<100 fs) intraband scattering, whereas the decay of ππ\* and/or nπ\* states of thymine/adenine single bases corresponds to the shorter components. Schwab and Temps<sup>[10]</sup> reported similar results using a tri-exponential fitting function (0.52–0.63 ps, 2.6–5.8 ps, and 16.2–97.0 ps) to analyze their up-conversion experiments [(dA)<sub>20</sub> and (dA)<sub>20</sub>·(dT)<sub>20</sub>]. Phillips and coworkers<sup>[11]</sup> proposed decay mechanisms based on their Kerr-gated fluorescence spectra [(dA)<sub>20</sub>]: in their view,

all components originate from monomeric adenine excitation but embark on different decay paths including radiationless IC (~0.39 ps) and the formation of two excimers E<sub>1</sub> (~4.3 ps) and E<sub>2</sub> (~182 ps). This brief overview over recent experimental work shows that different interpretations are advanced to rationalize the observations (including both localized and delocalized excited states) and that we are still far from a firm consensus on DNA excited-state dynamics.

The enigma of DNA photochemistry has also aroused much interest on the theoretical side. There have been many efforts to establish sound theoretical models and to explain the experimental observations. The simplest models, stacked base dimers (as well as trimers) and base pairs, have been studied most. Density functional theory (DFT), complete-active-space self-consistent-field (CASSCF) methodology, and configuration interaction approaches have been applied to model virtually every aspect of DNA photochemistry, including energetics,<sup>[12,13]</sup> π-stacking and/or base pairing,<sup>[14,15]</sup> electrostatic interactions,<sup>[16]</sup> damage and repair reactions,<sup>[17]</sup> excited-state delocalization (charge transfer, excimer/exciple, exciton),<sup>[18]</sup> and decay dynamics.<sup>[19]</sup> Spectroscopic measurements of DNA strands are usually done in solution, and hence, solvent effects may play a crucial role. The polarizable continuum model<sup>[20]</sup> (PCM) is an efficient technique to describe such effects without introducing extra atoms into the system. Using PCM combined with time-dependent DFT, Improta and coworkers<sup>[21]</sup>

[a] Y. Lu, W. Thiel

Max-Planck-Institut für Kohlenforschung, Kaiser-Wilhelm-Platz 1, D-45470 Mülheim an der Ruhr, Germany  
 E-mail: thiel@mpi-muelheim.mpg.de

[b] Z. Lan

Qingdao Institute of Bioenergy and Bioprocess Technology, Chinese Academy of Sciences, 189 Songling Road, Qingdao, 266101 Shandong, China

© 2012 Wiley Periodicals, Inc.

have investigated a number of excited-state DNA models, such as  $\pi$ -stacked single-stranded adenine dimer, trimer, and oligomers as well as double-stranded  $(dA)_2 \cdot (dT)_2$  with both intrastrand and interstrand interactions.<sup>[22]</sup> However, such calculations quickly become much more costly when going to larger systems like polynucleotides. In such cases, semiempirical methods are attractive because of their efficiency and still acceptable accuracy. The INDO/S<sup>[23]</sup> method has proven to give reasonable results for the excitation energies of homogeneous adenine single strands<sup>[12]</sup> and delocalized excitonic states.<sup>[24]</sup> Voityuk<sup>[25]</sup> showed the merits of the semiempirical INDO/S method in dealing with bulky systems as large as double-stranded DNA polymers. A recent study of DNA fragments<sup>[26]</sup> with a direct semiclassical simulation method<sup>[27]</sup> used the semiempirical Hamiltonians AM1<sup>[28]</sup> and PM3.<sup>[29]</sup>

Even semiempirical methods meet their computational limit when dealing with large molecules in the condensed phase, for example, solvated DNA. For such systems, quantum mechanical/molecular mechanical (QM/MM) approaches<sup>[30]</sup> become the method of choice. They partition the system into two subsystems: the active site (e.g., the chromophore in an excited state) is treated in the QM layer at an appropriate QM level, whereas the whole environment (MM layer) is mimicked at a lower but computationally more efficient level. The QM/MM approach allows a realistic description of the chromophore in its native environment, accounting for the effects of steric repulsion, transient hydrogen bonding, van der Waals (vdW) interactions, and so forth, and it thus enables full-scale atomistic simulations. Some successful QM/MM studies on DNA excited states, including nonadiabatic dynamics simulations, have already been presented.<sup>[31–33]</sup>

In our opinion, none of the currently available theoretical approaches is yet quantitatively reliable in modeling a system as large as solvated DNA. In our own work, we have followed the strategy to start from a single isolated nucleobase and then successively increase the complexity toward DNA using the semiempirical OM2/MRCI<sup>[34,35]</sup> method (Orthogonalization Model 2 combined with multireference configuration interaction, MRCI). We first investigated a single adenine in the gas phase (QM)<sup>[36]</sup> and in the aqueous phase (QM/MM).<sup>[37]</sup> We then extended this work by embedding a single QM adenine in solvated single-stranded and double-stranded DNA oligomers,<sup>[38]</sup> as a logical next step toward modeling the actual biological systems. These OM2/MRCI-based studies have covered energy evaluations, geometry optimizations, and nonadiabatic dynamics. We found for adenine in water that, after around 100 fs, the decay of the  $S_1$  population starts and the IC to the  $S_0$  state proceeds with a time constant of 410 fs. For adenine in DNA strands, the  $S_2 \rightarrow S_1$  decay takes place extremely rapidly ( $\sim 7$  fs), distinctly faster than *in vacuo* or in water. Thereafter, the  $S_1$  state undergoes nonradiative decay through  $S_0/S_1$  conical intersections (CIs) with lifetimes of 5.7 and 4.1 ps, 10 times longer than *in vacuo* and in water, for monomeric adenine in  $(dA)_{10}$  and  $(dA)_{10} \cdot (dT)_{10}$ , respectively. These time constants match one of the experimental components, and the underlying decay processes could actually contribute to the latter. Our

simulations indicate that the  ${}^6S_1$  channel (conical intersection structure with puckered  $C_6$  atom and bent amino group) plays a leading role in the nonradiative decay of a single adenine in water and in  $(dA)_{10}$ , whereas the  ${}^2E$  channel (with  $C_2$ -puckering and  $H_2$ -bending) coexists. By contrast, for adenine in  $(dA)_{10} \cdot (dT)_{10}$ , the  ${}^6S_1$  mechanism is completely suppressed by hydrogen bonding between adenine and thymine, and the  ${}^2E$  channel becomes dominant.

In this article, we continue our study of the limiting case of adenine monomer excitation in solvated single-strand and double-strand DNA oligomers. We give a more detailed account of our computational results than in the original short communication,<sup>[38]</sup> with a structural characterization of all relevant species and a quantitative analysis of the effects of the environment on the decay dynamics. In addition, we present the absorption and emission spectra of a single QM adenine in the DNA oligomer environment.

## Computational Details

In this work, we focus on the effect of the biological environment on the decay dynamics of a single adenine within the QM/MM framework. According to the setup described in Ref. [38], two B-type oligonucleotides  $(dA)_{10}$  and  $(dA)_{10} \cdot (dT)_{10}$  were constructed as single- and double-stranded DNA models with Maestro 7.5.<sup>[39]</sup> They were entirely solvated in TIP3P<sup>[40]</sup> spherical water droplets with a diameter of about 60 Å. The negative charges on phosphoric acids were neutralized with  $Na^+$  ions using SYBYL 8.0.<sup>[41]</sup> Overall, 12,457 and 12,515 atoms were included in the two models, respectively. Thermal equilibration of each system was reached after 1 ns classical molecular dynamics (MD) simulations.

The QM/MM calculations were done using the ChemShell package.<sup>[42]</sup> One adenine (14 atoms) located near the center of the oligonucleotide was chosen as the QM region. It was treated by the OM2/MRCI approach.<sup>[34,35]</sup> An active space consisting of 12 electrons in 10 orbitals was adopted,<sup>[36–38]</sup> which covered the six highest occupied orbitals and the four lowest virtual orbitals of adenine. This choice was found to minimize failures of orbital mapping in two consecutive MRCI steps during the excited-state dynamics. The remaining atoms comprised the MM part, which was handled by the DL\_POLY package<sup>[43]</sup> applying the CHARMM27 force field.<sup>[44]</sup> This MM force field is not polarizable; it was chosen because there is not yet a robust and well-validated polarizable force field for DNA that could be used with the same confidence as established fixed-charge force fields.<sup>[45]</sup> The biological environment of an active site in proteins or in DNA is generally described in a realistic manner by these standard fixed-charge force fields.<sup>[46]</sup> This appears to be true also in the theoretical modeling of excited states, including CT states.<sup>[47]</sup> In this context, we note that the effects of explicit MM solvent polarization on reaction barriers were found to be rather small in previous QM/MM work.<sup>[48]</sup> Moreover, as the studied adenine moiety is neutral and the excitations do not involve long-range electron transfer, the QM/MM approach with electrostatic embedding is expected to work well, so that it should not be necessary to account for

the dynamical (solvent) effects of fast electronic rearrangement in the MM environment in our approach.

We have reported in Ref. [38], the electronic absorption spectra of both oligonucleotides obtained at geometries taken from 2 ps (0.5 fs  $\times$  4000) Born–Oppenheimer molecular dynamics (BOMD) simulations at 300 K. Subsequent nonadiabatic dynamics up to 1.5 ps (3000 MD steps) were simulated by QM/MM on-the-fly surface-hopping simulations.<sup>[49,50]</sup> Initial conditions, such as geometries, velocities, and electronic states, were adapted from snapshots of the ground-state BOMD. To reduce the computational cost, all atoms further than 16 Å away from the center were frozen in the MD simulations. Each trajectory normally takes about 15 days on a single AMD Opteron x86\_64 CPU with 2 GB of memory. Time-dependent fluorescence spectra of single adenine in (dA)<sub>10</sub> were derived from the nonadiabatic trajectories. The overall steady-state fluorescence maxima of single adenine in (dA)<sub>10</sub> were plotted using an overlay (with Gaussian broadening) of the S<sub>1</sub>→S<sub>0</sub> vertical emission energies calculated at the optimized S<sub>1</sub> minima of all trajectories considered. All geometry optimizations were performed using the open-source geometry optimizer DL-FIND<sup>[51]</sup> integrated in ChemShell. The middle part of the single (or double) strand, that is, seven bases (or five base pairs) and an 18-Å water sphere enveloping the QM adenine, was treated as the active region in the optimization. In addition, the S<sub>0</sub>, S<sub>1</sub>, and conical intersection structures were minimized starting from the hopping geometries.

## Results and Discussion

### Absorption and emission

In our previous studies using the OM2/MRCI method, we have reported the calculated absorption spectra of single adenine in the gas phase,<sup>[36]</sup> in the aqueous phase,<sup>[37]</sup> and in oligonucleotides.<sup>[38]</sup> For single adenine in DNA strands, OM2/MRCI (at the QM/MM level) predicts that the first absorption band [4.71 eV in (dA)<sub>10</sub> and 4.78 eV in (dA)<sub>10</sub>·(dT)<sub>10</sub>] arises from three overlapping transitions at 4.60, 4.80, and 4.93 eV in (dA)<sub>10</sub> and at 4.66, 4.91, and 4.99 eV in (dA)<sub>10</sub>·(dT)<sub>10</sub> (see Ref. [38]). There is a small red shift (0.06 eV) when going from the gas phase to aqueous solution, and a small blue shift (0.09–0.17 eV) when going from the latter to the DNA strands. Various experimental spectra show similar red shifts<sup>[1,52]</sup> (0.14–0.31 eV) and blue shifts<sup>[12,53,54]</sup> (0.01–0.07 eV). These shifts are induced by the complex electrostatic and steric environment in the condensed phase. In the case of the DNA strands, our calculations exclude (by design) contributions from delocalized excimer and exciton states, which are present in the experimental spectra.

Despite this inherent limitation of our presently adopted model, the QM/MM results for a single QM adenine compare reasonably well with experiment, as the absorption maxima of oligonucleotides are observed at 4.82 eV [(dA)<sub>20</sub>] for single strands<sup>[12]</sup> and at 4.78 eV [(dA)<sub>20</sub>·(dT)<sub>20</sub>] or 4.84 eV [(dA)<sub>n</sub>·(dT)<sub>n</sub>] for double strands.<sup>[54]</sup> The deviations of the computed (monomeric) band maxima from experiment are quite uniform (red

shift) in the gas phase, in water, and in DNA. They are well within the usual error margin of OM2/MRCI.<sup>[35]</sup> They can be compared with the QM/MM results for (dA)<sub>10</sub>·(dT)<sub>10</sub> [QM = MSPT2//CASSCF(12,10)/ANO-1 and MM = AMBER] by Conti et al.,<sup>[33]</sup> who find the L<sub>a</sub> (ππ\*) excited state at 4.83 eV, L<sub>b</sub> (ππ\*) at 5.04 eV, and nπ\* at 5.49 eV. Hence, the OM2/MRCI and MSPT2//CASSCF calculations both assign L<sub>a</sub> (ππ\*) character (intrinsically bright) to the lowest state that is most intense in this DNA oligomer; they show reasonable agreement in the energies of the ππ\* states, whereas the nπ\* state occurs at a higher energy in MSPT2//CASSCF.<sup>[33]</sup>

The quoted OM2/MRCI energies were obtained by averaging more than 200 snapshots from a ground-state MD simulation (superposition with Gaussian broadening). As these MD snapshots sample a range of geometries around the equilibrium, the three lowest excited states are generally of mixed character, with contributions from L<sub>a</sub> (ππ\*), L<sub>b</sub> (ππ\*), and nπ\*. Because of the strong coupling between these states (especially at the distorted geometries encountered during the surface-hopping simulations), we refrain from a diabatic description in terms of L<sub>a</sub>, L<sub>b</sub>, or nπ\* potential energy surfaces (PESs) and discuss the excited states in adiabatic language (i.e., S<sub>1</sub> and S<sub>2</sub> states). The computed ultrafast (~7 fs) decay<sup>[38]</sup> from S<sub>2</sub> to S<sub>1</sub> reflects such strong mixing.

To estimate the steady-state emission of single adenine in (dA)<sub>10</sub>, we optimized the S<sub>1</sub> excited-state geometries for all trajectories and reached convergence for 121 of 200 snapshots. In subsequent single-point calculations, we found relatively large oscillator strengths (about 0.08–0.10, see Supporting Information, Fig. S1a) for emission from two groups of S<sub>1</sub> local minima with energies around 410 nm (3.0 eV, mostly ππ\*) and 340 nm (3.6 eV, mixed ππ\* and nπ\* character). Experimentally, the steady-state fluorescence spectrum of oligonucleotide (dA)<sub>20</sub> has a broad emission maximum at ~360 nm (~3.4 eV) that envelops our predicted peaks.<sup>[11]</sup> We expect that dynamic effects can mix the emissions arising from the optimized excited-state local minima. Figure 1a shows the calculated temporal evolution of adenine fluorescence emission derived from the nonadiabatic dynamics simulations, where three MD snapshots spanning 20 fs were broadened over all trajectories for each recorded time (50, 400, and 1000 fs). This calculation predicts spectral shapes that are compatible with the experimental time-resolved fluorescence spectra of the adenine oligomer.<sup>[11]</sup> Both the calculated and experimental contours possess prominent tails extending to longer wavelengths. In the calculated emission spectra, these tails arise from a progressive red shift of the monomeric emission as time goes on. There is an accompanying attenuation of the fluorescence intensity over time, as also reported in the experimental work.<sup>[11]</sup> However, the computed red shift is more pronounced than the observed one (see Fig. 1b). We note again in this context that the calculated emission spectra refer to a single QM adenine and thus do not account for delocalized excimer/excimer states that are believed to be indispensable,<sup>[2]</sup> which will cause some systematic errors. Other conceivable long-lived species may also be missing in our dynamics simulations due to the limitations of the surface-hopping technique.

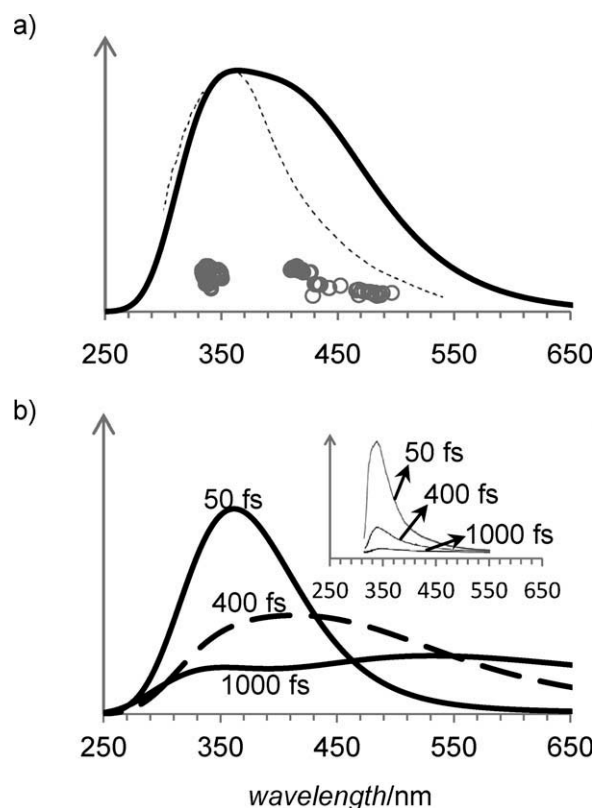


**Figure 1.** Single adenine in (dA)<sub>10</sub>: a) computed emission spectrum (black line): envelope of  $E_{\text{emission}}(S_1 \rightarrow S_0)$  based on 121 optimized  $S_1$  structures (grey circles). The experimental steady-state fluorescence of (dA)<sub>20</sub> from Ref. [11] is shown as dashed line. b) Time-resolved monomeric emission spectra of adenine calculated at the QM/MM (QM = OM2/MRCI) level by averaging over the nonadiabatic dynamics simulations (with Gaussian broadening): recorded at 50 fs (solid), 400 fs (dashed), and 1000 fs (solid), respectively. Inset: experimental time-resolved fluorescence spectra of (dA)<sub>20</sub> adapted from Ref. [11].

For a single QM adenine in (dA)<sub>10</sub>·(dT)<sub>10</sub>, the successful geometry optimizations of the  $S_1$  excited state in 129 snapshots resulted in three main groups of local minima, with emission energies of 480 nm (2.6 eV), 440 nm (2.8 eV), and 340 nm (3.6 eV), respectively [see Supporting Information, Fig. S1b]. The former two transitions carry only little oscillator strength (0.04–0.06), whereas the third one is brighter (oscillator strength  $\sim 0.12$ ). Experimentally, the steady-state fluorescence maximum is recorded at 324–327 nm (3.79–3.83 eV)<sup>[55]</sup> for (dA)<sub>n</sub>·(dT)<sub>n</sub>. Time-resolved fluorescence spectra of (dA)<sub>20</sub>·(dT)<sub>20</sub><sup>[8]</sup> show a fluorescence maximum close to the steady-state maximum, with a slightly increasing red shift when going from 0.2 to 2.2 ps (from 3.82 to 3.78 eV). The OM2/MRCI emission maxima (Supporting Information, Fig. S2) of a single QM adenine in double-stranded DNA are significantly below the experimental value in both the steady-state and time-resolved spectra. We present the results of single adenine in (dA)<sub>10</sub>·(dT)<sub>10</sub> for the purpose of documentation and without further discussion, because the actual emission process may involve the other nucleobase (i.e., thymine) and various delocalized electronic states.

### Slower internal conversion

The nonradiative decay process of the adenine monomer after photoexcitation in the Franck–Condon (FC) region can be divided into two stages. In stage I, the molecule distorts in response to the excited-state gradient until it reaches the conical intersection realm. Then, the system oscillates around the distorted conformation until hopping takes place—this is stage II. In our previous theoretical simulations, we have observed a remarkable slowdown in both stages for a single QM adenine in DNA, compared with the situation *in vacuo* and in solution. Overall there is a slowdown by a factor of 10. We have previously proposed that electronic effects, steric effects, and an extra local minimum are mainly responsible for the deceleration.<sup>[38]</sup> In this subsection, we analyze these effects in a more detailed and quantitative manner.

**Steric hindrance.** As already pointed out in many theoretical studies, (see, for example, Ref. [56]) the conical intersection structures of adenine typically involve out-of-plane deformations. In the condensed phase, such deformations can easily be affected by the environment. For example, in aqueous solution, we have observed hydrogen-bond-like interactions<sup>[37]</sup> between the amino group (N<sub>6</sub> atom) and neighboring water molecules, helping 9*H*-adenine to approach the “amino-bending”  ${}^6S_1$  conical intersection structure and thus accelerating stage I mildly. By contrast, the competing out-of-plane bending of the C<sub>2</sub>H<sub>2</sub> moiety that leads to the  ${}^2E$  conical intersection structure is less favored in aqueous solution, because of the very weak interactions between the C<sub>2</sub>H<sub>2</sub> moiety and water.

Adenine embedded in DNA single strands primarily interacts with the nearest bases along the stacking direction and with solvent water molecules at the end of the strand that is exposed to the solvent. We assess vdW interactions by assuming that the vdW force between two atoms is attractive (repulsive) when the distance between them is greater (smaller) than the sum of their vdW radii (i.e., the vdW contact distance).<sup>[57]</sup> During the nonadiabatic dynamics trajectories, we have monitored the real-time change of the minimum distance between the QM adenine A and the nearest MM adenine A' or A''. The results for selected atom pairs from A and A' or A'' are shown in the panels of Figure 2. We find that these minimum distances often fluctuate near and above the vdW contact distance, indicating attractive vdW interactions, except for panels (c) and (h) where these distances are too large to cause significant attraction. Nevertheless, we also find significant instantaneous vdW repulsions during all trajectories in (b) between amino H<sup>A</sup> and amino N<sup>A'/A''</sup>, in (d) between amino H<sup>A</sup> and ring N<sup>A'/A''</sup>, in (e) between amino H<sup>A</sup> and ring C<sup>A'/A''</sup>, and in (j) between amino N<sup>A</sup> and ring C<sup>A'/A''</sup>, where the minimum distance is frequently below the vdW contact distance. Moreover, if we adopt the “extended amino group” convention proposed by Karplus and coworkers,<sup>[58]</sup> and treat the amino group as a single entity with a vdW radius of 1.75 Å, the vdW repulsion between the QM and MM amino groups becomes more conspicuous in most of the simulations, see, for example, Figures 2g and 2j.



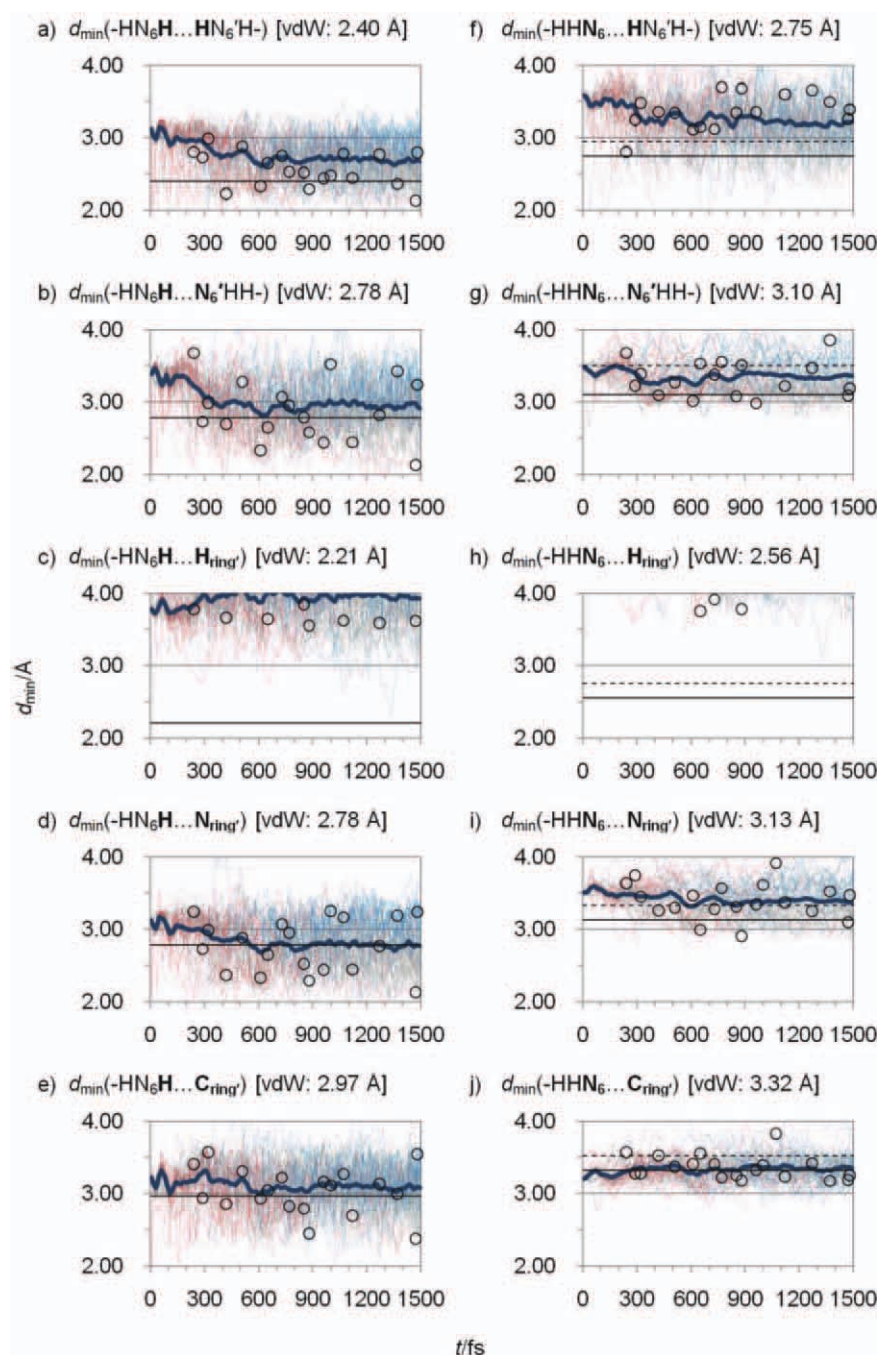


**Figure 2.** Minimum distance  $\angle$  between the QM adenine (A) and its adjacent base ( $A'$  or  $A''$ ) in  $(dA)_{10}$  during all surface-hopping trajectories over the entire simulation time (fs), for the following atom pairs: a) amino  $H^A$  to amino  $H^{A'}$  or  $A''$ ; b) amino  $H^A$  to amino  $N^{A'}$  or  $A''$ ; c) amino  $H^A$  to ring  $H^{A'}$  or  $A''$ ; d) amino  $H^A$  to ring  $N^{A'}$  or  $A''$ ; e) amino  $H^A$  to ring  $C^{A'}$  or  $A''$ ; f) amino  $N^A$  to amino  $H^{A'}$  or  $A''$ ; g) amino  $N^A$  to amino  $N^{A'}$  or  $A''$ ; h) amino  $N^A$  to ring  $H^{A'}$  or  $A''$ ; i) amino  $N^A$  to ring  $N^{A'}$  or  $A''$ ; j) amino  $N^A$  to ring  $C^{A'}$  or  $A''$ . Legends: before  $S_1 \rightarrow S_0$  hops (.....); after  $S_1 \rightarrow S_0$  hops (.....); no  $S_1 \rightarrow S_0$  hops up to 1.5 ps (.....); hop events ( $\circ$ ); average minimum distance (—). The sum of the corresponding van der Waals (vdW) radii (—) is given in square brackets on top of each figure. The sum of the vdW radii according to the 'extended amino group' convention (----) is computed using a vdW radius of 1.75 Å for the whole amino group.<sup>[58]</sup>

These repulsions between adjacent adenine moieties in close contact cause steric hindrance and impede the out-of-plane deformation that is required to reach the  ${}^6S_1$  conical intersection region. When adenine is embedded in  $(dA)_{10}$ , the bending motion of the amino group is seen in our simulations

only after  $\sim 350$  fs due to such steric hindrance.<sup>[38]</sup> By contrast, during all trajectories *in vacuo* and in water, this bending motion appears already after  $\sim 150$  fs and quickly leads to dihedral angles  $[\angle(N_1C_5C_6N_6)]$  of  $\sim 140^\circ$ . Hence, stage I needs more time in the DNA environment than *in vacuo* or water. Moreover, when executing the amino bending motion, the nonadiabatic dynamics trajectories of single-stranded DNA show a sudden rise in the length of the oligomer, as if the QM adenine that is willing to rise its "arm" (amino group) has to push away its "neighbors" as it "feels" too narrowly confined. We note that Conti et al.<sup>[33]</sup> also interpret the slower component of the DNA decay as the result of steric hindrance (barrier  $\sim 0.2$  eV) in their *ab initio* QM/MM study. In the single-stranded DNA model, we also see a few hop events by the  ${}^2E$  mechanism with  $C_2H_2$  out-of-plane motion, which however happen rather late. Because of the small vdW radius of hydrogen, there is no obvious repulsion between  $C_2H_2$  and the environment, so that steric hindrance should be less important. This may actually indicate the possibility that the  ${}^2E$  channel is intrinsically slow in this case.

We find little evidence for hydrogen-bonding interactions between the stacked bases in the present simulations. According to Figure 2g, the minimum distance between the amino N atoms is in general much greater than the typical value of 3.1 Å in such a hydrogen bond.<sup>[59]</sup> As in adenine the  $p_z$  orbital of the amino N atom ( $sp^2$ ) is involved in a delocalized  $\pi$  orbital and will thus not be a good hydrogen bond acceptor, any hydrogen-bonding-like interaction between two amino groups in the adenine oligomer should be very weak. Likewise, the hydrogen-bonding interaction between an amine and a  $\pi$ -acceptor ( $N-H \cdots \pi$ ) will be rather weak; for example, an equilibrium  $N \cdots ring$  distance of  $\sim 3.6$  Å has been reported between ammonia and benzene.<sup>[60]</sup> However, Figure 2i and especially 2j show that the average minimum distance between the amino  $N^A$  atom and the ring plane of the adjacent base is basically below 3.6 Å, indicating steric repulsion rather than hydrogen bonding. In short, we do not identify any substantial hydrogen-bonding interaction between the stacked QM and MM adenine molecules, in contrast to a recent *ab initio* QM/MM dynamics model study<sup>[19]</sup> of a stacked

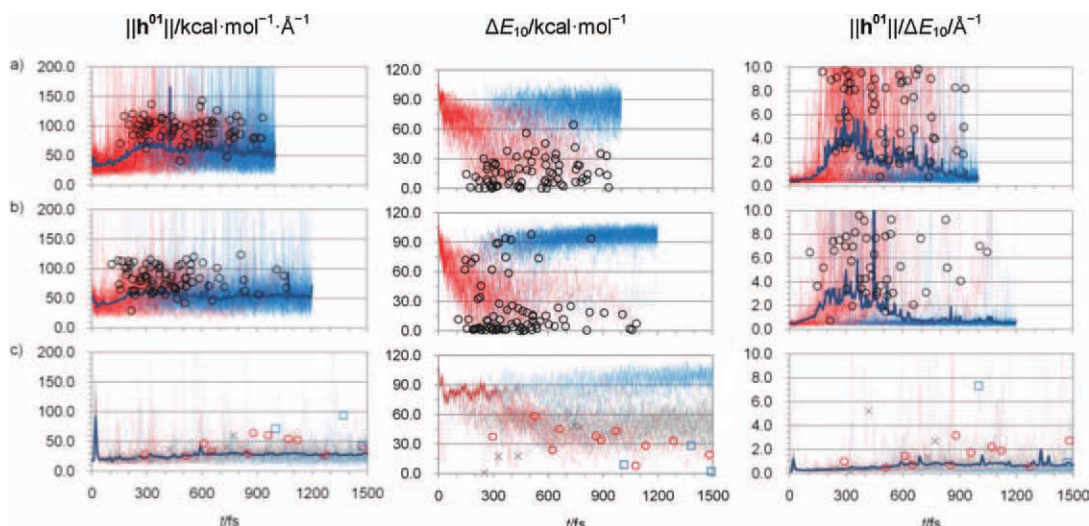


**Figure 3.** Left panel: norm of  $S_0/S_1$  interstate coupling vector; middle panel: energy gap between the  $S_1$  and  $S_0$  states  $\Delta E_{10}$ ; right panel: norm of  $S_0-S_1$  interstate coupling divided by energy difference of the  $S_0$  and  $S_1$  states  $\|\mathbf{h}^{01}\|/\Delta E_{10}/\text{\AA}^{-1}$ . The plots cover all surface-hopping trajectories over the entire simulation time (fs) for adenine: a) *in vacuo*, b) in water, and c) in (dA)<sub>10</sub>. Color code for the trajectories: before  $S_1 \rightarrow S_0$  hops (.....); after  $S_1 \rightarrow S_0$  hops (.....); no  $S_1 \rightarrow S_0$  hops up to 1.5 ps (.....); mean value (—). Hopping events: a) and b) *in vacuo* and in water (○); c) <sup>6</sup>S<sub>1</sub> channel (□), <sup>2</sup>E channel (×), and side reactions (×). Only final hops are displayed and no back hops are counted.

trimer (QM 4-aminopyridine between two MM methyl-guanines) that reports the dynamical formation and disappearance of hydrogen bonds between the bases.

**Electronic effects.** It has been argued that steric effects alone do not account for the full experimental observations in DNA oligomers.<sup>[4]</sup> This is consistent with our simulations. *In vacuo* and in water, a majority of the  $S_1 \rightarrow S_0$  nonradiative decays in adenine take place soon after the conformational preparation of stage I is finished (mainly out-of-plane motion,  $\sim 150$  fs). By contrast, adenine in single-stranded DNA enters stage II later ( $\sim 350$  fs) but then tends to remain longer in the excited state, as only a surprisingly small fraction of the population hops to the  $S_0$  surface within 2 ps. In other words, adenine in DNA does not hop easily even after being geometrically prepared to do so. In an attempt to rationalize this low hopping rate, we examine the electronic probability of nonadiabatic hopping. The probability for hopping from state  $S_1$  to state  $S_0$  is determined<sup>[50]</sup> by

$$p^{01} = \frac{2 \int_t^{t+\Delta t} dt \operatorname{Re}(C_1^*(t)C_0(t)\dot{\mathbf{R}} \cdot \mathbf{d}^{01})}{|C_1(t)|^2}, \quad (1)$$

where  $\dot{\mathbf{R}} \cdot \mathbf{d}^{01}$  is the nonadiabatic coupling term and the quantum population  $|C_1(t)|^2$  is considered constant during the small time interval  $\Delta t$ . We reckon that the velocity  $\dot{\mathbf{R}}$  is similar in different environments (at a given temperature) and that its direction is arbitrary. In the current OM2/MRCI calculations, the nonadiabatic coupling element component (in standard notation)

$$d_R^{01}(\mathbf{R}) = \overset{\text{CI}}{d_R^{01}}(\mathbf{R}) + \overset{\text{SCF}}{d_R^{01}}(\mathbf{R}) = \frac{h_R^{01}(\mathbf{R})}{\Delta E_{10}} + \sum_{ij} \gamma_{ij}^{01} \left\langle \phi_i(\mathbf{r}; \mathbf{R}) \left| \frac{\partial \phi_j(\mathbf{r}; \mathbf{R})}{\partial R} \right. \right\rangle \quad (2)$$

is approximated by the dominant first term. The norm  $\|\mathbf{h}^{01}\|$  of the  $S_0/S_1$  interstate coupling vector during the nonadiabatic

trajectories is plotted in Figure 3 against the simulation time. The left panel shows its evolution in the gas phase, in water, and in (dA)<sub>10</sub>. Obviously,  $\|\mathbf{h}^{01}\|$  of adenine is significantly smaller in the DNA strand than in the gas phase or in water (on average typically by a factor of 2). The biological environment of adenine in DNA thus lowers the nonadiabatic  $S_1 \rightarrow S_0$  hopping probability. Hence, the low hopping rate is at least partly due to electronic effects exerted by the environment.

To further explore these effects, we performed a QM/MM model study of a stacked 9H-adenine dimer (see Fig. 4), for a

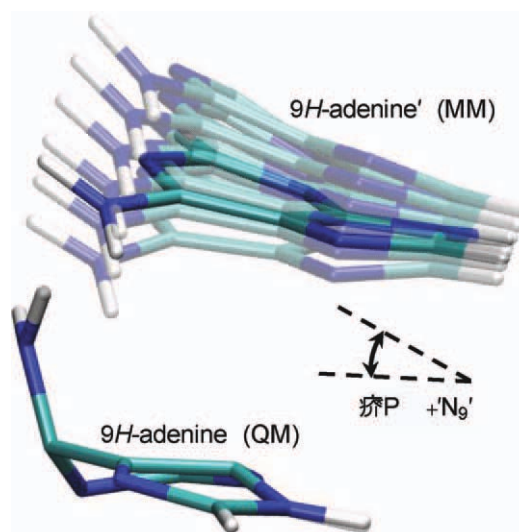


**Figure 4.** QM/MM model study of a stacked 9H-adenine dimer. The reference geometry is adapted from a hopping structure in the nonadiabatic dynamics simulations. Hydrogen atoms  $H_9$  and  $H_9'$  are added at the positions of the connecting sugar carbon atoms without optimization. The other geometries are generated by fixing the QM molecule (bottom) and rotating the MM molecule (top) upward such that the angle  $\angle(\text{N}_7\text{H}_9'\text{N}_9')$  is increased.



Table 1. QM/MM model study of a stacked 9H-adenine dimer: norms of  $\mathbf{h}$ ,  $\mathbf{Z}$ , and  $\mathbf{F}$  (in a.u.) at different conformations (see Fig. 4 and text).

$\angle(\text{N}_7\text{H}'_9\text{N}'_9)$ (°)	$r(\text{N}_6\text{N}_6')$ (Å)	$\ \mathbf{h}^{01}\ $ ( $10^{-02}$ )	static $\ \mathbf{h}^{01}\ $ ( $10^{-03}$ )	response $\ \mathbf{h}^{01}\ $ ( $10^{-02}$ )	$\ \mathbf{Z}\ $ ( $10^{-01}$ )	$\ \mathbf{F}_R\ $	$\Delta E_{10}$ ( $10^{-02}$ )
22.3	2.32	3.290	1.733	3.316	6.045	2.070	2.721
27.3	2.72	3.429	1.764	3.459	6.246	2.070	2.617
32.3	3.14	3.543	1.786	3.576	6.407	2.070	2.532
37.3	3.58	3.625	1.802	3.661	6.521	2.070	2.472
42.3	4.02	3.681	1.813	3.719	6.598	2.070	2.433
47.3	4.47	3.720	1.820	3.758	6.650	2.070	2.407
$\Delta_{\text{max}}/\%$ <sup>[a]</sup>		13.1	5.0	13.3	10.0	0.01	-11.6

[a] Maximum deviation (%) between the data in rows 1 and 6.

series of conformations with increasing monomer distances. The results are consistent with those for (dA)<sub>10</sub>: the nearer the adjacent DNA bases approach each other, the smaller  $\|\mathbf{h}^{01}\|$  becomes. There is a drop of  $\sim 5$  kcal mol<sup>-1</sup> Å<sup>-1</sup> ( $\sim 13\%$ ) when the C<sub>6</sub>-C<sub>6'</sub> distance is reduced from  $\sim 5$  to  $\sim 3$  Å (see Table 1). This effect is expected to be prominent in DNA oligomers due to their regularly stacked structure. By contrast, in aqueous solution, 9H-adenine is surrounded by more randomly distributed and moving water molecules so that there should be considerable cancellation of electronic effects from the environment.

The coupling vector component  $h_R^{01}$  for a given coordinate  $R$  is composed of static and response parts,<sup>[61]</sup>

$$h_R^{01}(\mathbf{R}) = \mathbf{C}^1(\mathbf{R})^* \frac{\partial \mathbf{H}}{\partial R} \mathbf{C}^0(\mathbf{R}) = \text{static } h_R^{01} + \text{response } h_R^{01}, \quad (3)$$

where the static term contributes only a small fraction ( $\sim 5\%$  in our model study, see Table 1) to the total first derivative nonadiabatic coupling norm. The response term is obtained by means of the Z-vector technique<sup>[62]</sup>:

$$\text{response } h_R^{01} = \mathbf{F}_R \cdot \mathbf{Z}, \quad (4)$$

where  $\mathbf{F}_R$  is the first derivative of the Fock matrix. Looking at the norms of the two vectors (see Table 1), we find that  $\mathbf{F}_R$  is basically constant at different monomer distances, while  $\mathbf{Z}$  varies to some extent. Being introduced to solve the coupled perturbed Hartree-Fock equations,<sup>[63]</sup> the vector  $\mathbf{Z}$  contains redundant and nonredundant parts that depend in a complicated manner on the two-electron integrals, orbital energies, two-electron transition densities and further terms, many of which are influenced by the MM point charges of the environment in a QM/MM calculation. We have not been able to attribute the changes in the vector  $\mathbf{Z}$  for different monomer distances to any single term.

**Energy gaps.** The energy gap  $\Delta E_{10}$  between the  $S_1$  and  $S_0$  states is another factor that directly affects the hopping probability, see eq. (2). In our nonadiabatic simulations for adenine, this gap quickly approaches zero in the gas phase and in water, and most of the hops occur at geometries with a small gap. By contrast, the gap remains sizable for most trajectories in (dA)<sub>10</sub> during stage II. This is illustrated in the middle panel of Figure 3, which clearly indicates that it is much harder for adenine in the DNA environment to reach conformations with a small energy gap, compared with the gas phase or aqueous

solution. It is again difficult to pinpoint the reason for this different behavior. Although the external MM point charges in the well-ordered DNA strand will polarize the QM adenine and thus affect the vertical excitation energy (i.e., the energy gap), it is not obvious that this will cause such a large difference (see Fig. 3). In our QM/MM model study of the stacked adenine dimer (Fig. 4), we see a trend in the right direction which seems, however, less pronounced: the energy gap  $\Delta E_{10}$  increases by  $\sim 12\%$  when the two 9H-adenine molecules move closer by  $\sim 2$  Å (see Table 1). The right panel of Figure 3 displays the computed nonadiabatic coupling matrix element  $\|\mathbf{h}^{01}\|/\Delta E_{10}$  along the computed trajectories of adenine *in vacuo*, water, and DNA. It is evident that the trends in  $\|\mathbf{h}^{01}\|$  (left panel) and  $\Delta E_{10}$  (middle panel) reinforce each other and make the  $S_1 \rightarrow S_0$  nonadiabatic hopping of adenine much less favorable in DNA than *in vacuo* or in water.

**Local  $S_1$  minimum near  ${}^6S_1$  conical intersection.** We have found another factor that may delay the hop events. There is a local  $S_1$  minimum of adenine in the gas phase, both at the OM2/MRCI and the CASSCF level (MOLPRO 2008.2<sup>[64]</sup>), the geometry of which is very close to that of the  ${}^6S_1$  conical intersection (see Supporting Information, Fig. S3). This minimum lies only 0.01 (0.11) eV below the conical intersection at the CASSCF (OM2/MRCI) level. We have reevaluated its energy by single-point CASPT2//CASSCF calculations and find it 0.19 eV below the  ${}^6S_1$  conical intersection at this level (compared with 0.01 eV in CASSCF). The drawback of these single-point calculations is, of course, that the underlying CASSCF geometries are not optimum for CASPT2; for example, the CASPT2 energies for the  $S_0$  and  $S_1$  states differ appreciably at the CASSCF conical intersection (by 0.80 eV). However, we also obtain this  $S_1$  minimum at the MRCIS level (MRCI with single excitations, COLUMBUS 5.9.1<sup>[65]</sup>, optimization performed by Dr. Mario Barbatti). Therefore, we are confident that it is not an artifact—at the MRCIS level it is even deeper than in OM2/MRCI (0.26 vs. 0.11 eV). A crossing region featuring such a PES topology, with a minimum lying lower than the conical intersection, is called a ‘tilted cone’<sup>[66]</sup> (see Supporting Information, Fig. S4). Further energies of this  $S_1$  local minimum [ $\text{min}(S_1)$ ] relative to the  ${}^6S_1$  conical intersection (computed at different levels) are summarized in the Supporting Information.

We have located analogous minima of adenine in (dA)<sub>10</sub> by geometry optimizations starting from the  ${}^6S_1$  hopping structures (see Supporting Information, Fig. S3d). At the QM/MM level, they are typically 0.2 eV or more below the associated conical intersections (compared with 0.11 eV in the gas phase),

**Table 2.** Single adenine in (dA)<sub>10</sub>: energies (in eV) of fully optimized S<sub>1</sub> and CI(S<sub>0</sub>/S<sub>1</sub>) structures relative to the corresponding optimized S<sub>0</sub> structures.

	t (fs)	S <sub>0</sub>			S <sub>1</sub>			CI		
		E (eV)	α (°)	β (°)	E (eV)	α (°)	β (°)	E (eV)	α (°)	β (°)
<sup>6</sup> S <sub>1</sub>	297	0.00	177.6	−1.7		n/a			n/a	
	524	0.00	178.7	−1.7	4.08	−142.3	2.0	5.30	−121.1	32.9
	623	0.00	178.9	1.7	4.07	−135.8	33.0	4.39	−122.6	36.5
	661	0.00	179.6	0.3	4.02	−136.6	26.3	4.31	−121.8	42.1
	861	0.00	177.8	0.2		n/a		4.86	−120.6	32.1
	890	0.00	178.5	0.1	4.17	−133.8	31.9	5.09	−120.7	39.8
	971	0.00	178.0	−0.3	4.05	−138.6	12.0	5.33	−118.9	−4.9
	1079	0.00	179.8	7.8	3.51	131.1	−20.7	4.21	120.9	−27.6
	1133	0.00	176.9	2.1	3.76	−135.7	31.4	4.83	−111.6	14.0
	1284	0.00	178.8	−0.1	3.63	−134.5	29.7	4.20	−121.6	37.7
<sup>2</sup> E	1481	0.00	178.8	2.1	3.81	−135.9	31.2	4.09	−125.8	39.1
	1014	0.00	170.7	82.6		n/a		0.24	171.4	72.4
	1382	0.00	177.7	2.4		n/a		4.44	172.7	64.6
	1491	0.00	178.5	−1.9		n/a		4.27	−179.1	−64.8

n/a: optimization not converged.  
 S<sub>1</sub>→S<sub>0</sub> hopping structures from the nonadiabatic dynamics were taken as starting geometries (hopping at time t). Dihedral angles: α = ∠(N<sub>1</sub>C<sub>5</sub>C<sub>6</sub>N<sub>6</sub>) and β = ∠(N<sub>1</sub>C<sub>2</sub>N<sub>3</sub>C<sub>4</sub>).

and the S<sub>1</sub>→S<sub>0</sub> gaps are substantial at these geometries. The out-of-plane distortion in these minima is comparable to, but somewhat smaller than that at the corresponding conical intersections, and the surface-hopping trajectories are thus likely to pass these minima before reaching the conical intersections in (dA)<sub>10</sub>. Thus, it is conceivable that the trajectories may get trapped for a while in this region, more so than in the gas phase, thus leading to a slower decay.

Because of the complexity of the QM/MM PES, there may be other local minima that can trap or delay the system. For example, in Tables 2 and 3, some optimizations converge to conformations close to conical intersection structures other than <sup>6</sup>S<sub>1</sub>, whereas alternative optimization routes (hop→CI→S<sub>0</sub> or S<sub>1</sub> in our case) may not lead to min'(S<sub>1</sub>) even in the case of <sup>6</sup>S<sub>1</sub>.

**Summary.** The initial distortion (stage I) of adenine in (dA)<sub>10</sub> is impeded by steric hindrance that arises from the constraints imposed by the rather rigid environment. The subsequent repopulation of the ground state, that is, stage II, is slowed down by small nonadiabatic coupling elements **d**<sup>01</sup>, which are caused by electronic effects of environment ( $\|\mathbf{h}^{01}\|$  and ΔE<sub>10</sub>) and conformational restraints (ΔE<sub>10</sub>). Strictly speaking, the nonadiabatic coupling term **R** · **d**<sup>01</sup> also depends on the nuclear velocities, which at a given temperature should, however, be similar in water and DNA. Stage II appears to be the rate-limiting step of the slow hopping process of adenine in single-strand DNA. We note in this context that the S<sub>1</sub> state of single adenine in the double strand (dA)<sub>10</sub>-(dT)<sub>10</sub> is also computed to have a similar (large) time constant even though it follows a different decay pathway

**Table 3.** Single adenine in (dA)<sub>10</sub>-(dT)<sub>10</sub>: energies (in eV) of fully optimized S<sub>1</sub> and CI(S<sub>0</sub>/S<sub>1</sub>) structures relative to the corresponding optimized S<sub>0</sub> structures. S<sub>1</sub>→S<sub>0</sub> hopping structures from the nonadiabatic dynamics were taken as starting geometries (hopping at time t).

	t (fs)	S <sub>0</sub>			S <sub>1</sub>			CI			
		E (eV)	α (°)	β (°)	E (eV)	α (°)	β (°)	E (eV)	α (°)	β (°)	
<sup>2</sup> E	186	0.00	−179.1	1.3	4.20	−179.4	59.0	4.31	174.5	64.2	
	283	0.00	−179.0	0.4	4.23	−177.8	55.7	4.27	174.6	64.3	
	360	0.00	−179.4	0.6	4.21	−177.9	57.6	4.43	174.7	62.6	
	403		n/a		–	176.6	62.7	–	176.4	62.6	
	620	0.00	−179.9	−0.5	4.20	178.9	61.0	4.26	174.5	63.5	
	942		n/a		–	179.2	61.9	–	174.2	64.8	
	943		n/a		–	−177.4	−64.5	–	−171.5	−68.3	
	984	0.00	−179.9	2.0	4.15	173.9	65.6	4.14	174.1	65.4	
	1116	0.00	−180.0	0.2	4.34	174.2	67.3	4.37	174.6	67.3	
	1120	0.00	−179.4	0.8	4.20	−178.2	55.8	4.21	174.6	65.1	
	1184	0.00	−179.4	−0.3	4.25	177.2	63.6	4.28	175.0	64.3	
	1260	0.00	−179.5	0.1	n/a			4.61	−174.6	−67.6	
	1375	0.00	−179.4	0.9	4.20	−176.4	56.2	4.52	175.5	63.6	
	1452	0.00	179.9	0.0	4.33	180.0	60.5	4.34	174.2	65.7	
	<sup>4</sup> S <sub>3</sub>	427		n/a			n/a		–	−168.9	14.7
		661	0.00	179.9	−0.5		n/a		4.58	−169.0	14.3
		1157	0.00	179.7	0.1	4.09	−174.3	9.4	4.73	−168.0	12.7
1238		0.00	−178.6	0.3	4.18	−173.3	10.2	4.86	−166.4	12.3	

Dihedral angles: α = ∠(N<sub>1</sub>C<sub>5</sub>C<sub>6</sub>N<sub>6</sub>) and β = ∠(N<sub>1</sub>C<sub>2</sub>N<sub>3</sub>C<sub>4</sub>).

(<sup>2</sup>E), with an out-of-plane bend of the C<sub>2</sub>H<sub>2</sub> moiety, that suffers from much less steric hindrance. Furthermore, in (dA)<sub>10</sub>, the existence of an S<sub>1</sub> minimum close to the dominant conical intersection (<sup>6</sup>S<sub>1</sub>) may further delay the hopping event (stage II).

### Decay channels

As already pointed out in the Introduction section, different experimental groups have arrived at different conclusions in the analysis and interpretation of their data. There is not yet a consensus on the localized or delocalized character of the relevant excited states and their role in the decay.<sup>[5,11]</sup> Given that the analysis of the experimental data usually gives rise to several different time constants, the nonadiabatic decay of excited DNA oligomers has multiple components,<sup>[1]</sup> and the physics of the decay thus apparently involves a mixture of various pathways and mechanisms—which may neither be fully localized nor fully delocalized. Monomeric mechanisms are believed to contribute to the multiexponential character of the decay in different ways.<sup>[2]</sup> Buchvarov et al.<sup>[5]</sup> have assumed the localized excitations to occur in disordered stacked sequences, and they have assigned the observed subpicosecond time constant to monomeric ICs. These authors have stressed the significance of monomer-type pathways competing with other delocalized states as “critical from an evolutionary viewpoint.”<sup>[5]</sup> Although being generally assigned to unstacked or poorly stacked domains,<sup>[2]</sup> there is to our knowledge no unequivocal experimental evidence that rules out monomeric decay in stacked domains and restricts them to unstacked (or poorly stacked) domains. Indeed, Phillips and coworkers<sup>[11]</sup> have suggested in their experimental work that photoexcitation of adenine oligomers initially leads to entirely localized FC states. Although we acknowledge the importance of delocalized states (such as excitons and excimers), our strategy in this work is to study the dynamics of the monomeric states as a limiting case and a first step toward a more complete simulation of DNA models that would also include delocalized states. This focus has allowed us to identify two major qualitative effects, namely the substantial deceleration of monomeric decay in the DNA oligomers (see above) and the switch in the decay mechanism in the double-strand oligomer because of hydrogen bonding (see below).

As already noted, we find in our nonadiabatic dynamics simulations two distinct IC pathways for the nonadiabatic decay of a single adenine in (dA)<sub>10</sub> and (dA)<sub>10</sub>·(dT)<sub>10</sub>. Starting from dozens of hopping geometries, we have optimized the structures of the corresponding conical intersection and of the associated S<sub>0</sub> and S<sub>1</sub> minima at the QM/MM level (see Tables 2 and 3). These structures can be distinguished and characterized by the dihedral angles ∠(N<sub>1</sub>C<sub>5</sub>C<sub>6</sub>N<sub>6</sub>) and ∠(N<sub>1</sub>C<sub>2</sub>N<sub>3</sub>C<sub>4</sub>). The decay via the <sup>6</sup>S<sub>1</sub> mechanism is dominant in the single strand but is completely locked in the latter. We ascribe this difference to interstrand hydrogen-bonding interactions that are present in double strands but are of course missing in single strands. The value of the N<sub>6</sub>H<sup>A</sup>...O<sub>2</sub><sup>T</sup> distance (between the base pair of QM adenine and MM thymine) is plotted in Figure 5 against simulation time. In most of the computed trajec-

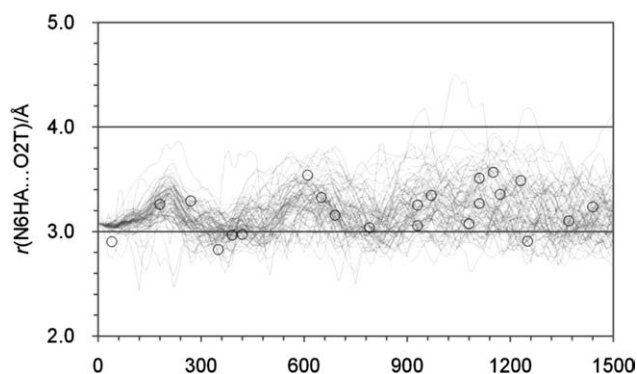


Figure 5. Hydrogen bond lengths  $r(\text{N}_6\text{H}^{\text{A}}\cdots\text{O}_2^{\text{T}})$  (gray dotted lines: ..... ) during all surface-hopping trajectories for the entire simulation time (fs) for adenine in (dA)<sub>10</sub>·(dT)<sub>10</sub>. Black circles (○) denote hopping events. Hydrogen bond length in the crystal: 2.95 Å.<sup>[67]</sup>

ries for (dA)<sub>10</sub>·(dT)<sub>10</sub>, this distance remains between 2.8 and 3.6 Å, that is, reasonably close to the equilibrium value of 2.95 Å in the crystal structure.<sup>[67]</sup> In (dA)<sub>10</sub>, the decay through both competing pathways occurs with a ratio of approximately 4:1 (<sup>6</sup>S<sub>1</sub> vs. <sup>2</sup>E), despite the more pronounced steric hindrance on the <sup>6</sup>S<sub>1</sub> pathway. In (dA)<sub>10</sub>·(dT)<sub>10</sub>, the stabilization energy of the Watson–Crick (WC) base pair gained from the N<sub>6</sub>H<sup>A</sup>...O<sub>2</sub><sup>T</sup> hydrogen bonding (see Ref. [68] for a detailed discussion) favors the <sup>2</sup>E over the <sup>6</sup>S<sub>1</sub> pathway. Actually, this effect was already predicted in 2005 by Perun et al.<sup>[69]</sup> in their CASPT2//CASSCF study of the radiationless decay mechanisms of electronically excited 9H-adenine in the gas phase: they pointed out that the required out-of-plane deformations could become inactive in the WC base pairs because of strong interbase hydrogen bonding. Finally, as a cautionary note, we emphasize that the hydrogen bond occurs between QM adenine and MM thymine in our model; hence, we cannot capture any hydrogen or electron transfer processes mediated through this hydrogen bond, which have been studied both theoretically<sup>[31,70]</sup> and experimentally.<sup>[15,71]</sup>

During our nonadiabatic dynamics simulations, 5 of 19 (S<sub>1</sub>→S<sub>0</sub>) trajectories in (dA)<sub>10</sub> and 4 of 22 in (dA)<sub>10</sub>·(dT)<sub>10</sub> led to dissociation in the excited state before hopping to the ground state. We report these results at face value, as they come out of the simulations. We currently view these side reactions as follows: the chosen (12,10) active space for the OM2/MRCI treatment is somewhat larger than needed for a minimal description of the three lowest excited states. For “normal” geometries, for example, in the FC region, it includes four virtual orbitals, that is, the three lowest π\* orbitals and the lowest σ\* orbital (which is compact as diffuse Rydberg-type orbitals are not present in the OM2 minimal basis). This active space will thus in principle allow for σ-bond breaking, as dissociative πσ\* states can be accessed through some conical intersections involving the optically prepared S<sub>1</sub> or S<sub>2</sub> state. During the dynamics in the DNA environment, it is conceivable that unusual geometries are reached where other types of antibonding orbitals might mix into the active space and open new reactive pathways. Their occurrence should not affect our

main qualitative conclusions, because the trajectories are independent from each other. Such bond-breaking events have also been reported in other on-the-fly surface-hopping dynamics studies, for example, at the *ab initio* level in Refs. [56] and [72]. We also note the suggestion by Chung et al.<sup>[73]</sup> that singlet excitation of 9*H*-adenine can lead to photodissociation in the gas phase via conical intersections involving the  $^1\pi\sigma^*$  states.

## Conclusions

This study addresses the role of dynamical effects on the excited-state decay for solvated single-stranded and double-stranded DNA oligomer models. Our simulations have uncovered two such major effects: first, the monomeric decay in the DNA oligomers is decelerated by one order of magnitude compared with adenine in the gas phase or in solution; second, the interstrand hydrogen bonding causes the dominant decay mechanism in the double-stranded oligomer to be different from that in the single-stranded oligomer. In this article, we have analyzed both these effects in detail to understand how the DNA environment influences both the emissive and nonradiative decay of an excited adenine monomer. During the initial stage I, the steric hindrance which arises from the close contact of neighboring stacked bases impedes the necessary out-of-plane motion to reach suitable conical intersection structures. After arriving at such distorted geometries, the system remains for a rather long time in this region of the excited-state PES (stage II) because of the small nonadiabatic coupling element. The latter directly determines the hopping probability; compared with adenine in the gas phase or in aqueous solution, it is much reduced as a result of electronic effects of the environment and a larger inter-state energy gap. Interstrand hydrogen bonding in double strands prevents the out-of-plane distortion of the adenine amino group and thus causes a switch to another decay channel involving an out-of-plane bending of the C<sub>2</sub>H<sub>2</sub> moiety.


Finally, we emphasize again that our present work addresses the limiting case of localized excitations in an adenine monomer embedded in solvated DNA model oligomers, and their subsequent decay to the electronic ground state. We aim at identifying the leading effects driving the ultrafast decay in this limit. Delocalized states and processes, which are not covered in the current model, can be taken into consideration in future work by extending the QM subsystem along the stacking direction. Likewise, the effects of proton and charge transfer through base pairs can be modeled by extending the QM region to a WC pair. Combining the information from such future studies with our present findings will hopefully help to arrive at a more complete picture of DNA photochemistry.

## Acknowledgments

The authors are grateful to Dr. Mario Barbatti and Dr. Eduardo Fabiano for valuable discussions and to Dr. Tell Tuttle for his help in setting up the QM/MM calculations.

**Keywords:** DNA · fluorescence · hydrogen bond · nonadiabatic coupling · surface hopping

How to cite this article: Y. Lu, Z. Lan, W. Thiel, *J. Comput. Chem.* **2012**, *33*, 1225–1235. DOI: 10.1002/jcc.22952

 Additional Supporting Information may be found in the online version of this article.

- [1] C. T. Middleton, K. de La Harpe, C. Su, Y. K. Law, C. E. Crespo-Hernández, B. Kohler, *Annu. Rev. Phys. Chem.* **2009**, *60*, 217.
- [2] C. E. Crespo-Hernández, B. Cohen, B. Kohler, *Nature* **2005**, *436*, 1141.
- [3] T. Takaya, C. Su, K. de La Harpe, C. E. Crespo-Hernández, B. Kohler, *Proc. Natl. Acad. Sci. U.S.A.* **2008**, *105*, 10285.
- [4] B. Kohler, *J. Phys. Chem. Lett.* **2010**, *1*, 2047.
- [5] I. Buchvarov, Q. Wang, M. Raytchev, A. Trifonov, T. Fiebig, *Proc. Natl. Acad. Sci. U.S.A.* **2007**, *104*, 4794.
- [6] T. Fiebig, *J. Phys. Chem. B* **2009**, *113*, 9348.
- [7] (a) D. Markovitsi, A. Sharonov, D. Onidas, T. Gustavsson, *ChemPhys Chem* **2003**, *4*, 303; (b) D. Markovitsi, T. Gustavsson, F. Talbot, *Photochem. Photobiol. Sci.* **2007**, *6*, 717; (c) D. Markovitsi, T. Gustavsson, I. Vayá, *J. Phys. Chem. Lett.* **2010**, *1*, 3271.
- [8] D. Onidas, T. Gustavsson, E. Lazzarotto, D. Markovitsi, *J. Phys. Chem. B* **2007**, *111*, 9644.
- [9] (a) J. Frenkel, *Phys. Rev.* **1931**, *37*, 1276; (b) E. I. Rashbah, M. D. Sturge, *Excitons*; North-Holland: Amsterdam, **1982**; (c) A. S. Davydov, *Theory of Molecular Excitons*; Plenum Press: New York, **1971**.
- [10] N. Schwalb, F. Temps, *Science* **2008**, *322*, 243.
- [11] W.-M. Kwok, C. Ma, D. L. Phillips, *J. Am. Chem. Soc.* **2006**, *128*, 11894.
- [12] L. Hu, Y. Zhao, F. Wang, G. Chen, C. Ma, W.-M. Kwok, D. L. Phillips, *J. Phys. Chem. B* **2007**, *111*, 11812.
- [13] L. Jensen, N. Govind, *J. Phys. Chem. A* **2009**, *113*, 9761.
- [14] (a) P. Jurečka, J. Šponer, J. Černý, P. Hobza, *Phys. Chem. Chem. Phys.* **2006**, *8*, 1985; (b) K. B. Bravaya, O. Kostko, M. Ahmed, A. Krylov, *Phys. Chem. Chem. Phys.* **2010**, *12*, 2292.
- [15] A. Abo-Riziq, L. Grace, E. Nir, M. Kabelac, P. Hobza, M. S. de Vries, *Proc. Natl. Acad. Sci. U.S.A.* **2005**, *102*, 20.
- [16] D. Nachtigallová, P. Hobza, H.-H. Ritze, *Phys. Chem. Chem. Phys.* **2008**, *10*, 5689.
- [17] (a) H. Tachikawa, H. Kawabata, *Chem. Phys. Lett.* **2008**, *462*, 321; (b) J. J. Serrano-Pérez, I. González-Ramírez, P. B. Coto, M. Merchán, L. Serrano-Andrés, *J. Phys. Chem. B* **2008**, *112*, 14096.
- [18] (a) E. Emanuele, D. Markovitsi, P. Millié, K. Zakrzewska, *ChemPhysChem* **2005**, *6*, 1387; (b) E. R. Bittner, *J. Chem. Phys.* **2006**, *125*, 094909; (c) S. Tonzani, G. C. Schatz, *J. Am. Chem. Soc.* **2008**, *130*, 7607; (d) G. Olaso-González, M. Merchán, L. Serrano-Andrés, *J. Am. Chem. Soc.* **2009**, *131*, 4368.
- [19] D. Nachtigallová, T. Zelený, M. Ruckebauer, T. Müller, M. Barbatti, P. Hobza, H. Lischka, *J. Am. Chem. Soc.* **2010**, *132*, 8261–8263.
- [20] (a) S. Miertus, E. Scrocco, J. Tomasi, *Chem. Phys. Lett.* **1981**, *55*, 117; (b) J. Tomasi, B. Mennucci, R. Cammi, *Chem. Rev.* **2005**, *105*, 2999; (c) M. Cossi, N. Rega, G. Scalmani, V. Barone, *J. Chem. Phys.* **2001**, *114*, 5691.
- [21] (a) F. Santoro, V. Barone, R. Improta, *Proc. Natl. Acad. Sci. U.S.A.* **2007**, *104*, 9931; (b) R. Improta, *Phys. Chem. Chem. Phys.* **2008**, *10*, 2656; (c) R. Improta, F. Santoro, V. Barone, A. Lami, *J. Phys. Chem. A* **2009**, *113*, 15346; (d) F. Santoro, V. Barone, A. Lami, R. Improta, *Phys. Chem. Chem. Phys.* **2010**, *12*, 4934; (e) R. Improta, V. Barone, *Angew. Chem. Int. Ed.* **2011**, *50*, 12016.
- [22] (a) F. Santoro, V. Barone, R. Improta, *ChemPhysChem* **2008**, *9*, 2531; (b) F. Santoro, V. Barone, R. Improta, *J. Am. Chem. Soc.* **2009**, *131*, 15232.
- [23] (a) J. E. Ridley, M. C. Zerner, *Theor. Chim. Acta* **1973**, *32*, 111; (b) M. C. Zerner, G. H. Lowe, R. F. Kirchner, U. T. Mueller-Westerhoff, *J. Am. Chem. Soc.* **1980**, *102*, 589; (c) M. C. Zerner, P. C. de Mello, M. Hehenberger, *Int. J. Quantum Chem.* **1982**, *21*, 251; (d) M. C. Zerner, In *Reviews of Computational Chemistry*; K. B. Lipkowitz, D. B. Boyd, Eds.; VCH Publishing, New York, **1991**; pp. 313–365.
- [24] E. B. Starikov, G. Cuniberti, S. Tanaka, *J. Phys. Chem. B* **2009**, *113*, 10428.



- [25] A. A. Voityuk, *Phys. Chem. Chem. Phys.* **2008**, *12*, 7403.
- [26] A. N. Alexandrova, J. C. Tully, G. Granucci, *J. Phys. Chem. B* **2010**, *114*, 12116.
- [27] G. Granucci, M. Persico, A. Toniolo, *J. Chem. Phys.* **2001**, *114*, 10608.
- [28] M. J. S. Dewar, E. F. Zebisch, E. F. Healy, J. J. P. Stewart, *J. Am. Chem. Soc.* **1985**, *107*, 3902.
- [29] (a) J. J. P. Stewart, *J. Comput. Chem.* **1989**, *10*, 209; (b) J. J. P. Stewart, *J. Comput. Chem.* **1989**, *10*, 221.
- [30] (a) H.-M. Senn, W. Thiel, *Top. Curr. Chem.* **2007**, *268*, 173; (b) H.-M. Senn, W. Thiel, *Angew. Chem.* **2009**, *121*, 1220; (c) H.-M. Senn, W. Thiel, *Angew. Chem. Int. Ed.* **2009**, *48*, 1198.
- [31] G. Groenhof, L. V. Schäfer, M. Boggio-Pasqua, M. Goette, H. Grubmüller, M. A. Robb, *J. Am. Chem. Soc.* **2007**, *129*, 6812.
- [32] A. W. Lange, J. M. Herbert, *J. Am. Chem. Soc.* **2009**, *131*, 3913.
- [33] I. Conti, P. Altoè, M. Stenta, M. Garavelli, G. Orlandi, *Phys. Chem. Chem. Phys.* **2010**, *12*, 5016.
- [34] (a) W. Weber, PhD thesis, Universität Zürich (Switzerland), **1996**; (b) W. Weber, W. Thiel, *Theor. Chem. Acc.* **2000**, *103*, 495; (c) A. Koslowski, M. E. Beck, W. Thiel, *J. Comput. Chem.* **2003**, *24*, 714.
- [35] M. R. Silva-Junior, W. Thiel, *J. Chem. Theor. Comput.* **2010**, *6*, 1546.
- [36] E. Fabiano, W. Thiel, *J. Phys. Chem. A* **2008**, *112*, 6859.
- [37] Z. Lan, Y. Lu, E. Fabiano, W. Thiel, *ChemPhysChem* **2011**, *12*, 1989.
- [38] (a) Y. Lu, Z. Lan, W. Thiel, *Angew. Chem.* **2011**, *123*, 6996; (b) Y. Lu, Z. Lan, W. Thiel, *Angew. Chem. Int. Ed.* **2011**, *50*, 6864.
- [39] Maestro, version 7.5, Schrödinger, LLC, New York, NY, **2005**.
- [40] W. L. Jorgensen, J. Chandrasekhar, J. D. Madura, R. W. Impey, M. L. Klein, *J. Chem. Phys.* **1982**, *79*, 926.
- [41] SYBYL 8.0, Tripos International, 1699 South Hanley, St. Louis, Missouri, 63144, USA.
- [42] (a) P. Sherwood, M. S. de Vries, M. F. Guest, G. Schreckenbach, C. R. A. Catlow, S. A. French, A. A. Sokol, S. T. Bromley, W. Thiel, A. J. Turner, S. Billeter, F. Terstegen, S. Thiel, J. Kendrick, S. C. Rogers, J. Casci, M. Watson, F. King, E. Karlsen, M. Sjøvoll, A. Fahmi, A. Schäfer, C. Lennartz, *J. Mol. Struct. (Theochem.)* **2003**, *632*, 1; (b) Available at: <http://www.chemshell.org>. Accessed on: 30 November 2011.
- [43] W. Smith, *Mol. Simul.* **2006**, *32*, 933.
- [44] (a) A. D. Mackerell, N. K. Banavali, *J. Comp. Chem.* **2000**, *21*, 105; (b) N. Foloppe, A. D. Mackerell, *J. Comp. Chem.* **2000**, *21*, 86.
- [45] (a) A. Warshel, M. Kato, A. V. Pislakov, *J. Chem. Theory Comput.* **2007**, *3*, 2034; (b) E. Vladimirov, A. Ivanova, N. Rösch, *J. Phys. Chem. B* **2009**, *113*, 4425; (c) M. A. Ditzler, M. Otyepka, J. Šponer, N. G. Walter, *Acc. Chem. Res.* **2010**, *43*, 40.
- [46] (a) Y. Hagiwara, T. Ohta, M. Tateno, *J. Phys. Condens. Matter* **2009**, *21*, 064234; (b) T. Kubař, U. Kleinekathöfer, M. Elstner, *J. Phys. Chem. B* **2009**, *113*, 13107; (c) S. Keinan, R. Venkatramani, A. Balaeff, D. N. Beratan, *J. Phys. Chem. C* **2010**, *114*, 20496; (d) E. Cauët, M. Valiev, J. H. Weare, *J. Phys. Chem. B* **2010**, *114*, 5886.
- [47] (a) P. Altoè, A. Cembran, M. Olivucci, M. Garavelli, *Proc. Natl. Acad. Sci. U.S.A.* **2010**, *107*, 20172; (b) M. Ruckebauer, M. Barbatti, B. Sellner, T. Muller, H. Lischka, *J. Phys. Chem. A* **2010**, *114*, 12585; (c) M.-E. Moret, I. Tavernelli, M. Chergui, U. Rothlisberger, *Chem. Eur. J.* **2010**, *16*, 5889; (d) A. M. Virshup, C. Punwong, T. V. Pogorelov, B. A. Lindquist, C. Ko, T. J. Martínez, *J. Phys. Chem. B* **2009**, *113*, 3280.
- [48] D. P. Geerke, S. Thiel, W. Thiel, W. F. van Gunsteren, *J. Chem. Theory Comput.* **2007**, *3*, 1499.
- [49] (a) J. C. Tully, *J. Chem. Phys.* **1990**, *93*, 1061; (b) S. Hammes-Schiffer, J. C. Tully, *J. Chem. Phys.* **1994**, *101*, 4657.
- [50] E. Fabiano, Z. Lan, Y. Lu, W. Thiel, In *Conical Intersections: Theory Computation and Experiment*; H. Köppel, W. Domcke, D. R. Yarkony, Eds.; World Scientific: Singapore, **2011**; pp. 463–496.
- [51] J. Kästner, J. M. Carr, T. W. Keal, W. Thiel, A. Wander, P. Sherwood, *J. Phys. Chem. A* **2009**, *113*, 11856.
- [52] (a) L. B. Clark, G. G. Peschel, I. Tinoco, Jr., *J. Phys. Chem.* **1965**, *69*, 3615; (b) L. Li, D. M. Lubman, *Anal. Chem.* **1987**, *59*, 2538; (c) H. Du, R.-C. A. Fu, J. Li, L. A. Corkan, J. S. Lindsey, *Photochem. Photobiol. Sci.* **1998**, *68*, 141.
- [53] B. Bouvier, J. P. Dognon, R. Lavery, D. Markovitsi, P. Millié, D. Onidas, K. Zakrzewska, *J. Phys. Chem. B* **2003**, *107*, 13512.
- [54] D. Markovitsi, T. Gustavsson, A. Banyasz, *Mutat. Res. Rev.* **2010**, *704*, 21.
- [55] (a) G. Ge, S. Georghiou, *Photochem. Photobiol. Sci.* **1991**, *54*, 477; (b) I. Vayá, T. Gustavsson, F.-A. Miannay, T. Douki, D. Markovitsi, *J. Am. Chem. Soc.* **2010**, *132*, 11834.
- [56] M. Barbatti, H. Lischka, *J. Am. Chem. Soc.* **2008**, *130*, 6831.
- [57] A. Bondi, *J. Phys. Chem.* **1964**, *68*, 441.
- [58] (a) J. A. McCammon, P. G. Wolynes, M. Karplus, *Biochemistry* **1979**, *18*, 927; (b) B. R. Brooks, R. E. Bruccoleri, B. D. Olafson, D. J. States, S. Swaminathan, M. Karplus, *J. Comput. Chem.* **1983**, *4*, 187.
- [59] V. Leskovic, *Comprehensive Enzyme Kinetics*; Kluwer Academic/Plenum Publishers: New York, **2003**.
- [60] (a) G. R. Desiraju, T. Steiner, *The Weak Hydrogen Bond in Structural Chemistry and Biology*; Oxford University Press: Oxford, **1999**; (b) D. A. Rodham, S. Suzuki, R. D. Suenram, F. J. Lovas, S. Dasgupta, W. A. Goddard, III, G. A. Blake, *Nature* **1993**, *362*, 735.
- [61] (a) S. Patchkovskii, W. Thiel, *Theor. Chim. Acta* **1996**, *93*, 87; (b) S. Patchkovskii, W. Thiel, *Theor. Chem. Acc.* **1997**, *98*, 1.
- [62] N. C. Handy, H. F. Schaefer, III, *J. Chem. Phys.* **1984**, *81*, 5031.
- [63] J. Gerratt, I. M. Mills, *J. Chem. Phys.* **1968**, *49*, 1719.
- [64] (a) H.-J. Werner, P. J. Knowles, *J. Chem. Phys.* **1985**, *82*, 5053; (b) P. J. Knowles, H.-J. Werner, *Chem. Phys. Lett.* **1985**, *115*, 259.
- [65] H. Lischka, R. Shepard, I. Shavitt, R. M. Pitzer, M. Dallos, Th. Müller, P. G. Szalay, F. B. Brown, R. Ahlrichs, H. J. Böhm, A. Chang, D. C. Comeau, R. Gdanitz, H. Dachsel, C. Ehrhardt, M. Ernzerhof, P. Höchtl, S. Irle, G. Kedziora, T. Kovar, V. Parasuk, M. J. M. Pepper, P. Scharf, H. Schiffer, M. Schindler, M. Schüler, M. Seth, E. A. Stahlberg, J.-G. Zhao, S. Yabushita, Z. Zhang, M. Barbatti, S. Matsika, M. Schuurmann, D. R. Yarkony, S. R. Brozell, E. V. Beck, J.-P. Blaudeau, COLUMBUS, an ab initio electronic structure program, release 5.9.1, **2006**.
- [66] D. R. Yarkony, *J. Phys. Chem. A* **2001**, *105*, 6277.
- [67] W. Saenger, *Principles of Nucleic Acid Structure*; Springer Verlag: New York, Berlin, Heidelberg, Tokyo, **1984**.
- [68] K. Brameld, S. Dasgupta, W. A. Goddard, III, *J. Phys. Chem. B* **1997**, *101*, 4851.
- [69] S. Perun, A. L. Sobolewski, W. Domcke, *J. Am. Chem. Soc.* **2005**, *127*, 6257.
- [70] (a) A. L. Sobolewski, W. Domcke, C. Hättig, *Proc. Natl. Acad. Sci. U.S.A.* **2005**, *102*, 17903; (b) P. R. L. Markwick, N. L. Doltsinis, *J. Chem. Phys.* **2007**, *126*, 175102; (c) T. Schultz, E. Samoylova, W. Radloff, I. V. Hertel, A. L. Sobolewski, W. Domcke, *Science* **2004**, *306*, 1765; (d) S. Perun, A. L. Sobolewski, W. Domcke, *J. Phys. Chem. A* **2006**, *110*, 9031.
- [71] N. K. Schwalb, F. Temps, *J. Am. Chem. Soc.* **2007**, *129*, 9272.
- [72] I. Antol, M. Eckert-Maksić, M. Barbatti, H. Lischka, *J. Chem. Phys.* **2007**, *127*, 234303.
- [73] W. C. Chung, Z. Lan, Y. Ohtsuki, N. Shimakura, W. Domcke, Y. Fujimura, *Phys. Chem. Chem. Phys.* **2007**, *9*, 2075.

Received: 1 December 2011  
 Revised: 9 January 2012  
 Accepted: 16 January 2012  
 Published online on 13 March 2012



paper (5)

***Nonadiabatic Decay Dynamics of a Benzylidene  
Malononitrile***

Z. Lan,<sup>a</sup> Y. Lu,<sup>a</sup> O. Weingart, and W. Thiel

*J. Phys. Chem. A*, **2012**, *116*, 1510-1518.

---

<sup>a</sup> contributed equally



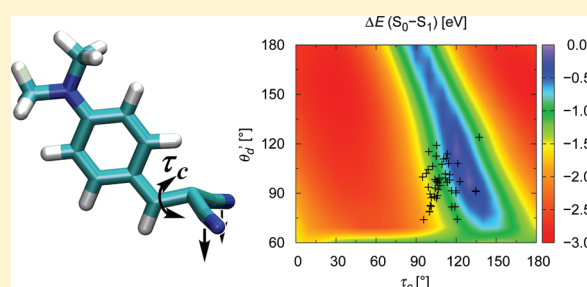


## Nonadiabatic Decay Dynamics of a Benzylidene Malononitrile

Zhenggang Lan,<sup>\*,†,¶</sup> You Lu,<sup>‡,¶</sup> Oliver Weingart,<sup>‡</sup> and Walter Thiel<sup>\*,‡</sup><sup>†</sup>Qingdao Institute of Bioenergy and Bioprocess Technology, Chinese Academy of Sciences, 189 Songling Road, Qingdao, 266101 Shandong, China<sup>‡</sup>Max-Planck-Institut für Kohlenforschung, Kaiser-Wilhelm-Platz 1, D-45470, Mülheim an der Ruhr, Germany

## Supporting Information

**ABSTRACT:** The photoinduced nonadiabatic decay dynamics of 2-[4-(dimethylamino)benzylidene]malononitrile (DMN) in the gas phase is investigated at the semiempirical OM2/MRCI level using surface hopping simulations. A lifetime of 1.2 ps is predicted for the  $S_1$  state, in accordance with experimental observation. The dominant reaction coordinate is found to be the twisting around the C7=C8 double bond accompanied by pronounced pyramidalization at the C8 atom. Motion along this coordinate leads to the lowest-energy conical intersection ( $CI_{01a}$ ). Several other  $S_0/S_1$  conical intersections have also been located by full optimization but play no role in the dynamics. The time-resolved fluorescence spectrum of DMN is simulated by computing emission energies and oscillator strengths along the trajectories. It compares well with the experimental spectrum. The use of different active spaces in the OM2/MRCI calculations yields similar results and thus demonstrates their internal consistency.



## 1. INTRODUCTION

Benzylidene malononitriles represent a group of disubstituted benzenes of the type D-Ph-A, where D is an electron donor and A is an electron acceptor. Their photophysics and photochemistry have aroused much interest<sup>1–26</sup> because the photoinduced processes in these molecules are highly sensitive to the interplay between their D → A push–pull electronic properties and the surrounding environment. Several groups have chosen 2-[4-(dimethylamino)benzylidene]malononitrile (DMN, see Figure 1a) and its derivatives to investigate the photoinduced processes of benzylidene malononitriles in different environments.<sup>1–26</sup> The first singlet excited state ( $S_1$ ) of DMN and DMN derivatives has a large oscillator strength and thus gives rise to an intense absorption band.<sup>1–3,23–26</sup> Its fluorescence quantum yield strongly depends on the environment.<sup>1–19</sup> The fluorescence emission is rather weak in low-viscosity solutions (indicating the existence of efficient nonradiative processes) but is significantly enhanced when the viscosity of the surrounding medium increases.<sup>3,4</sup> The  $S_1$  state shows considerable charge-transfer character, and hence, the fluorescence is also strongly dependent on the polarity of the solvent.<sup>1–10</sup> Therefore, DMN and its derivatives are often used to probe the polarity and microviscosity of solvents,<sup>1,8,10,13</sup> polymers,<sup>9,15,16</sup> ionic liquids,<sup>4,17,20</sup> and biological media.<sup>11,14,18</sup>

Despite this broad spectrum of applications, our understanding of the excited-state dynamics of DMN is still quite limited. All previous studies agree that fast  $S_1 \rightarrow S_0$  internal conversion is responsible for the fluorescence quenching and the nonradiative decay of these systems.<sup>1–13,15–22</sup> Recent time-resolved experiments have shown that this internal conversion proceeds with time constants of 1–5 ps in low-viscosity media

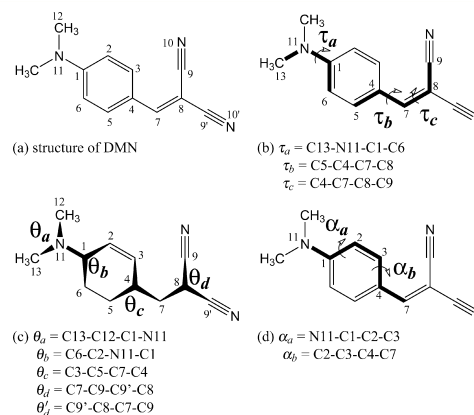


**Figure 1.** Conventions used for DMN in this work: (a) chemical structure and atom numbering; (b) definition of dihedral angles  $\tau_a$ ,  $\tau_b$ , and  $\tau_c$  for bond twisting; (c) definition of dihedral angles  $\theta_a$ ,  $\theta_b$ ,  $\theta_c$ , and  $\theta_d$  for pyramidalization; and (d) definition of dihedral angles  $\alpha_a$  and  $\alpha_b$  for out-of-plane motion.

and becomes slower in more viscous solutions.<sup>3,4</sup> While there is consensus about the existence of a fast  $S_1 \rightarrow S_0$  internal conversion, various conflicting proposals have been made concerning its mechanism.<sup>1–4,6–13,15–22</sup> Some authors have suggested that twisting motions around the C1–N11 and/or the C4–C7 bond (Figure 1) are responsible for the fluorescence

Received: December 7, 2011

Revised: January 18, 2012

Published: January 19, 2012

quenching,<sup>6–13,15–18,20</sup> in analogy to the twisted intramolecular charge-transfer (TICT) mechanism observed in other push–pull chromophores. Others have proposed that the isomerization of the C7=C8 double bond causes the quenching.<sup>10,13,15</sup> Combinations of all of these motions have also been considered to be involved in the  $S_1 \rightarrow S_0$  decay.<sup>1–4</sup>

The excited-state properties of DMN and its derivatives have been the subject of a number of recent theoretical studies, which have mostly addressed the electronic structure of the  $S_1$  state.<sup>1,3,21–26</sup> Many of these theoretical calculations focused on the Franck–Condon region<sup>23–26</sup> that can be accessed by electronic absorption or resonance Raman spectroscopy, while only limited efforts were made to understand the mechanism of the  $S_1 \rightarrow S_0$  decay.<sup>1,3</sup> These latter studies concluded that the nonradiative decay is driven by internal torsion around the C7=C8 double bond that brings the system to an  $S_0/S_1$  conical intersection (CI),<sup>27–29</sup> thus enabling the fast  $S_1 \rightarrow S_0$  internal conversion. It was shown that dynamics simulations using a one-dimensional model potential energy surface (PES) reproduce the experimental emission spectra reasonably well.<sup>3</sup>

In this article, we aim at a more precise atomistic understanding of the  $S_1 \rightarrow S_0$  decay mechanism. For this purpose, we perform nonadiabatic dynamics simulations of DMN using on-the-fly surface hopping methods.<sup>30–32</sup> These surface hopping trajectory calculations provide very detailed insight into photoinduced processes. Here, we focus on the dynamics of an isolated DMN molecule, explicitly including all of its 72 nuclear degrees of freedom, as a first step toward future studies of DMN in different solvent environments. The semiempirical OM2/MRCI<sup>33–37</sup> approach, which provides a reasonable compromise between computational cost and accuracy, is used to calculate the input data for the surface hopping simulations (energies, gradients, and nonadiabatic couplings). It has been applied successfully in a number of recent excited-state studies on larger molecules.<sup>38–45</sup> In principle, it would clearly be desirable to employ high-level correlated ab initio methods in such surface hopping studies, but this is hardly feasible for a system as large as DMN. Time-dependent density functional theory (TDDFT) faces well-known problems with large conjugated systems,<sup>46</sup> charge-transfer states,<sup>47,48</sup> and quasi-degenerate situations as encountered around conical intersections<sup>49</sup> and is therefore less suitable for our present purposes.

## 2. COMPUTATIONAL DETAILS

All calculations were performed with a development version of the MNDO program.<sup>50</sup> The semiempirical orthogonalization model 2 (OM2)<sup>33–35</sup> combined with multireference configuration interaction (MRCI)<sup>36</sup> was employed to calculate the relevant energies, gradients, and nonadiabatic couplings. The restricted open-shell Hartree–Fock (ROHF) formalism was used in the self-consistent field (SCF) calculations as it provided a better description of the excited-state wave functions. The configurations of the MRCI expansion were generated from three reference configurations (the closed-shell ground-state configuration and single and double HOMO–LUMO excitations from the closed-shell configuration). The CI treatment always included all single and double excitations from these three reference configurations (MRCI-SD) and, in the case of the (12,12) active space (AS) (see below), also all triple and quadruple excitations (MRCI-SDTQ).

Geometry optimizations of the ground-state and excited-state minima were performed to study the DMN energetics.

The minimum-energy structures of the  $S_0/S_1$  conical intersections were located by using the Lagrange–Newton method<sup>27,28,37</sup> and the gradient-projection method.<sup>27,29,37</sup> Reaction paths were constructed by linear interpolation between the ground-state minimum and the relevant conical intersection structures.

The photoinduced nonadiabatic dynamics of DMN was studied by on-the-fly simulations using Tully’s surface hopping algorithm.<sup>30–32</sup> The initial geometries and velocities were generated from the Wigner distribution function of normal modes.<sup>51,52</sup> The initial sampling was performed by evaluating the transition probability at each generated geometry.<sup>52</sup> All relevant energies, gradients, and nonadiabatic couplings were calculated on-the-fly. The nuclear motion on the PES was described by quasi-classical trajectories, and the nonadiabatic transitions near conical intersections were treated with the fewest switches algorithm.<sup>30,31</sup> The time step to propagate the nuclear motion was 0.1 fs, and a 100 times smaller time step was used in the propagation of the time-dependent electronic Schrödinger equation. Following a recently proposed procedure,<sup>53,54</sup> a decoherence correction was applied, and the relevant parameter was chosen to be 0.1 hartree.

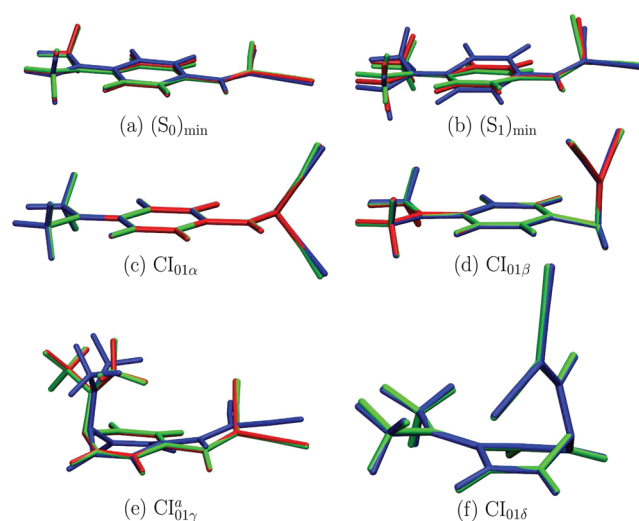


**Figure 2.** Overlays of the optimized excited-state minima and conical intersections of DMN obtained with semiempirical MRCI-SD(12,10) (blue), MRCI-SDTQ(12,12) (red), and MRCI-SD(14,14) (green).

**Table 1. Relative Energies (eV) of the Two Lowest Electronic States and of the Conical Intersections at Different Optimized Structures<sup>a</sup>**

	state	MRCI-SD/ (12,10)	MRCI-SDTQ/ (12,12)	MRCI-SD/ (14,14)
$(S_0)_{\min}$	$S_0$	0.00 [7.0]	0.00 [6.8]	0.00 [6.9]
	$S_1$	3.53 [16.1]	3.56 [16.6]	3.55 [16.3]
$(S_1)_{\min}$	$S_0$	0.09 [7.6]	0.13 [7.6]	0.18 [7.5]
	$S_1$	3.43 [15.7]	3.39 [16.3]	3.41 [15.8]
$CI_{01\alpha}$	$S_0/S_1$	2.76	2.55	2.51
$CI_{01\beta}$	$S_0/S_1$	4.10	3.90	3.86
$CI_{01\gamma}^a$	$S_0/S_1$	3.55	–	–
$CI_{01\gamma}^b$	$S_0/S_1$	–	4.40	4.48
$CI_{01\delta}$	$S_0/S_1$	3.71	–	3.47

<sup>a</sup>Dipole moments ( $\|\vec{\mu}\|$  in Debye) are given in square brackets. Three types of OM2/MRCI results are compared (see text).

**Table 2. Net Charges (in e) at Selected Atoms and Molecular Fragments from OM2/MRCI Population Analyses at Optimized  $S_0$  Mimima<sup>a</sup>**

state	MRCI-SD/(12,10)		MRCI-SDTQ/(12,12)		MRCI-SD/(14,14)	
	$S_0$	$S_1$	$S_0$	$S_1$	$S_0$	$S_1$
N11	-0.28	-0.09	-0.27	-0.09	-0.27	-0.07
C1	0.20	0.12	0.21	0.15	0.20	0.12
C4	-0.01	0.18	-0.01	0.18	0.00	0.18
C7	-0.09	-0.32	-0.09	-0.30	-0.09	-0.31
$C_6H_4$	0.12	0.26	0.10	0.27	0.11	0.25
$CH=C(CN)_2$	-0.10	-0.51	-0.14	-0.53	-0.11	-0.51
$N(CH_3)_2$	0.00	0.27	0.02	0.26	0.00	0.26
$f_{01}$	0.82		0.74		0.78	
$\Delta_{01} \ \vec{\mu}\  / D$	9.1		9.8		9.4	

<sup>a</sup>Calculated  $S_1 \rightarrow S_0$  oscillator strengths ( $f_{01}$ ) and the change of dipole moments between  $S_0$  and  $S_1$  ( $\Delta_{01} \|\vec{\mu}\|$ , in Debye) are also listed. For complete data, see Supporting Information.

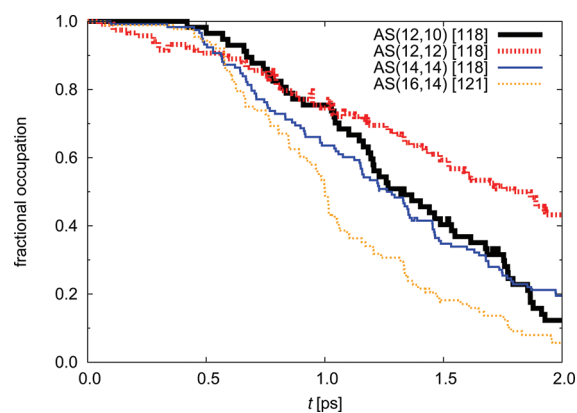


**Figure 3.** Average occupation of the electronic states  $S_0$  and  $S_1$  as a function of simulation time. The simulations were performed using OM2/MRCI-SD with different active spaces. The number of trajectories of each simulation is indicated in brackets.

According to previous work<sup>1,22–26</sup> and our own preliminary test calculations, it is mainly the  $\pi$  and  $\pi^*$  orbitals that are involved in the photoinduced dynamics of DMN. In setting up the AS for the MRCI calculations, we thus initially applied a method that selects the  $\pi$ -type orbitals automatically by assigning any molecular orbital (MO) with  $\pi$ -type population greater than a given threshold (PIPOP) as a  $\pi$  orbital.<sup>41</sup> Different thresholds were examined in OM2/MRCI test calculations using a (12,10) AS with 12 electrons distributed in 10  $\pi$  orbitals. It turned out to be difficult for DMN to maintain a consistent AS in consecutive steps of geometry optimization and trajectory propagation because the molecule is quite flexible and can undergo drastic geometric distortions in the excited state so that the concept of  $\sigma/\pi$  separation becomes questionable. We nevertheless tried to keep the chosen AS consistent by using orbital tracking with thresholds for PIPOP of 40, 30, and 25%.<sup>41</sup> The first choice led to failures in most of the CI optimization attempts; the other two choices proved better but also failed occasionally, so that the problem of orbital tracking could not be solved completely for DMN. When using the (12,10) AS in the following, we will normally specify the chosen PIPOP value; if not, the default PIPOP = 30% was used.

Given this situation and the inevitable orbital mixing at distorted geometries, we also adopted an alternative definition of the AS solely based on orbital energies (i.e., without

considering the  $\sigma$  or  $\pi$  character of the MOs). We defined larger ASs, namely, (12,12), (14,14), and (16,14), simply by including the successive highest occupied and lowest unoccupied MOs. Technical problems were normally not encountered in OM2/MRCI calculations with these ASs, indicating that the underlying PESs are sufficiently continuous, and the results from corresponding geometry optimizations and surface hopping simulations were generally similar to those from converged runs with the original (12,10) AS. This also demonstrates that the OM2/MRCI results for DMN are rather insensitive to an extension of the AS beyond (12,10). In the next section, we present some results obtained with different ASs to substantiate this claim.

The time-dependent emission spectrum  $I(\omega, t)$  of DMN was determined from the nonadiabatic dynamics simulation as follows. The relevant spectroscopic information (including state energies, oscillator strengths, and current electronic state) was recorded for all trajectories. Then, for a given range of  $S_1 \rightarrow S_0$  emission energies, the fluorescence intensity at time  $t$  was evaluated every 10 fs by summing up the oscillator strengths over all trajectories still remaining in the  $S_1$  state (see Supporting Information for details).

### 3. RESULTS

The photoinduced processes of DMN involve various nuclear motions that may be characterized by the dihedral angles depicted in Figure 1b–d.  $\tau_a$ ,  $\tau_b$ , and  $\tau_c$  describe the torsion around the C1–N11, C4–C7, and C7=C8 bonds, respectively.  $\theta_a$ ,  $\theta_b$ ,  $\theta_c$ , and  $\theta_d$  measure the pyramidalization at the N11, C1, C4, and C8 atoms, respectively. Finally,  $\alpha_a$  and  $\alpha_b$  reflect the out-of-plane motion of the  $N(CH_3)_2$  and  $CH=C(CN)_2$  groups, respectively, with regard to the plane of the six-membered ring (see Table S2, Supporting Information).

**3.1. Potential Energy Surfaces.** At the OM2/SCF level (without MRCI), the ground-state optimization converges to a planar geometry when the starting structure is also planar. Frequency analysis shows that this planar geometry is a stationary point rather than a minimum. The actual ground-state OM2/SCF minimum is nonplanar with some twist around the C4–C7 bond ( $\tau_b = -155^\circ$ ) but almost no torsion around the C7=C8 bond ( $\tau_c = 2^\circ$ ). There is some pyramidalization at the N11 atom ( $\theta_a = 10^\circ$ ,  $\tau_a = 8^\circ$ ). The nonplanar OM2/SCF minimum lies only 0.16 kcal/mol lower in energy than the planar stationary structure. At the OM2/MRCI level, the  $S_0$  minimum is almost planar (see Figure 2a and Supporting

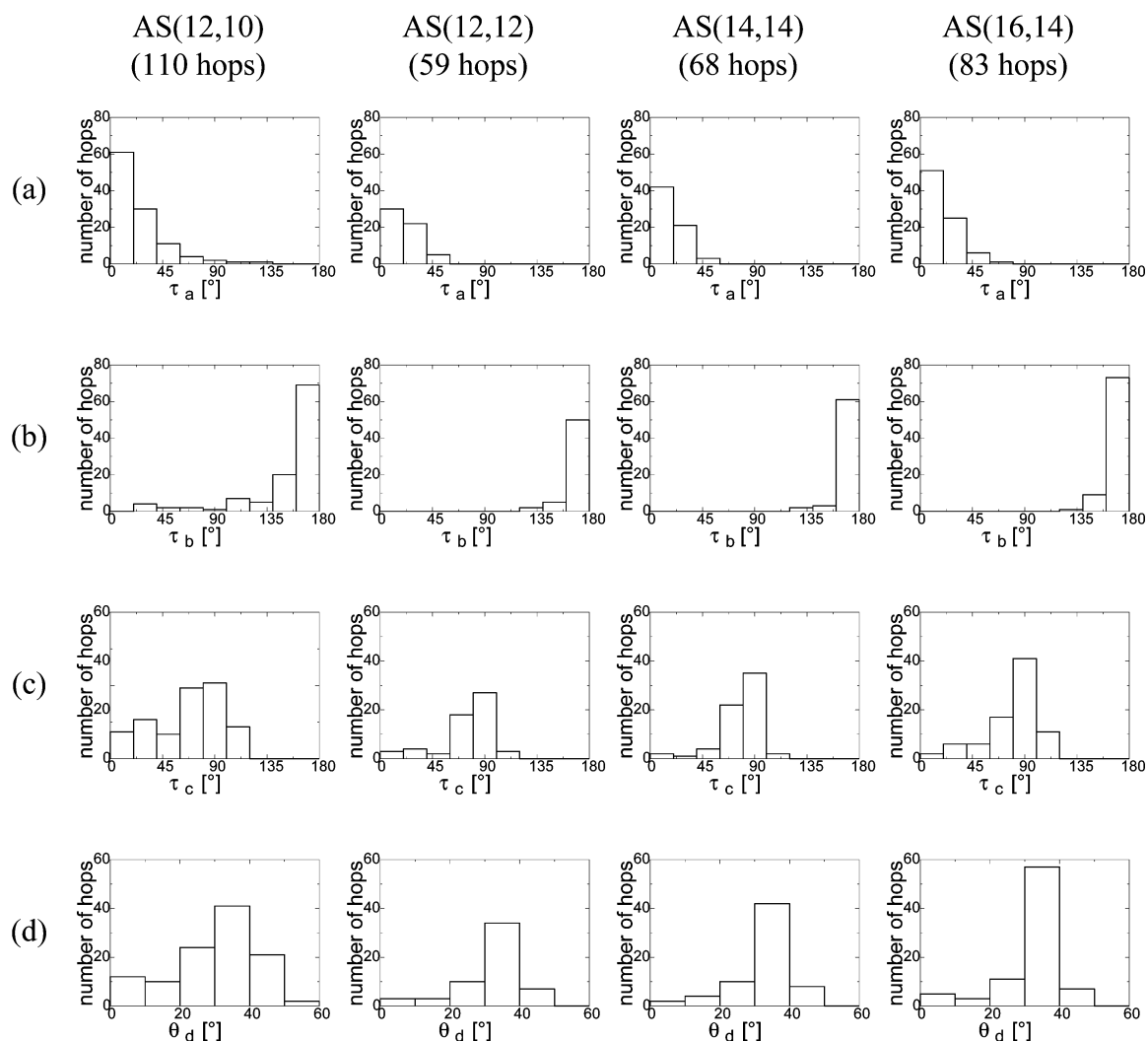


**Figure 4.** Distribution of  $\tau_a$  (a),  $\tau_b$  (b),  $\tau_c$  (c), and  $\theta_d$  (d) at the  $S_1 \rightarrow S_0$  hopping events, obtained with OM2/MRCI-SD employing different active spaces, (12,10), (12,12), (14,14), and (16,14). The numbers of hopping events are given in parentheses.

Information). OM2/MRCI optimizations with different ASs, that is, (12,10), (12,12), and (14,14), give similar bond lengths and angles. These OM2 results are consistent with recent ab initio and DFT calculations<sup>3</sup> in which the type of optimized  $S_0$  structure (planar versus nonplanar) was found to depend on the level of theory and basis set; DFT methods gave planar geometries, while correlated ab initio methods yielded slight deviations from planarity (e.g., by  $8^\circ$  at the amino nitrogen atom in the RI-CC2/def2-TZVP optimized structure).<sup>3</sup> Experimentally, DMN is nearly planar in the crystalline state.<sup>3</sup>

At the  $S_0$  minimum, the first singlet excited state  $S_1$  corresponds to the HOMO  $\rightarrow$  LUMO ( $\pi \rightarrow \pi^*$ ) transition. The vertical excitation energy is calculated to be 3.53–3.56 eV with the different ASs employed (see Table 1), reasonably close to the experimental value of  $3.38 \pm 0.06$  eV and the theoretical values of 3.38–3.44 eV (RI-CC2).<sup>3</sup> As pointed out previously, the photoexcitation to the  $S_1$  state causes a substantial charge transfer to the  $\text{CH}=\text{C}(\text{CN})_2$  moiety.<sup>1,3,22–26</sup> Selected atomic and fragment charges from OM2/MRCI population analyses are listed in Table 2. According to OM2/MRCI, the negative charge at the  $\text{CH}=\text{C}(\text{CN})_2$  moiety increases upon photoexcitation by about  $-0.4$  e (from  $-0.1$  to  $-0.5$  e), at the expense of the  $\text{N}(\text{CH}_3)_2$  and  $\text{C}_6\text{H}_4$  groups, which become more positive overall by about 0.25 and 0.15 e, respectively. As a

consequence, the permanent dipole moment in the  $S_1$  state is much larger than that in the  $S_0$  ground state (see Table 1); the computed increase of 9.1–9.8 D (OM2/MRCI, see Table 2) is somewhat higher than that found experimentally (8.8 D), whereas the published theoretical values of 7.12–8.15 (RI-CC2) and 3.75–4.54 D (DFT) are too low.<sup>3</sup> The second singlet excited state  $S_2$  lies 4.44 eV above the ground state (OM2/MRCI) and is not discussed in the current work because it is a dark state and not involved in the photoinduced processes of DMN considered presently.

Our OM2/MRCI calculations predict a nearly planar geometry also for the  $S_1$  minimum (see Figure 2b). Interestingly, there is only a slight difference between the structures of the  $S_0$  and  $S_1$  minima, with a very small root-mean-square deviation (rmsd) of 0.045 Å. The energy of the  $S_0$  state at the optimized  $S_1$  minimum is 0.09–0.18 eV (for different ASs) relative to the ground-state minimum. The adiabatic excitation energy ( $T_a$ ) of the  $S_1$  state is lower than the vertical excitation energy ( $T_v$ ) by 0.10–0.17 eV (again for different ASs).

We have located several  $S_0/S_1$  conical intersections that differ in the type of geometric distortion. Two of them are characterized by twists around the C4–C7 single and C7=C8 double bonds ( $\tau_c$  and  $\tau_b$ ), and the other two are characterized



by pronounced deformations of the benzene ring and out-of-plane displacements of the substituents.

According to OM2/MRCI(12,10), the lowest  $S_0/S_1$  conical intersection  $CI_{01\alpha}$  lies 2.76 eV above the ground-state minimum (see Table 1). When using the (12,12) and (14,14) ASs, it is found at 2.55 and 2.51 eV, respectively.  $CI_{01\alpha}$  is characterized by a strongly twisted C7=C8 double bond with  $\tau_c \approx 120^\circ$  and a pronounced pyramidalization at the C8 atom ( $\theta_d \approx 35^\circ$ ), as shown in Figure 2c. On the other hand, both C–C–N groups remain linear, and there is no internal rotation related to  $\tau_a$  or  $\tau_b$ . Swalina and Maroncelli also identified this conical intersection in their recent CASSCF study.<sup>3</sup> Conical intersections of this kind, with C–C double-bond twisting and pyramidalization at the end of the double bond, are often observed in unsaturated molecules, for example, in ethylene<sup>55</sup> or in xylene derivatives.<sup>45</sup> The pyramidalization is induced by the so-called sudden polarization effect.<sup>56</sup>

A second  $S_0/S_1$  conical intersection  $CI_{01\beta}$  is located at 4.10/3.90/3.86 eV by OM2/MRCI when using the (12,10)/(12,12)/(14,14) ASs (Table 1). It contains a strongly twisted C4–C7 bond ( $\tau_b \approx 103^\circ$ ), and the C7=C8 bond is almost perpendicular to the benzene plane (see Figure 2d). As in the case of  $CI_{01\omega}$  there is a strong pyramidalization at the C7 atom.

The third  $S_0/S_1$  conical intersection  $CI_{01\gamma}$  is encountered in two variants that differ notably in energy but are similar in geometry (rmsd  $\approx 1.0$  Å).  $CI_{01\gamma}^a$  is found only with the (12,10) AS, while  $CI_{01\gamma}^b$  is found only with the (12,12) and (14,14) ASs; their energies relative to the ground-state minimum are 3.55, 4.40, and 4.48 eV, respectively (see Table 1). In terms of geometry, the most prominent difference between  $CI_{01\gamma}^a$ (12,10),  $CI_{01\gamma}^b$ (12,12), and  $CI_{01\gamma}^b$ (14,14) concerns the N11–C1 single-bond twist, which is found to be of opposite direction ( $\tau_a = -19^\circ/10^\circ/12^\circ$ ). A strong out-of-plane deformation of the N(CH<sub>3</sub>)<sub>2</sub> group is seen in all three structures (see Figure 2e); the N11–C1 bond is nearly perpendicular to the ring plane, with the dihedral angle N11–C1–C2–C3 reaching 73/89/91°. Furthermore, the six-membered ring shows a conspicuous boat-like distortion, with pronounced puckering at the C1 atom ( $\theta_b = -27^\circ/-35^\circ/-35^\circ$ ) and little puckering at the C4 atom ( $\theta_c = 8/4/5^\circ$ ). We note that  $CI_{01\gamma}$ -type conical intersections often play an important role in the nonadiabatic decay of five- and six-membered ring systems.<sup>32,39,40</sup>

A fourth  $S_0/S_1$  conical intersection  $CI_{01\delta}$  is found at 3.71 eV with the (12,10) AS and at 3.47 eV with the (14,14) AS, but could not be located with the (12,12) AS (Table 1). It is characterized by ring distortions as well. There is moderate and strong ring puckering at the C1 atom ( $\theta_b = -5^\circ/-5^\circ$ ) and the C4 atom ( $\theta_c = 30^\circ/30^\circ$ ), respectively. The C4–C7 bond is nearly perpendicular to the ring plane with a dihedral angle C3–C4–C7–C8 of 30°/29° (see Figure 2f). There is no out-of-plane deformation of the N(CH<sub>3</sub>)<sub>2</sub> group.

We have computed energy profiles for linearly interpolated reaction paths between the Franck–Condon geometry and the minimum-energy conical intersections for 21 evenly spaced points [OM2/MRCI single-point calculations with AS(12,12)]. In the case of  $CI_{01\omega}$  the resulting energy curve is essentially flat on the first half of the path and then drops off gradually to reach the lower-lying conical intersection, while in the other cases, we find sizable barriers and overall uphill profiles (see Supporting Information, Figure S7). This suggests that only  $CI_{01\alpha}$  will be easily accessible during the dynamics.

**3.2. Nonadiabatic Dynamics.** In the OM2/MRCI surface hopping simulation runs, the fractional occupations of the

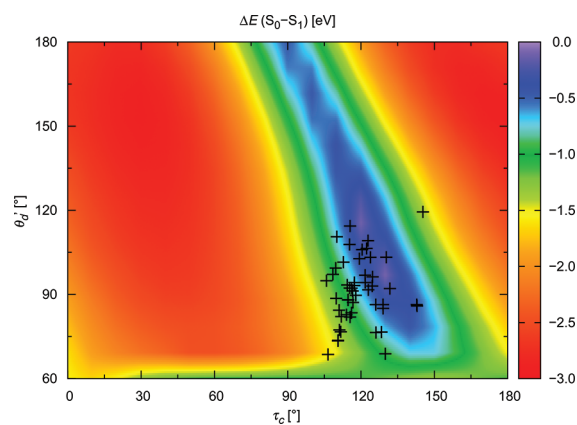


**Figure 5.** Two-dimensional contour of the energy difference between the  $S_0$  and  $S_1$  PES as a function of  $\tau_c$  and  $\theta_d$  (C9–C8–C7–C9) [248 OM2/MRCI-SDTQ(12,12) single-point calculations], with the remaining geometric parameters taken from the optimized  $CI_{01\alpha}$  structure. The blue/violet area indicates the crossing seam. The  $S_1 \rightarrow S_0$  hopping events simulated with OM2/MRCI-SD(12,12) are marked by black crosses.

states and the adiabatic electronic populations agree well with each other because decoherence corrections are taken into account in our approach. Hence, we only show the time-dependent fractional occupations of the  $S_0$  and  $S_1$  states in Figure 3. The results are rather stable toward the selection of the ASs because similar  $S_1$  decay behavior is found in the simulations employing the following ASs: (12,10), (14,14), and (16,14). In these simulations, DMN is initially excited to the  $S_1$  state. Within the first 400 fs, less than 5% of all trajectories decay to the  $S_0$  state (see Figure 3). This implies that it takes most trajectories hundreds of femtoseconds to propagate on the  $S_1$  surface and seek the  $S_0/S_1$  conical intersection. After  $\sim 400$  fs, many trajectories have approached the region of conical intersection and started the  $S_0 \rightarrow S_1$  hopping process. After 2.0 ps, the  $S_0$  population has grown to over 90%, and the decay is essentially complete. The results with the (12,12) AS differ somewhat from the others; the decay is slightly slower so that there remains almost  $\sim 30\%$   $S_1$  population after 2.0 ps.

To estimate the  $S_1$  lifetime, we use an exponential decay function to fit the time-dependent fractional occupations

$$P(t) = \exp(-(t - t_0)/\tau) \quad (1)$$

where  $t_0$  is the starting time for the  $S_1$  population decay and  $\tau$  is the decay time constant. The initial 400 fs are excluded from the fitting because there is no obvious population decay of  $S_1$  within the period. Combining the data calculated with the ASs (12,10), (14,14), and (16,14) (see Figure 3), the fitting gives  $t_0 = 468$  fs and  $\tau = 770$  fs. Thus, the computed lifetime of the  $S_1$  state is  $t_0 + \tau = 1.24$  ps. In the slightly slower dynamics obtained with the (14,14) AS,  $t_0$  still reaches 400 fs, while the total lifetime is  $\sim 1.6$  ps. Our results are compatible with a recent theoretical estimate of 1.1 ps for DMN in acetonitrile by Swalina and Maroncelli (referring to the decay time of the fluorescence intensity to  $1/e$  of its initial value); in their work, DMN was modeled as two rigid bodies connected by the C7=C8 double bond and interacting with the acetonitrile solvent molecules via Lennard-Jones and electrostatic forces, and the spectral dynamics was simulated by following the motion of this model system in a one-dimensional torsional potential around the C7=C8 bond derived from ab initio energies.<sup>3</sup>

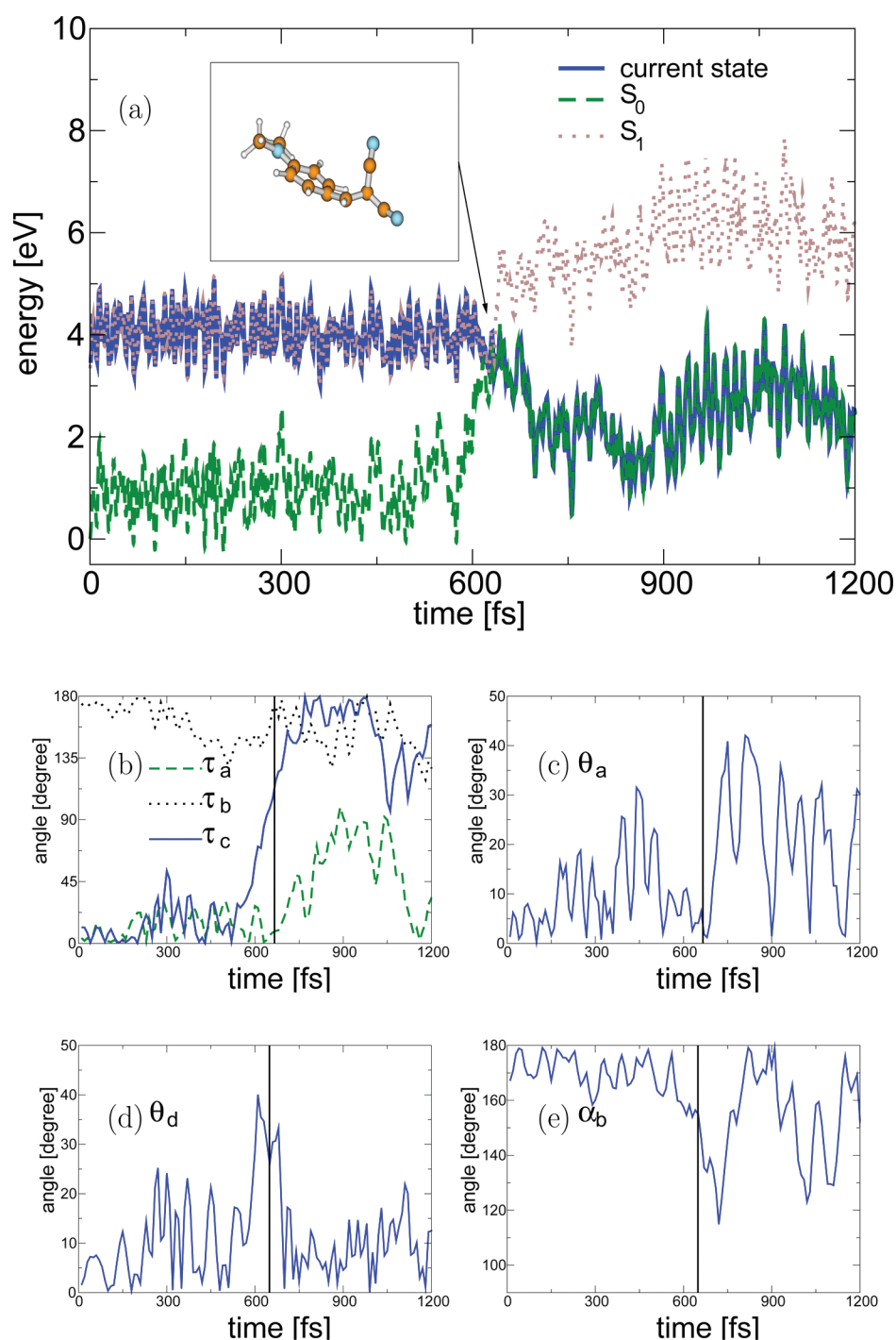


**Figure 6.** A typical trajectory [OM2/MRCI-SD(12,10)] over the entire simulation time (fs): (a) potential energies (eV) of  $S_0$  and  $S_1$ ; (b)  $\tau_a$ ,  $\tau_b$ , and  $\tau_c$ ; (c)  $\theta_a$ ; (d)  $\theta_d$ ; and (e)  $\alpha_b$ . The vertical lines in (b–e) indicate the hop.

The simplifications in this model are drastic but apparently still capture some of the essential physics because they yield a lifetime close to the one from our surface hopping simulations. The experimental fluorescence lifetime in solution varies between  $\sim 0.7$  ps in nonpolar solvents (*n*-hexane, etc.) to  $\sim 1.4$  ps in polar solvents (acetonitrile, etc.).<sup>4</sup> Our computed gas-phase value falls into this range.

The reaction mechanism responsible for the nonadiabatic decay of DMN can be identified by checking the values of some key geometric parameters at the  $S_1 \rightarrow S_0$  hopping events, as shown in Figure 4. First of all, we need to figure out the bond

twisting motion (characterized by  $\tau_a$ ,  $\tau_b$ , or  $\tau_c$ ) that is involved in the nonadiabatic decay. At most of the  $S_1 \rightarrow S_0$  hopping events, neither the C1–N11 nor the C4–C7 single bond experience significant twisting (see  $\tau_a$  and  $\tau_b$  in Figure 4a and b). By contrast, there is substantial C7=C8 double-bond torsion; the angle  $\tau_c$  reaches  $60$ – $120^\circ$  at the hops (see Figure 4c). This clearly indicates that  $CI_{01\alpha}$  (see Figure 2a) is mainly responsible for the internal conversion of DMN. This is confirmed by the histogram of the  $\theta_d$  distribution of all hopping events that shows a maximum between  $30$  and  $40^\circ$  (Figure 4d), matching the pyramidalization angle at C8 in the optimized  $CI_{01\alpha}$

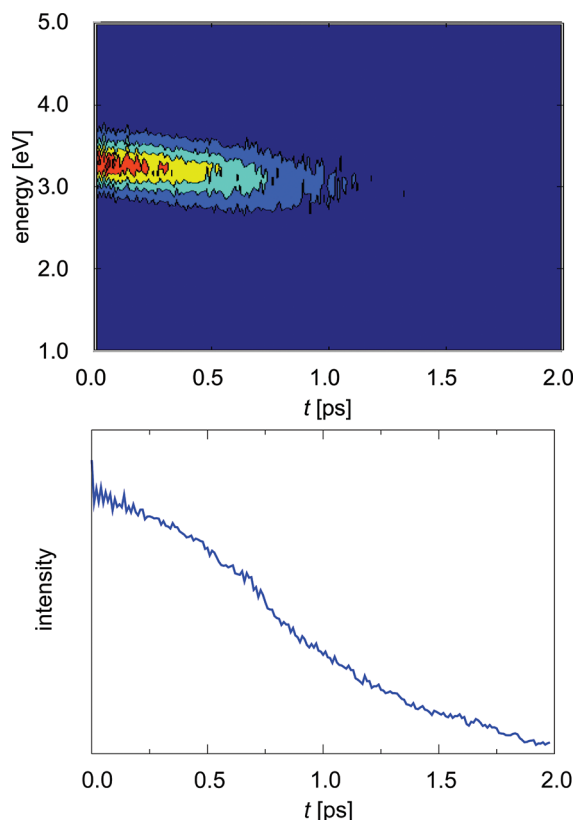


**Figure 7.** Time-dependent emission spectrum of DMN simulated with OM2/MRCI-SD(12,10). (Top) Two-dimensional contour of the emission intensity with respect to the simulation time and emission energy. (Bottom) Emission intensity evolving in the time domain. In 1.0 ps, the intensity decays to  $1/e$  of the initial value.

structure (Figure 2a). We note again that the calculations with different ASs, namely, (12,10), (14,14), and (16,14), lead to the same conclusion; they all support nonadiabatic decay via  $CI_{01\alpha}$ . This mechanism has also been favored by Allen et al.,<sup>1</sup> Jee et al.,<sup>2</sup> and the Maroncelli group.<sup>3,4</sup>

The PES topology around the  $CI_{01\alpha}$  conical intersection has been visualized by computing the  $S_0$  and  $S_1$  energies on a grid as a function of the two relevant reaction coordinates, that is, C7=C8 torsion and pyramidalization at the C8 atom. Figure 5 shows that the  $S_0$  and  $S_1$  PESs come close to each other in a seam-like region for a range of  $\tau_c$  values from about 90 to 150°, which overlaps with the distribution of  $\tau_c$  at the hopping events (see Figure 4c). The pyramidalization at the C8 atom is here characterized by  $\theta'_d$  (C9'-C8-C7-C9; see Figure 1c), which ranges from 150 (close to planar) to about 75° on the crossing seam. The lowest-energy crossing point, that is,  $CI_{01\alpha}$ , is found at  $\tau_c = 121^\circ$  and  $\theta'_d = 119^\circ$ . Most hopping events occur in the bottom section of the seam where  $\theta'_d$  is less than 120°, that is, often before the trajectories arrive at the lowest-energy crossing point (see Figure 5).

To gain more insight into the nonadiabatic decay of DMN, we take a typical trajectory as an example and examine the nuclear motions in more detail. The results are plotted in Figure 6. During the first 630 fs, the trajectory evolves on the  $S_1$  surface (Figure 6a). The most important reactive nuclear motions involve twisting around the C7=C8 double bond and pyramidalization at the C8 atom (Figure 6b and d). At the  $S_1 \rightarrow S_0$  hopping event ( $\sim 630$  fs), when the trajectory accesses the conical intersection, the geometry is mainly characterized

by two key parameters,  $\tau_c \approx 110^\circ$  and  $\theta'_d \approx 35^\circ$ . For this particular trajectory, significant pyramidalization at the N11 atom emerges at  $\sim 450$  fs ( $\theta'_a > 30^\circ$ ) but vanishes again before the hop (Figure 6c). The twisting motion about the C4-C7 bond is also visible before hopping (Figure 6b). In addition, the whole functional group  $CH=C(CN)_2$  undergoes an out-of-plane deformation with respect to the six-membered ring (Figure 6e). This typical trajectory clearly demonstrates that the nonadiabatic decay is primarily driven by two key reactive coordinates (C7=C8 twisting and C8 pyramidalization), but there are also other nuclear motions that play an important role. The latter are involved in the excited-state dynamics before the hops, and because the current system is relatively large and the internal conversion takes place on a time scale of hundreds of femtoseconds, there may be some energy transfer between pairs of different vibrational modes before the nonadiabatic transition at  $CI_{01\alpha}$ ; this contributes to the vibrational energy flow.<sup>57</sup>

**3.3. Time-Dependent Fluorescence.** The  $S_0 \rightarrow S_1$  transition is allowed and carries a large oscillator strength,<sup>1-3,23-26</sup> which amounts to  $\sim 0.74-0.82$  at the  $S_0$  minimum (OM2/MRCI; see Table 2). The emission spectrum  $I(\omega, t)$  of DMN from the surface hopping dynamics can be determined as a function of the simulation time by summing up the oscillator strengths over all trajectories that are still remaining in the  $S_1$  state at that time (see Supporting Information for details). The resulting spectrum is shown in Figure 7. Obviously, the fluorescence emission declines gradually and shows a red shift as the simulation proceeds. It attenuates rapidly in the first 500 fs, with a loss of nearly two-thirds of the initial intensity. During this time, there is a red shift of  $\sim 0.1$  eV. Then, the sharp emission band turns much broader, and the position of the maximum becomes too ambiguous to be located precisely. After 2 ps, the  $S_1 \rightarrow S_0$  emission has almost completely vanished in the spectrum. These features of declining intensity and red-shifting emission maximum have been reported in previous time-resolved experiments and associated simulations.<sup>3</sup> In our computed spectrum, the intensity has decreased to  $1/e$  of its initial value after about 1.0 ps, which again falls into the range of the reported experimental fluorescence lifetimes. Our simulated gas-phase emission spectrum agrees well with experimental spectra recorded in the condensed phase,<sup>3,4</sup> implying that some intrinsic features of fluorescence emission seem to be well-captured by our approach. We note, however, that the emission may become more complex in the solution phase due to the charge-transfer character of the  $S_1$  state, which may interact strongly with polar solvents. Moreover, the excited-state dynamics involves internal rotation of the medium-sized  $CH=C(CN)_2$  moiety around the C7=C8 double bond, which may be sterically hindered by surrounding solvent molecules.

#### 4. CONCLUSION

In the current work, we have studied the nonadiabatic dynamics of DMN in the gas phase by performing on-the-fly surface hopping simulations with the semiempirical OM2/MRCI method. We obtained a nonradiative lifetime of the  $S_1$  state of 1.2 ps that is compatible with previous theoretical and experimental results.<sup>3,4</sup>

In the nonadiabatic dynamics of DMN, the twisting around the C7=C8 double bond acts as the driving coordinate toward the lowest-energy  $S_0/S_1$  conical intersection ( $CI_{01\alpha}$ ), which mediates the internal conversion to the electronic ground state. This conical intersection is also characterized by a pronounced



pyramidalization at the C8 atom that accompanies the double-bond twisting. In addition, the excited-state dynamics involves some other photoinactive modes before the nonadiabatic transition occurs.

The chosen approach, that is, surface hopping simulations at the OM2/MRCI level, describes the nonadiabatic dynamics of medium-size molecules in a realistic manner and at reasonable computational costs. It will thus be feasible to conduct analogous studies for DMN derivatives. Furthermore, in view of the well-known strong dependence of the photoinduced dynamics of DMN on the environment (see Introduction), it will clearly be worthwhile to study the nonadiabatic dynamics of DMN and its derivatives in different solvents using the recently developed QM/MM surface hopping methodology.<sup>58</sup> The current work provides the foundation for such future investigations. In addition, it will be interesting to check the theoretical insights and the proposed dynamics scenario for gas-phase DMN from the current OM2/MRCI simulations by high-level ab initio calculations.

## ■ ASSOCIATED CONTENT

### ● Supporting Information

A survey of the available data, geometric parameters of the optimized structures, net atomic charges, absorption and emission spectra, the distribution of dihedral angles at the hopping events, PES scans and reaction paths, and optimized Cartesian coordinates. This material is available free of charge via the Internet at <http://pubs.acs.org>.

## ■ AUTHOR INFORMATION

### Corresponding Author

\*Phone: +86-532-80662630. Fax: +86-532-80662778. E-mail: [lan@qibebt.ac.cn](mailto:lan@qibebt.ac.cn) (Z.L.); Phone: +49-208-3062150. Fax: +49-208-3062996. E-mail: [thiel@mpi-muelheim.mpg.de](mailto:thiel@mpi-muelheim.mpg.de) (W.T.).

### Author Contributions

<sup>¶</sup>Contributed equally to this work.

### Notes

The authors declare no competing financial interest.

## ■ ACKNOWLEDGMENTS

Z.L. is grateful for the partial support from the 100 Talent Project of CAS, from NSFC (No. 21103213) and from the Director Innovation Foundation of the Qingdao Institute of Bioenergy and Bioprocess Technology of CAS.

## ■ REFERENCES

- (1) Allen, B. D.; Benniston, A. C.; Harriman, A.; Rostron, S. A.; Yu, C. *Phys. Chem. Chem. Phys.* **2005**, *7*, 3035.
- (2) Jee, A.-Y.; Bae, E.; Lee, M. J. *Phys. Chem. B* **2009**, *113*, 16508.
- (3) Swalina, C.; Maroncelli, M. J. *Phys. Chem. C* **2010**, *114*, 5602.
- (4) Jin, H.; Liang, M.; Arshantsev, S.; Li, X.; Maroncelli, M. J. *Phys. Chem. B* **2010**, *114*, 7565.
- (5) Loutfy, R. O.; Law, K. Y. J. *Phys. Chem.* **1980**, *84*, 2803.
- (6) Yoshikawa, K.; Kumazawa, N.; Terada, H.; Akagi, K. *Int. J. Quantum Chem.* **1980**, *18*, 539.
- (7) Yoshikawa, K.; Kumazawa, N.; Terada, H.; Ju-Ichi, M. *Bull. Chem. Soc. Jpn.* **1981**, *54*, 1108.
- (8) Loutfy, R. O.; Arnold, B. A. J. *Phys. Chem.* **1982**, *86*, 4205.
- (9) Loutfy, R. O. *Pure Appl. Chem.* **1986**, *58*, 1239.
- (10) Safarzadeh-Amiri, A. *Chem. Phys. Lett.* **1986**, *129*, 225.
- (11) Kung, C. E.; Reed, J. K. *Biochemistry* **1989**, *28*, 6678.
- (12) Abdel-Mottaleb, M. S. A.; Loutfy, R. O.; Lapouyade, R. J. *J. Photochem. Photobiol., A* **1989**, *48*, 87.
- (13) Mqadmi, S.; Pollet, A. J. *Photochem. Photobiol., A* **1990**, *53*, 275.
- (14) Iwaki, T.; Torigoe, C.; Noji, M.; Nakanishi, M. *Biochemistry* **1993**, *32*, 7589.
- (15) Hooker, J. C.; Torkelson, J. M. *Macromolecules* **1995**, *28*, 7683.
- (16) Dreger, Z. A.; White, J. O.; Drickamer, H. G. *Chem. Phys. Lett.* **1998**, *290*, 399.
- (17) Gutkowski, K. I.; Japas, M. L.; Aramendia, P. F. *Chem. Phys. Lett.* **2006**, *426*, 329.
- (18) Haidekker, M. A.; Theodorakis, E. A. *Org. Biomol. Chem.* **2007**, *5*, 1669.
- (19) Jin, H.; Li, X.; Maroncelli, M. J. *Phys. Chem. B* **2007**, *111*, 13473.
- (20) Paul, A.; Samanta, A. J. *Phys. Chem. B* **2008**, *112*, 16626.
- (21) Moran, A. M.; Eglolf, D. S.; Blanchard-Desce, M.; Kelley, A. M. *J. Chem. Phys.* **2002**, *116*, 2542.
- (22) Moran, A. M.; Kelley, A. M.; Tretiak, S. *Chem. Phys. Lett.* **2003**, *367*, 293.
- (23) Ferrighi, L.; Frediani, L.; Cappelli, C.; Salek, P.; Ågren, H.; Helgaker, T.; Ruud, K. *Chem. Phys. Lett.* **2006**, *425*, 267.
- (24) Guthmuller, J.; Champagne, B. *J. Chem. Phys.* **2007**, *127*, 164507.
- (25) Mennucci, B.; Cappelli, C.; Cammi, R.; Tomasi, J. *Theor. Chem. Acc.* **2007**, *117*, 1029.
- (26) Mennucci, B.; Cappelli, C.; Guido, C. A.; Cammi, R.; Tomasi, J. *J. Phys. Chem. A* **2009**, *113*, 3009.
- (27) Domcke, W.; Yarkony, D. R.; Köppel, H., Eds. *Conical Intersections: Electronic Structure, Dynamics and Spectroscopy*; World Scientific: Singapore, 2004.
- (28) Yarkony, D. R. *Rev. Mod. Phys.* **1996**, *68*, 985.
- (29) Bearpark, M. J.; Robb, M. A.; Schlegel, H. B. *Chem. Phys. Lett.* **1994**, *223*, 269.
- (30) Tully, J. C. *J. Chem. Phys.* **1990**, *93*, 1061.
- (31) Hammes-Schiffer, S.; Tully, J. C. *J. Chem. Phys.* **1994**, *101*, 4657.
- (32) Fabiano, E.; Keal, T. W.; Thiel, W. *Chem. Phys.* **2008**, *349*, 334.
- (33) Weber, W. Ein neues semiempirisches NDDO-Verfahren mit Orthogonalisierungskorrekturen: Entwicklung des Modells, Implementierung, Parametrisierung und Anwendungen. Ph.D. thesis, Universität Zürich, Switzerland, 1996.
- (34) Weber, W.; Thiel, W. *Theor. Chem. Acc.* **2000**, *103*, 495.
- (35) Otte, N.; Scholten, M.; Thiel, W. *J. Phys. Chem. A* **2007**, *111*, 5751.
- (36) Koslowski, A.; Beck, M. E.; Thiel, W. *J. Comput. Chem.* **2003**, *24*, 714.
- (37) Keal, T. W.; Koslowski, A.; Thiel, W. *Theor. Chem. Acc.* **2007**, *118*, 837.
- (38) Fabiano, E.; Thiel, W. *J. Phys. Chem. A* **2008**, *112*, 6859.
- (39) Lan, Z.; Fabiano, E.; Thiel, W. *J. Phys. Chem. B* **2009**, *113*, 3548.
- (40) Lan, Z.; Fabiano, E.; Thiel, W. *ChemPhysChem* **2009**, *10*, 1225.
- (41) Keal, T. W.; Wanko, M.; Thiel, W. *Theor. Chem. Acc.* **2009**, *123*, 145.
- (42) Lan, Z.; Lu, Y.; Fabiano, E.; Thiel, W. *ChemPhysChem* **2011**, *12*, 1989.
- (43) Lu, Y.; Lan, Z.; Thiel, W. *Angew. Chem., Int. Ed.* **2011**, *50*, 6864.
- (44) Weingart, O.; Lan, Z.; Koslowski, A.; Thiel, W. *J. Phys. Chem. Lett.* **2011**, *2*, 1506.
- (45) Kazaryan, A.; Lan, Z.; Schäfer, L. V.; Thiel, W.; Filatov, M. *J. Chem. Theory Comput.* **2011**, *7*, 2189.
- (46) Grimme, S.; Parac, M. *ChemPhysChem* **2003**, *4*, 292.
- (47) Tozer, D. J.; Amos, R. D.; Handy, N. C.; Roos, B. O.; Serrano-Andrés, L. *Mol. Phys.* **1999**, *97*, 859.
- (48) Dreuw, A.; Weisman, J. L.; Head-Gordon, M. *J. Chem. Phys.* **2003**, *119*, 2943.
- (49) Levine, B. G.; Ko, C.; Quenneville, J.; Martínez, T. *Mol. Phys.* **2006**, *104*, 1039.
- (50) Thiel, W. *MNDO Program*, version 6.1. Max-Planck-Institut für Kohlenforschung, Mülheim an der Ruhr: Germany, 2007.
- (51) Wigner, E. *Phys. Rev.* **1932**, *40*, 749.
- (52) Barbatti, M.; Granucci, G.; Persico, M.; Ruckebauer, M.; Vazdar, M.; Eckert-Maksić, M.; Lischka, H. *J. Photochem. Photobiol., A* **2007**, *190*, 228.



- (53) Zhu, C.; Nangia, S.; Jasper, A. W.; Truhlar, D. G. *J. Chem. Phys.* **2004**, *121*, 7658.
- (54) Granucci, G.; Persico, M. *J. Chem. Phys.* **2007**, *126*, 134114.
- (55) Ben-Nun, M.; Martínez, T. J. *J. Chem. Phys.* **2000**, *259*, 237.
- (56) Levine, B. G.; Martínez, T. J. *Annu. Rev. Phys. Chem.* **2007**, *58*, 613.
- (57) Gruebele, M.; Wolynes, P. G. *Acc. Chem. Res.* **2004**, *37*, 261.
- (58) Fabiano, E.; Lan, Z.; Lu, Y.; Thiel, W. In *Conical Intersections: Theory, Computation and Experiment*; Köppel, H., Domcke, W., Yarkony, D. R., Eds.; Advanced Series in Physical Chemistry; World Scientific: Singapore, 2011; Vol. 17, pp 463–496.



paper (6)

***Electronic Excitation Energies, Three-State Intersections, and Photodissociation Mechanisms of Benzaldehyde and Acetophenone***

G. Cui, Y. Lu, and W. Thiel

*Chem. Phys. Lett.*, **2012**, 537, 21-26.





# Electronic excitation energies, three-state intersections, and photodissociation mechanisms of benzaldehyde and acetophenone

Ganglong Cui, You Lu, Walter Thiel\*

Max-Planck-Institut für Kohlenforschung, Kaiser-Wilhelm-Platz 1, D-45470 Mülheim an der Ruhr, Germany

## ARTICLE INFO

### Article history:

Received 7 December 2011

In final form 2 April 2012

Available online 13 April 2012

## ABSTRACT

We report a theoretical study on the electronically excited states and the mechanisms of photodissociation of  $C_6H_5CHO$  and  $C_6H_5COCH_3$ . For both molecules, we find an  $S_1/T_2/T_1$  three-state intersection region, which allows for an efficient  $S_1 \rightarrow T_1$  intersystem crossing via the  $T_2$  state that acts as a relay. Consequently,  $T_1$  reactions become the major radical photodissociation channels. According to the computed energy profiles,  $T_1$  photodissociation mainly yields phenyl and formyl radicals in the case of benzaldehyde, and benzoyl and methyl radicals in the case of acetophenone, with different C–C bonds being cleaved preferentially. The computational results agree well with the available experimental data.

© 2012 Elsevier B.V. All rights reserved.

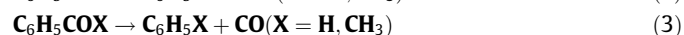
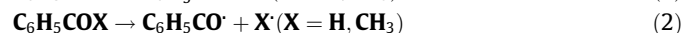
## 1. Introduction

The photodissociation of polyatomic molecules is relevant to atmospheric chemistry, biology, and many other fields [1–3]. The photodissociation dynamics of carbonyl compounds has been widely studied over the past decades since it plays a unique role in understanding the spectroscopy, photochemistry, and photophysics of polyatomic molecules [4–7]. Aromatic carbonyl compounds differ from their aliphatic counterparts by exhibiting  $\pi$  electron conjugation between the aromatic and carbonyl groups, which influences the ordering of the  $n \rightarrow \pi^*$  and  $\pi \rightarrow \pi^*$  states, their photochemical reactivities, and the photodissociation mechanisms [8–10].

Benzaldehyde ( $C_6H_5CHO$ ; BA) and acetophenone ( $C_6H_5COCH_3$ ; AP) (see Figure 1) are prototypical aromatic carbonyl compounds that have been studied experimentally for decades, especially with regard to their absorption spectra [11–24]. Their first and second singlet excited states ( $S_1$  and  $S_2$ ) were assigned as  $n \rightarrow \pi^*$  and  $\pi \rightarrow \pi^*$  transitions. It is commonly accepted that there are two close-lying triplet states ( $T_1$  and  $T_2$ ) below the  $S_1$  minimum. The relaxation dynamics of  $C_6H_5CHO$  in the  $S_1$  state was reported to be orders of magnitude faster than that of noncarbonyl aromatic compounds, which was ascribed to the presence of the  $n \rightarrow \pi^*$  state [24].

There are three main photodissociation channels experimentally, see Eqs. (1)–(3), the importance of which is different in  $C_6H_5CHO$  and  $C_6H_5COCH_3$ . The experimental results prior to 2006 have been summarized by Zewail and coworkers [25]. Briefly, most of the early experimental studies on BA report benzene and carbon monoxide as major products upon photoexcitation into the  $S_2$  state

(Eq. (3)), whereas benzoyl and methyl radicals are the dominant products in the case of AP (Eq. (2)). However, depending on the experimental conditions, other channels and competing reactions are observed. For example, Zhu and Cronin studied the photodissociation dynamics of  $C_6H_5CHO$  at wavelengths of 280–308 nm using excimer and dye laser photolysis in combination with cavity ring-down spectroscopy, and measured HCO radical yields of  $0.32 \pm 0.05$ ,  $0.45 \pm 0.05$ , and  $0.29 \pm 0.05$  at 280, 285, and 308 nm, respectively [23]. In another recent experimental investigation of the photodissociation dynamics of  $C_6H_5CHO$ , Bagchi et al. identified two major channels yielding HCO (Eq. (1)) and CO (Eq. (3)) upon photolysis at 248 and 266 nm, with the former becoming dominant at 193 nm [26]. The situation is quite different in  $C_6H_5COCH_3$ . Using time-of-flight mass spectrometry after photoexcitation, Zhao et al. found [18] that the C1–C7 and C7–C9 bond fissions (Eqs. (1) and (2)) are of comparable importance at 193 nm, whereas C7–C9 bond fission (Eq. (2)) becomes overwhelmingly dominant at 248 nm; the molecular channel (Eq. (3)) is minor at both wavelengths.



Experimentally, at low excitation energy, the major photodissociation products in the radical dissociation channels are thus formed by cleavage of different C–C bonds, namely between the phenyl and carbonyl groups in  $C_6H_5CHO$  and between the carbonyl and methyl groups in  $C_6H_5COCH_3$ . It is an obvious challenge to understand this discrepancy theoretically. In the past decades, electronic structure calculations for BA and AP have mainly focused on vertical and adiabatic excitation energies [27–31] and on intersections between potential energy surfaces, [4,8] while

\* Corresponding author. Fax: +49 208 306 2996.

E-mail address: [thiel@mpi-muelheim.mpg.de](mailto:thiel@mpi-muelheim.mpg.de) (W. Thiel).

theoretical studies on their photodissociation mechanisms are rather limited [25,26,32]. In this work, we use high-level ab initio methods to re-evaluate the vertical and adiabatic excitation energies of the two lowest singlet and triplet excited states and to explore the radical photodissociation mechanisms. We focus on the bond cleavage reactions in the lowest triplet state, without addressing the competing molecular photodissociation processes [25,26].

## 2. Computational methods

Equilibrium structures, transition states, and intersection geometries were determined for the  $S_0$ ,  $S_1$ ,  $S_2$ ,  $T_1$ , and  $T_2$  states by means of the complete-active-space self-consistent field (CASSCF) method. The state-averaged CASSCF calculations for intersections employed equal weights for the relevant states. All CASSCF calculations were done using the 6-31 + G\* basis set [33]. For  $C_6H_5CHO$ , the active space included ten electrons in eight orbitals (i.e., the five highest occupied and three lowest unoccupied orbitals), hence denoted as CASSCF(10,8); at the planar ground-state geometry, the active space comprised one oxygen lone pair, four occupied  $\pi$ , and three unoccupied  $\pi^*$  orbitals. For  $C_6H_5COCH_3$ , 12 electrons were correlated at the CASSCF level using the six highest occupied and five lowest unoccupied orbitals [CASSCF(12,11)]; at the ground-state geometry, the active space contained the same types of orbitals as in the case of  $C_6H_5CHO$ , plus the highest-lying  $\sigma$ -CC-bonding orbital and the two next-lowest unoccupied orbitals (with a node in the molecular plane, mixed  $\pi^*$  and  $\sigma$ -CH-type). The character of the CASSCF orbitals was inspected for all relevant species and transition states (TS) to make sure that the chosen active space was able to properly describe them (e.g., including the required  $\sigma$  and  $\sigma^*$  orbitals in the nonplanar TS structures). Minimum and TS geometries were generally fully optimized without imposing any constraint, except for the TS structures of the two C–C bond cleavage reactions in  $C_6H_5COCH_3$  where the highest points along the corresponding minimum-energy reaction paths were taken as transition states.

The CASSCF method only accounts for correlation within the active space. To include further (dynamic) correlation effects in the energetics, we performed single-point calculations at the CASSCF optimized structures using the combination of configuration interaction with second-order perturbation theory (CIPT2) proposed by Werner et al. [34]. In CIPT2, the excitations from active orbitals are treated by multi-reference configuration interaction (MRCI), while complete-active-space second-order perturbation theory (CASPT2) is employed to handle the remaining excitations involving inactive orbitals; both approaches are coupled by minimizing an appropriate energy functional [34]. The CIPT2 method is able to treat electronically difficult cases, for example, problems arising from strong intruder states. In addition, the multi-state multi-reference CASPT2 method implemented by the Werner group [35,36] was also applied to compute single-point energies for the sake of comparison. The second-order perturbation treatment in CIPT2 and CASPT2 is expected to counterbalance gradual changes in the CASSCF orbitals

along the reaction paths and thus help to provide realistic energy profiles. All CIPT2 and CASPT2 calculations were carried out using the cc-pVDZ basis set [37] and a level shift of 0.2 au.

Oscillator strengths of vertical excitations were calculated by using time-dependent density functional theory (TDDFT) with the B3LYP hybrid functional. [38,39] Spin-orbit matrix elements were computed at the CASSCF level using the cc-pVDZ basis set. [37] All CASSCF, CIPT2, and CASPT2 calculations were performed with MOLPRO-2006, [40] while GAUSSIAN09 was employed for the TDDFT and DFT calculations [41].

## 3. Results and discussion

For conciseness, we use the following notation. S0-MIN-BA, S1-MIN-BA, S2-MIN-BA, T1-MIN-BA, and T2-MIN-BA denote the minimum-energy structures in the  $S_0$ ,  $S_1$ ,  $S_2$ ,  $T_1$ , and  $T_2$  electronic states of BA; S1T2-MIN-BA is the minimum-energy crossing point (MECP) between the  $S_1$  and  $T_2$  states; T1T2-MIN-BA is the minimum-energy conical intersection between the  $T_1$  and  $T_2$  states; TS-CC-BA and TS-CH-BA refer to the transition states for C1–C7 and C7–H9 bond cleavage in the  $T_1$  state of BA. Analogous symbols are used for AP, except that TS-CC-L-AP and TS-CC-R-AP are used to represent the  $T_1$  transition states for C1–C7 and C7–C9 bond cleavage, respectively.

### 3.1. Equilibrium structures

Key geometric parameters of the optimized structures of BA and AP are listed in Tables 1 and 2, respectively (see Figure 1 for the numbering of the atoms). All the minimum structures have  $C_s$  symmetry. In the  $S_0$  ground state, both molecules have a typical phenyl ring with almost equal C–C bond lengths (around 1.40 Å) and a carbonyl group with a typical C=O double bond (1.21–1.23 Å). The  $S_1$  and  $T_1$  states are dominated by an  $n \rightarrow \pi^*$  transition both in BA and AP, and their optimized geometries are thus generally quite similar: compared with the ground state, the C=O bond is elongated by 0.12–0.15 Å to about 1.35 Å, the C1–C7 bond between the carbonyl group and the phenyl ring is shortened by 0.05–0.08 Å to 1.42–1.45 Å, and some bond alternation is induced in the phenyl ring (see C1–C2 and C2–C3 bond lengths). In both molecules the  $S_2$  and  $T_2$  states arise from a  $\pi \rightarrow \pi^*$  transition mainly localized in the aromatic ring. Hence, relative to the ground state, there is only a rather small increase in the C=O bond length to about 1.22–1.25 Å, but rather strong changes in the phenyl ring: the C–C bonds in the phenyl moiety all become longer in the  $S_2$  state, while the ring adopts a quinoid-type structure with pronounced C–C bond alternation in the  $T_2$  state (see Tables 1 and 2).

### 3.2. Vertical and adiabatic excitation energies

The calculated excitation energies of  $C_6H_5CHO$  and  $C_6H_5COCH_3$  are listed in Table 3, respectively, along with the available experimental data [12,31,42]. There is obviously excellent agreement between the computed CIPT2//CASSCF values and the experimental

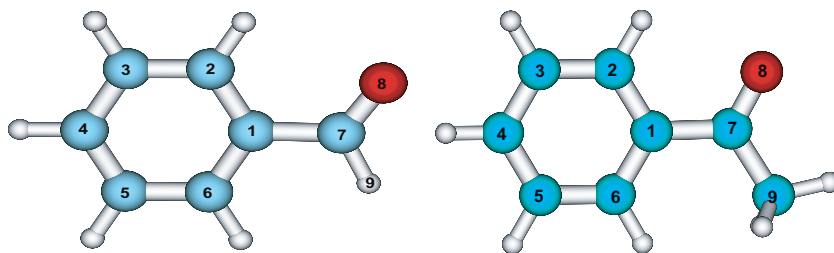


Figure 1. Schematic structures of benzaldehyde  $C_6H_5CHO$  (left) and acetophenone  $C_6H_5COCH_3$  (right) with the atomic numbering used in this work.

**Table 1**

$C_6H_5CHO$ : key geometric parameters (in Å for bond lengths and degree for dihedral angles) of the optimized structures and relative energies (in kcal/mol) at the CIPT2/CASPT2 level.

	C1C2	C1C7	C2C3	C7O8	C7H9	O8C7C1H9	Energy	State
S0-MIN-BA	1.403	1.484	1.388	1.207	1.091	180.0	0.00/0.00	S <sub>0</sub>
T1-MIN-BA	1.419	1.414	1.370	1.343	1.072	180.0	71.8/75.4	T <sub>1</sub>
T2-MIN-BA	1.488	1.422	1.362	1.237	1.087	180.0	76.4/80.4	T <sub>2</sub>
S1-MIN-BA	1.425	1.404	1.366	1.355	1.073	180.0	77.6/81.3	S <sub>1</sub>
S2-MIN-BA	1.448	1.440	1.463	1.223	1.089	180.0	99.9/99.4	S <sub>2</sub>
S1T2-MIN-BA	1.455	1.381	1.393	1.338	1.076	180.0	79.2/83.0	S <sub>1</sub>
T1T2-MIN-BA	1.471	1.383	1.374	1.301	1.079	180.0	79.8/80.1	T <sub>1</sub>
TS-CC-BA	1.377	1.987	1.391	1.234	1.097	124.5	92.1/92.7	T <sub>1</sub>
TS-CH-BA	1.392	1.501	1.387	1.235	1.556	110.4	96.1/99.3	T <sub>1</sub>

**Table 2**

$C_6H_5COCH_3$ : key geometric parameters (in Å for bond lengths and degree for dihedral angles) of the optimized structures and relative energies (in kcal/mol) at the CIPT2/CASPT2 level.

	C1C2	C1C7	C2C3	C7O8	C7C9	O8C7C9C1	Energy	State
S0-MIN-AP	1.405	1.498	1.393	1.232	1.512	180.0	0.00/0.00	S <sub>0</sub>
T1-MIN-AP	1.429	1.425	1.387	1.348	1.502	180.0	72.5/76.3	T <sub>1</sub>
T2-MIN-AP	1.488	1.448	1.362	1.250	1.513	180.0	78.7/80.7	T <sub>2</sub>
S1-MIN-AP	1.433	1.417	1.386	1.356	1.503	180.0	78.1/81.7	S <sub>1</sub>
S2-MIN-AP	1.442	1.469	1.436	1.240	1.513	180.0	101.2/100.3	S <sub>2</sub>
S1T2-MIN-AP	1.457	1.401	1.375	1.335	1.505	180.0	78.8/85.4	S <sub>1</sub>
T1T2-MIN-AP	1.472	1.418	1.374	1.299	1.513	180.0	77.2/80.3	T <sub>1</sub>
TS-CC-L-AP	1.381	2.0	1.399	1.216	1.523	-113.4	99.0/96.5	T <sub>1</sub>
TS-CC-R-AP	1.404	1.504	1.414	1.190	2.0	-131.4	82.5/90.2	T <sub>1</sub>

**Table 3**

Vertical ( $T_v$ ) and adiabatic ( $T_e$ ) excitation energies in kcal/mol (eV) of benzaldehyde  $C_6H_5CHO$  (BA) and acetophenone  $C_6H_5COCH_3$  (AP) in the lowest four electronically excited states (T<sub>1</sub>, S<sub>1</sub>, T<sub>2</sub>, and S<sub>2</sub>) from the current CIPT2/CASPT2 calculations (calc.). Experimental values (exp.) taken from references [12,31,42].

	T <sub>1</sub>	T <sub>2</sub>	S <sub>1</sub>	S <sub>2</sub>
$T_v$ calc. (BA)	82.0/84.3 (3.56/3.66)	88.2/92.7 (3.83/4.02)	90.4/92.7 (3.92/4.02)	104.9/103.8 (4.55/4.50)
$T_e$ calc. (BA)	71.8/75.4 (3.12/3.27)	76.4/80.4 (3.32/3.49)	77.6/81.3 (3.37/3.52)	99.9/99.4 (4.33/4.31)
$T_v$ exp. (BA)	-	-	-	104.0 (4.51)
$T_e$ exp. (BA)	71.9 (3.12)	76.1 (3.30)	77.0 (3.34)	100.5 (4.36)
$T_v$ calc. (AP)	81.4/83.6 (3.53/3.63)	85.0/87.4 (3.69/3.79)	89.0/91.2 (3.86/3.96)	105.6/106.3 (4.58/4.60)
$T_e$ calc. (AP)	72.5/76.3 (3.14/3.31)	78.7/80.7 (3.41/3.50)	78.1/81.7 (3.39/3.54)	101.2/100.3 (4.39/4.35)
$T_v$ exp. (AP)	-	-	88.0 (3.82)	104.0 (4.51)
$T_e$ exp. (AP)	73.8 (3.20)	-	77.9 (3.38)	101.2 (4.39)

values, both for the vertical and the adiabatic excitation energies: the deviations are typically less than 1 kcal/mol (0.04 eV), and the maximum deviation is 1.6 kcal/mol (0.07 eV). The excited-state energies are rather similar in both molecules: for example, the vertical excitation energies to the S<sub>1</sub> and S<sub>2</sub> states are calculated to be 90.4 and 104.9 kcal/mol for  $C_6H_5CHO$ , and 89.0 and 105.6 kcal/mol for  $C_6H_5COCH_3$ . It is noteworthy that the three lowest states lie close to each other in both cases: the T<sub>1</sub> minimum is computed to be 5–6 kcal/mol below the T<sub>2</sub> minimum, which is almost isoenergetic with the S<sub>1</sub> minimum (within 1 kcal/mol, see Table 3).

The calculated excitation energies from CASPT2//CASSCF are generally slightly higher than those from CIPT2//CASSCF in the case of the T<sub>1</sub>, T<sub>2</sub>, and S<sub>1</sub> states (rather uniformly by 2.0–4.5 kcal/mol, i.e., 0.09–0.19 eV) so that the agreement with experiment deteriorates slightly for these states, while the CASPT2//CASSCF and CIPT2//CASSCF results for S<sub>2</sub> are within 1.0 kcal/mol (0.04 eV). The three lowest excited states lie close to each other also at the CASPT2//CASSCF level.

The favorable agreement between the theoretical and experimental excitation energies (Table 3) may to some extent be considered fortuitous, especially in view of the use of the medium-size cc-pVDZ basis set. It should be noted in this context, however, that extensive benchmarks show only a relatively minor basis set dependence of CASPT2 excitation energies for valence excited states in medium-size organic chromophores [43]. Other recent

studies on specific molecules (benzene, linear acenes, pyrrole) also demonstrate that CASPT2/cc-pVDZ excitation energies for low-lying valence states are often close to the CASPT2 results obtained with larger basis sets or at the complete basis set limit [44,45]. We thus expect that the current CIPT2/cc-pVDZ and CASPT2/cc-pVDZ energies (Table 3) are rather insensitive to basis set extension.

As expected, the  $n \rightarrow \pi^*$  singlet state is essentially dark, while the  $\pi \rightarrow \pi^*$  singlet state is bright: the oscillator strengths computed at the TD-B3LYP level (without considering vibronic or spin-orbit coupling) for BA (AP) are 0.0206 (0.0205) for the S<sub>0</sub> → S<sub>2</sub> transition and 0.0001 (0.0001) for the S<sub>0</sub> → S<sub>1</sub> transition. One should note, however, that the latter transition could gain some intensity by vibronic coupling to A'' vibrational modes.

### 3.3. S<sub>1</sub>/T<sub>2</sub>/T<sub>1</sub> Three-state intersection region

We have approximately located the minimum-energy crossing point (S1T2-MIN-BA) and the minimum-energy conical intersection (T1T2-MIN-BA) of  $C_6H_5CHO$  at the CASSCF level. At the corresponding geometries (Table 1) there is still a small difference in the CASSCF energies, with an S<sub>1</sub>–T<sub>2</sub> energy gap at S1T2-MIN-BA of 1.2 kcal/mol and a T<sub>1</sub>–T<sub>2</sub> energy gap at T1T2-MIN-BA of 0.4 kcal/mol (Table 4). More importantly, the CASPT2 single-point energies are also very close to each other at these geometries, with corre-

**Table 4**

Energy gap (CASSCF/CASPT2: kcal/mol) of the relevant two states at the optimized minimum-energy crossing points.

	S1T2-MIN-BA	T1T2-MIN-BA	S1T2-MIN-AP	T1T2-MIN-AP
Energy gap	1.2/0.5	0.4/0.7	1.1/3.1	0.4/0.3

**Table 5**

CASSCF spin-orbit matrix elements ( $\text{cm}^{-1}$ ) calculated at minimum-energy crossing points with the full Breit-Pauli operator [47].

	$\langle S_1   \hat{H}_x^{\text{BP}}   T_2 \rangle$	$\langle S_1   \hat{H}_y^{\text{BP}}   T_2 \rangle$	$\langle S_1   \hat{H}_z^{\text{BP}}   T_2 \rangle$
S1T2-MIN-BA	1.965i	2.469	0.00
S1T2-MIN-AP	0.136i	1.978	0.00

sponding gaps of 0.5 and 0.7 kcal/mol, respectively, so that the states remain nearly degenerate after including dynamic correlation (beyond the active space). The CIPT2 gaps at these geometries are not available because the CIPT2 single-point calculations converged only for one of the two states. In any event, the  $S_1$  energy at S1T2-MIN-BA lies only slightly above the minimum of the lowest excited singlet S1-MIN-BA, by 1.7 (CASPT2) or 1.6 (CIPT2) kcal/mol, so that this point (S1T2-MIN-BA) can be reached easily after the initial photoexcitation to the  $S_1$  state.

The geometric parameters of S1T2-MIN-BA and T1T2-MIN-BA are quite similar (Table 1); see, for example, the C7–O8 bond length (1.338 vs. 1.301 Å) and the C1–C7 bond length (1.381 vs. 1.383 Å). Thus, the energies of these three states should be close to each other around S1T2-MIN-BA and T1T2-MIN-BA. While we have not located a rigorous three-state crossing point, the structural and energetic similarities between S1T2-MIN-BA and T1T2-MIN-BA indicate that there exists an  $S_1/T_2/T_1$  three-state intersection region in their vicinity. It should be pointed out that this kind of three-state intersection has been discovered before in other aromatic carbonyl compounds [4,8,9]. The  $S_1 \rightarrow T_1$  intersystem crossing becomes efficient in such an  $S_1/T_2/T_1$  three-state intersection region because of the relay effect of the  $T_2$  state. According to the El-Sayed rules, [46] the  $S_1 \rightarrow T_2$  intersystem crossing is rather facile since the  $^1n \rightarrow \pi^*$  and  $^3\pi \rightarrow \pi^*$  states have the right symmetry to allow for substantial spin-orbit coupling (see Table 5). The subsequent  $T_2 \rightarrow T_1$  internal conversion then quickly populates the lowest triplet  $T_1$  at nearby geometries (around T1T2-MIN-BA). This relay mechanism explains the ultrafast  $S_1 \rightarrow T_1$  decay in  $C_6H_5CHO$ , which plays an essential role in its photodissociation dynamics [8,9].

The situation in acetophenone is analogous both with regard to the geometries and relative energies (see Tables 2 and 4), and the  $S_1/T_2/T_1$  three-state intersection region is again accessible both structurally and energetically.

### 3.4. Bond cleavage reactions in the $T_1$ state

As discussed above, the  $S_1/T_2/T_1$  three-state intersection region can efficiently funnel electron population from  $S_1$  to  $T_1$  as a consequence of the relay effect of the  $T_2$  state. Therefore we now focus on the dissociation reactions in the lowest triplet state.

We have located the transition states for C1–C7 and C7–H9 bond cleavage in the  $T_1$  state of  $C_6H_5CHO$  (TS-CC-BA and TS-CH-BA, respectively, see Figure 2); selected geometric parameters are listed in Table 1. Both transition states are nonplanar (see dihedral angle O8C7C1H9), and the breaking bonds are strongly elongated (C1–C7 1.987 Å in TS-CC-BA, C7–H9 1.501 Å in TS-CH-BA). The energies relative to S0-MIN-BA are computed (CIPT2) to be 92.1 and 96.1 kcal/mol for TS-CC-BA and TS-CH-BA, respectively, corre-

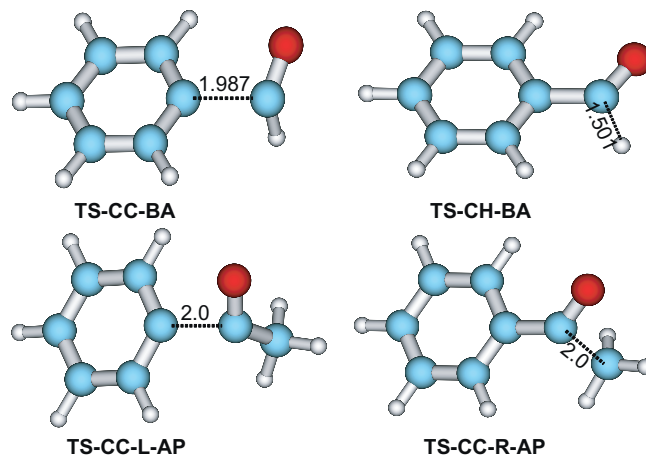


**Figure 2.** Schematic structures of the transition states for bond cleavage in the  $T_1$  state of benzaldehyde  $C_6H_5CHO$  (top) and acetophenone  $C_6H_5COCH_3$  (bottom). Key geometric parameters are listed in Tables 1 and 2.

sponding to barriers of 20.3 and 24.3 kcal/mol (relative to T1-MIN-BA). Hence, C1–C7 bond fission is somewhat more favorable than C7–H9 bond fission in the  $T_1$  state, since the computed barrier is lower by 4.0 kcal/mol. The preferred  $T_1$  reaction should thus be the formation mechanism of ground-state phenyl and formyl radicals.

The transition states for C1–C7 and C7–C9 bond cleavage in the  $T_1$  state of  $C_6H_5COCH_3$  (TS-CC-L-AP and TS-CC-R-AP, respectively) are also nonplanar (see Figure 2 and Table 2, dihedral angle O8C7C9C1), and the breaking C–C bond is elongated to 2.0 Å in both cases. In the  $S_0$  ground state, the C1–C7 and C7–C9 bonds are of similar length (1.498 vs. 1.512 Å, S0-MIN-AP), whereas the former is much shorter than the latter in the  $T_1$  state (1.425 vs. 1.502 Å, T1-MIN-AP) and should thus be harder to cleave. This expectation is confirmed by the computed TS energies (CIPT2, relative to S0-MIN-AP) of 99.0 and 82.5 kcal/mol for C1–C7 and C7–C9 bond fission in the  $T_1$  state, respectively, which translates into barriers of 26.5 and 10.0 kcal/mol. Hence, C7–C9 bond cleavage should be the dominant  $T_1$  channel, with formation of ground-state  $C_6H_5CO$  and  $CH_3$  radicals.

### 3.5. Photodissociation mechanism

On the basis of the present calculations, the radical photodissociation mechanism of  $C_6H_5CHO$  can be summarized as follows (see Figure 3). Upon photon absorption,  $C_6H_5CHO$  is initially excited to the bright  $S_2$  state (vertical excitation energy 104.9 kcal/mol), followed by an ultrafast  $S_2 \rightarrow S_1$  internal conversion and relaxation to the  $S_1$  minimum (S1-MIN-BA, 77.6 kcal/mol). The  $S_2 \rightarrow S_1$  conversion is experimentally known to occur on the femtosecond timescale [20,24,25]. The dark  $S_1$  state might also be directly populated in the Franck-Condon region, but this is less likely because of its small oscillator strength (see above). Since the  $S_1/T_2/T_1$  three-state intersection is structurally and energetically similar to S1-MIN-BA, the  $S_1 \rightarrow T_1$  intersystem crossing can occur efficiently (see above), in analogy to other systems [4,8,9,32]. With the available excess energy,  $C_6H_5CHO$  can overcome the barriers to C1–C7 and C7–H9 bond cleavage in the  $T_1$  state (TS-CC-BA at 92.1 kcal/mol; TS-CH-BA at 96.1 kcal/mol) and form the corresponding ground-state products. Given the rather small TS energy difference of only 4 kcal/mol, both dissociation channels are expected to be accessible, with a preference for C1–C7 cleavage that produces phenyl and formyl radicals ( $C_6H_5COH \rightarrow C_6H_5 \cdot + HCO \cdot$ ).



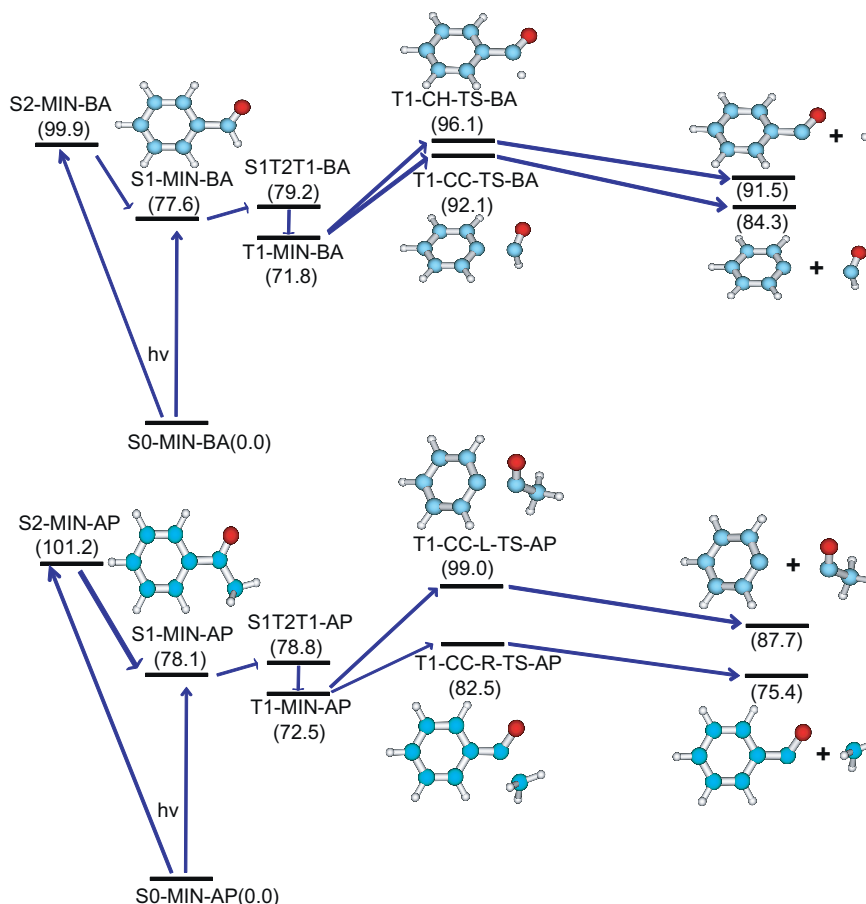


**Figure 3.** Proposed photodissociation channels of benzaldehyde  $C_6H_5CHO$  (top) and acetophenone  $C_6H_5COCH_3$  (bottom) with CIPT2/CASSCF single-point energies. The corresponding geometric parameters are listed in Tables 1 and 2.

On the whole, the radical photodissociation mechanism of  $C_6H_5COCH_3$  closely resembles that of  $C_6H_5CHO$  (see Figure 3), except for the final stage where these two aromatic carbonyl compounds exhibit different dissociation behavior in the  $T_1$  state: in  $C_6H_5COCH_3$ , C7–C9 bond cleavage is strongly dominant over the alternative C1–C7 dissociation channel because of the much smaller barrier (10.0 vs. 26.5 kcal/mol), whereas C1–C7 bond fission is preferred by a small margin over C7–H9 bond fission in  $C_6H_5CHO$ .

Finally, it should be noted that this mechanistic scenario is derived from static calculations and thus neglects dynamical effects. For example, an initial repartitioning of the excitation energy in the Franck-Condon region may have an impact on the excited-state lifetimes and ultimately also on the course of the photodissociation reactions. Such dynamical effects are beyond the scope of this work.

#### 4. Conclusion

In the current study, we report a theoretical study on the radical photodissociation mechanisms of benzaldehyde and acetophenone. The relevant equilibrium structures, transition states, and intersections for the  $S_0$ ,  $T_1$ ,  $T_2$ ,  $S_1$ , and  $S_2$  electronic states were determined by the CASSCF method, and accurate single-point relative energies were obtained using the high-level CASPT2 and CIPT2 methods. The calculated vertical and adiabatic excitation energies agree very well with the available experimental values. In both molecules, there is an  $S_1/T_2/T_1$  three-state intersection region, which allows for an efficient transition from  $S_1$  to  $T_1$  by intersystem crossing through  $T_2$  acting as a relay state. The radical photo-

dissociation reactions then occur in the  $T_1$  state. On the basis of the current calculations, photodissociation mechanisms are proposed for both molecules, which are consistent with and explain the experimental observations.

#### Appendix A. Supplementary data

Supplementary data associated with this article can be found, in the online version, at <http://dx.doi.org/10.1016/j.cplett.2012.04.008>.

#### References

- [1] N.J. Turro, *Modern Molecular Photochemistry*, Benjamin/Cummings Publishing Company, Inc., Menlo Park, CA, 1978.
- [2] R. Schinke, *Photodissociation Dynamics Spectroscopy and Fragmentation of Small Polyatomic Molecules*, Cambridge University Press, New York, USA, 1993.
- [3] W. Domcke, D.R. Yarkony, H. Köppel (Eds.), *Conical Intersections: Electronic Structure, Dynamics & Spectroscopy*, World Scientific, 2004.
- [4] W.H. Fang, *Acc. Chem. Res.* 41 (2008) 452.
- [5] S. de Feyter, E.W.G. Diau, A.H. Zewail, *Angew. Chem.* 112 (2000) 266.
- [6] S. Maeda, K. Ohno, K. Morokuma, *J. Phys. Chem. Lett.* 1 (2010) 1841.
- [7] L.J. Butler, *Annu. Rev. Phys. Chem.* 49 (1998) 125.
- [8] W.H. Fang, D.L. Phillips, *Chem. Phys. Chem.* 3 (2002) 889.
- [9] J. Li, F. Zhang, W.H. Fang, *J. Phys. Chem. A* 109 (2005) 7718.
- [10] Q. Fang, Y.J. Liu, *J. Phys. Chem. A* 114 (2010) 680.
- [11] J. Smolarek, R. Zwarich, L. Goodman, *J. Mol. Spectrosc.* 43 (1972) 416.
- [12] M. Berger, I.L. Goldblatt, C. Steel, *J. Am. Chem. Soc.* 95 (1973) 1717.
- [13] J. Metcalfe, R.G. Brown, D. Phillips, *J. Chem. Soc. Faraday Trans. II* 71 (1975) 409.
- [14] Y. Hirata, E.C. Lim, *J. Chem. Phys.* 72 (1980) 5505.
- [15] H. Abe, S. Kamei, N. Mikami, M. Ito, *Chem. Phys. Lett.* 109 (1984) 217.
- [16] N. Ohmori, T. Suzuki, M. Ito, *J. Phys. Chem.* 92 (1988) 1086.
- [17] C.R. Silva, J.P. Reilly, *J. Phys. Chem. A* 101 (1997) 7934.

- [18] H.Q. Zhao, Y.S. Cheung, C.L. Liao, C.X. Liao, C.Y. Ng, W.K. Li, *J. Chem. Phys.* 107 (1997) 7230.
- [19] T. Etzkorn, B. Klotz, S. Sørensen, I.V. Patroescu, I. Barnes, K.H. Becker, U. Platt, *Atmos. Environ.* 33 (1999) 525.
- [20] S.-H. Lee, K.-C. Tang, I.-C. Chen, M. Schmitt, J.P. Shaffer, T. Schultz, J.G. Underwood, M.Z. Zgierski, A. Stolow, *J. Phys. Chem. A* 106 (2002) 8979.
- [21] G. Thiault, A. Mellouki, G. Le Bras, A. Chakir, N. Sokolowski-Gomes, D. Daumont, *J. Photochem. Photobiol. A: Chem.* 162 (2004) 273.
- [22] B. Xiang, C.Z. Zhu, L. Zhu, *Chem. Phys. Lett.* 474 (2009) 74.
- [23] L. Zhu, T.J. Cronin, *Chem. Phys. Lett.* 317 (2000) 227.
- [24] B.K. Liu, B.X. Wang, Y.Q. Wang, L. Wang, *Chin. J. Chem. Phys.* 22 (2009) 597.
- [25] S. Park, J. Feenstra, A. Zewail, *J. Chem. Phys.* 124 (2006) 174707.
- [26] A. Bagchi, Y. Huang, Z. Xu, P. Raghunath, Y. Lee, C. Ni, M. Lin, Y. Lee, *Chem. Asian J.* 6 (2011) 2961.
- [27] T. Schaefer, T.A. Wildman, R. Sebastian, *J. Mol. Struct. (Theochem)* 93 (1982) 89.
- [28] C.W. Bock, M. Trachtman, P. George, *J. Mol. Struct. (Theochem)* 122 (1985) 155.
- [29] B. Coussens, K. Pierloot, R.J. Meier, *J. Mol. Struct. (Theochem)* 259 (1992) 331.
- [30] A.M. Rodriguez, F.A. Giannini, H.A. Baldoni, F.D. Suvire, S. Zaccchino, R.D. Enriz, P. Cszaszar, I.G. Csizmadia, *J. Mol. Struct. (Theochem)* 463 (1999) 283.
- [31] V. Molina, M. Merchán, *J. Phys. Chem. A* 105 (2001) 3745.
- [32] H.Y. Xiao, Y.J. Liu, W.H. Fang, *J. Mol. Struct. (Theochem)* 802 (2007) 99.
- [33] R. Ditchfield, W.J. Hehre, J.A. Pople, *J. Chem. Phys.* 54 (1971) 724.
- [34] P. Celani, H. Stoll, H.-J. Werner, *Mol. Phys.* 102 (2004) 2369.
- [35] H.-J. Werner, *Mol. Phys.* 89 (1996) 645.
- [36] P. Celani, H.-J. Werner, *J. Chem. Phys.* 112 (2000) 5546.
- [37] T.H. Dunning Jr., *J. Chem. Phys.* 90 (1989) 1007.
- [38] A. Becke, *Phys. Rev. A* 38 (1988) 3098.
- [39] C.T. Lee, W.T. Yang, R.G. Parr, *Phys. Rev. B* 37 (1988) 785.
- [40] H.J. Werner, P.J. Knowles, R. Lindh, F.R. Manby, M. Schütz, P. Celani, T. Korona, G. Rauhut, R.D. Amos, A. Bernhardsson, A. Berning, D.L. Cooper, M.J.O. Deegan, A.J. Dobbyn, F. Eckert, C. Hampel, G. Hetzer, A.W. Lloyd, S.J. McNicholas, W. Meyer, M.E. Mura, A. Nicklass, P. Palmieri, R. Pitzer, U. Schumann, H. Stoll, A.J. Stone, R. Tarroni, T. Thorsteinsson, MOLPRO, version 2006.6, a package of ab initio programs, 2006. See <http://www.molpro.net>.
- [41] M.J. Frisch, G.W. Trucks, H.B. Schlegel, G.E. Scuseria, M.A. Robb, J.R. Cheesem, G. Scalmani, V. Barone, B. Mennucci, G.A. Petersson, H. Nakatsuji, M. Caricato, X. Li, H.P. Hratchian, A.F. Izmaylov, J. Bloino, G. Zheng, J.L. Sonnenberg, M. Hada, M. Ehara, K. Toyota, R. Fukuda, J. Hasegawa, M. Ishida, T. Nakajima, Y. Honda, O. Kitao, H. Nakai, T. Vreven, J.A.M. Jr., J.E. Peralta, F. Ogliaro, M. Bearpark, J.J. Heyd, E. Brothers, K.N. Kudin, V.N. Staroverov, R. Kobayashi, J. Normand, K. Raghavachari, A. Rendell, J.C. Burant, S.S. Iyengar, J. Tomasi, M. Cossi, N. Rega, J.M. Millam, M. Klene, J.E. Knox, J.B. Cross, V. Bakken, C. Adamo, J. Jaramillo, R. Gomperts, R.E. Stratmann, O. Yazyev, A.J. Austin, R. Cammi, C. Pomelli, J.W. Ochterski, R.L. Martin, K. Morokuma, V.G. Zakrzewski, G.A. Voth, P. Salvador, J.J. Dannenberg, S. Dapprich, A.D. Daniels, O. Farkas, J.B. Foresman, J.V. Ortiz, J. Cioslowski, D.J. Fox, Gaussian 09, Revision A.02. Gaussian Inc. Wallingford CT, 2009.
- [42] Y.W. Wang, H.Y. He, W.H. Fang, *J. Mol. Struct. (Theochem)* 634 (2003) 281.
- [43] M.R. Silva-Junior, M. Schreiber, S.P.A. Sauer, W. Thiel, *J. Chem. Phys.* 133 (2010) 174318.
- [44] B. Hajgato, D. Szieberth, P. Geerlings, F. De Proft, M.S. Deleuze, *J. Chem. Phys.* 131 (2009) 224321.
- [45] T. Shiozaki, H.-J. Werner, *J. Chem. Phys.* 133 (2010) 141103.
- [46] M.A. El-Sayed, S.K. Lower, *Chem. Rev.* 66 (1966) 199.
- [47] H.A. Bethe, E.E. Salpeter, *Quantum Mechanics of One- and Two-Electron Systems*, Springer, Verlag, Berlin, 1957.